



**University of  
Nottingham**

UK | CHINA | MALAYSIA

**MODELLING DROPLET HEAT AND MASS TRANSFER IN AERO-  
ENGINE BEARING CHAMBERS**

Dafne Gaviria Arcila

BEng, MEng

**Thesis submitted to The University of Nottingham  
for the degree of Doctor of Philosophy**

**September 2019**

## **Abstract**

Bearings are critical elements of aero-engines because they support the axial and radial loads of the turbomachinery and allow the transfer of the engine thrust forces onto the airframe. The bearings are enclosed by a chamber to avoid oil leakages to other parts of the turbine. Inside bearing chambers, we can find a mixture of air and oil, where the oil has the function of cooling and lubricating the bearing elements and the chamber walls. This oil can be found in many forms; one of them (at one extreme end of the spectrum and which we try to avoid) is droplets, which travel across the chamber and interact with the swirling air (core flow). The droplet's interaction within the hot core flow might lead to the evaporation of the oil droplets, which is highly undesirable.

The two-phase flow inside bearing chambers has been studied by two main research groups, the Gas Turbine and Transmission Research Centre (G2TRC) at the University of Nottingham and the Karlsruhe Institute of Technology (KIT) in Germany, who studied the thin film formation and droplet–film interaction (Kakimpa et al., 2014, Peduto, 2015), the flow of isothermal droplets in bearing chambers (Chen et al., 2011a, Farrall et al., 2007, Farrall et al., 2006, Peduto, 2015) and the heat transfer mechanisms between the oil droplets and the surrounding air (Adeniyi, 2015, Rosenlieb, 1978, Sun et al., 2016a, Sun et al., 2016b), with one historical paper and some recent Chinese contributions from outside these groups. However, the evaporation process and its effect on the performance of the chamber lubrication and thermal management have received little to no attention. Therefore, the investigation of the heating process of oil droplets in high-speed swirling flow has been identified here as a relevant niche for research, with questions on the thermal role of droplets in modifying chamber temperature as well as the risk presented

by them as the temperature of the core keeps rising. Such a study will enable designers to better account for the need, or not, to design more carefully for droplets with a view to limiting their formation, accounting for their roles on the overall chamber temperature and/or better controlling their journey through the system.

The aim of this research is hence to analyse the process of oil droplet evaporation under conditions relevant to an aero-engine bearing chamber. The ultimate goal of developing a model to accurately predict the oil–air heat and mass transfer mechanisms in the core flow region is pursued. Additionally, a better understanding of the flow inside an oil droplet and how this affects evaporation is sought. This prediction can be significant because, apparently, only a few people have studied this before (Rosenlieb, 1978).

This research presents the results of a numerical study of the evaporation process of a single droplet under bearing chamber temperature and airflow conditions. The two-phase flow is simulated using the volume of fluid (VOF) method approach in the commercial ANSYS environment into which the D-square law evaporation model was implemented with a user-defined function (UDF). This model is validated using previously published results for fuel droplets in air (Daïf et al., 1998, Nomura et al., 1996).

The validated model is then applied to the investigation of smaller droplets, which are representative of those found in bearing chambers. Different conditions are studied in a parametric study that evaluates the droplet evaporation process for a range of representative conditions.

The oil evaporation rate and the evolution of the temporal reduction of the droplet's diameter are quantified, in relation to air velocity and the droplet core's temperature, for example. It is concluded that droplets with an initial diameter of less than 200  $\mu\text{m}$  (which

may remain in the chamber core region for more than 0.3 s) are likely to evaporate completely; this is significant because these can be considered relatively 'large' droplets in the chambers we studied. Droplets with diameters smaller than 100 $\mu\text{m}$  all evaporate very quickly. The evaporation rate is higher for droplets exposed to a higher velocity convective flow. The issue is therefore found to be very tangible.

This study estimates the droplet's heat and mass transfer and the associated phase change in a bearing chamber. The study also provides a best practice to predict the behaviour of small droplets under the effects of high-temperature and high-velocity convective airflows.

This work estimated the vapour concentration needed to reach the flammability limits for droplets of PEC5 travelling in the core flow of bearing chambers. The research found that the vapour concentration in the bearing chamber is lower than the flammability range. Additionally, it provides a calculation for the amount of vapour produced by different sized droplets of oil in bearing chamber conditions, as well as the estimation of the lifetime of oil droplets in bearing chamber conditions.

In this analysis, an internal convective flow was found in the heating-up and phase-change periods. The phase-change stage showed bubble formation inside the droplet with vortices associated with this effect. In some cases, the bubbles collapsed whilst releasing a portion of liquid, which sometimes caused the formation of a small secondary droplet. The radiation heat transfer was analysed from a parametric study to observe whether the radiation affects the heat and mass transfer from the environment to the droplet, which is travelling in the core flow. Radiation in the environment might have different effects on droplet evaporation. Firstly, it was noticed that the evaporation rate, at the beginning of

the evaporation process, might be lower in a case that does not include radiation. Furthermore, radiation affects the heating up period and it might also affect the oil vapour distribution around the droplet's surface at the beginning of the evaporation process as well as the droplet's internal flow field.

Moreover, we noticed that when the evaporation process is prolonged, radiation has no effect on the evaporation rate. In addition, it was observed that radiation might increase the droplet's internal velocity.

Finally, it must be highlighted that the present method was successfully validated against the correlations proposed in the literature, showing a good agreement with the theory used to formulate the correlations as mentioned above. Therefore, this confirms that the present study gives us the means to evaluate oil droplet evaporation in aero-engine bearing chambers.

## **List of Publications & Presentation Highlights**

### **Published**

- Gaviria Arcila Dafne, Morvan Hervé, Simmons Kathy, Ambrose Stephen, Kakimpa Bruce, Walsh Michael., “Modelling Droplet Heat and Mass Transfer in Aero-engine Bearing Chambers”, ASME, Turbo Expo 2019, Turbomachinery: Design Methods & CFD Modelling for Turbomachinery. GT2019-91657. In process

### **Pending/in review**

- Gaviria Arcila Dafne, Morvan Hervé, Simmons Kathy, Ambrose Stephen, Kakimpa Bruce, Walsh Michael., “Modelling Droplet Heat and Mass Transfer in Aero-engine Bearing Chambers representative conditions including radiation”. International Journal of Heat and Mass Transfer. To be submitted.

### **Poster and presentations**

- 3-minute of speech. Amelia Earhart Celebration Dinner in London. 2018
- Presentation at the European Parliament. 6<sup>th</sup> Symposium of CONACYT Fellows in Europe 2017

## Acknowledgements

This research was done at the Gas Turbine and Transmission Research Centre G2TRC with the valuable financial support of The National Council for Science and Technology of Mexico (CONACYT) and ZONTA International who recognized me with the Amelia Earhart fellowship 2017.

I am very grateful to Rolls-Royce for their technical and financial input. I would like to thank The University of Nottingham for the access to the High Performance Computing Facility. I would appreciate the financial support of the Graduate School and the G2TRC for cover my expenses in the presentation of my paper in the Turbo Expo 2019 in Phoenix Arizona.

I would like to express my sincere gratitude to my supervisors Prof. Hervé Morvan, Dr. Kathy Johnson and Dr. Stephen Ambrose for their guidance, supervision and valuable feedback. I would like to thanks to Dr. Richard Jefferson-Loveday for his patience and valuable comments in the progress of my research. Special thanks to Dr. Isaías Hernandez Carrillo, Dr. Bruce Kakimpa, Dr. Adeniyi Akinola, Dr. Andrea Bristot, Dr. Kiran Kumar PVS, Dr. Jee Loong Hee, Dr. Kuldeep Sing, Dr. Medhat Sharabi and Mike Walsh for their technical advice and their guidance. I would like to express my gratitude to Akram Radwan for his support from ANSYS Inc.

I thank to my colleagues and friends from the G2TRC, specially Dr. Paloma Paleo Cageao, Dr. Evgenia Korsukova, Piotr Zacharzewski, Martin Berthold, Dr. Omar Iracheta, Achinie Warusevitane, Sunil Chadha, Timothy Whitehouse, Bob Stables, Andrew Nicoli, Dr. Benjamin Rothwell, among others.

Last but no least to God, to my mom and to my boyfriend Isaías (muchas gracias a los dos por confiar siempre en mí) for your strong support and encouragement, to Robin for gave me a short hope, to my family and to all my friends, who are also part of my family, for sharing with me good and bad moments along this long journey.

*“Dripping water hollows out stone, not through force, but through persistence”*

*Ovid*

*“La gota de agua perfora la roca, no por su fuerza sino por su constancia”*

*Ovidio*

## Table of contents

1	Introduction .....	31
1.1	Aim.....	36
1.2	Objectives.....	36
1.3	Structure of the thesis.....	37
2	Literature review .....	38
2.1	Oil droplets in bearing chambers .....	38
2.1.1	Droplet formation .....	39
2.1.2	Droplet impingement and formation of secondary droplets .....	41
2.1.3	Droplet size distribution and particle tracking.....	47
2.1.4	Droplet motion.....	51
2.1.5	Oil droplet heat transfer and mass transfer in bearing chambers.....	62
2.2	Oil droplet evaporation in a convective environment.....	71
2.2.1	Oil droplet internal circulation.....	72
2.2.2	Droplet vaporisation of oil lubricant.....	76
2.2.3	Droplet evaporation including radiation effects .....	83
2.3	Summary .....	86
3	CFD Methodology.....	88
3.1	Physical model .....	88
3.1.1	VOF to track the gas–liquid interface.....	89

	11
3.1.2	Momentum equation .....95
3.1.3	Interfacial mass transfer: $D^2$ -law .....97
3.1.4	Species transport .....100
3.1.5	Energy equation .....102
3.1.6	Radiation modelling.....102
3.2	Numerical model.....106
3.2.1	Discretisation .....107
3.2.2	Pressure–velocity coupling .....108
3.2.3	Moving frame of reference .....108
3.3	Material properties .....111
3.3.1	Air properties .....111
3.3.2	n-heptane and n-decane properties .....112
3.3.3	Oil properties .....113
3.4	Summary .....118
4	Validation of the evaporation model .....119
4.1	Introduction .....119
4.2	Overview of the reference literature .....119
4.2.1	Experimental setup .....119
4.3	CFD case setup.....122
4.3.1	Geometry and boundary conditions.....124

	12
4.3.2 Solution methods .....	125
4.3.3 Mesh.....	127
4.4 Results and discussion .....	132
4.4.1 Internal circulation.....	134
4.4.2 Temperature .....	138
4.4.3 Vapour mass fraction.....	141
4.4.4 Wake length .....	143
4.5 Validation of radiation modelling with evaporation .....	147
4.5.1 Experimental setup .....	147
4.5.2 CFD setup .....	148
4.5.3 Solution methods .....	150
4.5.4 Mesh.....	150
4.5.5 Results and discussions.....	151
4.6 Guidelines and recommendations .....	154
4.7 Summary .....	155
5 Modelling oil droplet heat and mass transfer in aero-engine bearing chamber conditions .....	157
5.1 Case setup .....	159
5.1.1 Analysis with a non-adaptive mesh .....	159
5.2 Results and discussions .....	163

5.2.1	Results of a single oil droplet under a convective environment .....	163
5.2.2	Analysis with an adaptive mesh refinement .....	176
5.2.3	Effect of varying initial droplet diameter .....	182
5.2.4	Effect of air velocity .....	207
5.2.5	Effect of bearing chamber ambient temperature.....	221
5.2.6	Effect of radiation .....	239
5.2.7	Vapour mass fraction.....	258
5.2.8	Correlations.....	265
6	Conclusions .....	270
6.1	Main achievements.....	270
6.2	Contributions to knowledge .....	278
6.3	Future work.....	279
7	References .....	283
8	Annex .....	294
8.1	Literature review .....	294
8.1.1	Two-phase flow in bearing chambers .....	294
8.2	Modelling droplets inside bearing chambers-Case issues.....	298
8.3	Radiation models advantages and limitations. ....	298
8.4	Force balance analysis.....	299
8.5	Calculation of Reynolds numbers inside the bearing chamber. ....	300

8.6 Calculation of the time it takes for a drop to travel from the bearings to walls according to the literature review.....	303
8.7 User defined function to calculate the evaporation model in droplets and implement it in ANSYS Fluent.....	308
8.7.1 Validation of fuel droplets .....	308
8.7.2 Modelling of oil droplets inside bearing chamber conditions .....	309

## List of figures

Figure 1.1. Aero-engine (Aviation, 2019).....	31
Figure 1.2. Locations of bearing chambers on the Advance turbine (Adapted from Rolls-Royce, 2016) .....	32
Figure 2.1. Types of two-phase flow pattern inside bearing chambers (adapted from (Peduto, 2015) .....	39
Figure 2.2. Droplet formations according to jet break-up regimes: a) Rayleigh, b) First wind-induced, c) Second wind-induced and d) Atomisation (see Husted et al., 2004) ...	40
Figure 2.3. Fluid break-up regimes defined by Oh and Re numbers (see Hart, 2005) ....	40
Figure 2.4. Jet break-up of a full cone diesel spray (see Baumgarten, 2006) .....	41
Figure 2.5. Visualisation of droplet entrainment in wall oil film (see Gorse et al., 2004) .....	43
Figure 2.6. Crown formation characteristics (see Peduto, 2015) .....	44
Figure 2.7. Correlations between numerical and experimental results of the crown evolution during the impingement process (see Peduto, 2015) .....	45
Figure 2.8. Oil droplet trajectory according to its diameter (see Glahn et al., 1996).....	48
Figure 2.9. Droplet size distribution fitted to droplet counts with the Rosin–Rammler distribution (Hart, 2005).....	50
Figure 2.10. Secondary flow field at $n = 9700$ rpm: a) $\dot{m} = 6.2$ g/s; b) $\dot{m} = 8.5$ g/s; c) $\dot{m} = 12.7$ g/s; d) $\dot{m} = 16.9$ g/s (Gorse et al., 2003) .....	52
Figure 2.11. Recirculation zones inside bearing chambers (Aidarinis et al., 2011) .....	53
Figure 2.12. Effect of sealing air on droplet velocity (Sun et al., 2013).....	54
Figure 2.13. Residence time of a parent droplet (Weinstock and Heister, 2004) .....	56
Figure 2.14. Regimes of droplet deformation and break-up (adapted from Liu, 2000)...	60
Figure 2.15. Some modes of droplet break-up. <i>Left</i> : bag break-up, <i>Right</i> : shear break-up (Liu, 2000) .....	61
Figure 2.16. Calculation of the heat transfer coefficient at the wall of bearing chambers (see Adeniyi, 2015) .....	63
Figure 2.17. Flow regimes in the bearing chamber (adapted from Kurz et al., 2014) .....	64

Figure 2.18. Axisymmetric flow field and internal circulation of a vaporising droplet (Sirignano, 2010) .....	75
Figure 2.19 Operating conditions of HP/IP bearing chambers and ignition mechanisms of oil fires (adapted from Hashmi, 2012, Willenborg et al., 2002).....	78
Figure 2.20. Relationship between different flammability properties (Dimian et al., 2014) .....	81
Figure 3.1. Steps for the interpolation near the interface using the geometric reconstruction algorithm .....	91
Figure 3.2. Interface shape represented by the geometric reconstruction scheme (ANSYS, 2016b).....	92
Figure 3.3. Numerical diffusivities presented using the implicit formulation with the compressive scheme.....	93
Figure 3.4. Representation of the contact angle and surface tension forces between droplet and suspender.....	96
Figure 3.5. Graphical representation of the D <sup>2</sup> -law (Turns, 2000) .....	99
Figure 3.6. Balance force analysis of a suspended droplet under convective airflow ...	109
Figure 3.7. Droplet external forces (drag force and weight) vs droplet radius reduction for an oil droplet with an initial diameter of 200 $\mu\text{m}$ under airflow with a velocity of 1 m/s.....	110
Figure 4.1. Experimental setup schematic (see Daïf et al., 1998).....	120
Figure 4.2. Temporal evolution of droplet diameter of n-heptane and n-decane and droplet surface temperature of n-decane (Daïf et al., 1998) .....	121
Figure 4.3. Geometry and boundary conditions.....	124
Figure 4.4. Meshing zones .....	127
Figure 4.5 Mesh independence study of the temporal evolution of droplet diameter of n-heptane (Case 1) between the present predictions and experimental data (Daïf et al., 1998) .....	130
Figure 4.6. Mesh independence study of the temporal evolution of droplet diameter of n-decane (Case 2) between the present predictions and experimental data (Daïf et al., 1998) .....	132
Figure 4.7. Comparison of temporal evolution of droplet diameter of n-heptane and n-decane between the present predictions and experimental data (Daïf et al., 1998) .....	134
Figure 4.8. Schematic of the heat transfer by convection from the droplet's exterior to interior .....	135

Figure 4.9. Comparison of the streamlines of normalised velocity of an n-heptane droplet at 0.5 s: a) previous numerical predictions (Strotos et al., 2016); b) present predictions .....	136
Figure 4.10. Comparison of the streamlines of normalised velocity of an n-decane droplet at 0.25 s: a) previous numerical predictions (Strotos et al., 2016); b) present predictions .....	137
Figure 4.11. a) Internal droplet temperature contours, b) internal vortex of an n-decane droplet at 0.25 s .....	138
Figure 4.12. Temperature field of an n-decane droplet at 0.25 s: a) previous numerical predictions (Strotos et al., 2016), b) present predictions.....	139
Figure 4.13. Comparison of temperature contours of Case 1 (n-heptane) with Case 2 (n-decane) at 0.25 s .....	140
Figure 4.14. n-heptane droplet at 0.5 s: a) temperature contours, b) vapour mass fraction .....	141
Figure 4.15. Vapour mass fraction of an n-decane droplet at 0.25 s: a) previous numerical predictions (Strotos et al., 2016), b) present predictions.....	142
Figure 4.16. Comparison of vapour mass fraction contours of Case 1 (n-heptane) with Case 2 (n-decane) at 0.25 s .....	143
Figure 4.17. Axial velocity of an n-heptane droplet at 0.25 s .....	144
Figure 4.18. Axial velocity of an n-decane droplet at 0.25 s .....	146
Figure 4.19. Experimental setup to validate the radiation modelling (Nomura et al., 1996) .....	148
Figure 4.20. Geometry and boundary conditions to validate the radiation modelling...	149
Figure 4.21. Comparison of the temporal evolution of the droplet diameter with the experimental data of Nomura et al. (1996) .....	152
Figure 5.1. Variation of droplet velocity with droplet radius .....	159
Figure 5.2. Modifications to modelling droplets inside bearing chambers.....	162
Figure 5.3. Temporal evolution of droplet diameter of PEC5 under convective airflow at 350 K, 450 K and 550 K, with an initial diameter of 200 $\mu\text{m}$ at 5 m/s.....	164
Figure 5.4. Temporal evolution of droplet diameter of PEC5 under convective airflow at 350 K, 450 K and 550 K, with an initial diameter of 200 $\mu\text{m}$ at 1 m/s.....	164
Figure 5.5. Contours at 0.017 s of oil vapour mass fraction: a) Case 1, b) Case 2; temperature: c) Case 1, d) Case 2; velocity streamlines: e) Case 1, f) Case 2.....	166

Figure 5.6. Contours at 0.017 s of temperature: a) Case 3, b) Case 4; velocity streamlines: c) Case 3, d) Case 4 .....	167
Figure 5.7. Contours at 0.017 s of temperature: a) Case 5, b) Case 6; velocity streamlines: c) Case 5, d) Case 6 .....	168
Figure 5.8. Bubble rupture process and ligament formation (Avulapati et al., 2016) ...	171
Figure 5.9. Contours at 0.09 s of oil vapour mass fraction: a) Case 1, b) Case 2; temperature: c) Case 1, d) Case 2; velocity streamlines: e) Case 1, f) Case 2 .....	171
Figure 5.10. Contours at 0.09 s of oil vapour mass fraction: a) Case 3, b) Case 4; temperature: c) Case 3, d) Case 4; velocity streamlines: e) Case 3, f) Case 4 .....	172
Figure 5.11. Contours of temperature of the droplet's interior at 0.09 s: a) Case 5, b) Case 6 .....	173
Figure 5.12. Contours at 0.09 s of temperature: a) Case 5, b) Case 6; velocity streamlines: c) Case 5, d) Case 6 .....	173
Figure 5.13. Levels of refinement with the gradient adaptive meshing approach .....	178
Figure 5.14. Gradient adaptive meshing approach after 0.0017 s in Case 7: a) levels of refinement, b) mesh refinement with volume fraction contours .....	178
Figure 5.15. Comparison of temporal evolution of droplet diameter computed with a) non-adaptive mesh and b) adaptive mesh .....	181
Figure 5.16. Comparison of a) non-adaptive mesh and b) adaptive mesh at the droplet's interface .....	181
Figure 5.17. Comparison of initial droplet diameter versus average evaporation rate per surface area .....	183
Figure 5.18. Non-dimensional squared diameter evolution for different initial droplet diameters, with air at 5 m/s and 550 K .....	184
Figure 5.19. Variation of evaporation rate over droplet surface area for different initial droplet diameters .....	184
Figure 5.20. Heat transfer ratio varying the initial droplet diameter, with air at 550 K and 5 m/s .....	186
Figure 5.21. Axisymmetric flow field of the internal circulation of a vaporising droplet; schematic reproduced for a droplet with initial diameter of 100 $\mu\text{m}$ , at 550 K and 5 m/s (adapted from Sirignano, 2010) .....	188
Figure 5.22. Region of interest to compute the average velocity magnitude at the droplet's interior .....	189

Figure 5.23. Oscillation of oil vapour mass fraction around the droplet's interface. $D_0 = 100 \mu\text{m}$ , $T = 550 \text{ K}$ , $V_{\text{air}} = 5 \text{ m/s}$ .....	190
Figure 5.24. Comparison of the average velocity at the droplet's interior varying the initial droplet diameter .....	192
Figure 5.25. Temporal evolution of the droplet normalised square diameter versus temperature evolution at the droplet surface $T_s$ and the droplet core $T_{\text{int}}$ for an initial diameter of $100 \mu\text{m}$ , with air at $550 \text{ K}$ and $5 \text{ m/s}$ .....	194
Figure 5.26. Contours and streamlines for a droplet with an initial diameter of $100 \mu\text{m}$ at <b><math>DD02 = 1</math></b> , $0.0031 \text{ s}$ : a) external droplet temperature, b) internal droplet temperature, c) velocity streamlines, d) warm and cold zones at the droplet's interior due to internal circulation.....	195
Figure 5.27. Contours and streamlines for a droplet with an initial diameter of $100 \mu\text{m}$ at <b><math>DD02 = 0.99</math></b> and $0.0042 \text{ s}$ : a) oil vapour mass fraction, b) liquid volume fraction, c) external temperature, d) internal temperature, e) velocity streamlines .....	196
Figure 5.28. Contours and streamlines for a droplet with an initial diameter of $100 \mu\text{m}$ at <b><math>DD02 = 0.81</math></b> and $0.0081 \text{ s}$ : a) oil vapour mass fraction, b) liquid volume fraction, c) external temperature, d) internal temperature, e) velocity streamlines .....	198
Figure 5.29. Temporal evolution of a droplet normalised square diameter versus temperature evolution at the droplet surface $T_s$ and the droplet core $T_{\text{int}}$ for an initial diameter of $200 \mu\text{m}$ , with air at $550 \text{ K}$ and $5 \text{ m/s}$ .....	199
Figure 5.30. Contours and streamlines for a droplet with an initial diameter of $200 \mu\text{m}$ at <b><math>DD02 = 1</math></b> and $0.01 \text{ s}$ : a) oil vapour mass fraction, b) liquid volume fraction, c) external temperature, d) internal temperature, e) velocity streamlines .....	201
Figure 5.31. Contours and streamlines for a droplet with an initial diameter of $200 \mu\text{m}$ at <b><math>DD02 = 0.99</math></b> and $0.015 \text{ s}$ : a) oil vapour mass fraction, b) liquid volume fraction, c) external temperature, d) internal temperature, e) velocity streamlines .....	202
Figure 5.32. Droplet representation of the two regions formed by the internal flow ....	203
Figure 5.33. Contours and streamlines for a droplet with an initial diameter of $200 \mu\text{m}$ at <b><math>DD02 = 0.97</math></b> and $0.024 \text{ s}$ : a) oil vapour mass fraction, b) liquid volume fraction, c) external temperature, d) internal temperature, e) velocity streamlines .....	204
Figure 5.34. Temporal evolution of droplet normalised square diameter versus temperature evolution at the droplet surface $T_s$ and the droplet core $T_{\text{int}}$ for an initial diameter of $500 \mu\text{m}$ , with air at $550 \text{ K}$ and $5 \text{ m/s}$ .....	205
Figure 5.35. Contours and streamlines for a droplet with an initial diameter of $500 \mu\text{m}$ at <b><math>DD02 = 1</math></b> and $0.02 \text{ s}$ : a) external temperature, b) internal temperature, c) velocity streamlines.....	206

- Figure 5.36. Contours and streamlines for a droplet with an initial diameter of  $500\ \mu\text{m}$  at  $DD02 = 0.99$  and  $0.05\ \text{s}$ : a) oil vapour mass fraction, b) liquid volume fraction, c) external temperature, d) internal temperature, e) velocity streamlines.....207
- Figure 5.37. Non-dimensional squared diameter evolution for an initial droplet diameter of  $200\ \mu\text{m}$ , varying the air inlet velocity ( $5\ \text{m/s}$  and  $1\ \text{m/s}$ ).....209
- Figure 5.38. Variation of evaporation rate over a droplet's surface area for different air inlet velocity ( $5\ \text{m/s}$  and  $1\ \text{m/s}$ ).....209
- Figure 5.39. Heat transfer ratio varying the inlet air velocities and with air at  $550\ \text{K}$  and  $D_0 = 200\ \mu\text{m}$ .....210
- Figure 5.40. Comparison of the velocity magnitude at the droplet's interior varying the velocity of air .....212
- Figure 5.41. Temporal evolution of a droplet normalised square diameter versus temperature evolution at the droplet surface  $T_s$  and the droplet core  $T_{\text{int}}$  for an initial diameter of  $200\ \mu\text{m}$ , with air at  $550\ \text{K}$  and  $1\ \text{m/s}$  .....213
- Figure 5.42. Comparison of contours and streamlines for two cases varying the air velocity with an initial droplet diameter of  $200\ \mu\text{m}$  and air at  $550\ \text{K}$  at  $DD02 = 1$ : a) oil vapour mass fraction for the case at  $5\ \text{m/s}$ , b) oil vapour mass fraction for the case at  $1\ \text{m/s}$ , c) streamlines of internal velocity for the case at  $5\ \text{m/s}$ , d) streamlines of internal velocity for the case at  $1\ \text{m/s}$ .....214
- Figure 5.43. Contours and streamlines at  $DD02 = 1$  and  $0.021\ \text{s}$  for a droplet with an initial diameter of  $200\ \mu\text{m}$  under airflow at  $1\ \text{m/s}$ : a) oil vapour mass fraction, b) liquid volume fraction, c) external temperature, d) internal temperature, e) velocity streamlines .....215
- Figure 5.44. Contours and streamlines at  $DD02 = 0.99$  and  $0.023\ \text{s}$  for a droplet with an initial diameter of  $200\ \mu\text{m}$  under airflow at  $1\ \text{m/s}$ : a) oil vapour mass fraction, b) liquid volume fraction, c) external temperature, d) internal temperature, e) velocity streamlines.....216
- Figure 5.45. Comparison of velocity streamlines of two cases varying the air velocity with an initial droplet diameter of  $200\ \mu\text{m}$  and air at  $550\ \text{K}$  at  $DD02 = 0.99$ : a) streamlines of internal velocity for the case at  $5\ \text{m/s}$ , b) streamlines of internal velocity for the case at  $1\ \text{m/s}$ .....217
- Figure 5.46. Contours and streamlines at  $DD02 = 0.97$  and  $0.039\ \text{s}$  for a droplet with an initial diameter of  $200\ \mu\text{m}$  under airflow at  $1\ \text{m/s}$ : a) oil vapour mass fraction, b) liquid volume fraction, c) external temperature, d) internal temperature, e) velocity streamlines.....219
- Figure 5.47. Comparison of velocity streamlines of two cases varying the air velocity with an initial droplet diameter of  $200\ \mu\text{m}$  and air at  $550\ \text{K}$  at  $DD02 = 0.97$ : a)

streamlines of internal velocity for the case at 5 m/s, b) streamlines of internal velocity for the case at 1 m/s.....	220
Figure 5.48. Non-dimensional squared diameter evolution for an initial droplet diameter of 200 $\mu\text{m}$ varying the air inlet temperature .....	222
Figure 5.49. Variation of evaporation rate over a droplet's surface area for different ambient temperatures .....	223
Figure 5.50. Effects of air temperature on the average evaporation rate per surface area for a droplet with an initial diameter of 200 $\mu\text{m}$ and air velocity of 5 m/s .....	224
Figure 5.51. Heat transfer ratio for different ambient temperatures .....	225
Figure 5.52. Comparison of the velocity magnitude at the droplet's interior varying the temperature of air .....	226
Figure 5.53. Temporal evolution of droplet normalised square diameter versus temperature evolution at the droplet surface $T_s$ and the droplet core $T_{\text{int}}$ for an initial diameter of 200 $\mu\text{m}$ , with air at 450 K and 5 m/s .....	227
Figure 5.54. Contours and streamlines at <b><math>DD02 = 1</math></b> and 0.01 s for a droplet with an initial diameter of 200 $\mu\text{m}$ under airflow at 450 K: a) external temperature, b) internal temperature, c) velocity streamlines .....	228
Figure 5.55. Comparison of velocity streamlines of two cases varying the air velocity with an initial droplet diameter of 200 $\mu\text{m}$ and air at 5 m/s at <b><math>DD02 = 1</math></b> : a) streamlines of internal velocity for the case at 550 K, b) streamlines of internal velocity for the case at 450 K.....	229
Figure 5.56. Contours and streamlines at <b><math>DD02 = 0.99</math></b> and 0.031 s for a droplet with an initial diameter of 200 $\mu\text{m}$ under airflow at 450 K: a) oil vapour mass fraction, b) liquid volume fraction, c) external temperature, d) internal temperature, e) velocity streamlines.....	230
Figure 5.57. Comparison of velocity streamlines of two cases varying the air velocity with an initial droplet diameter of 200 $\mu\text{m}$ and air at 5 m/s at <b><math>DD02 = 0.99</math></b> : a) streamlines of internal velocity for the case at 550 K, b) streamlines of internal velocity for the case at 450 K.....	231
Figure 5.58. Contours and streamlines at <b><math>DD02 = 0.97</math></b> and 0.047 s for a droplet with an initial diameter of 200 $\mu\text{m}$ under airflow at 450 K: a) oil vapour mass fraction, b) liquid volume fraction, c) external temperature, d) internal temperature, e) velocity streamlines.....	232
Figure 5.59. Comparison of velocity streamlines of two cases varying the air velocity with an initial droplet diameter of 200 $\mu\text{m}$ and air at 5 m/s at <b><math>DD02 = 0.97</math></b> : a) streamlines of internal velocity for the case at 550 K, b) streamlines of internal velocity for the case at 450 K.....	233

Figure 5.60. Temporal evolution of droplet normalised square diameter versus temperature evolution at the droplet surface $T_s$ and the droplet core $T_{int}$ for an initial diameter of 200 $\mu\text{m}$ , with air at 350 K and 5 m/s .....	234
Figure 5.61. Contours and streamlines at <b><math>DD02 = 1</math></b> and 0.008 s for a droplet with an initial diameter of 200 $\mu\text{m}$ under airflow at 350 K: a) external temperature, b) internal temperature, c) velocity streamlines .....	235
Figure 5.62. Comparison of velocity streamlines of two cases varying the air velocity with an initial droplet diameter of 200 $\mu\text{m}$ and air at 5 m/s at <b><math>DD02 = 1</math></b> : a) streamlines of internal velocity for the case at 550 K, b) streamlines of internal velocity for the case at 350 K.....	236
Figure 5.63. Contours and streamlines at <b><math>DD02 = 0.99</math></b> and 0.135 s for a droplet with an initial diameter of 200 $\mu\text{m}$ under airflow at 350 K: a) oil vapour mass fraction, b) liquid volume fraction, c) external temperature, d) internal temperature, e) velocity streamlines.....	237
Figure 5.64. Comparison of velocity streamlines of two cases varying the air velocity with an initial droplet diameter of 200 $\mu\text{m}$ and air at 5 m/s at <b><math>DD02 = 0.99</math></b> : a) streamlines of internal velocity for the case at 550 K, b) streamlines of internal velocity for the case at 350 K.....	238
Figure 5.65. Combustor and HP/IP bearing chamber locations on the Ultrafan engine (Adapted from Rolls-Royce, 2016).....	239
Figure 5.66. Effect of radiation on temporal evolution of droplet diameter for different initial diameters, with air at 5 m/s and 550 K .....	241
Figure 5.67. Effect of radiation on temporal evolution of droplet diameter for an initial diameter of 500 $\mu\text{m}$ , with air at 5 m/s and 550 K .....	242
Figure 5.68. Comparison of the evaporation rate over a droplet's surface area for an initial diameter of 100 $\mu\text{m}$ , with airflow at 5 m/s .....	243
Figure 5.69. Comparison of oil vapour mass fraction for an initial droplet diameter of 100 $\mu\text{m}$ , with airflow of 5 m/s at 0.004 s: a) no radiative environment, b) a radiative environment with a wall at 550 K, c) a radiative environment with a wall at 850 K ....	244
Figure 5.70. Comparison of the evaporation rate over a droplet's surface area for an initial droplet diameter of 200 $\mu\text{m}$ , with airflow of 5 m/s.....	245
Figure 5.71. Comparison of the evaporation rate over a droplet's surface area for an initial droplet diameter of 500 $\mu\text{m}$ , with airflow of 5 m/s.....	245
Figure 5.72. Variation of heat transfer coefficient at the droplet's surface for different Reynolds numbers .....	247

Figure 5.73. Heat transfer ratio for different radiative ambient conditions at 5 m/s, surrounding a droplet with an initial diameter of 500 $\mu\text{m}$ .....	249
Figure 5.74. Heat transfer ratio for different radiative ambient conditions at 5 m/s, surrounding droplets with initial diameters of 200 $\mu\text{m}$ and 100 $\mu\text{m}$ .....	250
Figure 5.75. Comparison of the velocity magnitude for different radiative ambient conditions at 5 m/s, surrounding a droplet with initial diameter of 200 $\mu\text{m}$ .....	251
Figure 5.76. Comparison of the velocity magnitude for different radiative ambient conditions at 5 m/s, surrounding a droplet with initial diameter of 500 $\mu\text{m}$ .....	252
Figure 5.77. Temporal evolution of droplet normalised square diameter versus temperature evolution at the droplet surface $T_s$ and the droplet core $T_{\text{int}}$ for an initial diameter of 200 $\mu\text{m}$ with a radiative environment and a wall at 550 K.....	253
Figure 5.78. Contours and streamlines at $DD02 = 1$ and 0.007 s for a droplet with an initial diameter of 200 $\mu\text{m}$ with a radiative environment and a wall at 550 K: a) oil vapour mass fraction, b) liquid volume fraction, c) external temperature, d) internal temperature, e) velocity streamlines .....	254
Figure 5.79. Contours and streamlines at $DD02 = 0.99$ and 0.010 s for a droplet with an initial diameter of 200 $\mu\text{m}$ with a radiative environment and a wall at 550 K: a) oil vapour mass fraction, b) liquid volume fraction, c) external temperature, d) internal temperature, e) velocity streamlines .....	255
Figure 5.80. Temporal evolution of droplet normalised square diameter versus temperature evolution at the droplet surface $T_s$ and the droplet core $T_{\text{int}}$ for an initial diameter of 200 $\mu\text{m}$ with a radiative environment and a wall at 850 K.....	256
Figure 5.81. Contours and streamlines at $DD02 = 1$ and 0.007 s for a droplet with an initial diameter of 200 $\mu\text{m}$ with a radiative environment and a wall at 850 K: a) oil vapour mass fraction, b) liquid volume fraction, c) external temperature, d) internal temperature, e) velocity streamlines .....	257
Figure 5.82. Contours and streamlines at $DD02 = 0.99$ and 0.010 s for a droplet with an initial diameter of 200 $\mu\text{m}$ with a radiative environment and a wall at 850 K: a) oil vapour mass fraction, b) liquid volume fraction, c) external temperature, d) internal temperature, e) velocity streamlines .....	258
Figure 5.83. Diameter histogram at 12,000 rpm (see Glahn et al., 1996).....	260
Figure 5.84. Cumulative number of droplets and number of droplets per diameter in the population (see Glahn et al., 1996) .....	261
Figure 5.85. Probability of cumulative number of droplets and probability of number of droplets per diameter in the population.....	261

Figure 5.86. Mass associated per droplet diameter and cumulative mass of oil per droplet diameter.....	262
Figure 5.87. Probability of mass associated per droplet diameter and probability of cumulative mass of oil per droplet diameter .....	262
Figure 5.88. Linear regression of the average evaporation rate per surface area for each droplet diameter with an air temperature of 550 K.....	263
Figure 5.89. Time of residence of droplets travelling from the bearings to the walls ...	264
Figure 5.90. Comparison of mass transfer results with the correlation presented by Renksizbulut and Yuen (1983).....	267
Figure 5.91. Comparison of heat transfer results with the correlation presented by Renksizbulut and Yuen (1983).....	268
Figure 8.1. Main contributors in the research on two-phase flow in bearing chambers .	294
Figure 8.2. Overview of the literature review from the University Technology Centre and Gas Turbine and Transmissions Research Centre.....	295
Figure 8.3. Overview of the literature review from the Karlsruhe Institute of Technology.....	296
Figure 8.4. Overview of the literature review from others research institutes and universities such as the Northwestern Polytechnical University. ....	297
Figure 8.5. Modifications done to modelling droplets inside bearing chambers. ....	298
Figure 8.6. Available radiation models in ANSYS fluent. ....	298
Figure 8.7 Drag force vs Weight for an oil droplet with 200 $\mu$ m of diameter under the airflow with velocity of 1m/s .....	299
Figure 8.8 Drag force vs Weight for a heptane droplet with 1052 $\mu$ m of diameter under the airflow with velocity of 3.2m/s .....	299
Figure 8.9. Calculation of Reynolds numbers inside the bearing chamber taking into account the air velocity at 10 m/s.....	300
Figure 8.10. Calculation of Reynolds numbers inside the bearing chamber taking into account the air velocity at 5 m/s.....	301
Figure 8.11. Calculation of Reynolds numbers inside the bearing chamber taking into account the air velocity at 1 m/s.....	302
Figure 8.12. Effect on the droplet diameter on its velocity and trajectory (Sun et al., 2016b). ....	303

Figure 8.13. Effect on the droplet diameter on its velocity and trajectory (Chen et al., 2014). .....304

## List of Tables

Table 2.1. Droplet impingement transition criteria (see Tkaczyk and Morvan, 2011)....	42
Table 2.2. Bearing chamber environment.....	70
Table 2.3. Flash point, fire point and autoignition temperatures of lubricants (Kuchta and Cato, 1968, Rosenlieb, 1978).....	82
Table 3.1. Considerations of available radiation models (ANSYS, 2016b) .....	104
Table 3.2. Air properties .....	112
Table 3.3. Liquid phase properties of n-heptane and n-decane.....	112
Table 3.4. Gas-phase properties of n-heptane and n-decane.....	113
Table 3.5. Liquid phase properties of PEC5 .....	114
Table 3.6. Gas-phase critical constants of PEC5 (Razzouk et al., 2007).....	115
Table 3.7. Lennard-Jones parameters values of n-heptane validation against the experimental values reported by (Michailidou et al., 2014) .....	116
Table 3.8. Binary diffusivity of allyl chloride comparison between estimated value against experimental value (Poling et al., 2001) .....	117
Table 4.1. Cases validated.....	122
Table 4.2. Solution methods .....	125
Table 4.3. Mesh sizing for Case 1.....	129
Table 4.4. Mesh sizing for Case 2.....	131
Table 4.5. Wake length and diameter comparison between Strotos's case and this research .....	146
Table 4.6. Cases to validate radiation modelling .....	149
Table 4.7. Solution methods to validate the radiation modelling .....	150
Table 4.8. Mesh sizing for Case 1.....	151
Table 4.9. Comparison of linear regression slopes to validate the radiation modelling	153
Table 5.1. Cases analysed with a non-adaptive mesh.....	161
Table 5.2. Cases analysed with adaptive mesh refinement.....	180

Table 5.3. Comparison of initial droplet diameters, evaporation rates and surface area per volume ratios.....	182
Table 5.4. Cases analysed considering heat transfer by radiation.....	240
Table 5.5. Vapour concentration per the fraction of oil converted into droplets in the bearing chamber .....	265
Table 8.1. Calculation of droplet journey time for initial diameters of 385 $\mu\text{m}$ , 185 $\mu\text{m}$ , 85 $\mu\text{m}$ and 35 $\mu\text{m}$ according to Figure 8.12.....	303
Table 8.2. Calculation of droplet journey time for initial diameters of 79 $\mu\text{m}$ for a shaft speed of 5000rpm.....	304
Table 8.3. Calculation of droplet journey time for initial diameters of 50 $\mu\text{m}$ for a shaft speed of 5000rpm.....	305
Table 8.4. Calculation of droplet journey time for initial diameters of 100 $\mu\text{m}$ for a shaft speed of 12000rpm.....	306
Table 8.5. Calculation of droplet journey time for initial diameters of 200 $\mu\text{m}$ for a shaft speed of 12000rpm.....	306
Table 8.6. Calculation of droplet journey time for initial diameters of 300 $\mu\text{m}$ for a shaft speed of 12000rpm.....	307
Table 8.7. Calculation of droplet journey time for initial diameters of 400 $\mu\text{m}$ for a shaft speed of 12000rpm.....	307

## Nomenclature

Symbol	Units	Description
$A$	$[m^2]$	Area
$C_d$		Drag force
$C_s$		Stoichiometric ratio
$D$	$[m]$	Diameter
$D, D_{ij}$	$[m/s^2]$	Binary diffusivity
$E$	$[J/kg]$	Specific energy
$F$	$[N/m^3]$	Body Force
$h_{fg}$	$[J/kg]$	Enthalpy of evaporation
$J$	$[kg/m^2s]$	Species flux
$K$	$[W/m K]$	Thermal conductivity
$LL$		Lower flammability limit
$M_w$	$[kg/kmol]$	Molecular weight
$m_i'''$	$[kg/m^3s]$	Volumetric mass transfer term
$M$	$[kg]$	Mass of droplet
$\hat{n}$	$[-]$	Normal vector
$n$		Number of values
$p$	$[N/m^2]$	Pressure
$r$	$[m]$	Radius
$R$	$[J/kmol]$	Universal gas constant
$S$	$[-]$	Source Term
$T$	$[K]$	Temperature
$t$	$[s]$	Time
$t^*$		Non-Dimensional time $t^* = \frac{tv}{D_0}$
$UL$		Upper flammability limit
$V$	$[m^3]$	Volume
$u$	$[m/s]$	Velocity
$v$	$[m^3]$	Atomic diffusion volume

$x$	[-]	Mole fraction of the gas phase
$y$	[-]	Mass fraction of the gas phase
$z$		Value

## Greek symbols

$\alpha$	[-]	Volume fraction
$\rho$	[Kg/m <sup>3</sup> ]	Density
$\kappa$	[m <sup>-1</sup> ]	Curvature
$\sigma$	[N-m]	Surface Tension
$\mu$	[Pa s]	Viscosity

## Subscripts

0	[J/kg]	Initial State
b		boiling
B	[m <sup>3</sup> ]	Boiling point
c		calculated
cr		critical
cell		Cell
D	[J/kmol]	Droplet
e		experimental

E	[K]	energy
f		face
g	[J/kg]	Gas
ij	[kg/m <sup>2</sup> s]	Species of the mixture
l	[J/kg]	Liquid
m	[m/s <sup>2</sup> ]	Momentum
q	[kg]	qth phase
s		suspender
Tot	[m]	Total
vap	[W/m K]	Vapour

## **Abbreviations**

ICE	Internal Combustion Engines
PISO	Pressure Implicit with Splitting of Operators
RMSE	Root Mean Square Error
SIMPLEC	Semi-Implicit Method for Pressure Linked Equations-Consistent
UDF	User Defined Functions
VOF	Volume of Fluid
UDM	User Define Memory

# 1 Introduction

One of the major challenges that the aerospace industry faces is to continue to improve the efficiency of aero-engines (Figure 1.1), as these will continue to play a key role in air transport. There are two levers to efficiency: (1) thermodynamics and (2) mechanical. Architecturally, this leads to higher bypass ratio gas turbine engines and, practically, to smaller yet higher energy and higher temperature cores. The transmission system is therefore subjected to harsher conditions than ever, manifesting in high temperatures which require the precise management of the transmission lubrication and cooling.



**Figure 1.1. Aero-engine (Aviation, 2019)**

The primary role of the lubrication system is to remove the excess heat generated by the movement of the bearings, gears and shafts, and it is externally driven by the compressed gas path and combustion chamber positioned around a tight engine core. The lubrication system also allows a reduction in friction within the transmission system by reducing friction among moving and stationary components. The main moving component

is the shaft, which has the principal role of transmitting power from the turbine to the compressor and fan. Hence, the shaft must be lubricated, allowing the turbine operation and the transmission of power from the turbine to the compressor and fan system (Rolls-Royce, 2005).

The shaft is supported by rolling elements, which are enclosed within bearing chambers. The bearing chamber has the purpose of enclosing the oil injected into the shaft to prevent this oil spreading to other parts of the turbine. In a typical three-shaft aero-engine, one bearing chamber can be found to protect the bearings, as illustrated in Figure 1.2. Bearing chambers can be found as follows: one at the front, one between the intermediate pressure (IP) turbine and the high pressure (HP) turbine (IP–HP), one from the HP turbine to the IP turbine and one at the tail.

Cooling the HP and IP chambers is particularly important. This is because most of the radiant heat comes from the combustor, which surrounds these chambers as observed in Figure 1.2. Thus, thermal management in this area is of great importance.

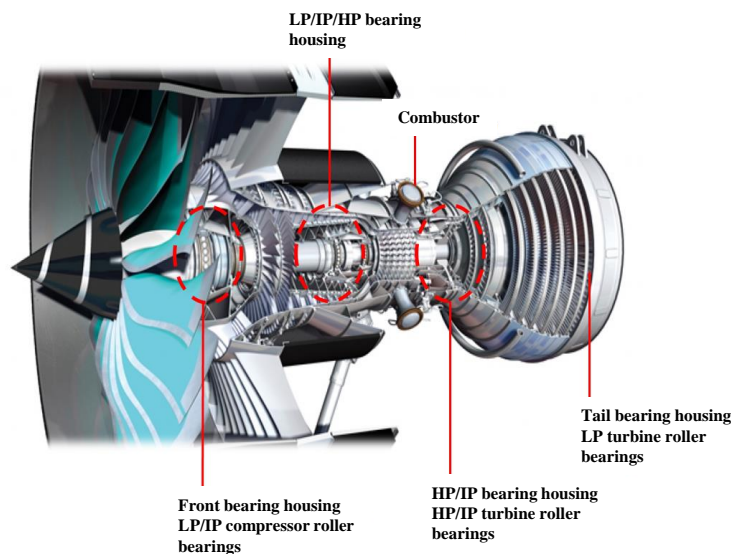


**Figure 1.2. Locations of bearing chambers on the Advance turbine (Adapted from Rolls-Royce, 2016)**

The bearing chamber hosts a mixture of sealing air and oil. The oil is injected towards the bearings to provide lubrication and cooling, whereas the sealing air prevents the oil from leaking out of the chamber. Furthermore, the bearing chamber prevents the propagation of the mixture to other parts of the engine and separates the oil–air mixture from hot areas in order to prevent oil fires (Wittig et al., 1994).

The two-phase flow inside aero-engine bearing chambers has been studied by many authors to improve engine efficiency and heat rate, to manage the heat and oil, and to reduce the power losses. In addition, the study of air–oil interaction, as well as the oil lubrication system, is of great interest to meet the design requirements of the air–oil system, namely (Schmidt et al., 1982):

- to enable low mission oil consumption,
- to ensure low heat to oil,
- to avoid oil leakage with effective sealing for all flight conditions,
- to avoid overheating of bearing chambers,
- moreover, to increase the life and reliability of the bearing.

Furthermore, the design improvements of lubrication oil systems imply the reduction of mission oil consumption, reduction of bearing chamber temperatures and pressures, optimisation of air and oil system design, and improvement of lubrication oils (Schmidt et al., 1982). The main task for the optimisation of air–oil design is the reduction of the residence time of air–oil mixtures in bearing chambers. This is because there is a risk of evaporation if the mixture has a high residence time, which drives in higher concentrations of oil vapour mixed with air. Consequently, the high concentration of oil

vapour can become a combustible mixture in certain conditions (dependent on temperature and pressure).

Various investigations have explored the ability to model the multi-phase flow within the bearing chamber, as well as to present experiments exploring the influence of the geometry and operating conditions in the oil flow performance (Glahn et al., 1997, Busam et al., 2000, Gorse et al., 2004, Krug et al., 2015).

Other research has presented the analysis of droplet distribution and particle tracking (Glahn et al., 1996, Farrall et al., 2000, Farrall, 2000, Simmons et al., 2002, Farrall et al., 2006, Chen et al., 2011a, Chen et al., 2011b, Tkaczyk and Morvan, 2011, Adeniyi et al., 2014), as well as the formation of secondary droplets after impingement onto the chamber wall (Farrall et al., 2007, Williams, 2009, Chen et al., 2011b, Wang et al., 2011, Adeniyi, 2015, Peduto, 2015, Hann et al., 2016). Many of these studies have been undertaken at the University of Nottingham.

The impingement of droplets favours the formation of a thin film of oil along the wall surface of the bearing chamber. This has been analysed numerically and experimentally over the past 25 years, mainly by two groups, one of which is the Gas Turbine and Transmission Research Centre (G2TRC) at the University of Nottingham (Williams, 2009, Tkaczyk, 2011, Wang et al., 2011, Bristot et al., 2016, Kakimpa et al., 2016, Crouchez-Pillot and Morvan, 2014) and the other is the Karlsruhe Institute of Technology in Germany (Wittig et al., 1994, Gorse et al., 2004, Hashmi, 2012, Kurz et al., 2013, Kurz et al., 2014, Krug et al., 2015).

Furthermore, the heat transfer between the air and oil flow around the wall chamber has been predicted by simulations and correlations of the convection coefficient in bearing

chambers and vents (Wittig et al., 1994, Chew, 1996, Glahn and Wittig, 1996, Glahn et al., 1997, Glahn and Wittig, 1999, Jakoby et al., 1999, Busam et al., 2000, Kanike et al., 2012, Adeniyi et al., 2014, Adeniyi, 2015, Flouros et al., 2015).

However, few studies have considered the heat transfer effects in oil droplets (Adeniyi, 2015 at Nottingham, Sun et al., 2016a, Sun et al., 2016b at Northwestern in China) and therefore the possible effects of vaporisation and radiation are consequently neglected.

A more precise understanding of the droplet flow and evaporation patterns under extreme operating conditions inside the bearing chamber is essential to avoid or limit risks of exothermic reactions and air cabin contamination due to those oil droplets.

A numerical analysis can quantify the oil vapour concentration in zones that might be difficult to access (Rosenlieb, 1978). Therefore, numerical analysis offers a means to predict the regions with high concentrations of oil vapour for engineering analysis and the reduction of risk associated with oil fires. Moreover, with the numerical analysis of the air–oil interaction, it might be possible to provide recommendations to improve lubrication systems, to manage the high temperatures and to enhance cooling within the system.

Therefore, this research provides the basis to quantify the amount of vapour produced by a single droplet travelling in the core flow. The methodology applied in this research can then be extrapolated to the quantification of the vapour concentration of several droplets and to model the evaporation of the thin film.

Moreover, the results of this project will enable the prediction of the behaviour of multi-phase flow and the heat and mass transfer of oil droplets travelling into the core

flow of bearing chambers. The predictions from this research will help to improve the performance of lubrication and transmission systems. In addition, the predictions will help to keep safe the operation of the engine and to enhance heat management, reducing the risk of oil vaporisation. It will also contribute to informing design best practices directly to our industrial partner, Rolls-Royce.

## **1.1 Aim**

The aim of this research, therefore, is to perform a micro-scale analysis of an oil droplet travelling in the core flow, as well as to understand the droplet evaporation process under the conditions of a typical aero-engine bearing chamber. The study is performed for a single oil droplet under the effects of a hot convective airflow using the volume of fluid (VOF) technique. The numerical simulations will quantify the evaporation rate, the mass fraction of oil vapour and the temporal evolution of the droplet's diameter, as well as assist with the visualisation of the internal droplet circulation.

## **1.2 Objectives**

The specific objectives of this research, in accordance with the aim previously mentioned, are:

- Determine whether there is a risk of vaporisation of the oil droplets inside the bearing chamber and, if so, what drives this.
- Understand the influence of the most representative parameter in the droplet evaporation process under bearing chamber conditions.
- Analyse the droplet's internal flow and the effects on the droplet evaporation rate.

- Estimate the heat and mass transfer of oil droplets and calculate the influence of external radiation on the droplet evaporation rate. These calculations will influence the bearing chamber operating conditions.
- Study the oil latent heat and ensure that it is properly accounted for in the model to estimate the heat and mass transfer of oil droplets at representative bearing chamber conditions.

### **1.3 Structure of the thesis**

The thesis is organised into six chapters. The first chapter introduces the motivation for this research, as well as the aim and objectives. The second chapter describes the state-of-the-art regarding oil droplets, heat and mass transfer and momentum exchange between droplets and air inside bearing chambers, and oil droplet evaporation, as well as gaps in the knowledge. Chapter 3 presents the CFD methodology, which includes the physical and numerical models as well as the calculation of thermodynamic properties of the oil used as a base stock lubricant in aviation turbines. Chapter 4 presents the validation of the evaporation model from the state-of-the-art of droplet's evaporation, the CFD case setup and the mesh independence study, as well as guidelines and recommendations for oil droplet evaporation modelling. Chapter 5 covers the application of the validated model to oil droplets under representative bearing chamber conditions. Moreover, a parametric study is presented to understand the most representative parameter in the oil droplet evaporation process. Finally, Chapter 6 provides the conclusions, main achievements, contribution to knowledge and future work.

## 2 Literature review

This chapter presents the relevant state-of-the-art knowledge in oil droplets in bearing chambers and the physics around the droplets that are suspended in the core flow. This literature review considers the droplet's journey from the bearings to the walls. It also includes the oil droplet formation, droplet impingement, formation of secondary droplets, droplet motion, and droplet heat and mass transfer. The review includes the analysis of droplet evaporation applied to internal combustion engines (ICEs) using the VOF approach. Additionally, the methodology used to model the droplet evaporation process in ICEs will be applied to understand oil droplet evaporation under representative bearing chamber conditions.

### 2.1 Oil droplets in bearing chambers

The lubricating oil in bearing chambers leads to the core fluid being primarily a multi-phase mixture of oil and pressurised hot air. This multi-phase flow presents different regimes, such as droplets, jets and ligaments. Droplets are of particular interest because they have a range of trajectories once they are released from the rotating elements and might experience evaporation throughout their journey. Some droplets can travel suspended within the convective air before they escape through the vent lines (Farrall et al., 2006); others can splash onto the walls of the chamber (Peduto, 2015) or might break up before coming into contact with the walls. In both splashing and breakup, there is the formation of smaller droplets called secondary droplets (Chen et al., 2011a), as indicated schematically in Figure 2.1.

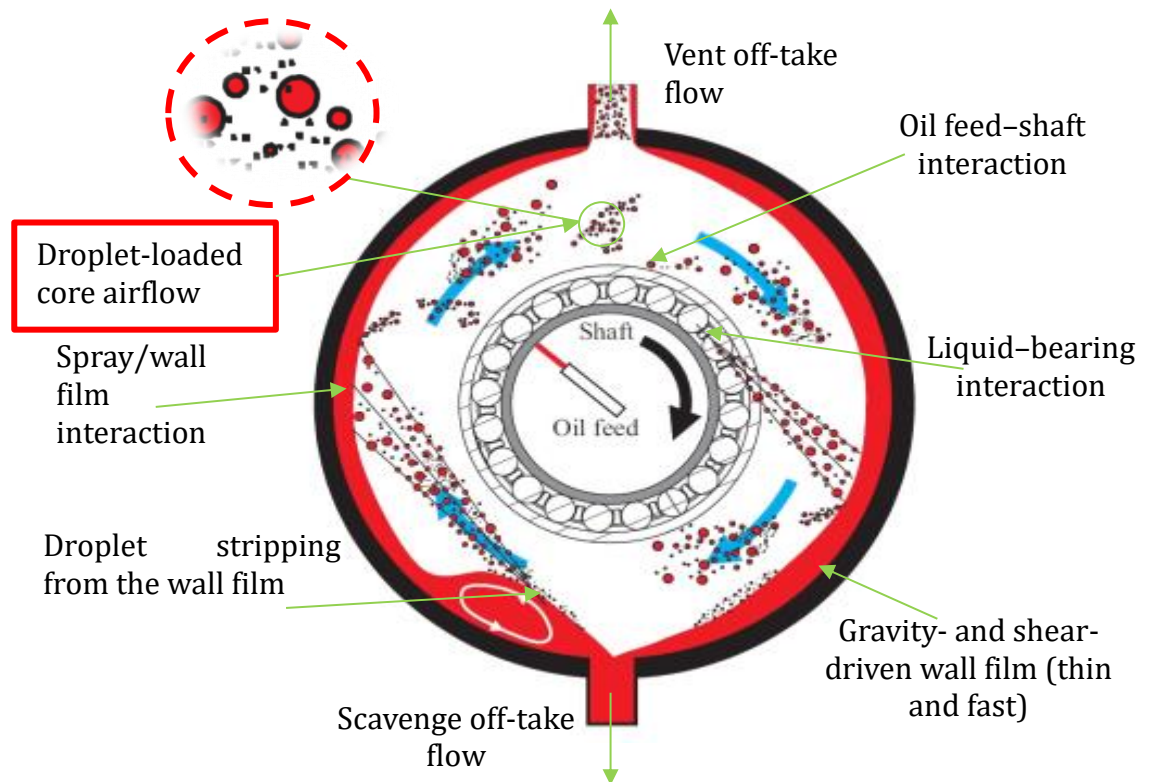


**Figure 2.1. Types of two-phase flow pattern inside bearing chambers (adapted from (Peduto, 2015))**

### 2.1.1 Droplet formation

The droplet formation process might start after shedding from bearings or from the oil jet disintegration (Hee, 2019). In both cases, the oil is influenced by the airflow and other bearing chamber operational conditions (Gorse et al., 2008).

The jet break-up process depends on the jet speed and diameter, and can be classified into four different regimes (Husted et al., 2004, Hart, 2005): Rayleigh break-up, first wind-induced break-up, second wind-induced break-up and atomisation, as shown in Figure 2.2.

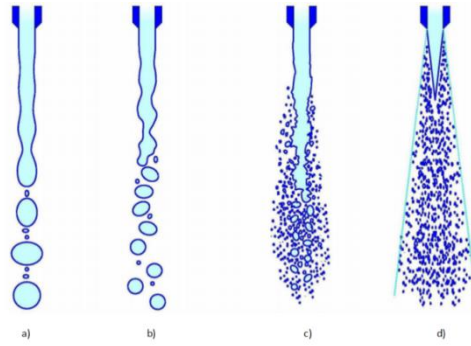


**Figure 2.2. Droplet formations according to jet break-up regimes: a) Rayleigh, b) First wind-induced, c) Second wind-induced and d) Atomisation (see Husted et al., 2004)**

Furthermore, each region can be separated according to Reynolds number and Ohnesorge number of the nozzle, as shown in Figure 2.3.

The Reynolds number describes the viscous behaviour of fluid, accounting for the inertial and viscous forces, and it is given by:

$$Re = \frac{\rho u D}{\mu} \quad 2.1$$

and the Ohnesorge number describes the drop impingement regimen and the influence of viscous forces and surface tension (Peduto, 2015), and it is given by:

$$Oh = \frac{\sqrt{We}}{Re^2} = \frac{\mu}{\sqrt{\rho \sigma D}} \quad 2.2$$

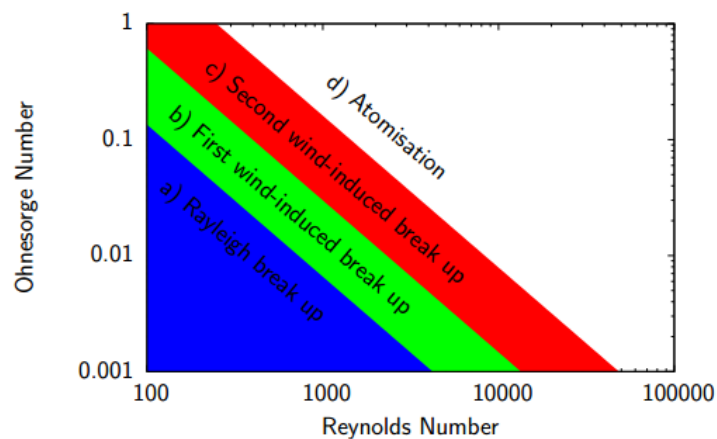


**Figure 2.3. Fluid break-up regimes defined by Oh and Re numbers (see Hart, 2005)**

The Oh range was calculated in bearing chamber conditions, which is from 0.015 to 0.5 (Peduto, 2015). Therefore, it could be said that the common break-up regimes in bearing chambers are the Rayleigh break-up. This is contrary to ICEs, where the break-up regime is in the atomisation region, as can be observed in Figure 2.4.

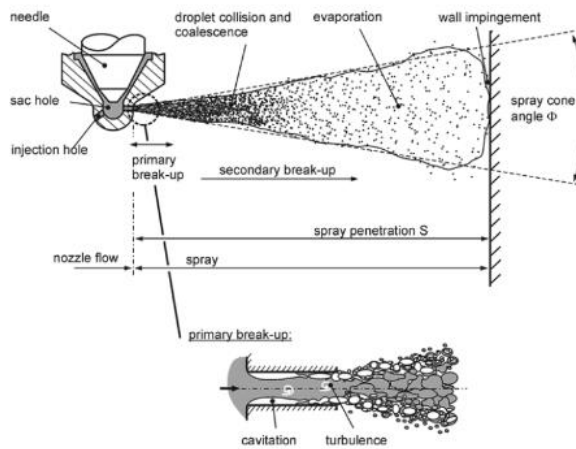


**Figure 2.4. Jet break-up of a full cone diesel spray (see Baumgarten, 2006)**

The analysis of droplet motion and trajectory is very important due to, first, the droplet impingement derived from the thin film formation and, second, the formation of secondary droplets (Weinstock and Heister, 2004)

### 2.1.2 Droplet impingement and formation of secondary droplets

The droplets travel from the bearings through the core flow. The droplets might stick, rebound, spread or splash, depending on the We number, as shown in Table 2.1 and generally adhere to film in the spread regime criterion.

The We number defines the relationship between inertial forces and surface tension. Therefore, this parameter provides the droplet impingement transition criteria, as can be observed in Table 2.1 as well as in the oil jet break-up process (Hart, 2005):

$$We = \frac{\rho u^2 D}{\sigma} \quad 2.3$$

**Table 2.1. Droplet impingement transition criteria (see Tkaczyk and Morvan, 2011)**

<b>Regime</b>	<b>Criterion of impingement</b>
Stick	$We < 5$
Rebound	$5 < We < 10$
Spread	$10 < We < 57.72 \min(h/D) + Re^{0.5}$
Splash	$We > 57.72 \min(h/D) + Re^{0.5}$

Tkaczyk (2011) and Tkaczyk and Morvan (2011) numerically analysed the film thickness  $h$  concerning the two-phase flow in pipes and bends, tracking the droplet–film interactions by using a Lagrangian technique. Their predictions showed that, at high gas velocities, the deposition of droplets plays an important role in the formation of the oil film at the top of the pipe. Moreover, they noticed that if the droplets are not considered in the analysis, the film remains at the bottom part of the pipe. Furthermore, they reported that the splashed droplets create secondary droplets, which have diameters four times smaller than the original droplets. These secondary droplets follow the airflow because they have little momentum on their own and low inertia energy (Flagan and Seinfeld, 2013).

The number of droplets increases according to the increase in shaft speed, as shown in Figure 2.5. This effect was observed in experimental measurements performed by (Gorse et al., 2004), where droplet entrainment on the wall film increased when the shaft speed increased. Moreover, Gorse et al. (2004) found that the size of droplets observed inside bearing chambers is 14–500  $\mu\text{m}$ .

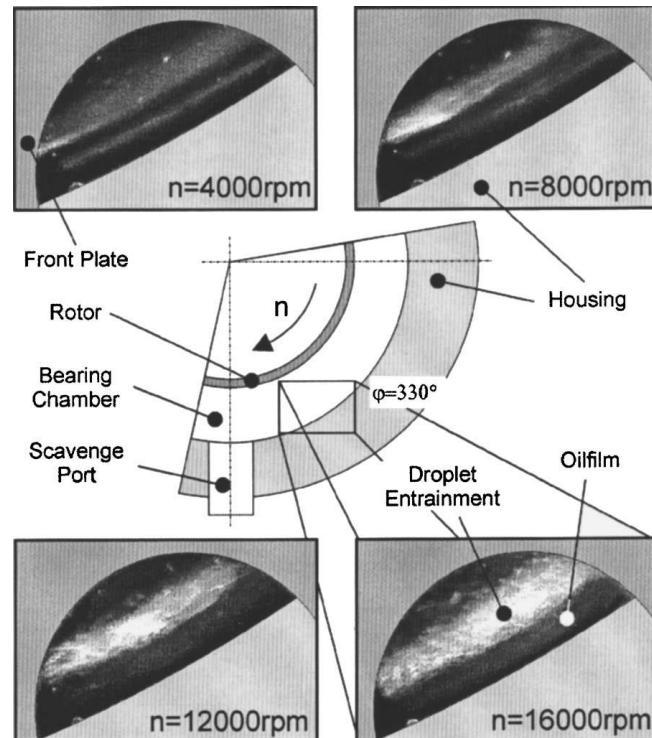


**Figure 2.5. Visualisation of droplet entrainment in wall oil film (see Gorse et al., 2004)**

Farrall et al. (2006) analysed numerically the influence of airflow and boundary conditions on the oil–film interaction in bearing chambers; this study takes into account the motion of the oil film and the motion of oil droplets. The analysis found that the 72% of the formation of the wall film is due to droplet impingement. Furthermore, the formation of secondary droplets increases with the shaft speed. The wall film distribution depends strongly on the oil droplet distribution and its interaction with the wall oil films.

The droplet impact outcome can be characterised by droplet and film parameters and conditions. The principal types of outcomes are floating, coalescence, crown formation, crown splashing, jet formation, jet break-up and prompt splashing (Mitchell et al., 2016). In the coalescence outcome, after the droplet impacts the film, a portion of the material is ejected. This ejection increases with time, forming a lamella (Peduto, 2015) which is part of the process of crown formation represented in Figure 2.6.

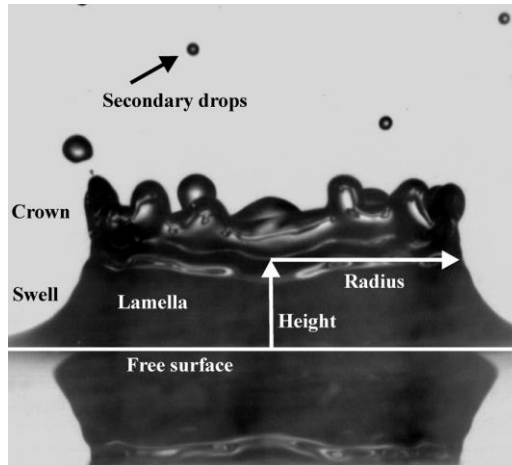


**Figure 2.6. Crown formation characteristics (see Peduto, 2015)**

The lamella expansion, crown formation and crown evolution were modelled by Peduto (2015), who considered the characteristics of secondary droplets created from the droplet–film interaction, e.g. size, velocity impingement angle and wall film depth. His research noted the importance of involving the Froude number to estimate the droplet crown evolution and crown height. The Froude number allows the describing of the mass and momentum exchange in the droplet–film interaction, besides the addition of the gravity and centrifugal forces affecting the flow.

The Froude number associates the inertial forces and gravitational acceleration, and helps to understand the crown evolution and crown height, as given by:

$$Fr = \frac{u^2}{gD} \quad 2.4$$

Peduto (2015) reported that the cavity depth and crown height increase when the Froude number is increased and the gravitational and centrifugal forces are decreased. Moreover, when the droplet size is reduced and the droplet momentum is constant, the Froude number increases and the number of secondary droplets formed increases. A comparison between simulations and experimental results can be observed in Figure 2.7,

which represents the impingement process, the evolution of the crown and the formation of secondary droplets.

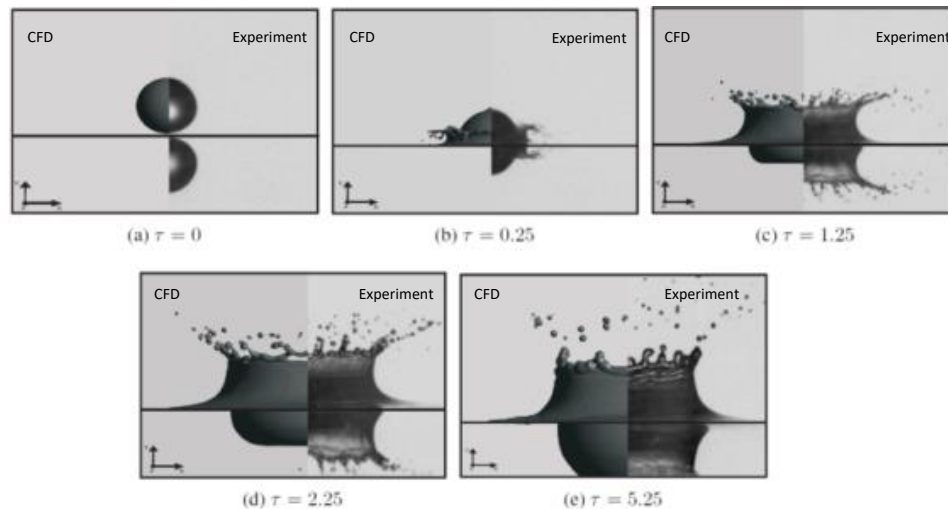


**Figure 2.7. Correlations between numerical and experimental results of the crown evolution during the impingement process (see Peduto, 2015)**

Furthermore, Hann et al. (2016) appraised the droplet impingement experimentally to identify variations of droplet impact, i.e. cavity evolution and crown and jet formation. The droplet impact variations were evaluated by changing the oil film depth and the droplet impact velocity. Measurements showed that crown formation appears when droplets have a high velocity and the film thickness is low. Jet formation is observed at high droplet velocity and low film thickness. Moreover, cavity formation is also affected by the impact velocity and film thickness.

Likewise, Mitchell et al. (2016) analysed the formation mechanism of secondary droplets and their properties. This analysis was addressed from the perspective of variations in droplet diameter and impingement angle. In addition, the influence of moving films in droplet impacts was investigated. It was noticed that there is a low influence of impingement angle on the formation of secondary droplets. Additionally, research

involving static films and moving films produced no significant differences concerning secondary droplet formations. However, this research did propose correlations, including the effects of moving films on the formation of secondary droplets. These correlations aimed to estimate the droplet impacts more accurately.

Despite this, Weinstock and Heister (2004) observed that the secondary droplets have less momentum and smaller diameters relative to the primary droplets. These conditions allow the secondary droplets to spread in the thin film, forming part of the film without splashing again. Also, the number of secondary droplets increases with the initial droplet size, i.e. if the initial droplet size is large, there are more secondary droplets formed from the impact with the wall. The number of secondary droplets is reduced with the radius ratio (radius of the shaft and radius of the bearing chamber). This is because if the radius ratio increases, the velocity of the parent droplets decreases and the impact of droplets onto the wall is with less momentum. Moreover, it was noticed that the number of secondary droplets increases with temperature, in contrast to the parent droplets where trajectory is not affected by temperature.

Altogether, the droplets can be classified into parent droplets and secondary droplets. The parent droplets are those travelling from the bearings to the walls and the secondary droplets are those formed when the parent droplets break up. The break-up might be due to the splashing with the thin wall film or when the parent droplet breaks up during its journey in the core flow. The break-up in the core flow might be due to the aerodynamic forces or collision among droplets. The secondary droplets usually have smaller diameters than the parent droplets and, therefore, are quicker to recirculate in the core flow and

evaporate. Hence, the droplets with a small diameter are relevant for the present research and are analysed in Section 5.

The evaporation of oil droplets in the core flow may be related to the droplet size and the heat transfer absorbed from the environment. Therefore, in Section 2.1.3 we will present some investigations about droplet size distribution and particle tracking.

### **2.1.3 Droplet size distribution and particle tracking**

The formation of droplets is strongly influenced by bearing chamber operating conditions. These influences were analysed experimentally and analytically by Glahn et al. (1996). The results of these measurements showed the effect of high rotational speeds on the size distribution of droplets inside bearing chambers. For high rotational speeds, the diameter of the droplets is reduced in comparison with low shaft speeds.

Moreover, the size of droplets is distributed in the range of 14  $\mu\text{m}$  to 500  $\mu\text{m}$ , where the most frequent diameters are between 70  $\mu\text{m}$  and 80  $\mu\text{m}$ . In addition, it was noticed that the droplets with diameters below 80  $\mu\text{m}$  are affected by air velocities. The air velocity increases the curvature of the droplet's trajectory, as observed in Figure 2.8. For this reason, the curvature of a droplet's trajectory is more pronounced with a diameter of 50 $\mu\text{m}$  than with a diameter of 100  $\mu\text{m}$  or 200  $\mu\text{m}$ .

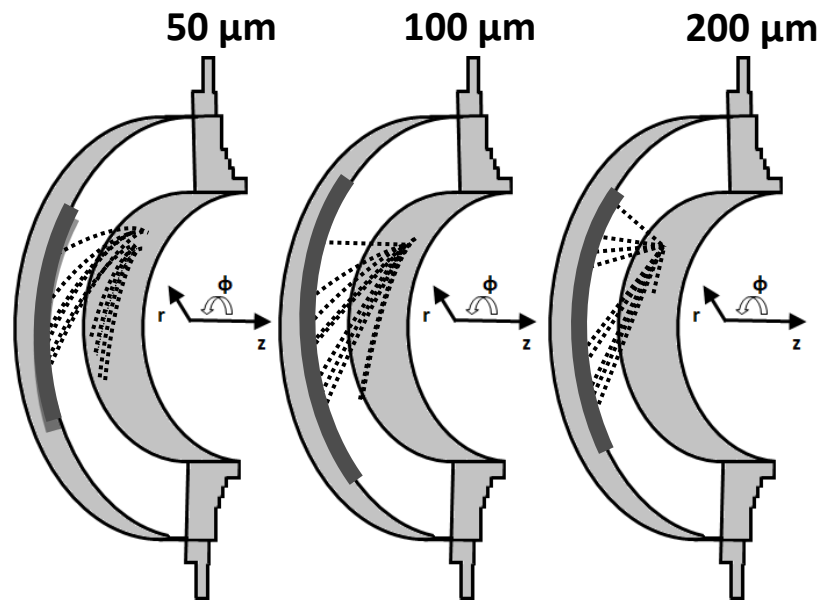


**Figure 2.8. Oil droplet trajectory according to its diameter (see Glahn et al., 1996)**

In the same way, Simmons et al. (2002) discuss the turbulent flow of air and the associated movement of the oil droplets. The trajectories of droplets were predicted with the Lagrangian tracking method. The range of droplet diameters considered in this research is 1–500  $\mu\text{m}$ . The numerical predictions showed that the droplets with diameters below 100  $\mu\text{m}$  resulted in a different deposition location. In addition, the droplets with diameters below 100  $\mu\text{m}$  were affected by airflow variations. This effect is caused by the low inertial energy of small droplets, i.e. the droplet has a small Stokes number which implies that droplets are governed by air velocity (Flagan and Seinfeld, 2013).

The Stokes number allows the calculation of the ratio of the inertia force of a particle to the resistance force when the particle is in motion (Wen, 1996). The Stokes number enables the definition of an equation regarding the motion of a particle, which is related to the stopping distance of the particle's motion and the length scale of the flow, as described equation 2.5. Thus, if there is a small stopping distance in a flow with a large

length scale, the Stokes number will be small and the particle will be dominated by flow characteristics (Flagan, 1988). When the particle is dominated by flow it means that the viscous forces beyond it are greater than the inertial forces, i.e. the particle has a low Reynolds number,  $Re \ll 1$ . If the particle is a sphere with  $Re \ll 1$ , the flow is called Stokes flow or creeping flow. Therefore, the Stokes number is given by:

$$Stk = \frac{2\rho r^2 u}{9\mu L} \quad 2.5$$

where  $u$  is the fluid velocity and  $L$  is the length scale of the flow.

Additionally, Farrall et al. (2007) reported that the droplets with diameters below  $200\mu\text{m}$  are governed by airflow conditions. The study evaluated the droplet size distribution to understand the interaction between droplets and oil film and the distribution of oil along the wall of the bearing chamber.

Furthermore, Weinstock and Heister (2004) mentioned that the secondary droplets with a Sauter mean diameter of  $108\mu\text{m}$  are formed from parent droplets of  $700\mu\text{m}$ . However, this relationship may vary due to shaft velocity and airflow conditions (operating conditions).

The distribution of oil is related to the droplets' trajectories, which depend on the particle sizes. Thus, the particle size distribution is of interest to investigate the droplet's interaction with the surrounding airflow. There are numerous empirical and analytical models to predict this distribution, such as Rosin–Rammler and discrete probability function, respectively (Hart, 2005). The most common distribution used to estimate the droplet size in a bearing chamber is the Rosin–Rammler (Farrall et al., 2000, Gorse et al., 2003, Farrall et al., 2006, Sun et al., 2013) and it is defined as follows (Hart, 2005):

$$Y(d) = 1 - e^{-\left(\frac{d}{\bar{d}}\right)^n} \quad 2.6$$

where  $Y(d)$  is the cumulative volume of droplets with a diameter less than  $d$ , the average diameter is given by  $\bar{d}$  and  $n$  is a measure of the spread of droplet sizes. Figure 2.9 shows an example of the droplet size distribution fitted to droplet counts using the Rosin–Rammler distribution.

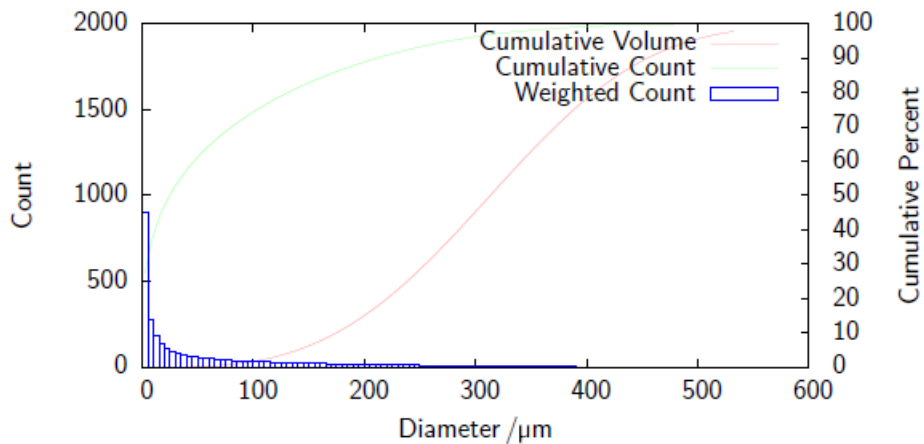


**Figure 2.9. Droplet size distribution fitted to droplet counts with the Rosin–Rammler distribution (Hart, 2005)**

Different operating conditions influence the particle size distribution. The variation of droplet size due to the operating conditions was predicted by Farrall et al.(2007). The results revealed that for high rotational speeds there is an increase in the number of droplets formed by splashing on the wall oil film, which agrees with the results predicted by Gorse et al. (2004) and also with the predictions by Peduto (2015).

On account of this, the oil droplet trajectory depends on the droplet size, which are important parameters to predict the droplet’s residence time in the core flow. The droplet residence time is relevant to compute the amount of vapour and the air–oil concentration inside the bearing chamber. Furthermore, understanding the evaporation process throughout the droplet’s motion is of interest because small droplets can recirculate in the

core flow for a long period, which is relevant for the present research. Therefore, droplet motion is discussed as follows in Section 2.1.4

## **2.1.4 Droplet motion**

The complexity of the flow patterns inside bearing chambers influences the motion of droplets and their interaction with the core flow. This section investigates the relevance of the airflow predictions and the location of recirculating zones. Patterns of droplet motion and the airflow will help to understand the air–oil interaction and how it might affect the droplet evaporation process. Furthermore, this section presents the development of the flow field around the droplet and its characteristics.

### ***2.1.4.1 Airflow development and recirculating zones***

Droplet motion is affected by the airflow pattern inside the bearing chamber; for this reason, it is important to understand the airflow development. As previously described in Section 1, sealing air is introduced into the bearing chamber to prevent oil leakage to different parts of the turbine. The sealing air presents the formation of vortices, which depends on the rotational speed and air mass flow as shown in Figure 2.10. Two main vortices are formed for air mass flows of 6.2 g/s and 8.5 g/s, and after 12.7 g/s there is a formation of one main vortex as observed in Figure 2.10.

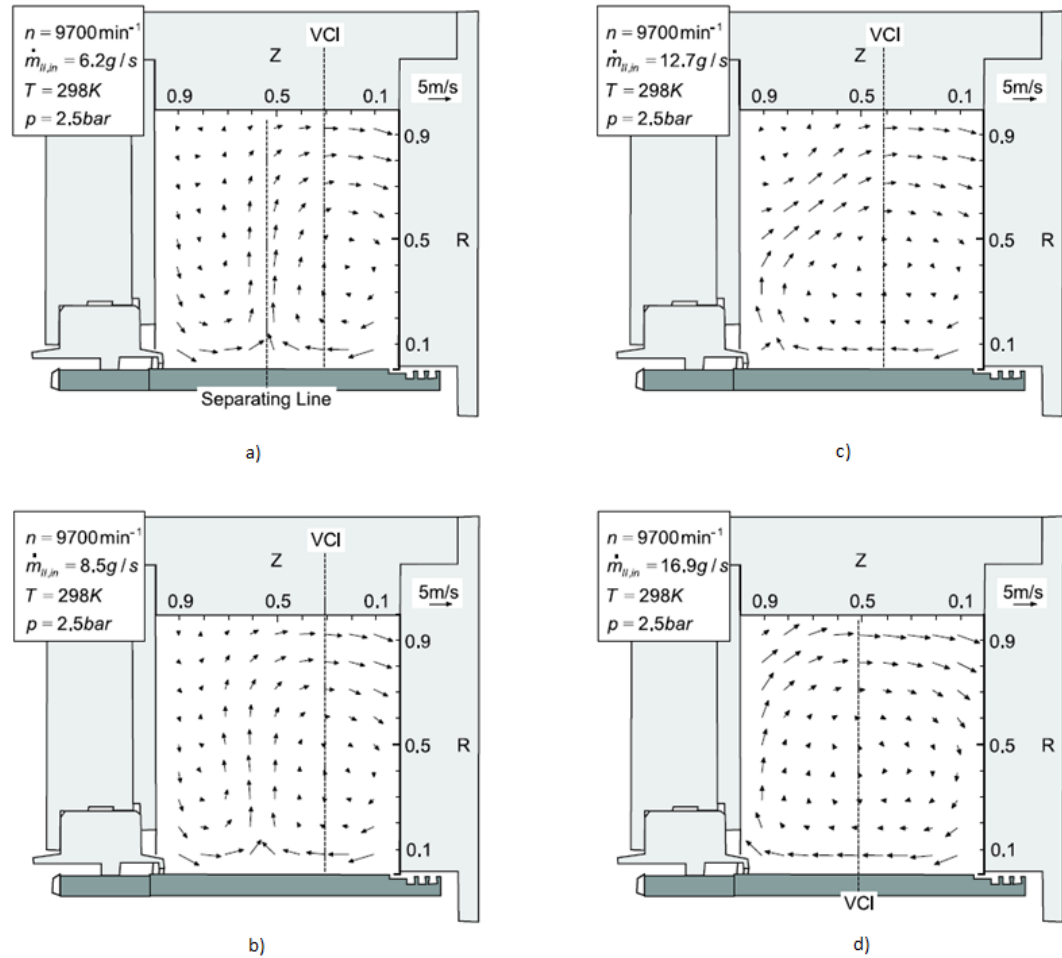


**Figure 2.10. Secondary flow field at  $n = 9700$  rpm: a)  $\dot{m} = 6.2$  g/s; b)  $\dot{m} = 8.5$  g/s; c)  $\dot{m} = 12.7$  g/s; d)  $\dot{m} = 16.9$  g/s (Gorse et al., 2003)**

Aidarinis et al. (2011) noticed that the rotational shaft induces the swirling air. Therefore, the recirculation zones are near to the rotational shaft and extend to the core of the bearing chamber, as can be observed in Figure 2.11.

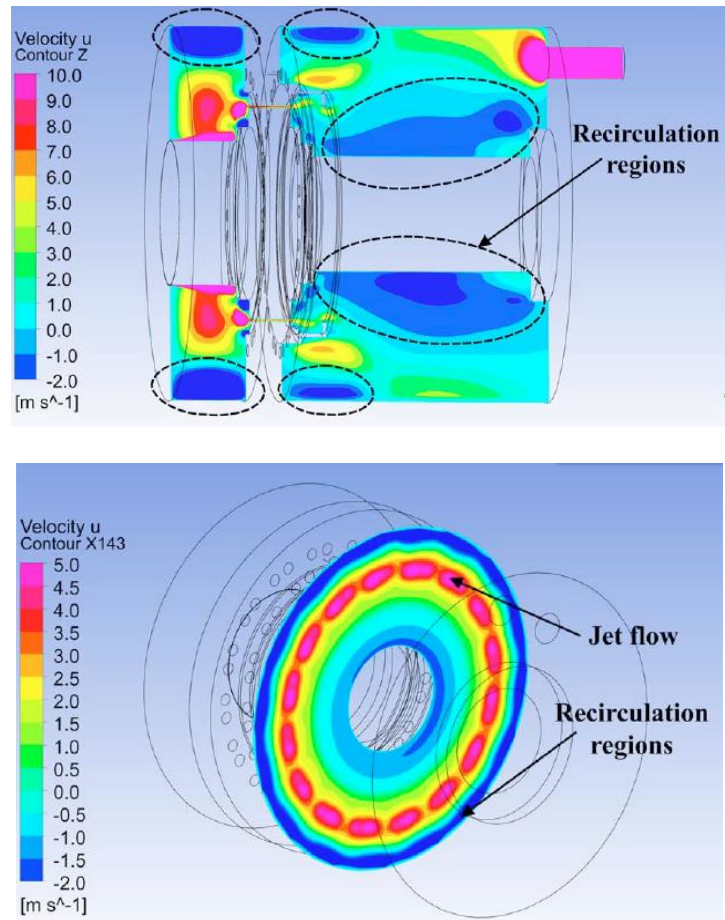


**Figure 2.11. Recirculation zones inside bearing chambers (Aidarinis et al., 2011)**

Furthermore, the rotational speed influences the airflow pressure (Kurz et al., 2014), which affects the oil droplet's velocity (Sun et al., 2013). For droplets with a diameter of  $80\ \mu\text{m}$ , the velocity decreases when the droplet is close to the walls and it is influenced by the increase in the sealing air pressure. Consequently, when the sealing air pressure is increased, the oil droplet is affected by the growth of the airflow drag forces, as observed in Figure 2.12.

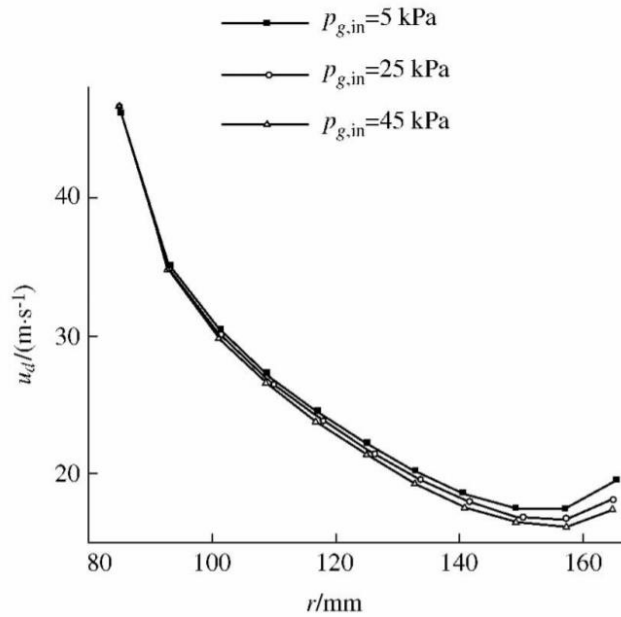


**Figure 2.12. Effect of sealing air on droplet velocity (Sun et al., 2013)**

As mentioned in Section 2.1.3, the core flow dominates the trajectories of droplets with diameters  $<200 \mu\text{m}$ . Thus, the study of the airflow is essential to predict droplet motion in the bearing chamber. Fei et al. (2017) highlighted that the air velocity decrease in the radial direction and the oil velocity tend to be the same as air. Additionally, the variation of air velocity with time is greater than that of the oil velocity and the relative velocities are computed to be around 1 m/s. Moreover, it was noticed that the oil and air velocities decrease suddenly from around 22 m/s to 12 m/s in the circumferential direction due to the vent and scavenge ports.

Chandra and Simmons (2017) defined the flow regimes inside the bearing chamber; namely, gravity dominated, windage dominated and wall film dominated. The droplets trapped in the core flow are observed in the gravity-dominated and windage-dominated regimes. However, the wall-film-dominated regime does not present airborne droplets. According to Chandra and Simmons (2017), the droplets trapped in the core flow can be

reduced if the geometry of the sump is improved. Therefore, the optimisation of the sump geometry can be designed to observe a wall-film-dominated regime. In addition, droplet splashing is reduced when the oil residence volume is reduced.

Moreover, Chandra and Simmons (2017) noticed that with a shaft speed of 15,000 rpm the formation of secondary droplets trapped in the core flow is less than with a shaft speed of 10,000 rpm. They found that with a higher shaft speed, the droplets travel faster and are deposited on the wall film. Moreover, they noticed that if the wall film is thin, the droplets are deposited on the wall which reduces the formation of secondary droplets. Thus, the sump design is essential to reduce the oil residence time and consequently the thickness of the wall film.

Moreover, the reduction of trapped droplets in the core flow is important because the airborne droplets tend to evaporate completely, producing high oil vapour concentrations.

The droplets suspended in the core flow are the subject of study in this research as they are more prone to evaporate when suspended in the airflow for a long period. The evaporation might be because the long interaction between the oil droplets and airflow increases their residence time and raises their temperature as a consequence (Sun et al., 2016b). The droplets with small diameters tend to be suspended and trapped in the core flow. Generally, the droplets with the smallest diameters are the secondary droplets (Chandra and Simmons, 2017, Weinstock and Heister, 2004).

In the same way, Weinstock and Heister (2004) reported that for the parent droplets in the bearing chamber of a Rolls-Royce AE3007 engine, the droplet trajectory time can be less than 1 ms as shown in Figure 2.13.

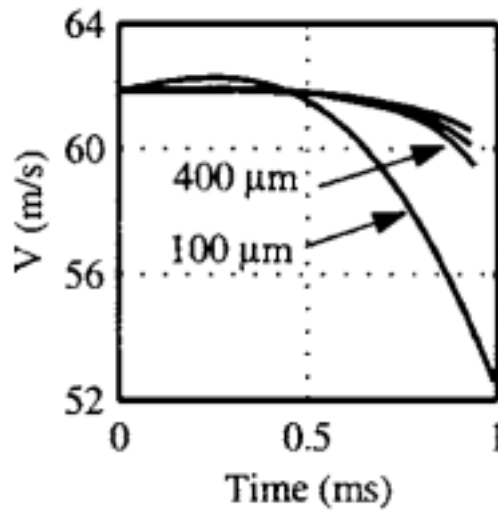


**Figure 2.13. Residence time of a parent droplet (Weinstock and Heister, 2004)**

Aroussi et al. (2003) determined experimentally that the velocity of recirculating air depended on the shaft speed, which increases when the shaft speed increases. Moreover, they noticed that if the shaft speed increases, the formation of secondary droplets increases. The formation of secondary droplets not only arises from the droplet splashing but it is also due to the droplet break-ups before they reach the walls. Aroussi et al. (2003) also found that the size of the droplet diameter increases when the liquid flow rate increases.

#### ***2.1.4.2 Droplet dynamics and droplet boundary layer***

As previously discussed, the main force that influences droplet motion is the aerodynamic drag force. If the gravitational and buoyancy forces are neglected, the oil droplet motion in the airflow is given by Newton's second law as follows (Husted et al., 2004, Sun et al., 2013, Sun et al., 2016b):

$$\frac{du}{dt} = \frac{3C_D \rho_g}{2r \rho_l} |u_g - u_d| (u_g - u_d) \quad 2.7$$

where  $u_g$  and  $u_d$  are the velocities of the air and droplet, respectively,  $C_D$  is the drag coefficient and  $r$  is the radius.

If the droplet is considered as a sphere, the drag coefficient is calculated according to the correlation for the ‘standard drag curve’ for a solid sphere. The drag forces can be calculated according to the drag coefficient  $C_D$  as a function of the Reynolds number  $Re_D$  (Faeth, 1977):

$$C_D = \frac{24}{Re_D} \left[ 1 + \frac{Re_D^{2/3}}{6} \right] \quad 2.8$$

The vapour film formed around the droplet may produce effects on the droplet’s motion due to the mass evaporation and the Stefan convection, which can be accounted for (Sazhin et al., 2005):

$$C_D = \frac{C_{D0}}{(1 + B_M)^\beta} \quad 2.9$$

$$\beta = \begin{cases} 1 & \text{when } B_M < 0.78 \\ 0.75 & \text{when } B_M \geq 0.78 \end{cases}$$

where  $B_M$  is the Spalding mass transfer number given by:

$$B_M = \frac{y_{i_s} - y_{i_\infty}}{1 - y_{i_s}} \quad 2.10$$

The Spalding mass transfer number will be used to estimate the evaporation rate in Section 5.

The droplet’s Reynolds number is given by:

$$Re_D = \frac{2r\rho_g|u_g - u_d|}{\mu_g} \quad 2.11$$

where  $\rho_g$  and  $\mu_g$  are the density and viscosity of the gas phase, respectively.

The development of the flow field around the droplet may classify the flow accounting for the Reynolds number  $Re_D$  given by equation 2.11. The regimes are presented according to the separation and the recirculation formed downstream of the droplet, which may vary due to the flow velocity and droplet diameter. Clift (2005) reported that the boundary layer around the droplet is described by a number of regimes as follows:

- unseparated flow ( $1 < Re < 20$ ),
- onset of separation ( $Re = 20$ ),
- steady wake region ( $20 < Re < 130$ ),
- onset of wake instability ( $130 < Re < 400$ ),
- high subcritical Reynolds number range ( $400 < Re < 3.5 \times 10^5$ ) and
- critical transition and supercritical flow ( $Re > 3.5 \times 10^5$ ).

The range of Reynolds numbers for oil droplets inside bearing chambers is  $0 < Re < 1400$ , as can be observed in the calculations presented in Section 8.5. Therefore, inside the bearing chamber the droplet regimes are from the unseparated flow to the beginning of the high subcritical Reynolds number range.

Moreover, the aerodynamic forces may affect the droplet shape and produce secondary droplets. Therefore, the droplet break-up and deformation processes are discussed in Section 2.1.4.3.

#### ***2.1.4.3 Droplet break-up and deformation***

The droplet break-up process is dependent on the interaction between the internal droplet forces acting on it, such as surface tension and viscosity, as well as the

aerodynamic forces. This interaction can produce deformation or disintegration of droplets. The disintegration of droplets is observed when the aerodynamic forces are greater than the internal droplet forces (Liu, 2000). Thus, the critical value for break-up can be calculated from the critical Weber number  $We_{cr}$  and critical droplet size  $D_{max}$  as follows:

$$We_{cr} = \frac{2r\rho_g(u_g - u_d)^2}{\sigma} = \frac{8}{C_d} \quad 2.12$$

$$D_{max} = 2r_{cr} = \frac{8\sigma}{C_d\rho_g(u_g - u_d)^2} \quad 2.13$$

Chen et al. (2011a) reported that drag forces can break up droplets during their motion from the bearings to the wall of the chamber. Additionally, the droplets with diameters of 400  $\mu\text{m}$  to 500  $\mu\text{m}$  can break up with more frequency, forming secondary droplets. This break-up is noted for high shaft speeds. Once the secondary droplets are formed, their trajectories are completely different from the primary droplets and these trajectories can be affected by the drag forces. Besides the drag forces, oil droplet motion is affected by shear forces due to air and gravity.

These shear forces can generate droplet deformation and break-up. There are six regimes of droplet deformation and break-up. These regimes are defined by Weber and Ohnesorge numbers and can be observed in Figure 2.14.

The Weber number defines the relationship between inertial forces and surface tension forces, as shown in equation 2.12, and the Ohnesorge number describes the influence of viscous forces and surface tension forces (Peduto, 2015), as mentioned in equation 2.2.

Figure 2.14 presents the range of Weber numbers and Ohnesorge numbers in bearing chambers for droplet deformation and break-up. The regimes range from no deformation to bag break-up, and the We and Oh numbers were calculated taking into account the typical droplet and air velocities in the ambient bearing chamber.

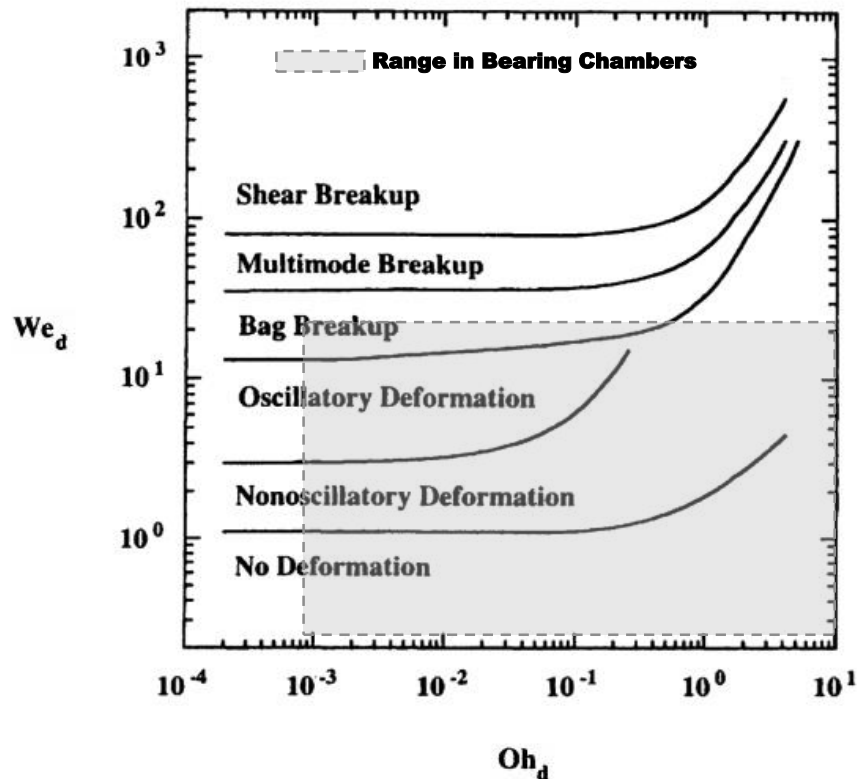


**Figure 2.14. Regimes of droplet deformation and break-up (adapted from Liu, 2000)**

The bag break-up is noticed in droplets with initial diameters above 200  $\mu\text{m}$  that are exposed to high drag forces. The external forces around the droplet's surface produce a deformation of it in the shape of a bag, with a concave surface forming fine secondary droplets. Figure 2.15 shows the difference between bag break-up and shear break-up; in the latter, the formation of filaments is observed and the break-up has a convex surface (Liu, 2000).



**Figure 2.15. Some modes of droplet break-up. *Left: bag break-up, Right: shear break-up* (Liu, 2000)**

As the break-up generates secondary droplets, it is thus of interest to quantify the size distribution of these droplets. Henceforth, the secondary droplets' size distribution can be determined by the Sauter mean diameter (SMD) and mass median diameter (MMD). The secondary droplet diameter  $D_s$  is given by Chen et al. (2011a) as follows:

$$D_s = \frac{12\sigma}{\rho_g u_r^2} \quad 2.14$$

where  $u_r$  is the relative velocity between the primary droplet and the airflow.

The quantification of the droplet distribution allows the computation of the total amount of vapour inside the bearing chamber. The concentration of vapour in the bearing chamber in a given time can be computed first from a single droplet and then extrapolated to the whole geometry. The calculation can be done knowing the droplet size distribution and the number of droplets in the core flow.

### **2.1.5 Oil droplet heat transfer and mass transfer in bearing chambers**

In essence, the trajectories of droplets from the bearings until their interaction with the wall film involves several mechanisms. One of these might be the interaction between droplets, as well as air–droplet interaction (Adeniyi, 2015). Additionally, the droplet can break up during its flight (Chen et al., 2011a). Furthermore, the temperature of the droplet can increase due to the long residence time in the core flow (Sun et al., 2016b). The droplets with a long residence might evaporate. Generally, the droplets trapped in the core flow are those with a long residence time. Thus, these droplets are more likely to evaporate. The vaporisation of droplets in bearing chamber regions has not been studied before. Consequently, the vaporisation of droplets in bearing chambers is an important aspect to analyse, as this can cause oil degradation or even oil fires (Willenborg et al., 2002).

Previous studies have considered the heat transfer phenomena in bearing chambers. These investigations are focused on the heat transfer between the airflow and oil film, as well as the heat transfer between the oil film and chamber wall. However, there has been little research into the analysis of the heat transfer between oil droplets and airflow.

The oil droplets provide cooling to the wall chambers once the contact has been established, as Adeniyi (2015) estimated with CFD modelling. The predictions indicated that there are regions with high heat transfer coefficients. These particular regions were not filled by oil (Kurz et al., 2014) and are shown in red in Figure 2.16. The hot spots presented in Figure 2.16 are zones that need to be covered by a thin film of oil to avoid any droplets having contact with them and suddenly evaporating, which leads to high vapour concentrations. The research of Adeniyi (2015) considers the droplet heat transfer,

although it requests further analysis to consider the effect of phase changes and the contribution of radiation from the chamber environment to the oil droplets.

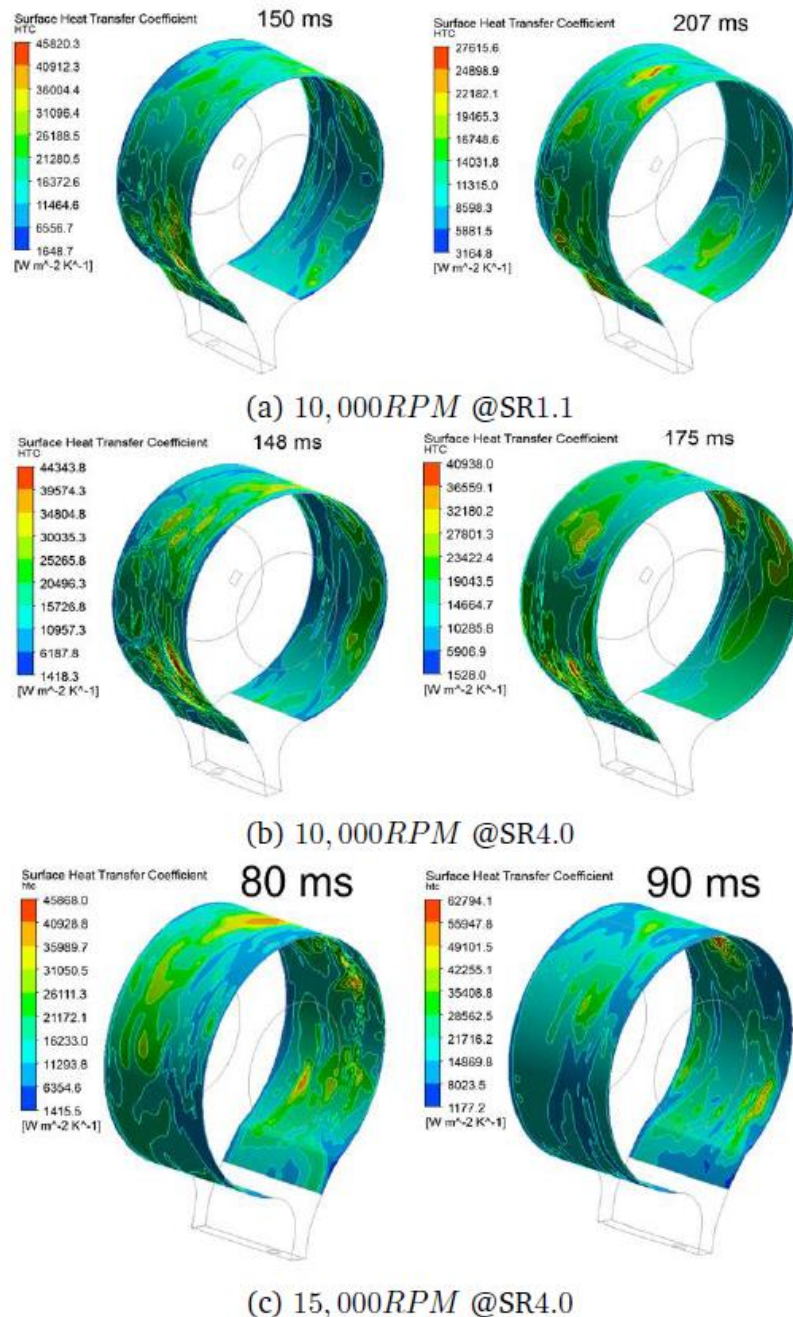


**Figure 2.16. Calculation of the heat transfer coefficient at the wall of bearing chambers (see Adeniyi, 2015)**

At the same time, the oil film distribution along the bearing chamber wall is influenced by many factors, such as the scavenge efficiency, shaft speed, chamber

geometry and airflow rate, amongst others. In the same way, the bearing chamber operating conditions influence the heat transfer inside the bearing compartment (Krug et al., 2015, Adeniyi et al., 2014). According to these operating conditions and oil properties, the flow regimes in the bearing chamber can be classified as smooth, shock and pool (see the work of Morvan, Hibber and Kakimpa, e.g. Kakimpa et al., 2014). A representation of flow regimes in the bearing chamber is shown in Figure 2.17.

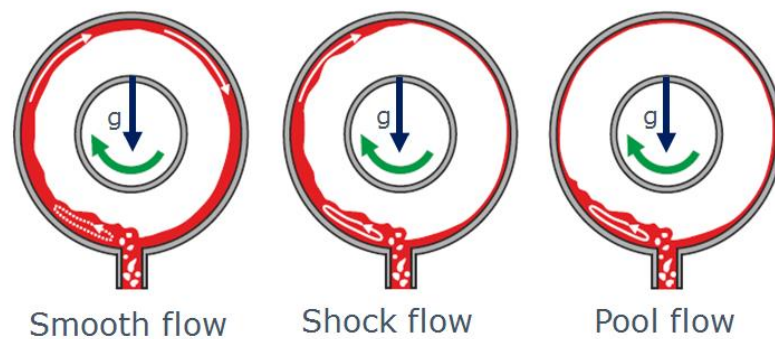


**Figure 2.17. Flow regimes in the bearing chamber (adapted from Kurz et al., 2014)**

Gravitational forces dominate the pool flow regime and this is because the interfacial shear stress between the air and oil becomes much less than the gravitational forces. However, the shear stress governs the oil film distribution in the smooth flow. The shear force at the interface of both fluids may be influenced by the formation of secondary flow in the gas phase. The increase in shear stress is proportional to the increase in the rotational speed. As well as this, the film thickness is limited by the shear force produced by the shaft speed (Tkaczyk and Morvan, 2011, Wang et al., 2011, Krug et al., 2015). Shock flow is the transition between smooth flow and pool flow. This transition is influenced by the shaft speed and chamber geometry, along with the oil and airflow parameters.

In addition, in the pool flow regime, some areas are observed not to be fully wetted. Dry zones over the bearing chamber walls are important aspects to consider. The non-

wetted areas imply high heat transfer coefficients (Busam et al., 2000, Adeniyi, 2015) with temperatures above 470 K (Willenborg et al., 2002, Hashmi, 2012). These temperatures can be above the limits of oil evaporation which is 477.15 K (ExxonMobil, 2016) and can cause a risk of oil ignition (Willenborg et al., 2002). For this reason, much attention has been paid to the oil film distribution.

A thorough understanding of the heat transfer inside the bearing case is essential to maintain the properties of the oil and ensure a good performance of the lubrication system (NASA, 2018). The main sources of heat into the chamber are ascribed to friction of the bearings, viscous dissipation, windage losses and heat from the walls which is due to their proximity to the combustion chamber as shown in Figure 1.2.

In addition, Wittig et al. (1994) observed the variation of local heat transfer with respect to the position along the circumference. They reported higher values near to the vent line due to droplets which were carried to this area by the gas phase. Moreover, it was observed that droplet impingement is frequent in this zone. Thus, this effect increases with the increase in shaft speed.

Likewise, with a horizontal drum partially filled with liquid, Chew (1996) evaluated experimentally the heat transfer coefficient from the oil inlet to the wall surface for laminar and turbulent flows. Moreover, Chew (1996) did numerical calculations assuming laminar and turbulent flows and it was noted that the results of numerical calculations assuming a laminar flow was not in good agreement with the experimental data. Furthermore, the results show that the inlet flow rate, film thickness and swirl velocity are relevant factors in the calculation of the heat transfer coefficient.

Moreover, Glahn et al. (1997) suggested that the heat transfer coefficient on the wall of a bearing chamber is a function of operating conditions such as airflow, oil flow and shaft speed. The research aimed to observe the dependency of the heat transfer coefficient on chamber geometry. The investigation found an increment in heat transfer coefficients for greater shaft speeds and sealing airflows. Additionally, it was noticed there is an essential relationship between the heat transfer coefficient and circumferential geometry, with greater values near to the bottom part of the bearing chamber.

Further investigations were assessed by Busam et al. (2000) considering the effects of the operating conditions in the heat transfer of the bearing chamber walls. Building on Glahn et al. (1997), the research of Busam et al. (2000) proposed a correlation based on non-dimensional parameters, namely Nusselt number, hydraulic diameter and Reynolds number, involving the operating conditions and chamber dimensions (width and height). This correlation provides the basis to the bearing chamber design reducing uncertainties.

Likewise, Jakoby et al. (1999) established correlations of the convective heat transfer airflow in annular channels by analysing the influence of the Taylor-vortex formation and flow characteristics. From these correlations, it is observed that the chamber geometry has an important implication on the heat transfer coefficient. The heat transfer coefficient increases dramatically when the air inlet height is reduced. This is a result of the increase in the axial velocity and hence shear stresses interacting in a small area at the sealing air entrance. Finally, Nusselt and Reynold numbers were proposed based on these correlations. The proposed non-dimensional numbers allow describing the convective heat transfer. Moreover, the impacts of Taylor vortices showed a lack of relevance to the increase in heat transfer.

Kanike et al. (2012) analysed the thermal behaviour inside bearing chambers, accounting for the heat sources from seals due to sliding motion, bearings by friction, oil pumping from kinetic energy loss and the heat transfer coefficient from bearings and walls to oil. The analysis found that the bearing temperature is more likely to increase than the oil temperature due to friction between components. However, further investigation is needed to account for the influence of the outside environment, materials and air leaks on the oil temperature.

Fei et al. (2017) reported that the oil temperature is higher in the lower part of the bearing chamber along the circumferential direction where the scavenge is located and oil has accumulated, which agreed with the results of Glahn et al. (1997). The air temperature is higher next to the shaft and lower at the core of the chamber and near to the walls. Therefore, the oil droplets may be prone to evaporate faster when they are travelling near to the shaft.

In a similar manner, Fang and Chen (2018) suggested that the droplet's temperature increases with the shaft speed and air velocity and it is highest for small droplet diameters, such as 50  $\mu\text{m}$ . Hence, for this diameter, the droplets might absorb more heat during their journey, which is longer than that of droplets with larger diameters. Equally important, the oil inlet temperature affects the droplet's velocity, because a high oil inlet temperature means there is a greater likelihood of droplet deformation, which reduces the droplet's velocity and increases the drag effects (Weinstock and Heister, 2004).

Additionally, Weinstock and Heister (2004) reported that the droplets' diameters are reduced with high shaft speeds and they are more affected by drag and airflow, giving the droplet a longer residence time. The parent droplet's trajectory is affected by the initial

droplet diameter, but its trajectory is not affected by the shaft speed, air temperature or oil inlet temperature. In other words, the droplet's velocity is affected by the parameters that do not affect the droplet's trajectory. Moreover, a reduction was observed in the momentum transfer between droplets and the wall film when the droplet's initial velocity is low. This reduction was observed for shaft speeds below 5000 rpm.

Another key point is that the temperature distributions inside a rotating annulus are affected by the mean droplet diameter (Maqableh et al., 2003). Furthermore, it was observed that the air temperature is higher near to the rotating shaft and it is reduced when the airflow approaches the walls (Fei et al., 2017, Maqableh et al., 2003). Moreover, Maqableh et al. (2003) calculated the air temperature within the bearing chamber, which showed good agreement with Fei et al. (2017). Both studies observed that the air temperature is higher near to the rotating shaft and it is reduced during the journey to the walls. In addition, it was noted that the air temperature near the wall was 60 K higher than in the core flow (Maqableh et al., 2003).

#### ***2.1.5.1 Limitations of these studies***

The oil droplets experience a number of heat and mass transfer mechanisms during their trajectories through the bearing chamber, namely convection due to the airflow, radiation from the chamber walls, and diffusion due to the concentration variation of the oil components and their surroundings. The heat transfer in the bearing chamber has been analysed mainly at the walls and specifically at the interaction between the air, oil and wall itself.

Many authors found that heat transfer variation effects depend strongly on the bearing chamber operating conditions, such as inlet flow rate, shaft speed, sealing airflow

and bearing chamber geometry (Wittig et al., 1994, Chew, 1996, Glahn and Wittig, 1996, Glahn et al., 1997, Glahn and Wittig, 1999, Jakoby et al., 1999, Busam et al., 2000, Yuan et al., 2011, Kanike et al., 2012, Adeniyi, 2015).

However, some of these studies mentioned above considered only the convection effects from the bulk flow to oil (Adeniyi, 2015, Jingyu et al., 2016, Sun et al., 2016a, Sun et al., 2016b); the radiation and diffusion effects on the oil droplets were not considered and, additionally, vaporisation was not investigated in those studies.

The evaporation of oil droplets was computed in research into the design of axial ventilation for a turbofan engine lubrication system (Jingyu et al., 2016). Their research focused more on the geometry design rather than understanding the evaporation of oil droplets. Furthermore, very little work has been reported to determine how droplet evaporation and the air–oil mixture may produce a risk of fires (Rosenlieb, 1978). Thus, it is of interest to analyse numerically the amount of oil vapour produced by a single oil droplet under different airflow conditions.

Additionally, further analysis is required to understand the oil droplet vaporisation and degradation, including not only the convection but also the radiation and diffusion effects, along with the consequences to the entire lubrication system. This analysis will provide recommendations to avoid the risk of oil coking, cabin air contamination and oil fires.

The analysis of oil vaporisation is important because the literature suggests that the air temperature inside bearing chambers is in the range of 450 K to 880 K (Hashmi, 2012), with the upper limit being above that of the operational temperature range for the oil (233.15 K to 474.15 K) to ensure safe operating conditions (ExxonMobil, 2016). When

the oil is not degraded, its evaporation starts at 477.15 K (see Table 2.2), but when the oil is chemically degraded the evaporation loss may start at lower temperatures (Livingstone, 2007). Therefore, some of these temperatures and air velocities are used as boundary conditions in Section 5.

**Table 2.2. Bearing chamber environment**

<b>Oil–liquid phase (Mobil Jet oil II)</b>	
T [K]	233.15 to 474.15
V [m/s]	14 to 53
Droplet diameter [ $\mu\text{m}$ ]	1 to 500
Re	0.2 to 1500
Flash point [K]	543.15
Evaporation loss 3%	477.15 K
<b>Air</b>	
T [K]	450 to 880
V [m/s]	0.1 to 10
P [kPa]	22 to 1,000 (0.022 to 1 MPa)

Several studies have modelled the evaporation of a single droplet. However, most of them were intended to enhance the combustion process of ICEs. The adoption of these models for the bearing chamber analysis will be useful for understanding the evaporation process and preventing oil fires, which might be produced by the interaction of air–oil mixtures and high temperatures in the interior of the chamber.

Section 2.2 presents a literature review of the analysis of droplet evaporation under convective flow, which is mainly applied to the study of combustion in the ICE.

## 2.2 Oil droplet evaporation in a convective environment

The process of droplet evaporation under the effects of convective airflow has been analysed already for ICEs, where fuel droplets were studied with the aim of enhancing fuel combustion. Most of these studies were performed to provide an understanding of the heat and mass transfer for single droplets surrounded by high-temperature gas. Moreover, these investigations have explained the effects of the convective environment on the evaporation rate, including the effects of variations in temperature and pressure (Sazhin, 2006, Sazhin et al., 2007b), the effects of convective flow on the internal flow dynamics of the droplet (Wong and Lin, 2006) and the influence of the Reynolds number on mass transfer (Renksizbulut et al., 1991).

Other studies have analysed the evaporation process of single component droplets and multi-component droplets, focusing on component volatilisation and reduction of the droplet lifetime (Godsave, 1949, Godsave, 1953, Chew, 1996, Daif et al., 1998). The enhancement of the mass transfer between droplet and air due to internal circulation was studied using numerical methods such as the VOF approach (Banerjee, 2013, Dong et al., 2014, Strotos et al., 2011, Strotos et al., 2016).

Moreover, Strotos et al. (2016) reported that recourse to the VOF approach is appropriate to investigate droplet heat and mass transfer during hot convective flow. This allows the user to track the two-phase flow interface, providing a visual representation of the droplet's internal circulation, as well as computing the transient evolution of the evaporation process. All the studies mentioned above were performed for fuel droplets; moreover, the research of Yi et al. (2015) and Yi et al. (2016) has analysed oil droplet evaporation but only for ICE conditions.

The analysis of evaporating oil droplets under aero-engine bearing chamber conditions has not been studied with the VOF technique. Therefore, it is important to analyse droplet evaporation using the VOF approach to observe the droplet's internal circulation, oil degradation, and the amount of vapour produced by a single droplet and then later extrapolate this to the entire bearing chamber geometry. Furthermore, aero-engine lubrication oil presents different properties than fuels, and the bearing chamber conditions present a different range of temperatures and pressures than typical ICE conditions.

It is thus of great interest to understand the effect of oil evaporation on the effectiveness of the lubrication system. Furthermore, the variation of properties in the vicinity of the droplet and the droplet's internal flow field are studied computationally under representative aero-engine bearing chamber conditions.

### **2.2.1 Oil droplet internal circulation**

The droplet's internal circulation can be due to the shear stresses at the droplet's surface, which are generated by the flow around it. Moreover, the internal vortices might be due to the concentration or temperature gradients within the droplet, as has been studied by Prakash and Sirignano (1980). Furthermore, according to Sazhin et al. (2006), it is relevant to include the internal circulation within the droplet in order to calculate the droplet evaporation process accurately.

The internal circulation is accounted for in the evaporation models when the temperature gradients within the droplet are considered in the analysis of the droplet's internal flow field. There are multiple models that include the internal droplet convection. Two of these are the finite thermal conductivity (FTC) model, which assumes a limited

thermal conductivity, and the effective thermal conductivity (ETC) model, which is based on the FTC model.

The FTC model presents a correction factor to include thermal conductivity in the calculation; this factor is called the effective conductivity factor and is dependent on the temperature gradient within the liquid. The ETC model accurately computes the recirculation inside the droplet (Wong and Lin, 2006). The recirculation inside droplets can also be accounted for with the vortex dynamics model. However, according to Sazhin (2006), it might be computationally expensive if the issue is solved numerically with CFD techniques.

Moreover, internal circulation is reduced with the liquid viscosity, which is a function of the temperature and consequently reduces the heat transport inside the droplets (Wong and Lin, 2006). Thus, the thermal gradient within the liquid and the internal circulation are critically important to obtain accurate predictions because the heat transfer within the droplet may reduce the droplet's lifetime (Prakash and Sirignano, 1978).

The internal circulation of evaporative droplets was studied using the VOF approach by Banerjee (2007), Banerjee (2013), Strotos et al. (2011), Strotos et al. (2008) and Strotos et al. (2016). They reported the formation of a vortex due to the diffusion between components in the liquid phase, where the evaporation occurs first for the most volatile component.

In addition, Strotos et al. (2016) found two circulation zones in the liquid phase with the use of the VOF technique. The two circulation zones seem to be constant through time. Moreover, they studied the Marangoni effects on the evaporation process and concluded that they have little influence on evaporation. The Marangoni effects are observed when

the surface tension changes with temperature and are found at the droplet's surface where there is an interface between liquid and liquid or liquid and gas. The Marangoni effects generate a circulating flow due to changes in temperature because the surface tension depends on the temperature variations (Albernaz et al., 2016). In other words, the surface tension shows a reduction with an increase in temperature.

Furthermore, Dong et al. (2014) modelled the internal circulation of droplets, accounting for the variation of surface tension due to the gradients of temperature (Marangoni effects). In addition, their numerical analysis studied the internal circulation due to droplet evaporation, using the VOF technique and the kinetical theory for the calculation of mass transfer between phases. Dong et al. (2014) reported that the Marangoni effects are reduced due to the evaporation mass transfer and that they are not perceptible when the time of evaporation and/or the time of droplet suspension is short.

Raghuram et al. (2013) evaluated the Marangoni effects in moving droplets. They reported that the gradients of the surface tension are produced by the difference between the species concentration during the evaporation. Moreover, they noticed that the Marangoni effects are reduced when the velocity of air is increased, whereas the streamlines of the internal vortex are similar among the evaluated cases for different temperatures. Therefore, the Marangoni effects are significant when the air velocity is low.

The droplet's internal circulation and interaction with the external flow are represented in Figure 2.18. It shows a main vortex inside the droplet, a gas boundary layer and a liquid boundary layer. The gas boundary layer in the vicinity of the droplet may be formed by the vapour produced by the phase-change process (Sirignano, 2010).

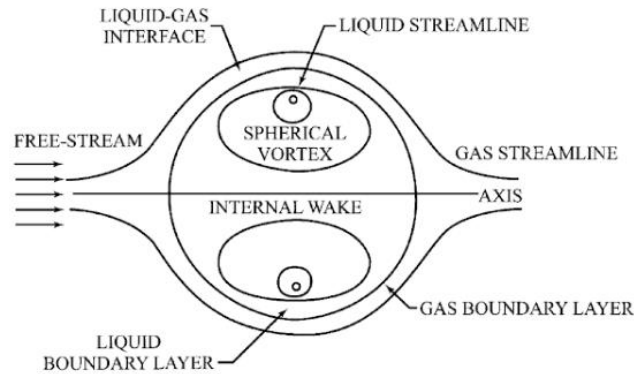


**Figure 2.18. Axisymmetric flow field and internal circulation of a vaporising droplet (Sirignano, 2010)**

Deepu et al. (2013) noticed that the internal circulation affects heat and mass transfer, and modifies the distribution of temperature and the concentration in multi-component droplets. Therefore, the droplet evaporation process should be addressed considering the droplet's internal and external flow fields.

The internal circulation depends strongly on the boundary conditions at the droplet's surface, such as air velocity and air temperature which can be accounted for in the droplet evaporation models through correlations. There are many correlations to calculate the heat and mass transfer between the droplet's surface and the external flow, such as Frossling, Ranz and Marshall, Renksizbulut, and Yuen among others.

The calculation of the heat and mass transfer at the droplet's interface is based on the Nusselt and Sherwood numbers, as follows (Clift et al., 2005):

$$Nu = 1 + (1 + RePr)^{1/3} f(Re) \quad 2.15$$

$$Sh = 1 + (1 + ReSc)^{1/3} f(Re) \quad 2.16$$

where  $f(Re) = 1$  at  $Re \leq 1$ , and  $f(Re) = Re^{0.077}$  at  $1 < Re \leq 400$ .

The Nusselt and Sherwood numbers are given in terms of Prandtl and Schmidt numbers, respectively. The Prandtl number is the ratio between momentum diffusivity and thermal diffusivity:

$$Pr = \frac{C_p \mu}{k} \quad 2.17$$

The Schmidt number is the relationship between momentum diffusivity and mass diffusivity:

$$Sc = \frac{\mu}{\rho D} \quad 2.18$$

On account of this, these investigations and parameters are of interest in the present investigation to predict the internal circulation of oil droplets under representative bearing chamber conditions. The main drivers to study the droplet vaporisation of oil lubricant are presented in Section 2.2.2.

### **2.2.2 Droplet vaporisation of oil lubricant**

The droplets travel from the bearings to the core flow and, in addition, can splash onto the thin wall film and form secondary droplets. The secondary droplets can have diameters less than 200  $\mu\text{m}$ , which are of interest in this investigation. This is because droplets with small diameters can remain suspended in the core flow; this is described with the Stokes number in equation 2.5.

The droplets that are recirculating in the core flow tend to evaporate completely. The oil vapour concentration is of interest in this study because the stoichiometric mixture of

air–oil in the presence of high temperatures and high pressures might be at levels conducive to starting a fire (Willenborg et al., 2002, Rosenlieb, 1978).

According to Rosenlieb (1978), the air inlet temperature and oil droplet size are the parameters with the greatest influence on the vapour concentration. Furthermore, the parameters with significant influence on the flammability are the oil inlet temperature and flow rate. Moreover, he noticed that there is no risk of fire when the oil inlet temperatures are below 417 K.

### ***2.2.2.1 Operating conditions that control oil fires***

The main parameters that control fire conditions inside a bearing chamber are:

- oil flow rate,
- oil inlet temperature,
- air leakage rate,
- air inlet temperature,
- shaft or bearing speed,
- ignition source and duration,
- geometric configuration,
- lubricant flammability, and
- temperatures of the bearings, shaft, seal and housing.

Figure 2.19 presents the operating conditions and the ignition sources of oil fires that can be found in an RB199 bearing chamber, which are the operational conditions available in the literature.

The zones with the highest probabilities of having a combustible air mixture are those with low velocities in the gas phase, where the air–oil mixture has a longer residence

time at high temperature (Willenborg et al., 2002). Furthermore, fires can appear in the small regions of the bearing chamber, where the air–oil mixture can stay for a long time (Rosenlieb, 1978).

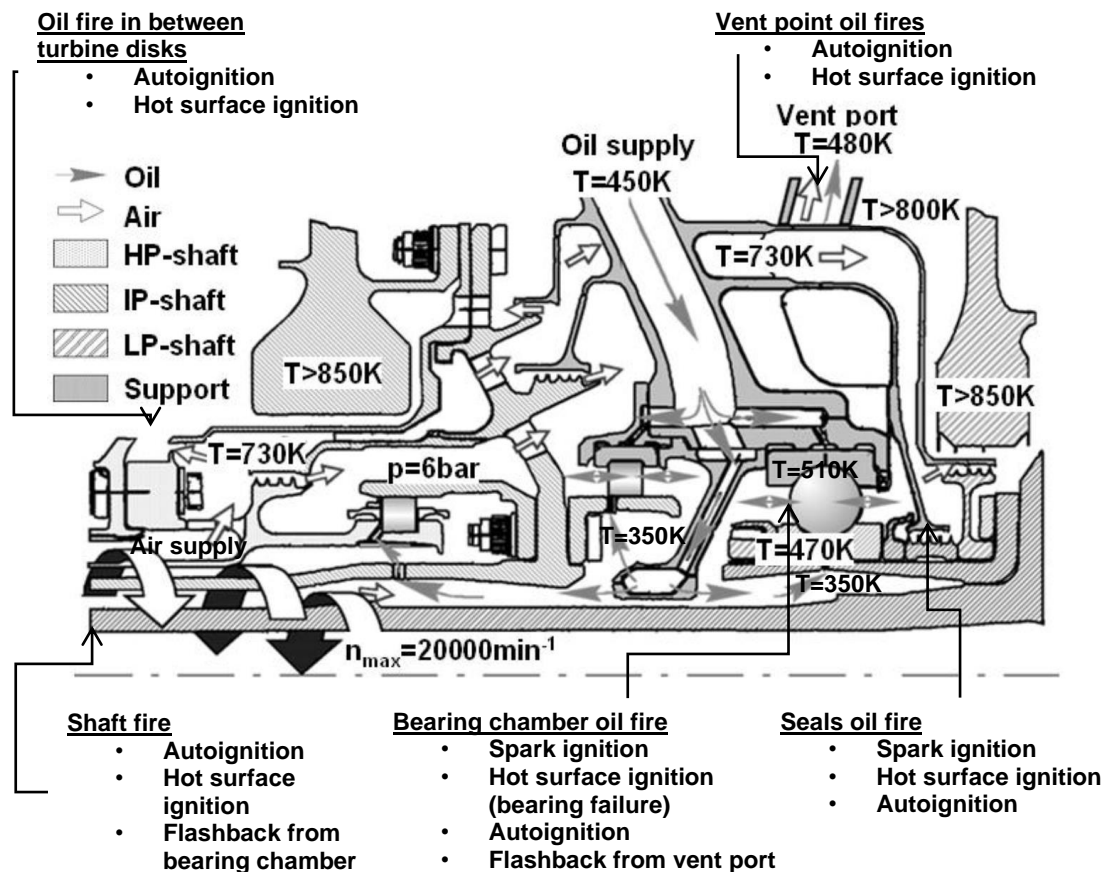


Figure 2.19 Operating conditions of HP/IP bearing chambers and ignition mechanisms of oil fires (adapted from Hashmi, 2012, Willenborg et al., 2002)

### 2.2.2.2 Ignition source of oil fires

Fires can be produced inside the bearing chamber, in the seals or in the vents. The three mechanisms to produce a fire inside the bearing chambers are as follows (Willenborg et al., 2002):

- Autoignition, which represents a spontaneous ignition of the oil.

- Hot surface ignition when the oil touches a hot surface, evaporates and ignites.
- Vent pipe flashback. This mechanism occurs when the mist in the vent produces a flame which can propagate from the vent to the bearing chamber.

The two mechanisms that may occur due to secondary droplets suspended in the core flow are autoignition and vent pipe flashback. Both of these happen when there is a long residence time of the oil droplets (Rosenlieb, 1978). The sources of ignition can be determined by the flammability conditions of the air–oil mixture. The conditions to produce a flame are as follows (Rosenlieb, 1978):

- The vapour concentration of droplets with diameters less than 10  $\mu\text{m}$ , which tends to be high and consequently air–oil mixture stoichiometric ratio.
- The oil temperature is above the critical value, which can create a combustible mixture or a self-sustainable flame. The self-sustainable flame depends on the flash point or the fire point of the substance.
- The temperature of the oil is above the autoignition temperature (AIT), which means that an external source is not needed to start a fire.
- There is a presence of an ignition source such as a hot surface, frictional sparks or hot gases. Where there is the presence of an ignition source, the oil temperature can be below the AIT.

Spontaneous ignition depends on the residence time of the air–oil mixture and the bearing chamber's wall temperatures and, thus, it is more likely to occur in the low velocity zones inside the bearing chamber (Schmidt et al., 1982).

### 2.2.2.3 Flammability

Flammability is the ability of any substance to produce a fire. Flammability limits are determined by the oil vapour concentration and the temperature of the mixture (Rosenlieb, 1978). It is important to know the flammability limits of oil vapour concentrations to avoid any risk of fire.

Flammability is defined by upper and lower limits. These limits determine the range of flammability above and below the stoichiometric ratio. A rich mixture is when the concentration of the mixture is above the stoichiometric ratio. In contrast, a lean mixture is when the concentration of the mixture is below the stoichiometric ratio.

The lower flammability limit is defined by the lowest oil vapour concentration required to create a flame in the presence of an oxidant. If the oil vapour concentration is below this limit, the mixture is too lean to burn (Kuchta and Cato, 1968, Rosenlieb, 1978). Conversely, the upper flammability limit is the highest concentration required to create an ignition and when the mixture reaches this point it is too rich to burn.

The flammability limits can be calculated as given below (Rosenlieb, 1978):

$$LL_{297K} = 0.55C_s \quad 2.19$$

$$UL_{297K} = 4.8C_s \quad 2.20$$

where  $LL$  is the lower flammability limit,  $UL$  is the upper flammability limit and  $C_s$  is the stoichiometric ratio.

The following equations can be used to predict the flammability range, which increases with the temperature:

$$LL_T = LL_{297K}[1 - 7.2 \times 10^{-4}(T - 297)] \quad 2.21$$

$$UL_T = UL_{297K}[1 + 7.2 \times 10^{-4}(T - 297)] \quad 2.22$$

Temperature is a very important property for the combustion process because it leads to the flammability of the substance and the ignition sources, as discussed in Section 2.2.2.2. Therefore, it is important to define the following concepts:

- Flash point: the lowest temperature at which the substance produces enough vapour to form a flammable mixture. In this case, the air–oil vapour mixture requires an ignition source to produce a flame.
- Fire point: the temperature after the flash point at which the mixture keeps burning after ignition.
- Autoignition temperature (AIT): the lowest temperature of a mixture at which a fire can start without an external source (e.g. spark or flame) under normal conditions. In other words, the substance ignites spontaneously when it reaches this temperature.

Figure 2.20 shows the flash point and AIT limits; the fire point is between these two limits and just above the flash point. Several specific values are presented in Table 2.3.

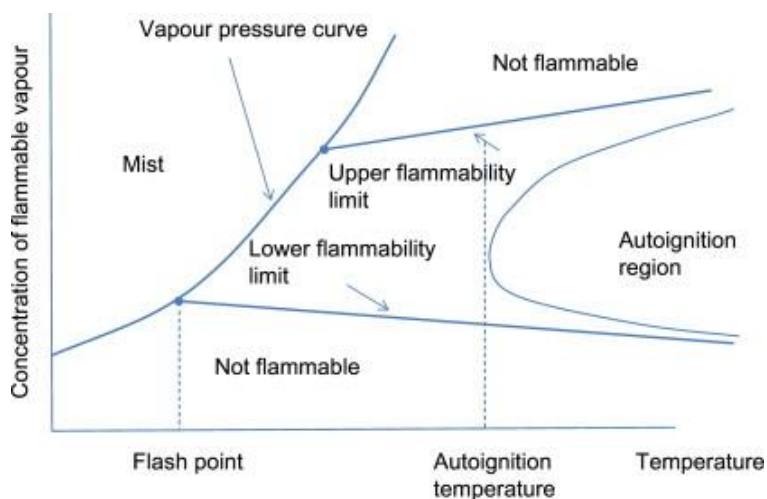


**Figure 2.20. Relationship between different flammability properties (Dimian et al., 2014)**

According to Willenborg et al. (2002), the AIT for Mobil Jet Oil II is 677 K at 1 bar and the AIT may vary with the ambient pressure. The AIT decreases with higher ambient pressures, e.g. at 4 bar, the AIT decreases to 581 K. Moreover, the ignition delay times vary from 0.5 s to 6.5 s and it depends on the ambient temperature. When the droplets touch a hot surface, the ignition delay time varies with the temperature of the surface.

However, these values are based on experiments applied to droplets splashing onto a hot surface. The ignition temperatures when droplets are exposed to a hot gas may be higher than the hot surface ignition temperatures. The ignition temperature depends on the size or shape of the jet or the droplets injected into the hot gas (Kuchta and Cato, 1968).

The flash point, fire point and AITs of some lubricants are presented in Table 2.3. Pentaerythritol tetrapentanoate (PEC5) is a base stock ester for which the fire point and AIT can be approximated by analysis to MIL-L7808 oil type in Section 5.

**Table 2.3. Flash point, fire point and autoignition temperatures of lubricants (Kuchta and Cato, 1968, Rosenlieb, 1978)**

<b>Material</b>	<b>Flash point [K]</b>	<b>Fire point [K]</b>	<b>Autoignition temperature [K]</b>
PEC5	493.55±301.95	-	-
MIL-L-7808	498.15	510.93	659.82/525.37
MIL-L-23699	525	558	705

According to Schmidt et al. (1982), the options to prevent oil fires are adjusting the air–oil ratio, providing optimum cooling of the bearing chamber walls, improving the design to observe low residence times of the air–oil mixture, proposing suitable materials to avoid sparks and avoiding hot spots along the bearing chamber walls.

In further chapters, the air–oil mixture produced by an oil droplet evaporating under a convective flow with a high temperature and different air velocities will be analysed with a parametric study to predict the temperature of the mixture and the evaporation rate.

### **2.2.3 Droplet evaporation including radiation effects**

Several studies have been performed to understand the heat and mass transfer of a single droplet surrounded by high-temperature gas, where a convective flow heats the droplet. The main goal of these studies has been to understand the spatial and temporal changes in the droplet. Most of these studies analysed the evaporation rate for different air temperatures and pressures. Some of them used numerical approaches for tracking the gas–liquid interface, e.g. VOF, and others reported it analytically. Most of the numerical studies aimed to analyse the evaporation due to convective heat transfer effects. However, thermal radiation plays an important role in the study of droplet phase change.

Sazhin (2006) reported a broad comparison of models, where it was concluded that the models that integrate the radiation effects into the analytical calculations result in a better agreement with experimental data, unlike the models where radiation is neglected.

Furthermore, Sazhin et al. (2007a) noticed that when convection and radiation are heat transfer mechanisms in droplet evaporation, the radiation distribution is not representative of the droplet evaporation process because the convection mechanism is dominant.

However, Abramzon and Sazhin, (2005) evaluated the accurate model and the most practical mode for CFD applications accounting the radiation effects in the evaporation process. One attempt at evaluating the radiation models is to analyse the effect of radiation absorption on the droplet evaporation process (Abramzon and Sazhin, 2005). Radiation

absorption is defined as the process of converting radiation intercepted by matter to internal energy (Incropera et al., 2007). The absorption can be considered by an approximated factor (Abramzon and Sazhin, 2005, Abramzon and Sazhin, 2006). Therefore, the distribution of radiation absorption can be treated as uniform (Lage and Rangel, 1993, Sazhin et al., 2007a).

The uniform absorption of radiation allows us to simplify the evaporation models being used in CFD simulations. The approximation of using an absorption efficiency factor is suitable to save time and cost in the computational analysis, as was implemented in the analysis by Abramzon and Sazhin (2006).

Another method to account for radiation is through the Mie theory, which calculates the spectral energy of thermal radiation. However, this takes more time to perform the calculation with CFD approaches (Sazhin et al., 2007a).

Additionally, radiation absorption at the droplet's surface was analysed by Long et al. (2015), who reported a dependence of the radiation absorption on the droplet diameter. Moreover, they also identified a proportional dependence between the radiation absorption and the temperature of the environment. They noticed that radiation absorption increased when the temperature of the environment increased.

In addition, they determined a diameter criterion to measure the computational efficiency modelling with and without radiation absorption. The diameter criterion proposed is a polynomial formula, which depends on ambient temperature and pressure. With this criterion, they determined that the error of the predictions with and without radiation was less than 5% for droplets with initial diameters less than 200  $\mu\text{m}$ . Therefore,

radiation absorption can be neglected for droplets with diameters less than 200  $\mu\text{m}$  in order to have more efficient computational times in the predictions.

However, as the error without radiation absorption is less than 5% for a diesel droplet, it is therefore worth analysing the radiation effects on the droplet evaporation process of a typical oil for a jet engine and the associated bearing chamber conditions in order to compare with the conclusions of Long et al. (2015). The previous reports were applied to understand the reduction of droplet diameter due to the evaporation of fuel droplets. However, it is important to mention that a few investigations were focused on oil droplets.

Yi et al. (2015) modelled the evaporation of oil droplets for ICEs. They considered ideal and real gas conditions, as well as the radiation in the environment for different pressures. Yi et al. (2015) agreed with Long et al. (2015) that the ideal gas assumption is a good approximation for low pressures; however, for high pressures, they recommended the real gas approximation. This is because real gas does not follow the kinetic-molecular theory. In other words, real gas does not follow the assumptions of ideal gas laws. Therefore, the real gas approach depends on the Van der Waals forces, compressibility effects, non-equilibrium thermodynamic effects, variable specific heat capacity and variable composition (Çengel, 2011).

The findings of Yi et al. (2015) are consistent with Sazhin et al. (2007b), who mentioned that the analysis that considers radiation in the calculation of droplet evaporation has better agreement with the experimental data. They concluded that ambient pressure has little effect on the vaporisation process. In addition, they recommended using lubricating oils with a high molecular weight to reduce the vaporisation rate.

According to the literature review presented in the previous sections, the present project will fill the gap of knowledge in the numerical simulations of the oil droplet vaporisation process. Additionally, the present analysis includes the VOF approach and considers the conditions within bearing chambers. This means that the contribution to the knowledge will be in the study of the evaporation of oil droplets, which will be applied to the design of aero-engine bearing chambers.

## **2.3 Summary**

In this chapter, a review is presented of the relevant literature about the formation of droplets inside the bearing chamber and from the bearings through the core flow until they reach the walls. Additionally, relevant investigations are presented about the droplet impingement onto the walls and the formation of secondary droplets. Furthermore, a literature review is presented regarding the droplet motion, droplet size distribution and particle tracking; which is of relevance to the study of heat and mass transfer of droplets and their interactions with the core flow. Various investigations have explored this interaction that may drive the droplet break-up and droplet deformation.

The majority of the studies are focused on the heat transfer in the bearing chamber walls, while there is also some progress made in understanding the thermal distribution of the airflow. However, very little work has been reported to determine the vaporisation process for droplets suspended in the bearing chamber core flow; in fact, it has only been done in a limited form for automotive applications so far and mainly over the past five years.

The evaporation of droplets in a convective flow has been studied experimentally and numerically to enhance the combustion of ICEs. Recourse to the VOF approach helped to understand the phase-change phenomena and observe internal circulation and mass transfer due to evaporation tracking at the droplet's interface. Only one study has considered oil as a fluid and looked into the risks of exothermic reactions.

The work done on ICEs has found that radiation played a role in the evaporation of fuel droplets, which further incentivises us to look into this for aero-engine bearing chambers.

### 3 CFD Methodology

This chapter presents the CFD methodology used to analyse and model the droplet evaporation process and the parameters that affect the heat and mass transfer at the droplet's surface. This methodology is based on the current state-of-the-art knowledge and previous investigations of droplet evaporation applied to ICEs.

Furthermore, this chapter addresses the solution methodology for the transport equations, evaporation model and oil properties calculations. The oil droplet evaporation process was computed using ANSYS© Fluent v18.0 to solve the generic Navier–Stokes equations, supplemented with the  $D^2$ -law (Godsave, 1953, Spalding, 1953) implemented as a user-defined function (UDF) to account for the evaporation process.

#### 3.1 Physical model

The droplet evaporation process was modelled numerically based on previous studies reported in the literature that analysed the evaporation of droplet fuel in ICE conditions. In this section, the equations used to understand the evaporation of oil droplets under representative bearing chamber conditions are presented. The methodology used is state of the art and is applied to, and enhanced with, the calculation of the properties of aero-engine-based stock oil.

Moreover, the two-phase flow is modelled using the VOF technique, which has been applied previously to model the transient evolution of the droplet evaporation process (Strotos et al., 2016, Banerjee, 2013). As a result, the VOF technique allows the user to track the two-phase flow interface, as well as providing a visual representation of the

droplet's internal circulation. Therefore, the present research computes the two-phase flow through the VOF approach.

### 3.1.1 VOF to track the gas–liquid interface

The VOF approach allows the characterisation of two immiscible fluids and the quantification of the volume fraction of each fluid in a cell. Accordingly, the amount of each fluid in a cell is computed in a range from zero to one, where one represents the liquid phase and zero represents the gas phase. When the value is between zero and one, e.g. 0.5, it signifies that two fluids occupy the volume cell. Additionally, the VOF method computes the average properties in each cell or control volume, following the continuity equation 3.1:

$$\frac{1}{\rho_q} \left[ \frac{\partial}{\partial t} (\alpha_q \rho_q) + \nabla \cdot (\alpha_q \rho_q \mathbf{u}_q) \right] = S_{\alpha q} \quad 3.1$$

$$\sum_{q=1}^n \alpha_q = 1 \quad 3.2$$

where  $\alpha$  is the volume fraction and  $q$  is the  $q$ th phase.

The mass flow is calculated as a source term for each phase, as in equations 3.3 and 3.4.

For the liquid phase:

$$S_{\alpha_l} = - \sum_{i=1}^n m_i''' \quad 3.3$$

For the gas phase:

$$S_{\alpha_g} = \sum_{i=1}^n m_i''' \quad 3.4$$

The density and viscosity are calculated by:

$$\rho = \sum_{i=1}^n \alpha_q \rho_q \quad 3.5$$

$$\mu = \sum_{i=1}^n \alpha_q \mu_q \quad 3.6$$

where a gas–liquid flow is represented as:

$$\rho = \alpha_g \rho_g + \alpha_l \rho_l \quad 3.7$$

$$\mu = \alpha_g \mu_g + \alpha_l \mu_l \quad 3.8$$

The VOF method is computed with an explicit formulation and Sharp interface modelling, which are described in Sections 3.1.1.1 and 3.1.1.2. Moreover, the computation considers a maximum Courant number of 0.25 and the volume fraction cut-off is 1e-12, which means that all the volume fraction values lower than 1e-12 are set to zero (ANSYS, 2016b).

### ***3.1.1.1 Interpolation near the interface***

There are different approaches for the interpolation at the interface in multi-phase flow calculations. One of these approaches is the geometric reconstruction algorithm, which assumes that the interface can be calculated as a linear slope and computes the fluid advection through the cell faces. The geometric reconstruction algorithm follows three steps, as follows, which are summarised in ANSYS (2016b) (see Figure 3.1):

1. Calculation of the linear slope position at the interface using the volume fraction approach and its derivatives.
2. Calculation of the fluid advection amount through each face using the computed linear slope at the interface and the normal and tangential velocity distribution on the face.

3. From the balance of fluxes obtained in the previous step, calculate the volume fraction in each cell.

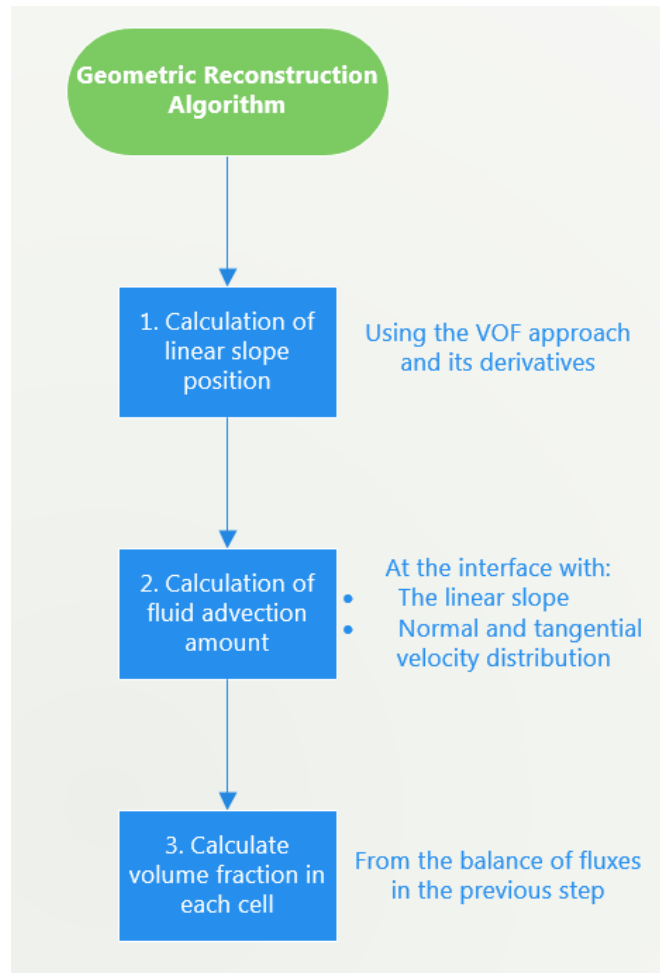


**Figure 3.1. Steps for the interpolation near the interface using the geometric reconstruction algorithm**

The geometric reconstruction approach allows the changes at the interface, such as the phase change in this work, to be computed with accuracy as can be observed in Figure 3.2. Thus, this algorithm was chosen for the present research.

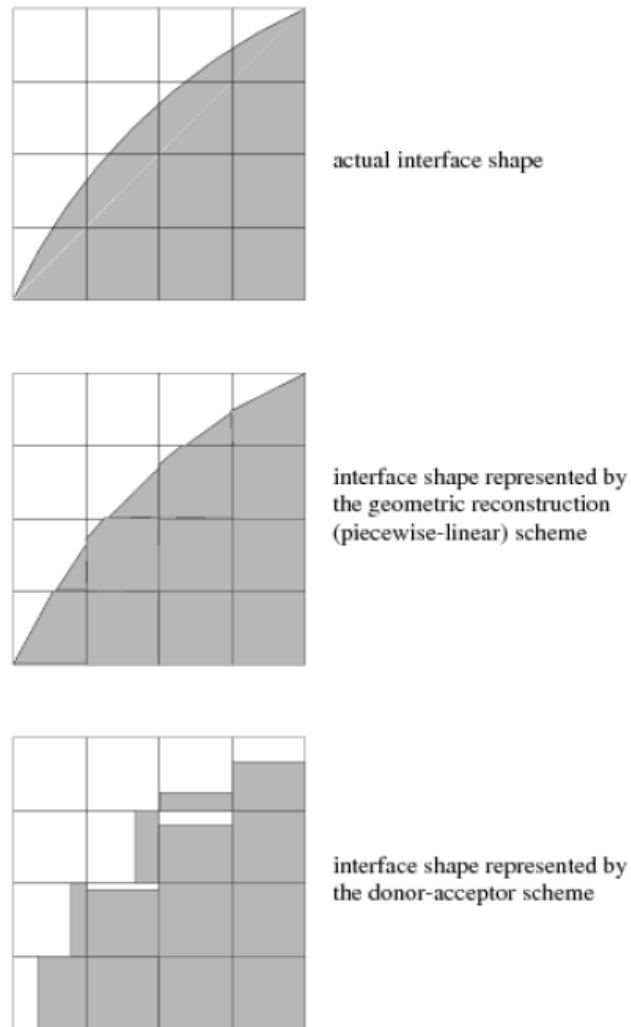


**Figure 3.2. Interface shape represented by the geometric reconstruction scheme (ANSYS, 2016b)**

Moreover, other schemes were also evaluated, such as the compressive scheme, under the implicit formulation. The compressive scheme has the capability to increment the time step of simulation. However, the compressive scheme might not compute with accuracy the interface changes, such as the evaporation, presenting numerical diffusivities at the droplet's interface, as shown in Figure 3.3.

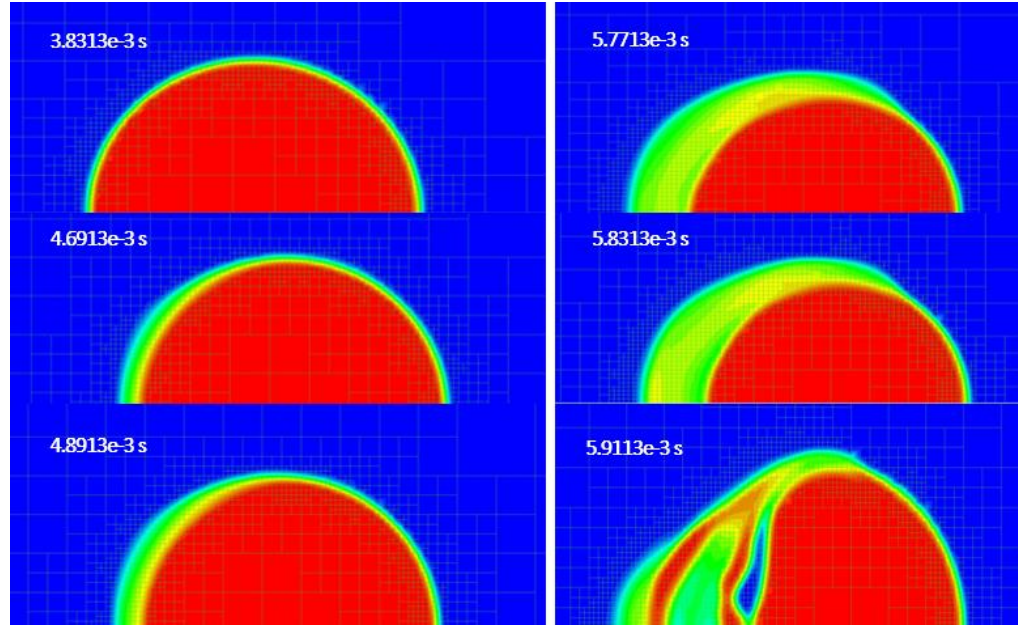


**Figure 3.3. Numerical diffusivities presented using the implicit formulation with the compressive scheme**

### 3.1.1.2 *The explicit formulation*

The VOF approach uses the geometrical reconstruction algorithm available in ANSYS© Fluent with the explicit formulation, which discretises the volume fraction as follows:

$$\frac{\alpha_q^{n+1} \rho_q^{n+1} - \alpha_q^n \rho_q^n}{\Delta t} V_{cell} + \sum_f (\rho_q U_f^n \alpha_{q,f}^n) = [S_{\alpha q}] V_{cell} \quad 3.9$$

where  $n + 1$  is the index for the current time step,  $n$  is the index for the previous time step,  $\alpha_{q,f}$  is the face value of the  $q^{th}$  volume fraction,  $V_{cell}$  is the volume of the cell and  $U_f$  is the volume flux through the face, based on normal velocity.

This formulation does not require the calculation of the transport equation during each time step because the volume fraction is calculated based on known quantities at the current time step. Additionally, the explicit formulation is a time-dependent solution; thus, the stability criterion is limited by the Courant number. The Courant number  $C_f$  accounts

the time-step length that any scalar flow quantity takes to transit in a control volume and it is given by the equation 3.10:

$$C_f = \frac{\Delta t}{\Delta x_c / u_{fluid}}. \quad 3.10$$

where  $\Delta t$  is the time-step size,  $\Delta x_c$  is the control volume length and  $u_{fluid}$  is the fluid velocity.

This work was modelled targeting a Courant number of 0.25. Keeping the Courant number below 0.25 is crucial to maintaining the accuracy and stability of results. This is because the evaporation rate model is linked to the VOF gradients. If the Courant number is higher than this value, volume fraction gradients diverge at the droplet's surface.

Furthermore, a variable time step from 1e-8 s to 1e-6 s was implemented. The variable time-stepping enables the time-step changing to be automated along a moving interface and it is given by ANSYS (2016c):

$$\Delta t_{global} = \frac{C_{f_{global}}}{\max\left(\sum \frac{outgoing\ fluxes}{volume}\right)}. \quad 3.11$$

where  $\Delta t_{global}$  is the global time step and the ratio  $\sum \frac{outgoing\ fluxes}{volume}$  is calculated for each control volume.

The time-stepping should increase gradually; however, the reduction should be sharp to avoid any divergence at the interface and to keep a  $C_{f_{global}} < 0.25$ . These recommendations should be followed because the VOF approach depends on the time-stepping when using the Geo-Reconstruct scheme to calculate an accurate and sharp interface. As a result, in some cases it is difficult to stabilise the solution and it is recommended to keep a low  $C_{f_{global}}$  (ANSYS, 2016a).

Moreover, the time step is limited to avoid the presence of spurious currents at the interface, which are associated with the computation of multi-phase flow and the surface tension modelling (Denner and van Wachem, 2015). The spurious currents are unphysical velocity fields at the interface, which create non-natural deformations leading to droplet break-up (Magnini, 2012).

In addition, the spurious currents are dominant in droplets with diameters less than 100  $\mu\text{m}$  and, as the shape of the droplets is a function of the surface tension and aerodynamic forces, this research should limit the time step to ensure the accuracy of the calculation at the droplet's interface.

### 3.1.2 Momentum equation

The momentum equation is given by the equation 3.12:

$$\frac{\partial(\rho u)}{\partial t} + \nabla \cdot (\rho u u) = -\nabla p + \nabla \cdot [\mu(\nabla u + \nabla u^T)] + F_\sigma + S_m. \quad 3.12$$

The source momentum term aims to compute the momentum exchange due to the phase change at the interface and is computed as in the equation 3.13:

$$S_m = (1 - \alpha_l) \sum_{i=1}^n m_i''' u \quad 3.13$$

During the phase change, the liquid phase experiences a loss of momentum as in equation 3.14:

$$S_m = m_i''' u - \alpha_l m_i''' u \quad 3.14$$

The surface tension is represented by  $F_\sigma$ , which is solved with the continuum surface force (CSF) model (Brackbill et al., 1992), computed as presented in equation 3.15:

$$F_\sigma = \sigma_{ij} \frac{\rho \kappa_i \nabla \alpha_i}{\frac{1}{2}(\rho_g + \rho_l)} \quad 3.15$$

where  $\kappa$  is the curvature defined by the divergence of the unit normal  $\hat{n}$  at surface given by:

$$\kappa = \nabla \cdot \hat{n}, \quad \hat{n} = \frac{n}{|n|}, \quad \hat{n} = -\nabla \alpha_q \quad 3.16$$

### 3.1.2.1 Wall adhesion and contact angle

The validation case models the evaporation process of a suspended droplet, where it is attached to a suspender by surface tension. The attachment from the droplet to the suspender wall depends on the intermolecular forces of adhesion and cohesion between the droplet's surface and the suspender wall.

Generally, the droplet moves along the suspender surface due to the balance of the body forces. As a result, the surface tension attachment is a function of the contact angle between the interface and the suspender wall, as shown in Figure 3.4.

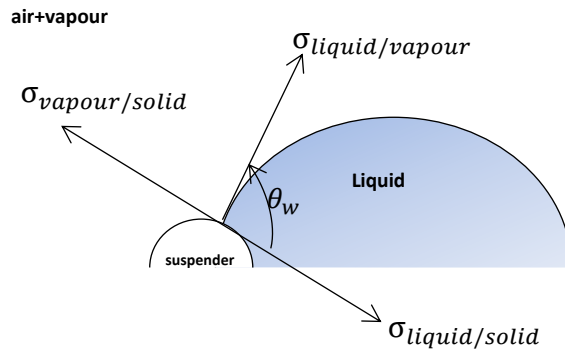


**Figure 3.4. Representation of the contact angle and surface tension forces between droplet and suspender**

Thus, the calculation of the surface tension force depends on the surface tension coefficients of three materials (solid, liquid and gas) and is given by:

$$\sigma_{vapour/solid} - \frac{\sigma_{liquid}}{solid} - \frac{\sigma_{liquid}}{vapour} \cos\theta_w = 0 \quad 3.17$$

Here, the contact angle at the wall  $\theta_w$  is expressed as a function of the surface normal at the cell next to the wall, as follows (ANSYS, 2016b):

$$\hat{n} = \hat{n}_w \cos\theta_w + \hat{t}_w \sin\theta_w \quad 3.18$$

where  $\hat{n}_w$  and  $\hat{t}_w$  are the unit vectors normal and tangential to the wall, respectively.

Moreover, the surface tension and contact angle calculations are based on equations 3.15 and 3.16.

### 3.1.3 Interfacial mass transfer: D<sup>2</sup>-law

Several studies have analysed the evaporation of single and multi-component droplets, including the VOF approach (Banerjee, 2007, Banerjee and Isaac, 2004). These investigations were applied in further studies, which included droplets with non-ideal mixtures such as ethanol and iso-octane (Banerjee, 2013, Banerjee and Gopinath, 2011). Similarly, Strotos et al. (2011) and Strotos et al. (2016) validated the evaporation of multi-component and rigid droplets for different cases according to the experimental results reported by Daïf et al. (1998).

The studies mentioned above calculated the mass transfer between the two phases based on the D<sup>2</sup>-law (Godsave, 1953, Spalding, 1953), which has been well accounted for in CFD programs and will be used in this research. The D<sup>2</sup>-law model is based on the Fickian diffusion principle between two components with different concentrations. This theory assumes that the mass transfer is a function of advection and diffusion, as can be observed on the right-hand side (RHS) of the following governing equation:

$$m_i''' = m_i''' \rho y_i - \rho_g D_i \nabla y_i \cdot \nabla \alpha_g \quad 3.19$$

However, advection, which is represented by the first term on the RHS, is neglected in this case, which means that the mass transfer between phases is merely by diffusion. Then, the evaporation rate per unit volume is represented as:

$$m_i''' = \frac{\dot{m}_i}{V_{cell}} = -\rho_g D_i \nabla y_i \cdot \frac{A}{V_{cell}} \quad 3.20$$

where the interface surface area is:

$$\vec{A} = V_{cell} \nabla \alpha_g \quad 3.21$$

The normal vector is pointing towards the liquid phase. Therefore, the interfacial mass transfer due to phase change is given by the equation 3.22:

$$m_i''' = -\rho_g D_i \nabla y_i \cdot \nabla \alpha_g. \quad 3.22$$

The D<sup>2</sup>-law mentions that the rate of evaporation of a droplet is directly proportional to the droplet's diameter squared. This can be observed by solving the equation 3.19, as explained below.

Rearranging the equation 3.19, the interfacial mass transfer can be expressed as:

$$m_i''' = -4\pi r^2 \rho_g \frac{D_i}{(1 - y_i)} \frac{\partial y_i}{\partial r} \quad 3.23$$

$$\therefore \frac{\partial y_i}{\partial r} = \frac{-m_i''' (1 - y_i)}{4\pi r^2 \rho_g D_i} \quad 3.24$$

Solving the differential equation 3.24 and expressing the equation in terms of the droplet diameter instead of the droplet radius gives:

$$m_i''' = 4\pi \frac{D}{2} \rho_g D_i \ln \left( \frac{1 - y_\infty}{1 - y_s} \right) \quad 3.25$$

In addition, it is known that:

$$m_i''' = \frac{\partial m}{\partial t} \quad 3.26$$

$$m = \rho_g \pi \frac{D^3}{6} \quad 3.27$$

Substituting equations 3.26 and 3.27 into equation 3.25 and performing the differentiation produces:

$$\frac{\partial D^2}{\partial t} = \frac{-8\rho_g D_i}{\rho_l} \ln\left(\frac{1-y_\infty}{1-y_s}\right) \quad 3.28$$

The equation 3.28 represents the  $D^2$ -law, where the time derivative of the square of the droplet diameter is constant and the slope is defined as the evaporation constant  $K$  and normally is expressed in  $\frac{mm^2}{s}$  (Turns, 2000):

$$K = \frac{-8\rho_g D_i}{\rho_l} \ln\left(\frac{1-y_\infty}{1-y_s}\right) \quad 3.29$$

$$\therefore D^2 = D_0^2 - Kt \quad 3.30$$

The equation 3.30 is represented graphically in Figure 3.5 and this is presented for the validation and modelling of fuel and oil droplets in Sections 4 and 5, respectively.

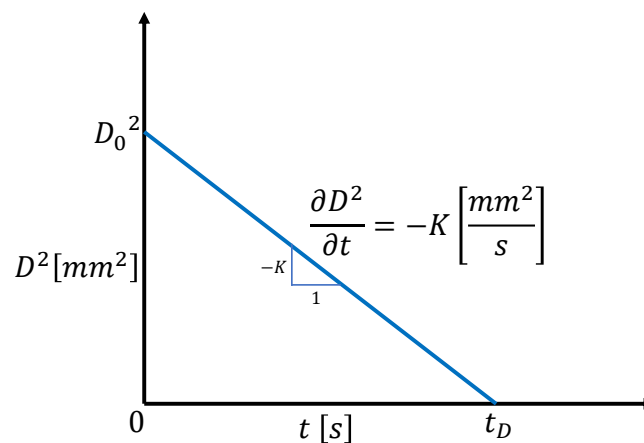


**Figure 3.5. Graphical representation of the  $D^2$ -law (Turns, 2000)**

The use of the  $D^2$ -law is convenient for the further modelling of oil droplets because this model calculates theoretically the mass transfer at the droplet's surface. Additionally, the  $D^2$ -law does not require experimental coefficients, as in the case of Lee's model which is the default model in ANSYS Fluent.

### 3.1.4 Species transport

The species transport equation is presented in equation 3.31 to calculate the mass fraction of the non-reactive chemical species in the gas phase, namely air and fuel or oil vapour:

$$\frac{\partial(\rho_g \alpha_g y_i)}{\partial t} + \nabla \cdot (\rho_g \alpha_g u y_i) = -\nabla \cdot (\rho_g \alpha_g D_i y_i) + S_i \quad 3.31$$

The source term accounting for the fuel vapour or oil vapour mass transfer at the interface due to the phase change is:

$$S_i = m_i''' \quad 3.32$$

The mole fraction of the vapour is obtained from Raoult's Law and is given by:

$$P_i = x_i P_{Tot} \quad 3.33$$

where the mole fraction is evaluated as the ratio of vapour pressure at the droplet's surface over the total pressure in the domain:

$$x_i = \frac{P_i}{P_{Tot}} \quad 3.34$$

The vapour pressure at the surface is calculated based on the Clausius–Clapeyron equation, considering that the fluid can be treated as an ideal gas mixture and the surface is saturated at the initial state; thus:

$$\ln \frac{P_{Tot}}{P_i} = \frac{h_{fg}}{R} \left( \frac{1}{T_i} - \frac{1}{T_b} \right) \quad 3.35$$

The partial pressure is computed according to Dalton's Law:

$$P_{Tot} = x_i P_{Tot} + x_j P_{Tot} \quad 3.36$$

Therefore, once the mole fraction at the droplet's surface is calculated with equations 3.34–3.36, the mass fraction of oil vapour is computed as follows:

$$y_i = \frac{x_i M_i}{x_i M_i + (1 - x_i) M_j} \quad 3.37$$

with the mass diffusion coefficient calculated using:

$$D_i = \frac{1 - x_i}{x_i / D_{ij}} \quad 3.38$$

Finally, the multi-component binary diffusivity is computed as follows (Poling et al., 2001):

$$D_{ij} = \frac{0.0143 T^{1.75}}{P M_{ij}^{1/2} [(\sum v)_i^{1/3} + (\sum v)_j^{1/3}]^2} \quad 3.39$$

$$\frac{2}{M_{ij}} = \frac{1}{M_i} + \frac{1}{M_j}$$

The gas phase computation accounts for two species, namely air and fuel vapour or oil vapour. Thus, the calculation of the species mixture density is based on the ideal gas law. In addition, the calculation of the properties in the gas phase mixture is given by the mass average rule, as follows:

$$\varphi_g = \sum_{k=1}^{ns} y_{g,k} \varphi_{i,k} + \left(1 - \sum_{k=1}^{ns} y_{g,k}\right) \varphi_{j,k} \quad 3.40$$

$$M_w = \left( \sum_{k=1}^{ns} \frac{y_{g,k}}{M_{w_i,k}} + \frac{1 - \sum_{k=1}^{ns} y_{g,k}}{M_{w_j}} \right)^{-1}$$

where  $\varphi_g$  is the fluid's physical properties, namely viscosity, thermal conductivity and specific heat.

### 3.1.5 Energy equation

The energy transport equation is written as in equation 3.41:

$$\frac{\partial(\rho E)}{\partial t} + \nabla \cdot [u(\rho E + p)] = -\nabla \cdot \left( k_{eff} \nabla T - \sum_j h_j J_j \right) - S_e \quad 3.41$$

where the third term on the RHS represents the energy source term due to mass transfer through evaporation:

$$S_e = m_i''' h_{fg} \quad 3.42$$

and  $k_{eff}$  is the effective thermal conductivity and the energy  $E$  and temperature  $T$  are mass-averaged variables, as follows:

$$E = \frac{\sum_{q=1}^n \alpha_q \rho_q E_q}{\sum_{q=1}^n \alpha_q \rho_q} \quad 3.43$$

$$T = \frac{\sum_{q=1}^n \alpha_q \rho_q T_q}{\sum_{q=1}^n \alpha_q \rho_q} \quad 3.44$$

### 3.1.6 Radiation modelling

The radiation effects on the droplet evaporation process are analysed based on the main assumptions, which are used in the literature to simplify the complexity of the radiation theory (Sazhin, 2006, Sazhin et al., 2006, Tseng and Viskanta, 2005). Therefore, the main assumptions are:

- the external thermal radiation is considered as a black body,
- the droplet's surface temperature is uniform but varies with time,
- the internal streamlines of liquid circulation within the droplet follows a spherical hill vortex pattern,
- the contribution of thermal radiation absorption is uniformly distributed throughout the droplet volume,
- droplets are considered as opaque grey spheres, characterised by emissivity,
- the scattering effects are neglected,
- droplets are treated as a black body,
- the thermal radiation absorption is considered to be homogeneous, and
- the medium is optically thick.

Moreover, this research takes into account the simplest model to provide a baseline approach for future modelling. For that reason, the following radiation models were considered and evaluated (ANSYS, 2016b):

- Discrete ordinates radiation model (DOM),
- Discrete transfer radiation model (DTRM),
- P-1 radiation model,
- Rosseland radiation model, and
- Surface to surface (S2S) radiation model.

The main considerations of each model are presented in Table 3.1 (ANSYS, 2016b). It is observed that the Rosseland model and the S2S model simplify the analysis of radiation modelling. The S2S model is frequently used in space applications and it

calculates the energy transfer between surfaces. This model is not suitable for this research because it is more focussed on the radiation effects on solid surfaces. The S2S model is more suitable for modelling radiation where there is not a participating media such as the radiation from the sun to a spacecraft.

**Table 3.1. Considerations of available radiation models (ANSYS, 2016b)**

<b>Considerations</b>	<b>DOM</b>	<b>DTRM</b>	<b>P-1</b>	<b>Rosseland</b>	<b>S2S</b>
Scattering and emissivity	YES	NO	YES	YES	NO
Particulate effects	YES	NO	YES	NO	NO
Semi-transparent walls	YES	NO	NO	NO	NO
Specular walls (e.g. for dust-free mirror)	YES	NO	NO	NO	NO
Partially specular walls (e.g. dusty mirror)	YES	NO	NO	NO	NO
Non-grey radiation	YES	NO	YES	NO	NO
Localised heat sources	YES	YES	YES	NO	NO
Enclosure radiative transfer with non-participating media	NO	NO	NO	NO	YES

The Rosseland model is a simplification of the P-1 equations. It assumes that the intensity can be calculated as a black body and is valid when the medium is optically thick (ANSYS, 2016b). However, this model does not properly account for the radiation absorption from the surroundings to the oil droplet, because it considers a media that is optically thicker than required in this research.

In other words, the optical thickness of the media is given by (ANSYS, 2016b):

$$\text{Optical thickness} \equiv (a + \sigma_s)L \quad 3.45$$

where  $a$  is the absorption coefficient,  $\sigma_s$  is the scattering coefficient and  $L$  is the typical distance between two opposing walls.

Therefore, the Rosseland model is valid for a medium with an optical thickness  $>5$ , and in this research the optical thickness is  $<5$ .

The DTRM model is applicable when it is important to consider the computation of radiation between walls. It can be expensive computationally because the accuracy of the computation depends on the number of rays added to the model. Thus, the two models that can be used to model the droplet evaporation process are DOM and P-1. The DOM model allows consideration of a non-grey radiation, which means accounting for the emissivity dependence of the wavelength media.

Accordingly, as this research is looking to provide a baseline from a simplification of the radiation phenomena, the model approach chosen in this research is the P-1, which assumes the media as a black body with non-scattering effects.

### 3.1.6.1 P-1 radiation model

The P-1 model is a simplification of the P-n model. The sum of all radiative intensity in all directions is given by ANSYS (2016b):

$$\frac{\partial}{\partial x_i} \left( \Gamma \frac{\partial}{\partial x_i} \right) + 4a\sigma_b T^4 = aG \quad 3.46$$

The first term on the left-hand side (LHS) of the equation 3.46 corresponds to the diffusion, the second term on the LHS represents the emission and the first term on the RHS computes the absorption. Where  $G$  is the incident radiation, the radiation heat flux  $q_i$  is given by:

$$q_i = -\frac{1}{(3(a + \sigma_s) - C\sigma_s)} \frac{\partial G}{\partial x_i} \quad 3.47$$

Moreover, the parameter  $\Gamma$  is introduced to simplify the equation 3.47, as follows:

$$\Gamma = -\frac{1}{(3(a + \sigma_s) - C\sigma_s)} \quad 3.48$$

where  $a$  is the absorption coefficient,  $\sigma_s$  is the scattering coefficient,  $G$  is the incident radiation and  $C$  is the linear-anisotropic phase function coefficient.

Therefore, the simplification of equation 3.47 is:

$$q_i = -\Gamma \nabla G \quad 3.49$$

The transport equation for  $G$  is:

$$\nabla \cdot (\Gamma \nabla G) - aG + 4an_r^2 \sigma_b T^4 = S_G \quad 3.50$$

where  $n_r$  is the refractive index of the medium,  $\sigma_b$  is the Stefan–Boltzmann constant and  $S_G$  is the source term added to the energy equation.

## 3.2 Numerical model

The transport equations 3.1, 3.12 and 3.41 are solved using second-order spatial discretisation. The pressure–velocity coupling was performed with the SIMPLEC scheme. The VOF multi-phase approach was used in conjunction with the geometric reconstruction algorithm and the body forces due to gravity were computed with the body-force-weighted scheme.

Moreover, a transient formulation was defined with a variable time step calculated from a Courant number of around 0.25 to avoid numerical diffusion at the interface and ensure the convergence of the phase-change process. The mass transfer interaction was computed through a UDF to compute the D<sup>2</sup>-law. The species transport model, equation

3.31, allows the computation of the gas phase properties with a first-order discretisation scheme. The gas-phase mixture's properties were calculated with the mass-weighted average law.

### 3.2.1 Discretisation

The generic Navier–Stokes equations were solved numerically through discretisation using the finite volume method. Each equation is solved by dividing the domain into control volumes or cells. The finite volume method interpolates the values at the centre of each control volume; therefore, the conservation law equations are integrated for each control volume as follows (ANSYS, 2016b):

$$\int_V \frac{\partial \rho \varphi}{\partial t} dV_c + \oint \rho \varphi \vec{v} \cdot \vec{dA} = \oint \Gamma_\varphi \nabla \varphi \cdot \vec{dA} + \int_V S_\varphi dV_{cell} \quad 3.51$$

where  $\varphi$  represents the scalar quantity characteristic of the specific transport equation,  $\Gamma_\varphi$  is the diffusion coefficient for  $\varphi$  and  $S_\varphi$  is the source term.

This method simplifies the solution converting the conservation law equations to algebraic equations, applying the divergence theorem to equation 3.51 as follows (ANSYS, 2016b):

$$\frac{\partial \rho \varphi}{\partial t} V_c + \sum_f^{N_f} \rho_f \varphi_f \vec{v}_f \cdot \vec{A}_f = \sum_f^{N_f} \Gamma_\varphi \nabla \varphi_f \cdot \vec{A}_f + S_\varphi V_{cell} \quad 3.52$$

where the number of faces in a cell is represented by  $N_f$ , the scalar quantity convected over each cell face is  $\varphi_f$ , the first term on the LHS of the equation 3.52 is the temporal discretisation and the second LHS term accounts for the mass flux through the cell face.

The discretisation of the scalar quantities is calculated in the cell centred values. As a result, in this investigation two schemes were used: the first-order upwind scheme for

the discretisation of the species transport equation 3.31 and the second-order upwind scheme for the discretisation of the transport equations 3.1, 3.12 and 3.41. The first scheme discretises the flow quantity with the cell average value considering the field values of the immediate neighbour cells. The second scheme uses the Taylor series expansion to account for the two neighbours' cell centred values upwards and backwards from the cell centre to analyse.

### **3.2.2 Pressure–velocity coupling**

The analysis performed to meet the aims of this research assumes that the flow is incompressible; therefore, the pressure-based solution algorithm was selected to calculate the pressure gradient for the momentum. Then, once the velocity field is calculated from the momentum equation, it should satisfy the continuity equation.

Accordingly, the numerical solver has different techniques to link the pressure and velocity equations. Therefore, this validation was performed with the Semi-Implicit Method for Pressure Linked Equations Consistent (SIMPLEC) scheme to create a base case from state-of-the-art cases such as the case of Banerjee (2013).

### **3.2.3 Moving frame of reference**

The study of droplet evaporation has followed different techniques to keep the droplet stationary to observe the complete phase-change process. One of these techniques is the use of a suspender or a wire to keep the droplet attached while is surrounded by a convective airflow. This option was evaluated for this research to model a single oil droplet under bearing chamber conditions. Thus, a balance force analysis was performed

accounting for the airflow drag force  $F_D$ , the droplet weight  $W$  and the surface tension force  $F_\sigma$  as depicted in Figure 3.6.

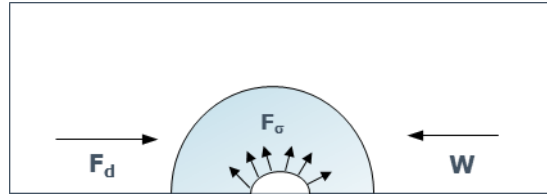


**Figure 3.6. Balance force analysis of a suspended droplet under convective airflow**

There are two scenarios to keep the droplet attached to the suspender: the first scenario is when the drag force is equal to the droplet's weight and the second scenario is when the difference of both forces is less than the surface tension force.

The surface tension force depends on the contact angle between the liquid and the suspender material, and it is reduced when the contact angle changes. As a result, the contact angle will change if the drag force is greater than the droplet's weight or vice versa. In addition, the droplet will stay attached when the difference between drag force and droplet weight is equal to the surface tension force. Hence, the greatest surface tension force is when the suspender is placed in the centre of the droplet.

For that reason, the evolution of force balance is analysed against the droplet's radius variation, as shown in Figure 3.7 where it can be seen that the drag force is greater than the droplet's weight for an oil droplet with a diameter of 200  $\mu\text{m}$  under a convective flow with a velocity of 1 m/s.

Therefore, to prevent the droplet separating from the suspender, the difference between both forces should be less than or equal to the surface tension force throughout all of the droplet evaporation process.

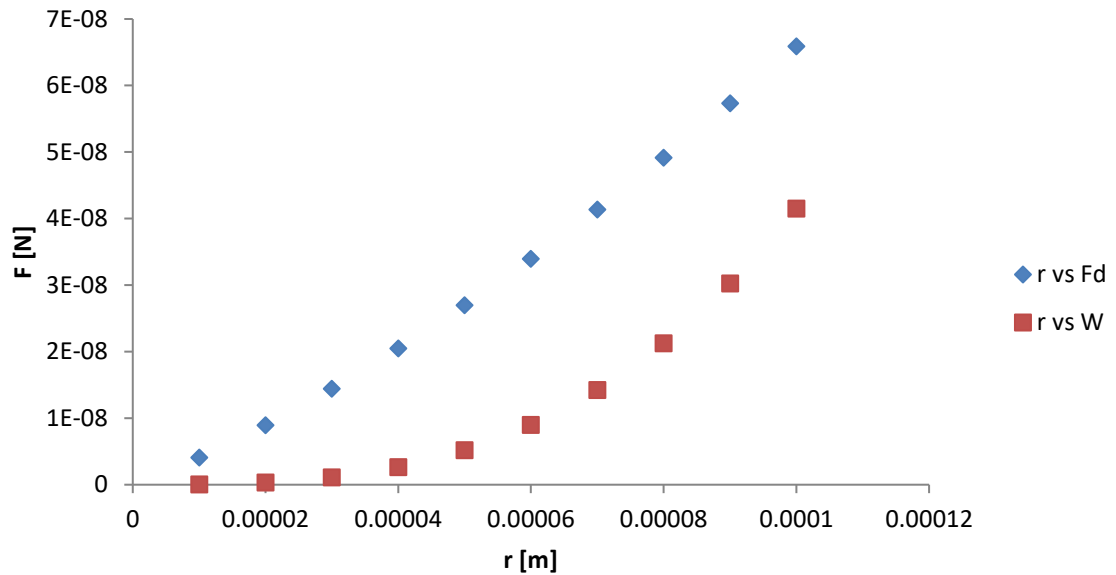


**Figure 3.7. Droplet external forces (drag force and weight) vs droplet radius reduction for an oil droplet with an initial diameter of 200  $\mu\text{m}$  under airflow with a velocity of 1 m/s**

The droplet radius evolution means the surface tension force cannot keep the droplet attached to the suspender when the airflow velocity is greater than 1 m/s. In this investigation, the airflow should be greater than 1 m/s. Therefore, the option of the suspender is not viable and, in this study, the role of the suspender is accounted for by using a moving frame of reference (MFR). This is because the use of an MFR allows the droplet to remain stationary regarding the mesh and therefore it will stay within the refined zone.

This approach is implemented via a UDF, where the velocity is computed from equation 3.53 (Abramzon and Sirignano, 1989):

$$\frac{du}{dt} = \frac{3C_D \rho_g}{2r \rho_l} |u_g - u_l| (u_g - u_l) \quad 3.53$$

The drag coefficient is calculated according to the correlation for the ‘standard drag curve’ for a solid sphere (Michaelides, 2006), which is recommended for a range of Reynolds numbers ( $1 < Re < 800$ ). The Reynolds number and the drag coefficient are computed as follows:

$$C_D = \frac{24}{Re_D} \left[ 1 + \frac{Re_D^{2/3}}{6} \right], \quad Re_D = \frac{2\rho_\infty |u_\infty - u_d| r_d}{\mu_g} \quad 3.54$$

Moreover, the use of an MFR avoids the secondary effects that the suspender has in the calculation of the droplet heat transfer and allows us to represent the droplet dynamics inside the bearing chambers. This is because, according to previous reports (Farrall et al., 2007), the motion of droplets with diameters less than 200  $\mu\text{m}$  is governed by air velocities.

### 3.3 Material properties

This section presents the material properties used to compute the evaporation of fuel droplets as well as oil droplets. Moreover, the oil properties in the gas phase had to be estimated. Therefore, the methodology to estimate it is presented in the following sections.

#### 3.3.1 Air properties

The air properties are considered constant throughout the time to simplify the calculation, since the aim of this research is to obtain a first approximation of the oil droplet evaporation process.

The air properties are presented in Table 3.2,

**Table 3.2. Air properties**

<b>Property</b>	<b>Value</b>
$M_w$ [kg/kmol]	28.966
$\rho$ [kg/m <sup>3</sup> ]	1.225
$c_p$ [J/kgK]	1006.43
$k$ [W/mK]	0.0242
$\mu$ [kg/ms]	1.79E-05

### 3.3.2 n-heptane and n-decane properties

According to the sections mentioned above, the validation of the methodology addressed in this research is based on the state of the art, which analysed the evaporation of fuel droplets (Daif et al., 1998, Strotos et al., 2016). The previous analysis studied the evaporation process by comparing two components to observe the effects of their volatility on the reduction of a droplet's diameter.

The two fluids analysed are n-heptane and n-decane, and their properties in the liquid phase are presented in Table 3.3.

**Table 3.3. Liquid phase properties of n-heptane and n-decane**

<b>Properties</b>	<b>n-heptane</b>	<b>n-decane</b>
$T_b$ [K]	371.53	447.25
$M_w$ [kg/kmol]	100.204	142.284
$\rho$ [kg/m <sup>3</sup> ]	684	730
$c_p$ [J/kgK]	2219	2090
$k$ [W/mK]	0.14	0.149
$\mu$ [kg/ms]	0.000409	0.0024
$\sigma$ [N/m]	0.02052	0.02475
$\Delta H_{vap}$ [KJ/mol]	31.86	37.42

The specific heat in the gas phase is calculated as a function of temperature with the piecewise polynomial function as follows:

$$C_p = C_0 + C_1T + C_2T^2 + C_3T^3 + C_4T^4 \quad 3.55$$

where the coefficients for each fluid and the gas-phase properties of n-heptane and n-decane are presented in Table 3.4.

**Table 3.4. Gas-phase properties of n-heptane and n-decane**

Properties	n-heptane	n-decane
$\rho$ [kg/m <sup>3</sup> ]	4.25	1
	$C_0 = 925.45$	$C_0 = 59.37375$
	$C_1 = -0.787785$	$C_1 = 5.332576$
$c_p$ [J/kgK]	$C_2 = 0.0162277$	$C_2 = 0.0005$
	$C_3 = -2.07234e-05$	$C_3 = -5.048318e-06$
	$C_4 = 8.17206e-09$	$C_4 = 2.340991e-09$
$k$ [W/mK]	0.0178	0.0178
$\mu$ [kg/ms]	7e-06	7e-06

### 3.3.3 Oil properties

The oils used for gas turbine applications are synthetic and present a wide range of operating temperatures. The composition of these oils is such that they have a base stock of synthetic ester, such as neopentyl polyol ester (MIL-PRF-23699F, 1997).

With this in mind, the literature reports that the neopentyl polyol ester can be assumed to be 80% pentaerythritol tetrapentanoate (PEC5) and 20% pentaerythritol tetranonanoate (PEC9) (Urness et al., 2016).

Thus, it is noted that a large percentage of the composition of this oil is PEC5, which is the oil used to analyse evaporation under bearing chamber conditions. Therefore, the liquid properties for the oil are listed in Table 3.5.

**Table 3.5. Liquid phase properties of PEC5**

<b>Thermophysical properties. Liquid phase</b>	
$T_b$ [K]	608.85
$M_w$ [kg/kmol]	472.62
$\rho$ [kg/m <sup>3</sup> ]	1010.8
$c_p$ [J/kgK]	1800
$k$ [W/mK]	0.15
$\mu$ [kg/ms]	0.0243
$\sigma$ [N/m]	0.0368 @ 25°C
$\Delta H_{vap}$ [KJ/mol]	119

Moreover, the oil vapour properties from experimental data are difficult to find in the literature. Therefore, the thermophysical properties of PEC5 in the gas phase are estimated theoretically, which is based on the kinetic theory assuming the gas phase can be treated as an ideal gas.

The detailed calculation is laid out in the following sections.

### **3.3.3.1 Viscosity**

The kinetic theory is based on the interaction between molecules in the gas phase, where the molecules are assumed to behave as non-attracting rigid spheres. As a result, the molecules move with a certain velocity and some distance between them. The sphere has a diameter of  $\sigma_s$  in Angstroms and the motion of this hard sphere allows us to determine the gaseous viscosity and thermal conductivity, among other aspects.

Therefore, if the molecules attract or repel each other, the Chapman–Enskog method is suitable to estimate the gas viscosity and can be written as (Poling et al., 2001, Monsalvo, 2006):

$$\mu = 2.67 \times 10^{-6} \frac{\sqrt{M_w T}}{\sigma_s^2 \Omega_\mu} \quad 3.56$$

where  $M_w$  is the molecular weight,  $T$  is the desired temperature and  $\Omega_\mu$  is the collision integral constant which is a function of Lennard-Jones potentials, given by equation 3.57:

$$\begin{aligned} \Omega_\mu &= [A(T^*)^{-B}] + C[\exp(-DT^*)] + E[\exp(-FT^*)] \\ A &= 1.16145, B = 0.14874, C = 0.52487 \\ D &= 0.77320, E = 2.16178, F = 2.43787 \\ T^* &= \frac{kT}{\varepsilon}, 0.3 \leq T^* \leq 100 \end{aligned} \quad 3.57$$

where  $k$  is the Boltzmann constant and  $\varepsilon$  is the minimum of the pair's potential energy.

The Lennard-Jones parameters are estimated using the semi-empirical method of Chung et al. (1988) and Chung et al. (1984), as given in equation 3.58:

$$\begin{aligned} \sigma [\text{\AA}] &= 0.809 v_c^{\frac{1}{3}} \\ \frac{\varepsilon}{k} [K] &= \frac{T_c}{1.2593} \end{aligned} \quad 3.58$$

where critical constants of PEC5 (Razzouk et al., 2007) are as given in Table 3.6.

**Table 3.6. Gas-phase critical constants of PEC5 (Razzouk et al., 2007)**

Gas-phase critical constants of PEC5	
$T_c$ [K]	851.05
$P_c$ [MPa]	1.19
$\omega$	1.059

The critical volume is calculated from equation 3.59:

$$v_c \left[ \frac{cm^3}{mol} \right] = \frac{RT_c}{P_c Z_c} \quad 3.59$$

where  $Z_c$  is the compressibility factor calculated from the first version of the Soave–Benedict–Webb–Rubin equation of state (Monsalvo, 2006), given by equation 3.60:

$$Z_c = 0.2908 - 0.099\omega + 0.04\omega^2 \quad 3.60$$

where  $\omega$  is the acentric factor of the substance.

Accordingly, the estimation of Lennard-Jones parameters for the gas viscosity calculation was validated against experimental values of n-heptane with an error estimation of 1% according to the data reported by Michailidou et al. (2014).

Table 3.7 shows that the error comparison between the estimation and experimental values is low; consequently, this method is applied to the calculation of Lennard-Jones parameters for PEC5 vapour.

**Table 3.7. Lennard-Jones parameters values of n-heptane validation against the experimental values reported by (Michailidou et al., 2014)**

Parameter	Estimated	Reported	Error
$\sigma$ [Å]	6.0512	6.1362	1%
$\frac{\epsilon}{k}$ [K]	428.8097	426.118	1%

### 3.3.3.2 Thermal conductivity

The thermal conductivity is estimated from kinetic theory, as given by (ANSYS, 2016c):

$$k = \frac{15}{4} \frac{R}{M_w} \mu \left[ \frac{4}{15} \frac{C_p M_w}{R} + \frac{1}{3} \right] \quad 3.61$$

### 3.3.3.3 Specific heat

The specific heat is estimated from the group contribution method (Poling et al., 2001), which has been estimated previously by (Yokozeki, 2005), as follows:

$$c_p = C_0 + C_1T + C_2T^2 + C_3T^3 \quad 3.62$$

$$C_0 = 57.97, C_1 = 2.1551, C_2 = -1.01 \times 10^{-3}, C_3 = 2.62 \times 10^{-7}$$

### 3.3.3.4 Density

The density is estimated from the ideal gas law, as given in equation 3.63:

$$\rho = \frac{RT}{P} \quad 3.63$$

### 3.3.3.5 Diffusivity

The diffusivity is estimated with the Fuller et al. method (Fuller et al., 1969, Fuller and Giddings, 1965, Fuller et al., 1966) taken from Poling et al. (2001), as stated in equation 3.39.

Moreover, the estimation of binary diffusivity was validated according to the experimental value reported for allyl chloride (Poling et al., 2001). Therefore, as depicted in Table 3.8, the error between the estimated value and the reported value is 2%.

**Table 3.8. Binary diffusivity of allyl chloride comparison between estimated value against experimental value (Poling et al., 2001)**

Parameter	Estimated	Reported	Error
$D_{ab}$ [cm <sup>2</sup> /s]	0.096	0.098	2%

The estimated value matches very well against the experimental value reported in the literature, as observed in Table 3.8. Therefore, this methodology is applied to the calculation of the binary diffusivity of PEC5 vapour.

### 3.4 Summary

This chapter describes the methodology used to model the droplet evaporation process. This methodology is based on the state-of-the-art knowledge that has been previously applied to fuel and combustion in ICEs. It has been observed that the VOF technique allows the representation of droplet evaporation as well as internal droplet convection.

Additionally, the transport equations that govern the flow were listed, along with the discretisation approach used to solve these equations. The established methodology also describes the evaporation model and allows quantification of the evaporation rate and the temporal evolution of the droplet diameter.

Furthermore, the description of the MFR approach is presented as it will be used later to keep the droplet stationary in the numerical model. Moreover, the use of the MFR allows the modelling of the droplet evaporation process under different air velocity conditions, which presents a significant advantage over the use of an experimental suspender (see Section 3.2.3 for a more detailed discussion).

Besides, this chapter has presented the properties of the two fuels used to analyse droplet evaporation in the gas and liquid phases. In the same way, the liquid properties of a base stock oil were shown, as well as the process to calculate the oil properties in the gas phase. Such a process was applied first to the calculation of well-known fluids and then compared with their experimental values (with a 2% error).

Finally, the radiation model used to analyse the effects of the radiative environment on the oil droplet evaporation process was introduced.

## **4 Validation of the evaporation model**

### **4.1 Introduction**

The process of droplet evaporation under the effects of convective airflow has been analysed already for ICEs, where fuel droplets were studied with the aim of enhanced fuel combustion. Most of these studies were performed to provide an understanding of the heat and mass transfer for single droplets surrounded by high-temperature gas, as presented in Section 2.2.

This chapter aims to generate a base case from state-of-the-art methods, which provide the guidelines to understand the droplet evaporation process in a micro-scale analysis of a single oil droplet.

Therefore, this chapter describes the validation case, which is performed using the VOF technique to quantify the evaporation rate, the mass fraction of oil vapour and the temporal evolution of the droplet diameter, as well as to assist with the visualisation of the droplet's internal circulation.

### **4.2 Overview of the reference literature**

#### **4.2.1 Experimental setup**

Two key papers were identified to test and validate the droplet evaporation process using the VOF approach: Banerjee (2013) and Strotos et al. (2011). These two pieces of work are based on the experimentation proposed by Daïf et al. (1998).

The experiments measured the evaporation rate under natural and forced convection of single and multi-component droplets. Consequently, the evaporation rate was observed using an infrared system and the droplet's diameter reduction was recorded and measured from image sequences.

The droplet was suspended by surface tension on a wire (suspender) with a diameter of  $400\ \mu\text{m}$  and surrounded by convective hot air at different temperatures and velocities. Additionally, two different fuels with different volatilities were analysed, namely n-heptane and n-decane.

The experimental setup is presented in Figure 4.1, where the red square represents the section to analyse numerically.

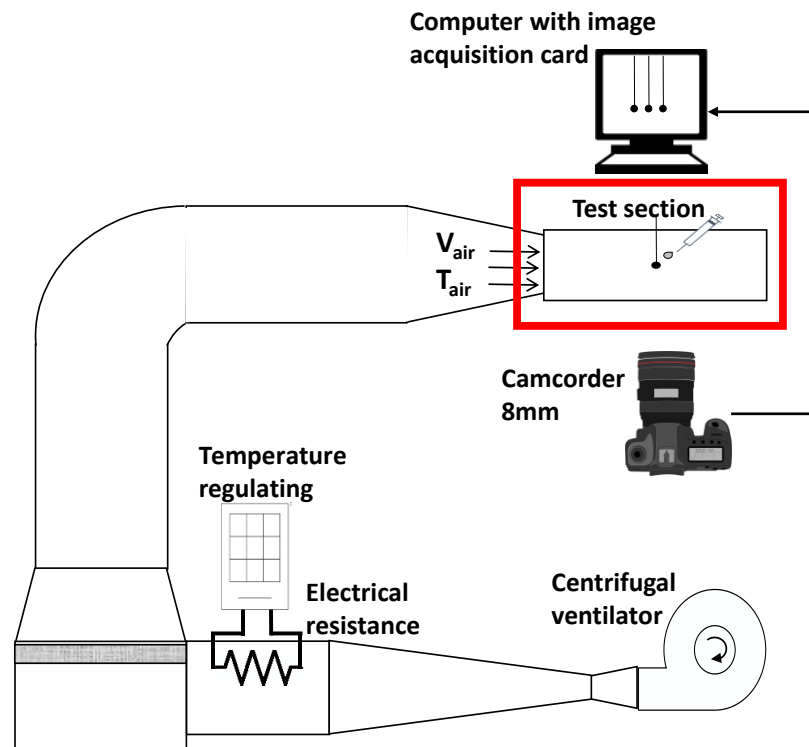
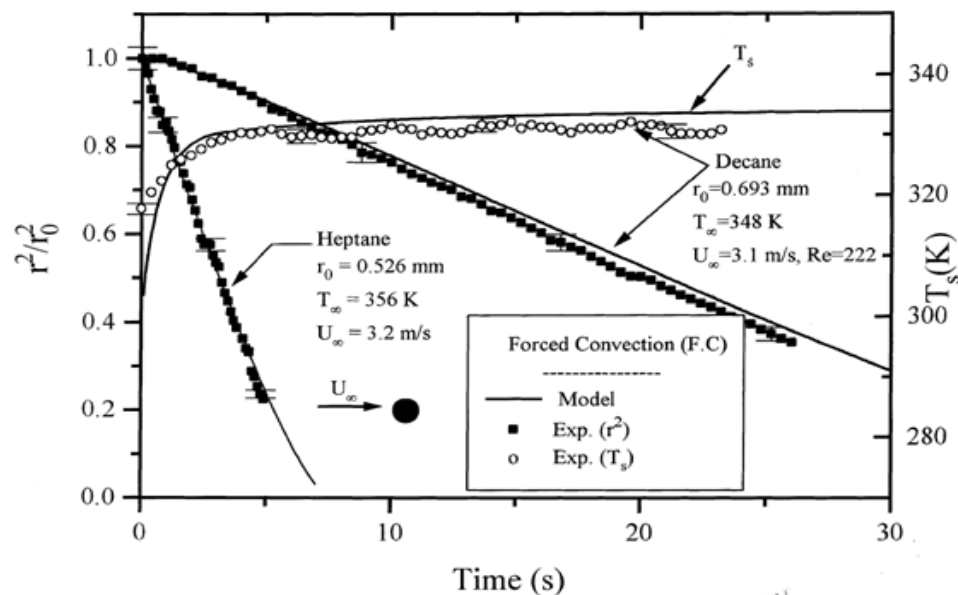


Figure 4.1. Experimental setup schematic (see Daïf et al., 1998)

In the test section, the suspender is the sphere located in the centre and the droplet is injected by a syringe. The droplet is located at the end of a wind tunnel where the air is heated with an electrical resistance before reaching the droplet's position.

In this experiment, Daïf et al. (1998) analysed the temporal evolution of the droplet's normalised square radius and surface temperature. It was noted that n-heptane, which is the more volatile component, has a shorter droplet lifetime – with an evaporation process of 7 s – compared with n-decane. As shown in Figure 4.2, n-decane takes longer than 30 s to evaporate completely. Thus, n-decane is a less volatile component with a higher saturation point than n-heptane.



**Figure 4.2. Temporal evolution of droplet diameter of n-heptane and n-decane and droplet surface temperature of n-decane (Daïf et al., 1998)**

The CFD case setup aims to simulate the same conditions of the single droplet component reported by Daïf et al. (1998). Thus, Section 4.3 presents the CFD case setup to validate the evaporation model.

### 4.3 CFD case setup

The methodology presented in Section 3 is validated against the experimental data for fuel droplets reported by Daif et al. (1998). Two cases were used to validate the numerical model of a single droplet under the effects of convective flow to obtain the temporal evolution of droplet diameter of n-heptane and n-decane.

For that reason, the droplet and ambient characteristics for both cases are presented in Table 4.1:

**Table 4.1. Cases validated**

<b>Droplet characteristics</b>	<b>Case 1</b>	<b>Case 2</b>
Radius [ $\mu\text{m}$ ]	526	693
Temperature [K]	300	315
Material	n-heptane	n-decane
<b>Ambient characteristics</b>	<b>Case 1</b>	<b>Case 2</b>
Gauge pressure [MPa]	0	0
Temperature [K]	356	348
Velocity [m/s]	3.2	3.1

Furthermore, the assumptions used to model these two cases are: no radiation is considered, laminar airflow, 2D axisymmetric flow, dry air, constant temperature, constant velocity, constant atmospheric pressure, thermodynamic equilibrium at the gas–liquid interface, the gas–liquid interface is saturated with fuel vapour, the gas phase is considered as an ideal gas, the droplet evaporates in a non-reactive environment, the liquid phase is a single component, the advection due to the fuel vapour is neglected and the

thermophysical properties, such as thermal conductivity, density and specific heat, are constant.

Moreover, the droplet evaporation process is analysed by examining the evolution of the droplet size, which is monitored with the total mass of the liquid present in the domain at every time step. The reduction of the droplet radius is calculated from the total volume  $V_T$ , which considers the volume of the droplet  $V_D$  and the volume of the suspender  $V_S$  as given in equation 4.1:

$$V_T = V_D + V_S \quad 4.1$$

The droplet volume  $V_D$  is calculated with the mass reduction (considering a constant density  $\rho$ ) as follows:

$$V_D = \frac{m_D}{\rho_D} \quad 4.2$$

Therefore, the parameter to compare with the experiment data is reduction of the total radius  $r_T$  as given by:

$$r_T = \sqrt[3]{\frac{\frac{m_D}{\rho_D} + V_S}{\frac{4}{3}\pi}} \quad 4.3$$

The total radius is analysed in the numerical predictions similarly than in the experiment, which recorded and measured the reduction in droplet diameter from image sequences. These images include the volume of the suspender and the volume of the droplet, as presented in equation 4.1.

As mentioned in Section 4.2.1, the experiment shows that the temporal evolution of the normalised square radius follows the D<sup>2</sup>-law; therefore, the main parameter to analyse is the normalised ratio  $\frac{r_T}{r_0}$  which is the ratio of the reduced radius  $r_T$  and the initial radius

$r_0$ . This radius ratio is the quantity that varies as a function of time and it is used to validate the mass and heat transfer in numerical modelling.

### 4.3.1 Geometry and boundary conditions

The domain is considered as a 2D axisymmetric simplification with the axis of the symmetry coincident with the axis of the suspender wire, as illustrated in Figure 4.3. The inlet air's temperature and velocity are presented in Table 4.1 for each case. The outlet gauge pressure is 0 Pa, the wall at the top is a freestream and the suspender is considered as a stationary wall.

The domain is defined with a region of  $30 D_0$  width and  $8 D_0$  height; these dimensions are based on the best practices from previous studies (Banerjee, 2013). In addition, the initial droplet temperatures are 300 K and 315 K for Case 1 and Case 2, respectively, and the droplet's initial velocity is 0 m/s.

The above-mentioned boundary conditions can be observed in Figure 4.3, where the origin is placed at the centre of the suspender.

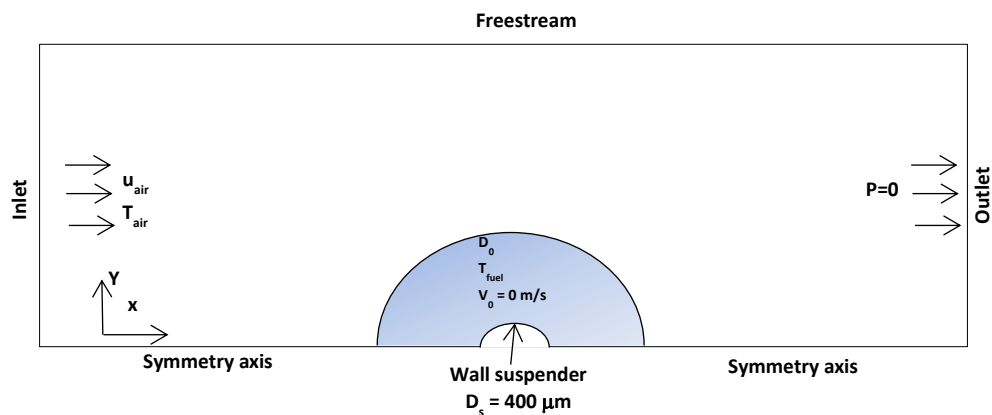


**Figure 4.3. Geometry and boundary conditions**

### 4.3.2 Solution methods

The solution method is to solve the transport equations, pressure–velocity coupling and volume fraction, as depicted in Table 4.2. The discretisation was computed from the second-order upwind scheme to solve the density, momentum and energy equations. However, the species transport equations are solved within the first-order upwind scheme in order to get solution stability. The species transport model is enabled to compute the gas phase properties and it must be highlighted that the calculation of species transport is set for non-reacting components.

**Table 4.2. Solution methods**

Equation	Scheme
Pressure–velocity coupling	SIMPLEC
Pressure	Body force weighted
Volume fraction	Geometric reconstruction algorithm
Density	Second-order upwind
Momentum	Second-order upwind
Energy	Second-order upwind
Species	First-order upwind

The evaporation model used is the  $D^2$ -law, which was implemented via UDF. The UDF is included in the multi-phase VOF phase interactions. The mass transfer is a function of volume fraction gradients and species transport gradients, as defined in equation 3.22, and the gradients were calculated in the macro DEFINE\_ADJUST, which allocates these gradients to be calculated in the mass transfer model, which is in the macro

DEFINE\_MASS\_TRANSFER. This macro allows for inclusion of the effect of mass transfer as a source term in the governing equations, as explained in Section 3.1.

To avoid errors in the initialisation of the species transport equations, it is important to initialise the mass transfer as a constant rate and, after two iterations, to calculate the mass transfer interaction with the UDF. Moreover, in this research the initial mass transfer rate was computed analytically using the procedure recommended by Abramzon and Sirignano (1989).

Moreover, according to the best practices of phase-change modelling, the latent heat of vaporisation of the fuel vapour should be specified as a  $\frac{J}{kgmol}$  on the standard state enthalpy, which can be found in the materials section of the ANSYS Fluent setup. Additionally, for the liquid phase, the standard state enthalpy should be set as zero (Punekar, 2016).

The use of the  $D^2$ -law is convenient for further modelling of oil droplets, because it allows the mass transfer calculation based on theory due to the lack of experimental results of aero-engine oil evaporation. The default model in ANSYS Fluent is the model of Lee (1979) and it is not convenient for this analysis. Because it includes an experimental coefficient, which can vary over a wide range of values for different conditions and this coefficient should be adjusted to be consistent with the experimental results (Punekar, 2015). The mass interfacial coefficient for the model of Lee (1979) is given by:

$$m_i''' = coeff * \alpha_l \rho_l \frac{(T_l - T_i)}{T_l} \quad 4.4$$

and the mass intensity factor is represented by:

$$coeff = \frac{6}{D} \beta \sqrt{\frac{M_v}{2\pi RT_i}} \left( \frac{\rho_g \rho_l}{\rho_l - \rho_g} \right) \quad 4.5$$

where  $\beta$  is the accommodation coefficient and the physics characteristics of the vapour which shows the molecules transferred from the liquid phase surface. This coefficient is not very well known (ANSYS, 2016b). Thus, the values in equation 4.4 are based on empirical data. As such, the model of Lee(1979) requires a parametric study to obtain the correct coefficient to match the expected results and this would not necessarily be valid for the conditions required in this study.

### 4.3.3 Mesh

This study was performed with a 2D uniform unstructured mesh created with the ANSYS Meshing application, where the level of refinement is increased towards the droplet region. The mesh is divided into three zones, A, B and C, to account for the air, vapour fuel and liquid fuel, respectively, as well as the phase change at the interface. Zone C contains the liquid phase patched at the start of the calculation with a volume fraction of 1 and initial velocity of 0 m/s.

The meshing zones are shown in Figure 4.4.

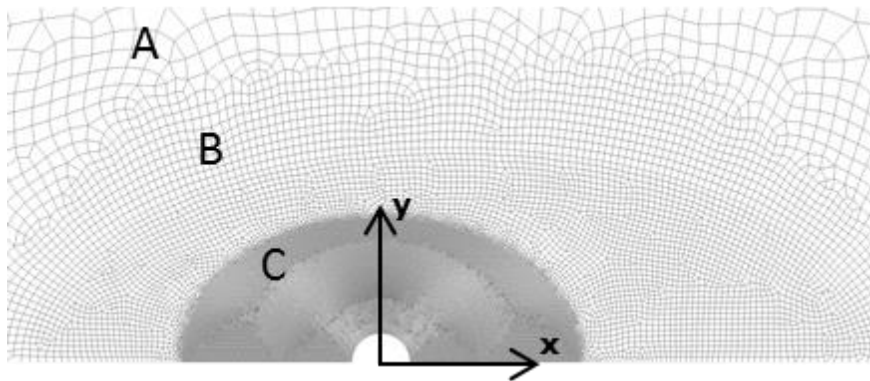


**Figure 4.4. Meshing zones**

A mesh independence study was performed for three different meshes to show that the model results are independent of mesh sizing, increasing the accuracy of the results. The independence study indicated that the difference in results decreases with each mesh refinement until this difference can be neglected. Moreover, the mesh independence study confirms that the accuracy of the results does not depend on the mesh sizing. Thus, the sizing is changed by pivoting the small element size and reducing the finest cell size by half of the previous value.

The mesh study is based on the monitoring of the non-dimensional square diameter, which is compared with the experimental data of Daïf et al. (1998). Therefore, the accuracy of the results is evaluated for each mesh with the root mean square deviation (RMSD), which is given as follows:

$$\text{RMSD} = \sqrt{\frac{\sum_{i=1}^n (z_{c,i} - z_{e,i})^2}{n}} \quad 4.6$$

where  $z_c$  is the calculated value,  $z_e$  is the experimental value and  $n$  is the number of values to analyse. The size of each zone in each mesh for Case 1 is presented in Table 4.3, where the error estimation comparison is performed against the droplet's diameter evolution of the experimental data. As a result, the most appropriate mesh for further analysis is Mesh 3, which is highlighted in light orange in Table 4.3.

**Table 4.3. Mesh sizing for Case 1**

<b>Zone</b>	<b>Mesh 1</b>	<b>Mesh 2</b>	<b>Mesh 3</b>	<b>Mesh 3a</b>
	<b>Element size</b>	<b>Element size</b>	<b>Element size</b>	<b>Element size</b>
A [ $\mu\text{m}$ ]	240	240	<b>240</b>	240
B [ $\mu\text{m}$ ]	96	64	<b>38.4</b>	32
C [ $\mu\text{m}$ ]	24	16	<b>9.6</b>	8
Number of cells	7008	10,884	<b>24,847</b>	33,132
RMSD of droplet diameter evolution	2%	2%	<b>2%</b>	1%

A comparison of the droplet's diameter evolution for each mesh size is presented in Figure 4.5, where from Mesh 1 to Mesh 3 the RMSD is the same; however, the difference between Mesh 3 and Mesh 3a is approximately 1%. In addition, in Figure 4.5 it is observed that increasing the mesh resolution further does not affect the solution; therefore, the size of Mesh 3 is most suitable to model oil droplet evaporation under representative bearing chamber conditions. Mesh 3 is proposed instead of Mesh 3a because the error estimation is within 2% and the prediction of results with Mesh 3 is more efficient than with Mesh 3a in terms of computational time.

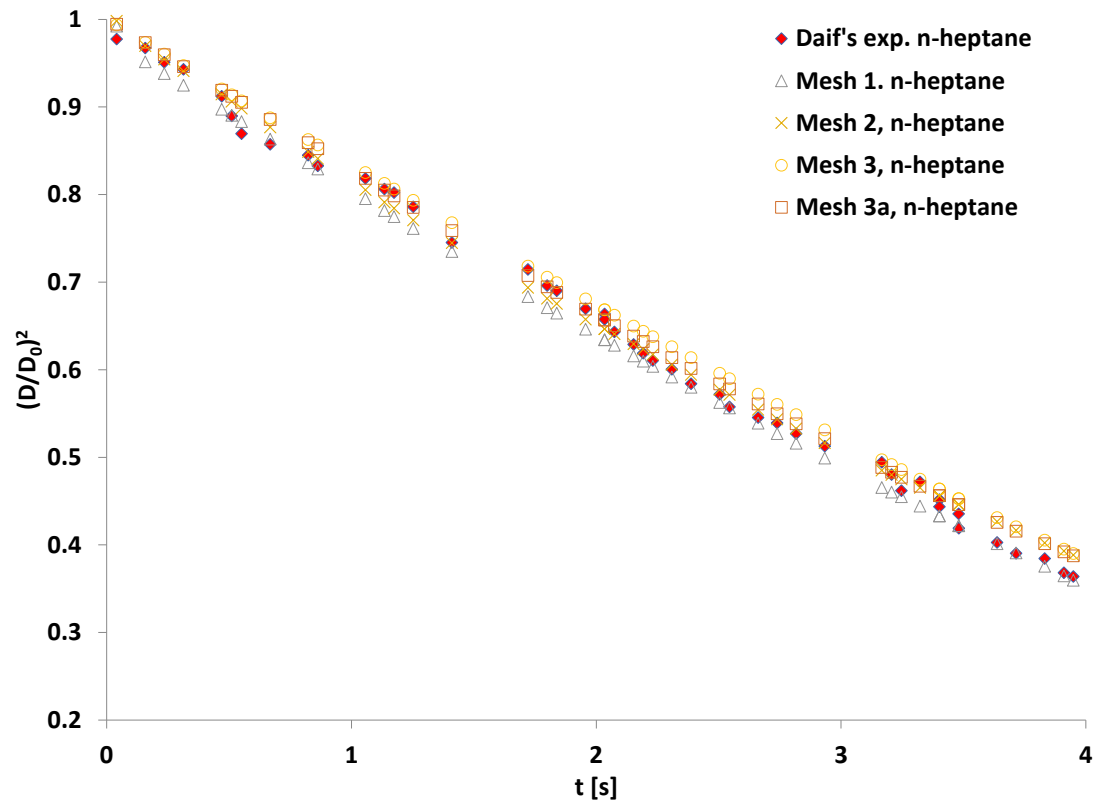


**Figure 4.5 Mesh independence study of the temporal evolution of droplet diameter of n-heptane (Case 1) between the present predictions and experimental data (Daif et al., 1998)**

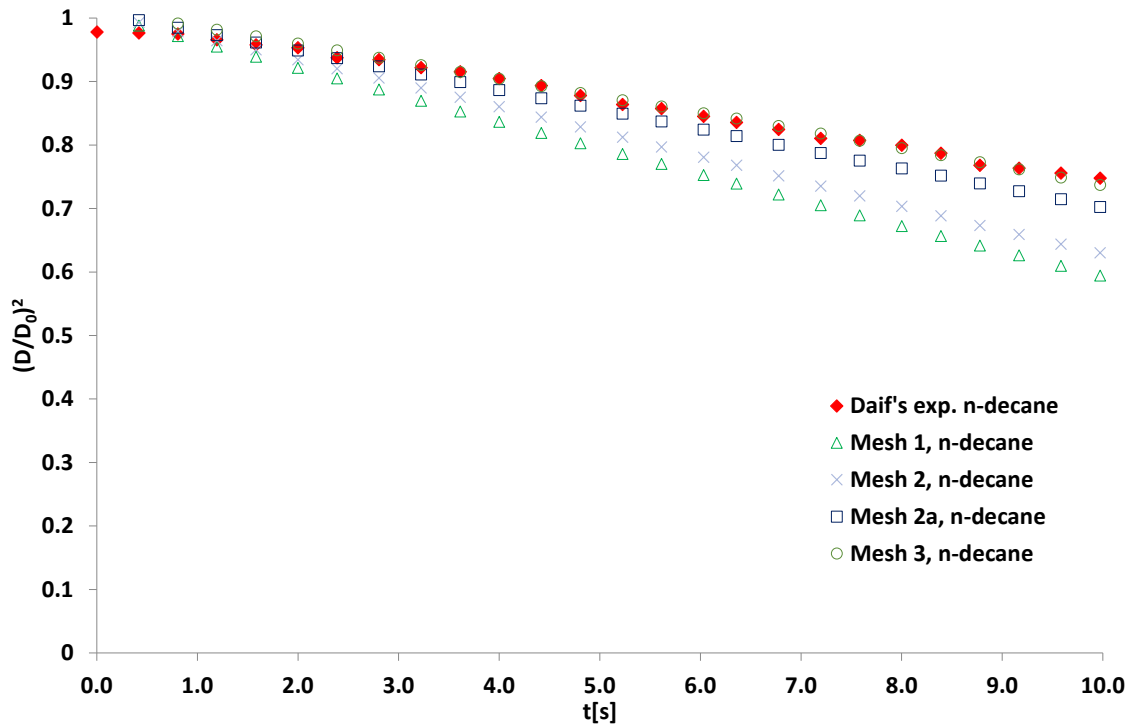
**Furthermore,**

Table 4.4 presents the mesh sizing for Case 2 (n-decane). Four different meshes are evaluated and it is noted that Mesh 1 and Mesh 2 have a minimum computational time, however the RMSD is more than 4%. Therefore, Mesh 2a and Mesh 3 are evaluated showing an error estimation of 3% which is less than 1% .

**Table 4.4. Mesh sizing for Case 2**

<b>Zone</b>	<b>Mesh 1 Element size</b>	<b>Mesh 2 Element size</b>	<b>Mesh 2a Element size</b>	<b>Mesh 3 Element size</b>
A [ $\mu\text{m}$ ]	240	240	240	<b>240</b>
B [ $\mu\text{m}$ ]	96	64	48	<b>38.4</b>
C [ $\mu\text{m}$ ]	24	16	12	<b>9.6</b>
Number of cells	8,971	15,985	24,893	<b>35,536</b>
RMSD of droplet diameter evolution	9%	4%	1.6%	<b>1.3%</b>

Figure 4.6 shows the mesh independence study, where it can be seen how the RMSD of the droplet's diameter evolution is reduced according to the reduction of the mesh sizing. Mesh 2a and Mesh 3 are within 2% versus the experimental results. In addition, Mesh 3 shows that the predictions compared with the experimental data closely follow the trending presented by Daïf et al. (1998). Therefore, as the sizing of Mesh 3 in Case 2 is the same as for the Case 1 and the RMSD is within 2%, this is the sizing that is proposed to be used in further analysis to understand the evaporation process of oil droplets under bearing chamber conditions.



**Figure 4.6. Mesh independence study of the temporal evolution of droplet diameter of n-decane (Case 2) between the present predictions and experimental data (Daïf et al., 1998)**

## 4.4 Results and discussion

The validation of the numerical modelling was presented in previous sections, where good accuracy and convergence with the mesh independence study can be observed. The mesh independence study was performed with three levels of refinement, where the last level shows an error estimation of around 3% as shown in Figure 4.7.

The mesh independence study was based on monitoring the non-dimensional square diameter's temporal evolution, which was compared with previous experimental data (Daïf et al., 1998). Additionally, the model was validated for two fluids with different volatilities and the accuracy of the results shows good agreement according to the experimental results, as can be observed in Figure 4.7. Furthermore, a qualitative

comparison was performed in Figure 4.12 and Figure 4.15 and it shows good agreement with previous numerical results of Strotos et al., (2016), where the parameters observed are the temperature at the vicinity of the droplet and the oil vapour mass fraction.

In Figure 4.7, it can be seen that the n-decane component is less volatile than the n-heptane component and consequently the vaporisation process of n-decane is slower than n-heptane. As shown in Figure 4.7, the overall error for the n-decane case is greater than for n-heptane and therefore a finer mesh is included in the n-decane case to ensure mesh independence.

However, we must consider the likely residence time of a droplet within the shearing region of a bearing chamber, which will be much shorter than the 10 s simulated in Case 2. The n-decane case serves as a base case in which to add the bearing chamber conditions and oil properties. This is because the aero-engine oils are less volatile than n-decane; thus, it is expected that the oil will have a slow evaporation process. The low volatility of oil is due to the properties of oil base stock and the additives that cause the oil to possess a high molecular weight and high boiling point.

Based on the validation presented in the previous sections and supported by the mesh independence study, it can be said that Mesh 3 will be used for further simulations to understand the oil droplet evaporation process.

The temporal evolution of the non-dimensional square diameter will be monitored in further simulations (as per Figure 4.7), because this parameter allows us to observe the droplet evaporation rate, the effects of flow conditions on the liquid's volatilisation, the temporal reduction of droplet diameter, and the evolution of the oil vapour and air mixture on the droplet's surface.

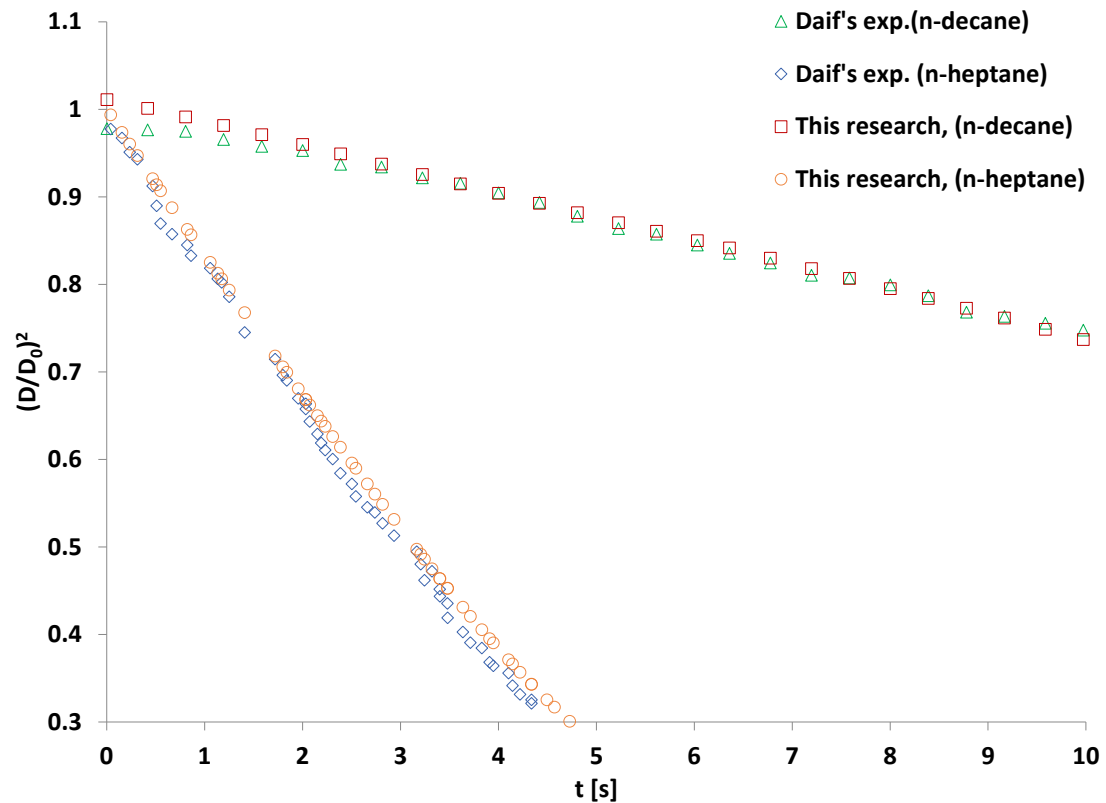


**Figure 4.7. Comparison of temporal evolution of droplet diameter of n-heptane and n-decane between the present predictions and experimental data (Daif et al., 1998)**

The following sections will describe the internal and external droplet flow performance to predict the droplet's internal circulation, temperature and oil vapour mass fraction.

#### 4.4.1 Internal circulation

The internal circulation is observed due to heat transfer by convection from the airflow to the droplet's surface and from the droplet's surface to the droplet's core, as observed in Figure 4.8.

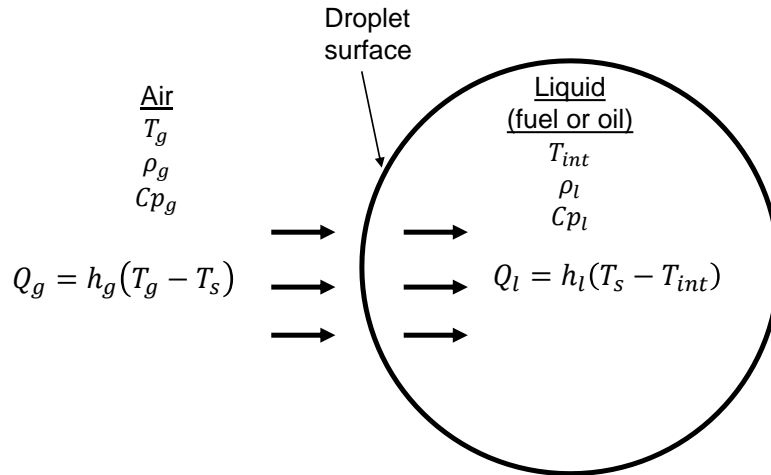


**Figure 4.8. Schematic of the heat transfer by convection from the droplet's exterior to interior**

In addition to the mesh independence study, we can observe the comparative analysis of the droplet's internal circulation during the evaporation process, where a spherical vortex has been observed in past predictions (Strotos et al., 2016) and also in the present predictions, as shown in Figure 4.9.

The internal circulation is due to the shear stresses caused by the velocity gradients at the droplet's surface. As a result, the vortex inside the droplet allows thermal distribution and also mixing of the species in the case where the droplet has two or more components.

Figure 4.9 and Figure 4.10 show a boundary layer of the gas phase around the droplet's surface with a separation at the rear part ending in a wake region. In addition, inside the droplet near to the surface, a liquid boundary layer is observed before the circulating region. According to Sirignano (2010), the circulating region is formed by an internal wake followed by a spherical vortex similar to the streamlines of normalised velocity presented in Figure 4.9 and Figure 4.10.

Figure 4.9 shows the internal vorticity of an n-heptane droplet after 0.5 s; Figure 4.9 a) and Figure 4.9 b) correspond to previous (Strotos et al., 2016) and present predictions, respectively.

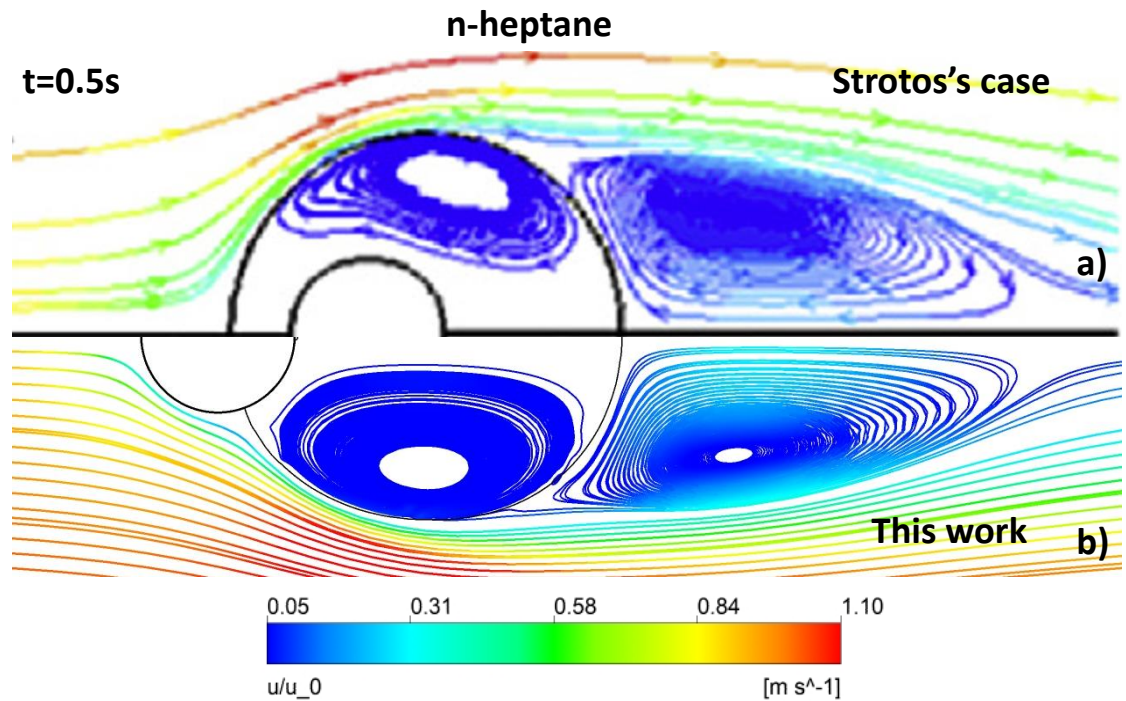


**Figure 4.9. Comparison of the streamlines of normalised velocity of an n-heptane droplet at 0.5 s: a) previous numerical predictions (Strotos et al., 2016); b) present predictions**

Figure 4.10 presents the internal vortex comparison for an n-decane droplet after 0.25 s of evaporation. Figure 4.10 a) corresponds to Strotos's predictions and Figure 4.10 b) corresponds to the present predictions, where the main vortex is shown in both cases and, in the present predictions, it is slightly inclined due to the effect of the suspender.

The droplet's position is different for Strotos's predictions than for the present predictions. The position predicted can be dependent on the parallelisation used when the simulation is performed. The position is not documented in the experimental data of Daïf et al. (1998) and the same cases have been computed in previous numerical reports

showing different droplet positions, as in Chen et al. (2016), Strotos et al. (2008) and Strotos et al. (2016). Despite the difference in droplet position, the contours were positioned taking as reference the suspender to observe the scale of each case and the flow performance. Consequently, the front parts of the droplets were aligned together to compare the similarities of both predictions, as shown in Figure 4.10.

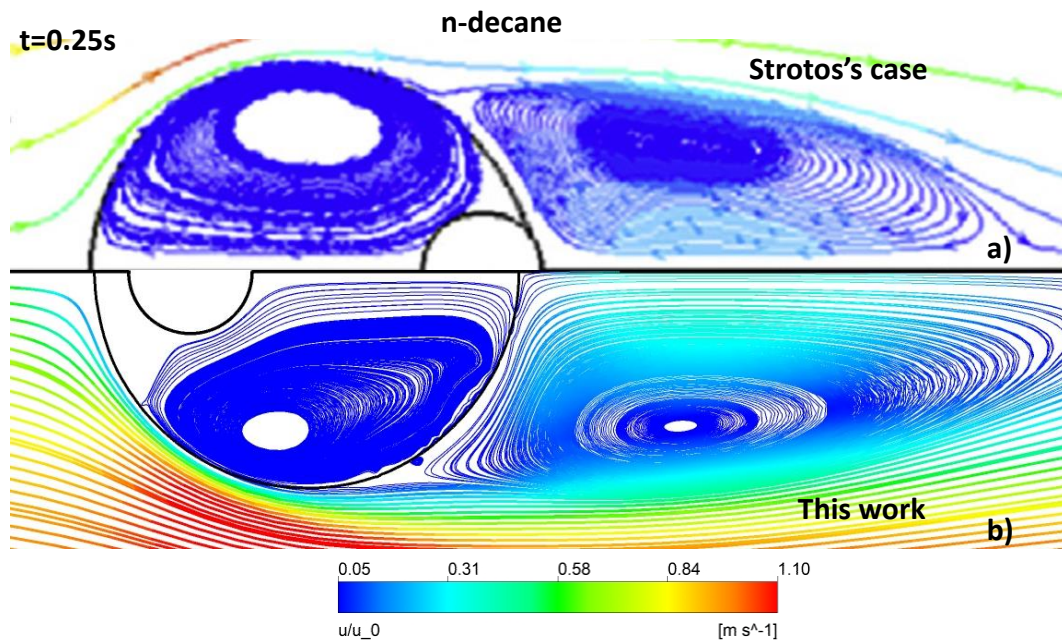


**Figure 4.10. Comparison of the streamlines of normalised velocity of an n-decane droplet at 0.25 s: a) previous numerical predictions (Strotos et al., 2016); b) present predictions**

The internal vorticity is observed particularly with axisymmetric flow. Despite the fact that there might be some internal and external differences (such as droplet rotation (Banerjee, 2013)) in the vortex formation, the results based on the assumption of the axisymmetric flow provide good approximations. Therefore, this assumption will be used for further simulations because, otherwise, the case can be computationally expensive in terms of resources and time.

The following section will discuss the effects of temperature on flow performance and how the flow temperature gradients are closely related to the droplet's internal circulation.

#### 4.4.2 Temperature

The heat transferred from the gas phase to the liquid phase at the initial state is due to convection at the droplet's surface and, subsequently, friction in the same area, which cause internal circulation and the heat transfer by convection from the surface to the core. The core remains at a lower temperature than the surface and the internal isotherms follow the same flow patterns as the streamlines, as shown in Figure 4.11, which mirrors the same performance as reported by Sirignano (2010).

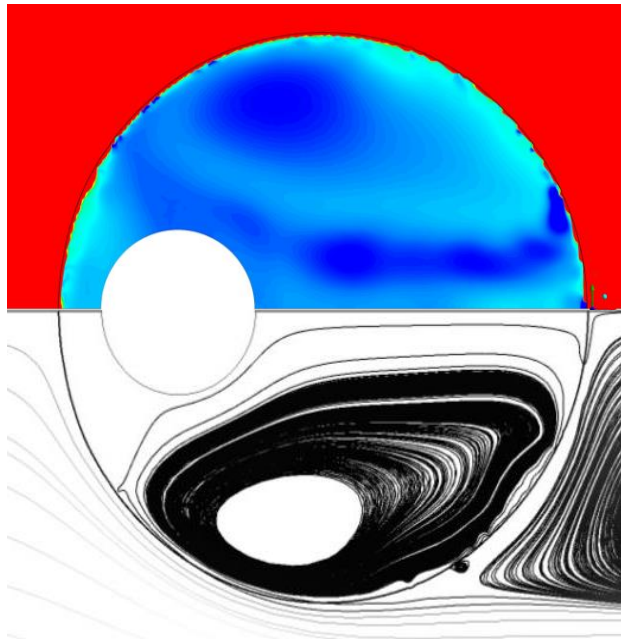


**Figure 4.11. a) Internal droplet temperature contours, b) internal vortex of an n-decane droplet at 0.25 s**

The temperature field is presented in Figure 4.12 where the temperature contours of the previous predictions (shown in Figure 4.12 a)) are compared with present predictions

(shown in Figure 4.12 b)). It can be seen that the results of both predictions share some similarities. Figure 4.12 shows that the temperature of the droplet changes progressively from the droplet's interface to the dry air, which is far away from the liquid's surface. There is a progressive change when the wake behind the droplet shows a boundary layer separation. Additionally, Figure 4.12 shows that the droplet's surface has reached the temperature of 317 K and at the rear part of the droplet, where the wake region is placed, the mixture of fuel vapour and air reaches an intermediate temperature of 336 K.

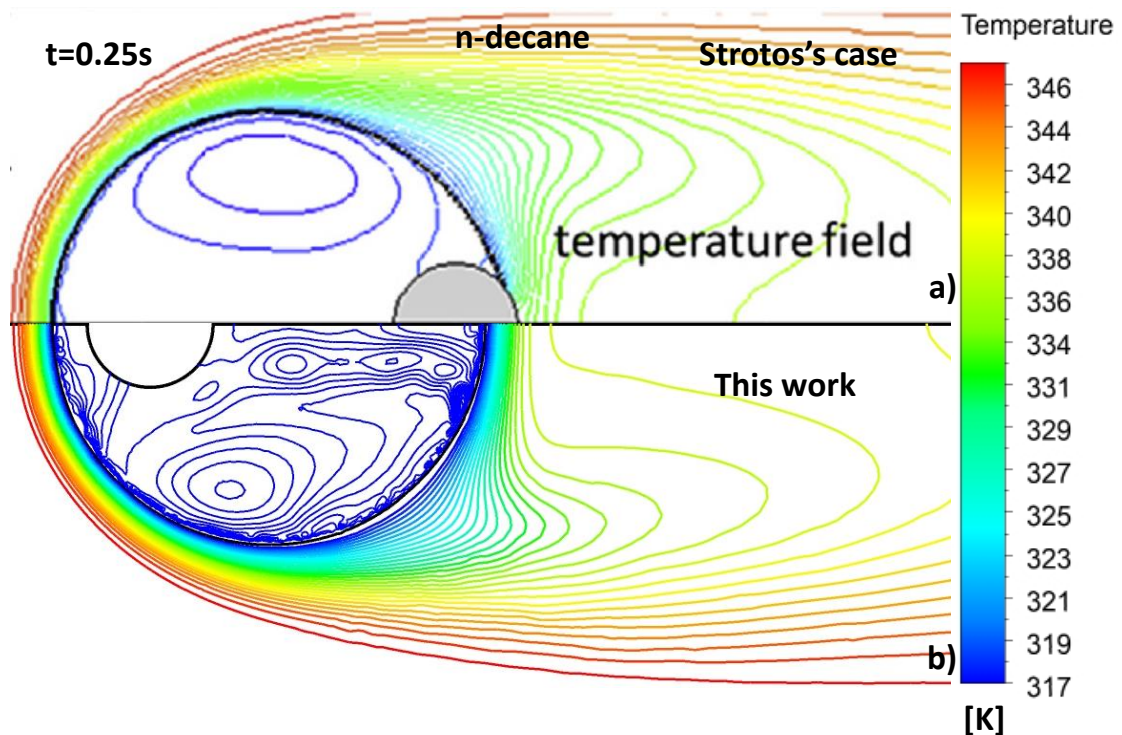


**Figure 4.12. Temperature field of an n-decane droplet at 0.25 s: a) previous numerical predictions (Strotos et al., 2016), b) present predictions**

Figure 4.13 shows a comparison of temperature contours for Case 1 (Figure 4.13) for an n-heptane droplet and also for Case 2 (Figure 4.13) for an n-decane droplet, both at 0.25 s of the evaporation process. Case 1 has a larger droplet diameter reduction in comparison with Case 2, which is probably due to n-heptane being more volatile than n-

decane. Furthermore, the temperature gradients from the droplet's surface to the droplet's vicinity can be observed in both cases, where a change in the contour curvature is apparent at the same position of the boundary layer separation. In addition, the droplet's position in Case 1 is displaced completely to the rear part of the suspender due to the drag force being higher than the droplet's weight; however, the droplet is still attached to the suspender by surface tension.

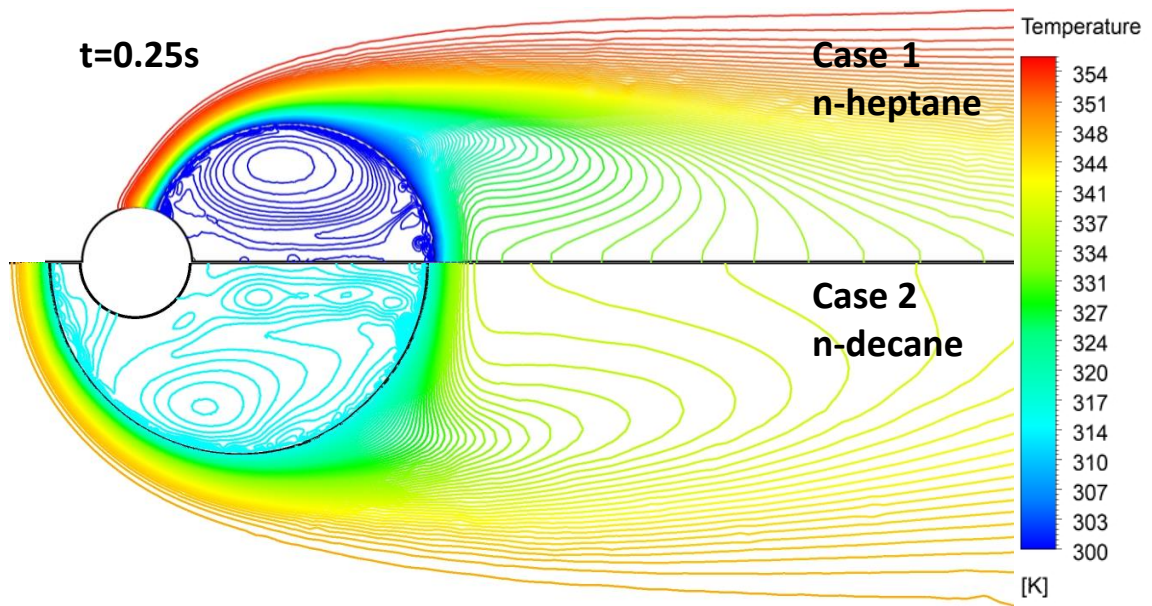


**Figure 4.13. Comparison of temperature contours of Case 1 (n-heptane) with Case 2 (n-decane) at 0.25 s**

Figure 4.14 presents the n-heptane droplet at 0.5 s, when during the early stages of the evaporation process the n-heptane vapour surrounds the droplet's surface, as shown in Figure 4.14 b). The fuel vapour forms a boundary layer around the droplet; in addition, in Figure 4.14 a) the thermal isotherms are extended until the end of the wake length. The highest fuel vapour concentration is at the interface, with 30% fuel vapour which is reduced to zero at the end of the boundary layer. Contrary to the vapour fields, the lowest temperature of 300 K is found at the interface and the highest temperature is found at the

end of the boundary layer, as shown in Figure 4.14 a). The temperature inside the droplet remains at 300 K, which is the saturation point of n-heptane. The fuel vapour mass fraction contours are explained in detail in Section 4.4.3.

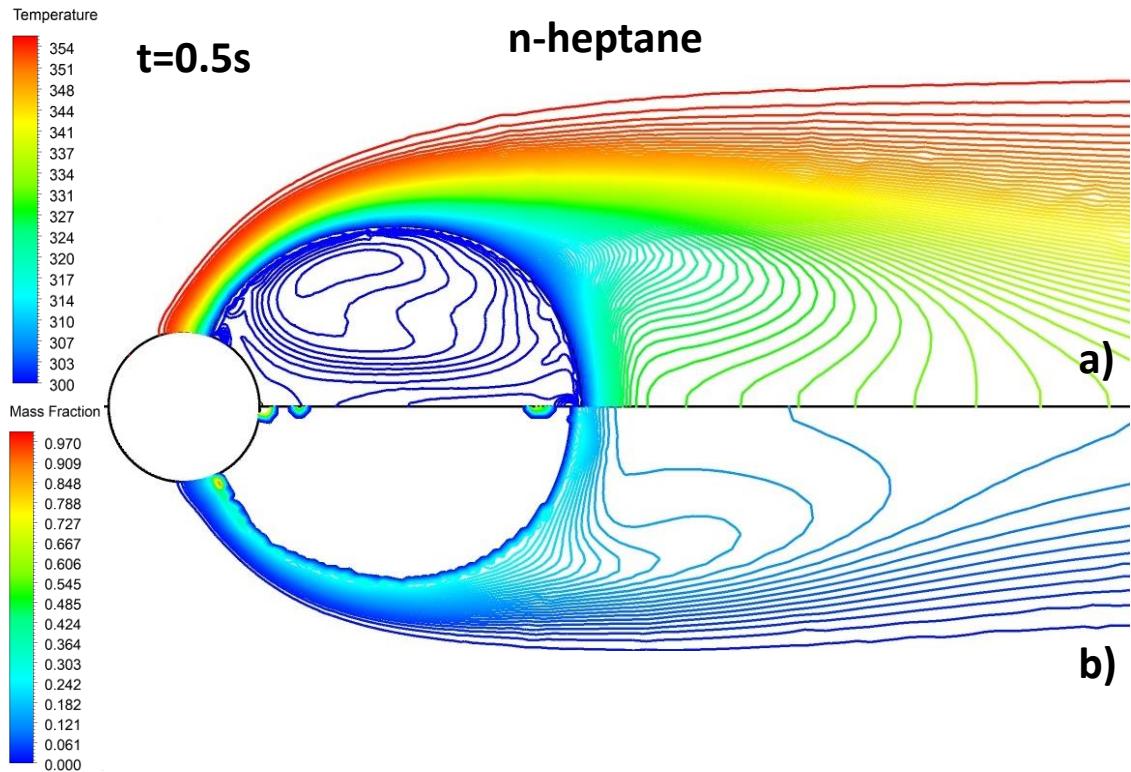


**Figure 4.14. n-heptane droplet at 0.5 s: a) temperature contours, b) vapour mass fraction**

### 4.4.3 Vapour mass fraction

Evaporation is observed when the droplet's surface temperature reaches the saturation point; in this case, saturation is assumed at the initial stage of the model. It is noted that the fuel vapour surrounds the droplet's interface following the boundary layer of the flow field. The recirculation at the rear part of the droplet enhances the heat and mass transfer, distributing the fuel mass fraction along the wake length. This can be observed in Figure 4.15, which also presents a comparison of the vapour fields between Strotos's case (Figure 4.15 a)) and the present predictions (Figure 4.15 b)) at 0.25 s for

Case 2 (n-decane). The present predictions show a 5% higher concentration of n-decane vapour at the droplet's interface; however, according to the comparison of droplet lifetimes with the experimental data of Daïf et al. (1998), the present predictions are within a 3% error, which means it may not affect the results. The higher concentration of vapour in the present predictions might be due to the element size at the droplet's interface, which is probably smaller than the case reported by Strotos et al. (2016). However, the droplet diameter is the same in both cases, although there is a difference in the droplets' positions. The reason for the difference in the droplets' positions was discussed in Section 4.4.1.

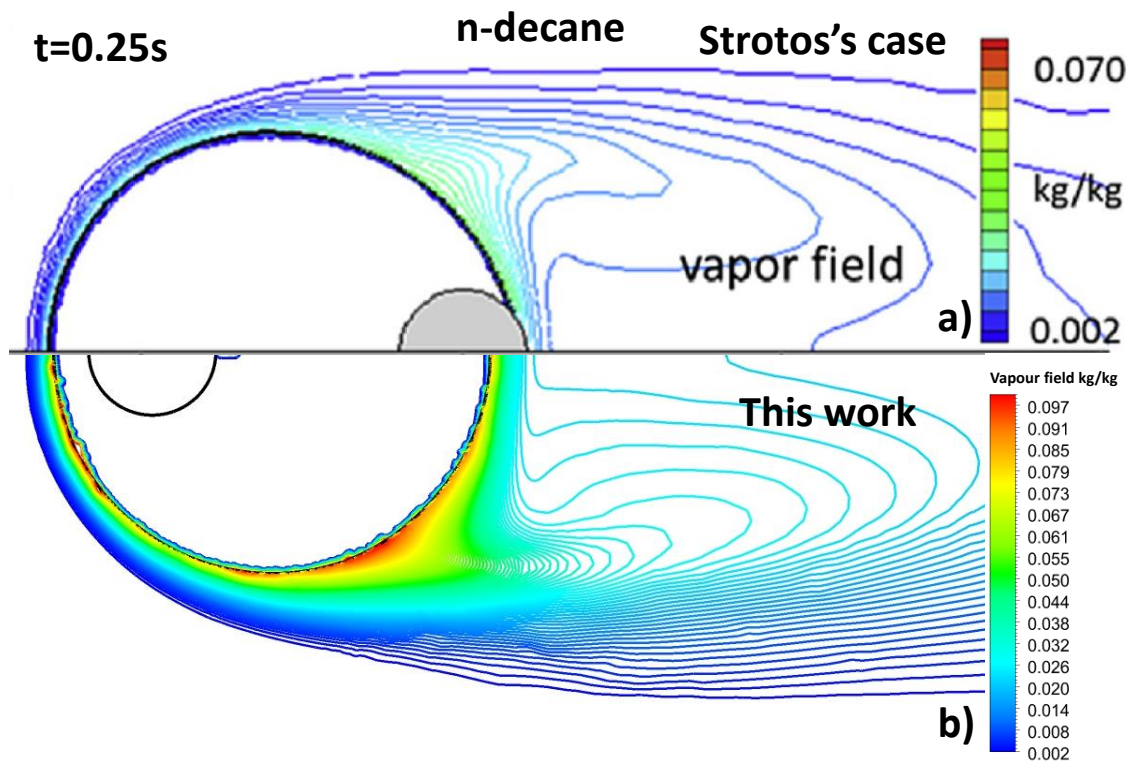


**Figure 4.15. Vapour mass fraction of an n-decane droplet at 0.25 s: a) previous numerical predictions (Strotos et al., 2016), b) present predictions**

Figure 4.16 displays a comparison of mass vapour contours between Case 1 and Case 2 at 0.25 s in both cases. Case 1 has around a 17% higher concentration of fuel vapour at the interface, which corresponds to the high volatility of n-heptane where the

saturation point is lower than for n-decane. Therefore, the n-heptane droplet evaporates faster than the n-decane droplet, as observed in Figure 4.16. The vapour mass fraction contours are important in the analysis of droplet evaporation because they can give us the fuel vapour and air mixture concentrations that are needed to know whether this mixture is prone to starting the combustion process; this is the effect that needs to be avoided inside the bearing chamber compartments. Recirculation boosts this process at the rear part of the droplet, which is discussed in Section 4.4.4.

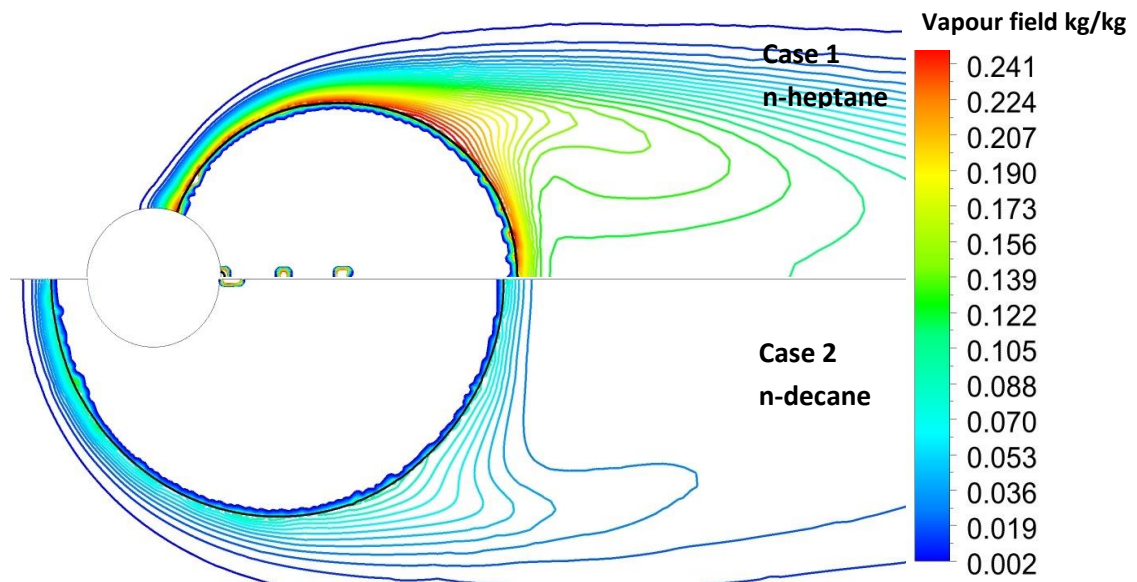


**Figure 4.16. Comparison of vapour mass fraction contours of Case 1 (n-heptane) with Case 2 (n-decane) at 0.25 s**

#### 4.4.4 Wake length

As discussed in previous sections, a separated flow is observed over the droplet. Two symmetrical vortices are seen at the rear part of the droplet, as shown in Figure 4.17 and Figure 4.18. This wake is typically presented in droplets under the effect of convective flow at intermediate Reynolds numbers (Clift et al., 2005). According to Clift et al. (2005), this flow performance is typical in the region of onset wake instability defined by a regime

of  $130 < Re < 400$ . The regime that is of interest for the numerical analysis of evaporative oil droplets inside bearing chambers is  $0 > Re > 500$ . Therefore, it is expected to perceive a flow separation in further simulations in Chapter 5.

Figure 4.17 presents the streamlines of axial velocity and a plot of the position of the droplet on the x axis and the axial velocity on the y axis. This axial velocity is plotted along the symmetry axis of an n-heptane droplet (Case 1) at 0.25 s. Two vortices are observed: one at the rear part of the suspender and one main vortex in the middle of the droplet. The first vortex is due to the suspender effects where there is a stagnation point at the rear part of the suspender.

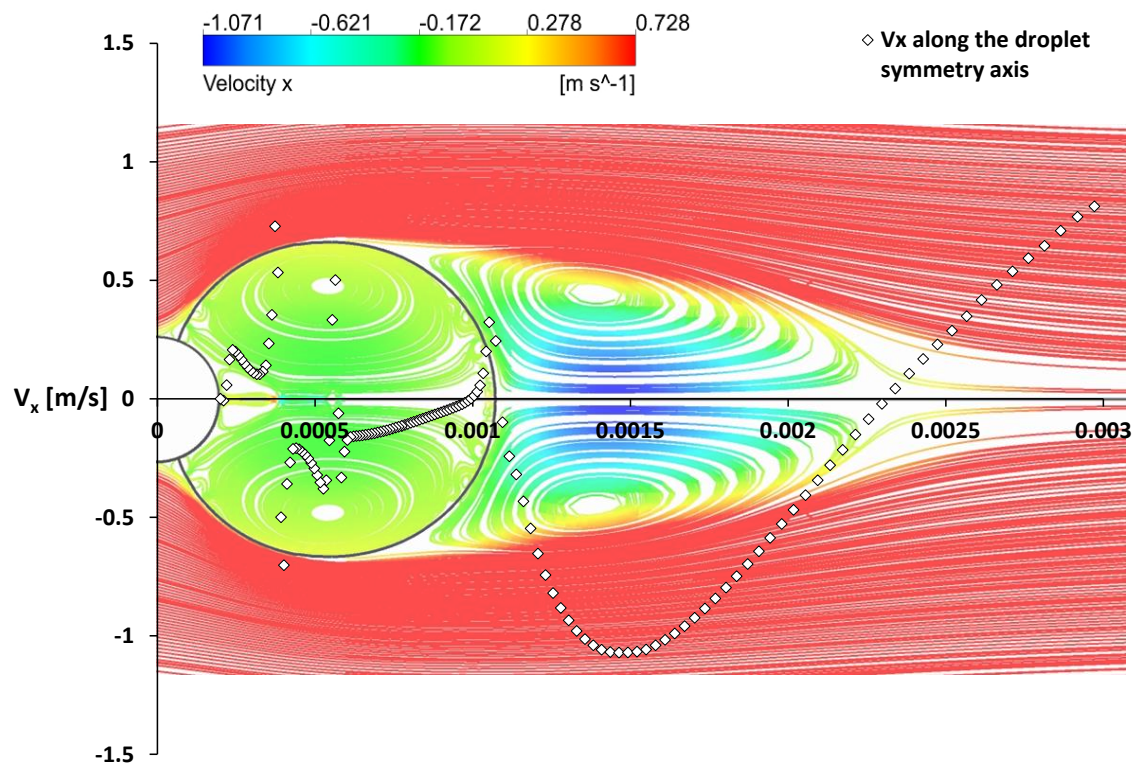


**Figure 4.17. Axial velocity of an n-heptane droplet at 0.25 s**

At the end of the first vortex, the velocity increases until reaching the highest value of 0.7 m/s; this is because the two vortices meet at this point. Following the axial position, a sharp reduction in the velocity can be observed at the droplet's interior, with a value of

$-0.7$  m/s which increases when reaching the rear part of the droplet located at  $0.00105$  m with a velocity of  $0.32$  m/s where the wake length starts.

The wake is observed on the downwind side of the droplet and this enhances the heat transfer from the exterior to the droplet's interior. The lowest velocity is observed at  $0.0015$  m with a value of  $-1.07$  m/s, which increases until the end of the wake length at  $0.0022$  m along the symmetry axis.

Figure 4.18 shows the streamlines of axial velocity overlapping a plot of the position of the droplet on the x axis and the axial velocity on the y axis of an n-decane droplet (Case 2) at  $0.25$  s. This axial velocity is plotted along the symmetry axis. Unlike Case 1 (Figure 4.17), in Case 2 there are three stagnation points: one at the front of the droplet, one at the rear side of the suspender and the last one at the rear part of the droplet. The first two stagnation points in Case 2 are due to the droplet's position, where it is not completely displaced to the rear side of the suspender as in Case 1. The third point is observed due to the change of flow direction on the downwind side of the droplet. It can be seen that the wake length in Case 2 (n-decane) is larger than in Case 1 (n-heptane). This is because the Reynolds number in Case 2 at  $0.25$  s is larger than for Case 1. The Reynolds number for Case 1 is  $230$  and for Case 2 it is  $294$ . It can also be seen that the droplet's internal vorticity is inclined, which is due to the effect of the suspender. Furthermore, Figure 4.18 shows the lowest axial velocity of  $-1.3$  m/s at the internal vortex of the wake, located at  $0.0017$  m of the axial position where a high concentration of fuel vapour is expected. Thus, the wake contains a mixture of air and fuel vapour, which enhances heat and mass transfer.

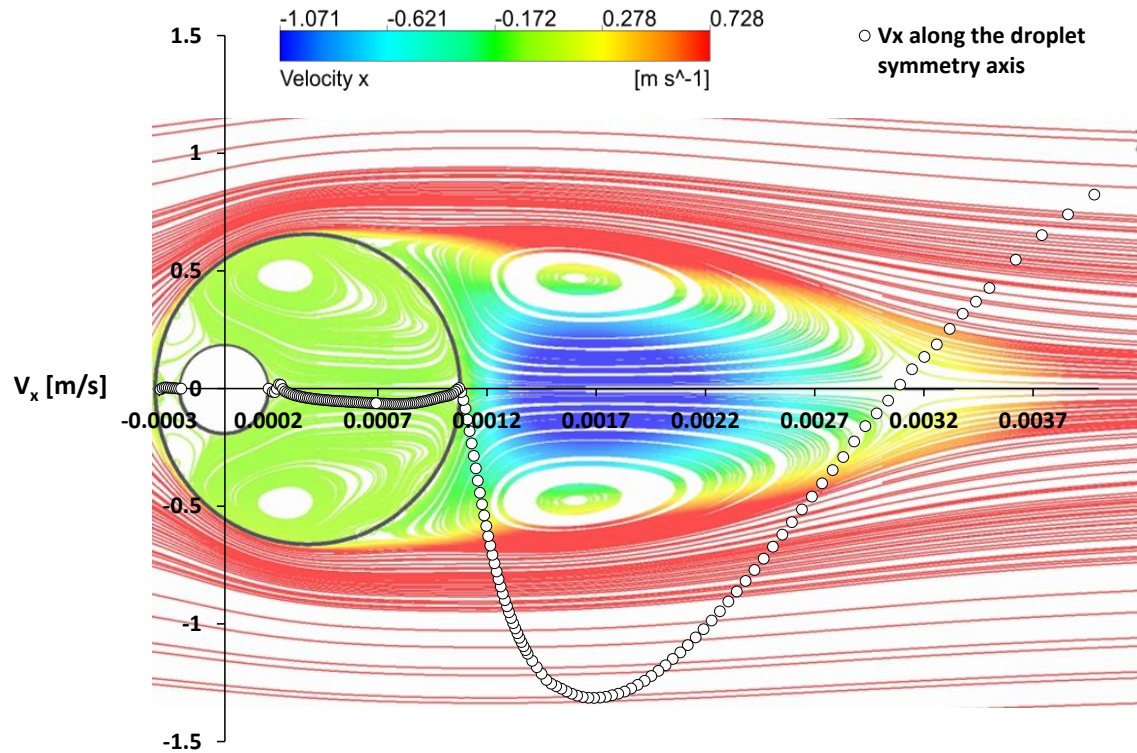


**Figure 4.18. Axial velocity of an n-decane droplet at 0.25 s**

Table 4.5 presents a comparison of the droplet diameters and wake lengths for Case 1 and Case 2 with the predictions of Strotos et al. (2016).

**Table 4.5. Wake length and diameter comparison between Strotos's case and this research**

Fluid	Parameter	Strotos's case	This research	Error estimation
n-heptane 0.5 [s]	Diameter [m]	0.00105	0.00104	1%
	Wake length [m]	0.00109	0.0011	1%
n-decane 0.25 [s]	Diameter [m]	0.0015	0.0014	7%
	Wake length [m]	0.0016	0.0019	19%

The error estimation to compare the wake length and diameter of the previous and present predictions is given by equation 4.7:

$$\% \text{ error} = \left| \frac{\text{Strotos's case} - \text{this research}}{\text{Strotos's case}} \right| \times 100 \quad 4.7$$

Where Case 1 has an error estimation of 1%, it is noticed that for Case 2 the present results predict a wake length error of 19% compared with the previous predictions. With regard to the diameter, the present prediction is 7% greater than Strotos's work. Despite this, the present work shows good agreement with experiments (Daïf et al., 1998), as can be observed in Figure 4.7.

## 4.5 Validation of radiation modelling with evaporation

In this section, the results obtained by adding the radiation of the environment are based on the experimental data reported by Nomura et al., (1996).

### 4.5.1 Experimental setup

The evaporation of a droplet exposed to the radiative effects of the environment was analysed experimentally by introducing droplets ranging from 0.6 mm to 0.8 mm in diameter into an electric furnace. Similar to the validation in Section 4.2.1, the droplet was attached to a suspender by surface tension. The suspender had a diameter of 0.15 mm, and the experiments were carried out under pressures ranging from 0.1 MPa to 5.0 MPa and ambient temperatures ranging from 400 K to 800 K. Moreover, the experiment was performed under microgravity conditions using a free-fall method with a drop tower and parabolic flights; more details are presented in Nomura's paper (Nomura et al., 1996). The droplet evaporation process was recorded with a CCD camera and a video was also filmed. The droplet diameter was measured assuming that each 10-pixel section had the same

spherical shape and volume as the droplet, which matched with the initial value of the sample. The experimental setup can be observed in Figure 4.19; the red box represents the area where the droplet was placed which is the section to be modelled.

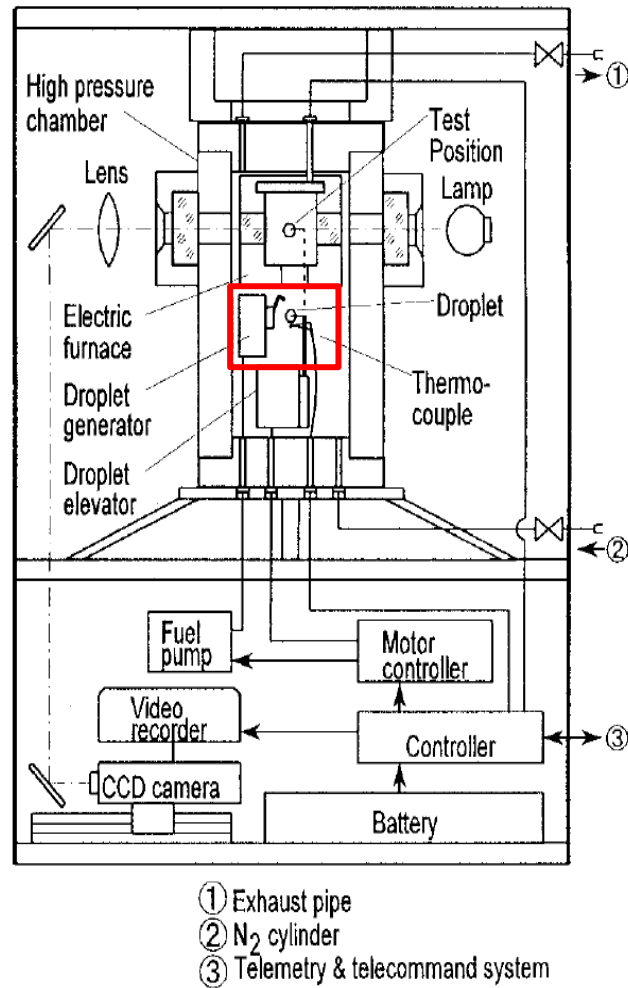


**Figure 4.19. Experimental setup to validate the radiation modelling (Nomura et al., 1996)**

#### 4.5.2 CFD setup

Based on the experimental setup described above, two cases were proposed to validate the radiation modelling, which are presented in Table 4.6. The cases include one

with radiation and one without radiation. Moreover, the boundary conditions are presented in Figure 4.20.

**Table 4.6. Cases to validate radiation modelling**

<b>Droplet characteristics</b>	<b>Case Rad</b>	<b>Case No Rad</b>
Radius [ $\mu\text{m}$ ]	300	300
Temperature [K]	298	298
Material	n-heptane	n-heptane
<b>Ambient characteristics</b>	<b>Case Rad</b>	<b>Case No Rad</b>
Gauge pressure [MPa]	0	0
Temperature [K]	471	471
Velocity [m/s]	0	0

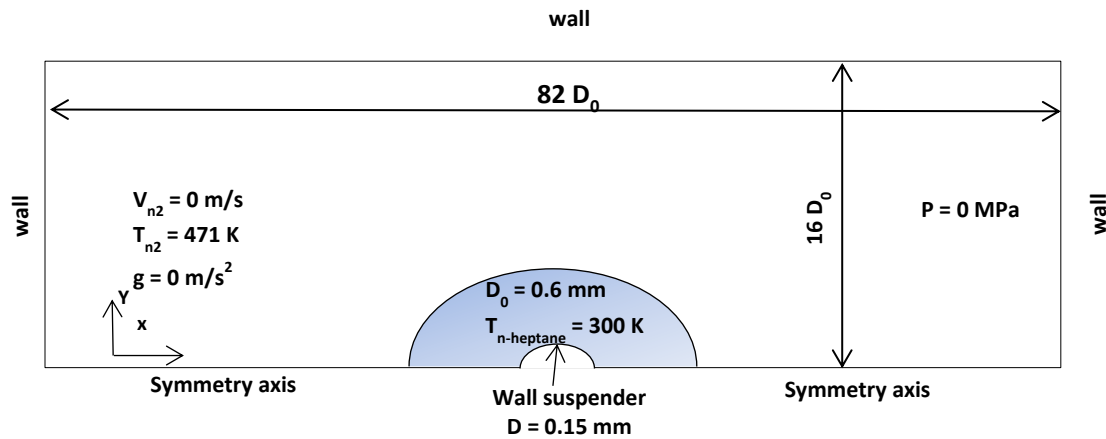


**Figure 4.20. Geometry and boundary conditions to validate the radiation modelling**

Furthermore, it is important to mention that in these cases convection is not taken into account. This is because in this section the author was focussed on validating only the radiation from the droplet surroundings and then implementing this in the modelling of oil droplets under representative bearing chamber conditions in Section 5.

### 4.5.3 Solution methods

The solution methods to validate the radiation modelling are presented in Table 4.7 and the evaporation model is included via UDF, similar to the description in Section 4.3.2. The discretisation used is second-order upwind for density, momentum and energy, and first-order upwind for species. The pressure–velocity coupling used is PISO, which is more stable for cases with high temperatures in the environment.

**Table 4.7. Solution methods to validate the radiation modelling**

Equation	Scheme
Pressure–velocity coupling	PISO
Pressure	Body force weighted
Volume fraction	Geometric reconstruction algorithm
Density	Second-order upwind
Momentum	Second-order upwind
Energy	Second-order upwind
Species	First-order upwind
Radiation	P-1

### 4.5.4 Mesh

The mesh includes three zones similar to those described in Section 4.3.3. In this case, the minimum cell size is kept as  $9.6 \mu\text{m}$  which is the zone that includes the droplet’s interface. However, for regions A and B, the mesh sizing was incremented in order to reduce the computational time. The total element size is 8,380, keeping the precision needed at the droplet’s interface (see Table 4.8).

**Table 4.8. Mesh sizing for Case 1**

<b>Zone</b>	<b>Element size</b>
A [ $\mu\text{m}$ ]	744.38
B [ $\mu\text{m}$ ]	48
C [ $\mu\text{m}$ ]	9.6
RMSE of droplet diameter evolution	8%

#### 4.5.5 Results and discussions

The parameter to analyse is the temporal evolution of the non-dimensionalised squared droplet diameter, as in the previous validation. This is taken into account after the heating-up period of the experimental data in order to observe the evaporation rate from the slope of the linear regression. The heating-up period of the experimental data finished after 0.0971 s and the time after this is compared with the numerical results, as can be observed in Figure 4.21.

The numerical data were plotted including cases one with radiation and one without radiation, and in both cases the evaporation rate follows the same trend as that of the experimental data. Moreover, it is observed that the experimental data starts the evaporation process from  $(D/D_0)^2 > 1$ , which is expected because during the heating-up period there is an expansion of the droplet's diameter.

Thus, the results of this research underestimate the values when these are compared with the experimental data because of the assumption that the thermophysical properties are constant. Moreover, Nomura's report does not specify the initial droplet diameter, which is in the range from 0.6 mm to 0.8 mm, nor the initial droplet temperature. In this

research, the heating-up period is not considered, the initial diameter is assumed to be 0.6 mm and the initial temperature is assumed to be 298 K.

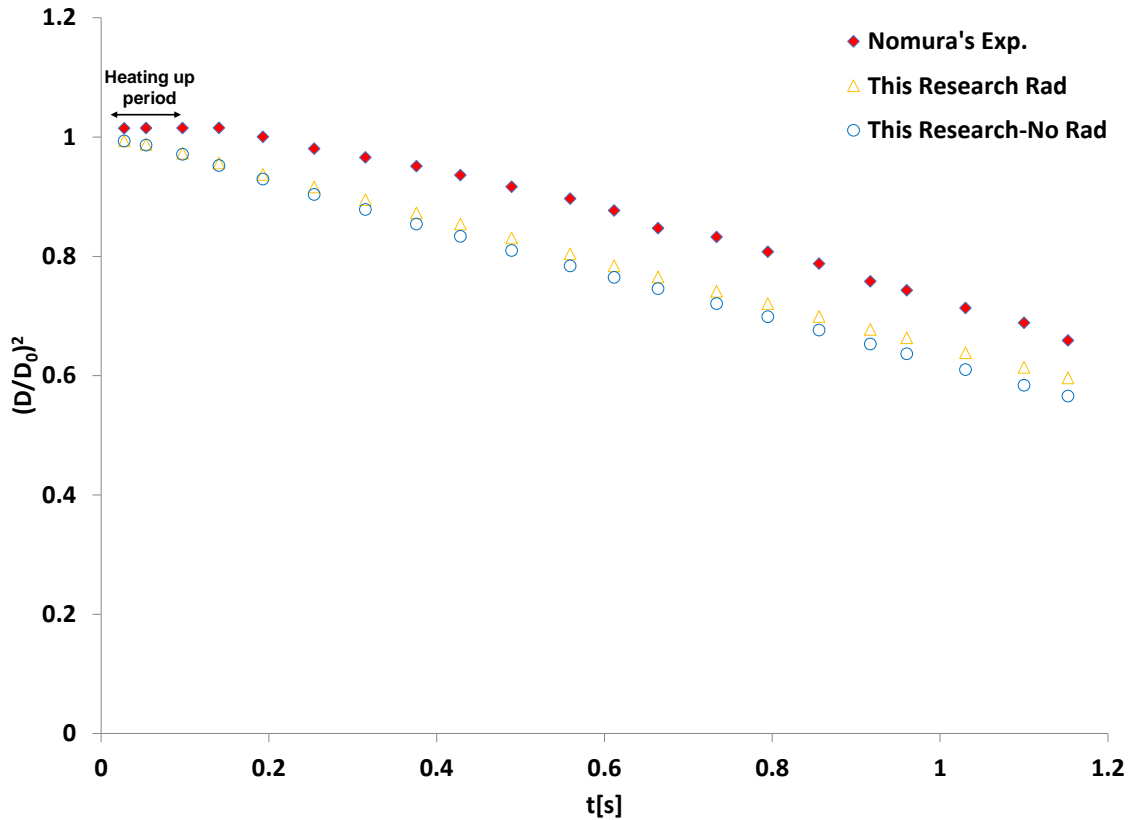


**Figure 4.21. Comparison of the temporal evolution of the droplet diameter with the experimental data of Nomura et al. (1996)**

Despite this, comparing the case with radiation with Nomura's results shows a RMSD of 8% and comparing the experimental results with the case without radiation shows a RMSD of 10%. However, when comparing the slope of the linear regression for all cases, it can be noted that the experimental data has a slope of 0.3545, the slope for the radiation case is 0.3553 and the slope for the case without radiation is 0.3749. This means that the error in the radiation case is less than 1% compared with Nomura's data and in the case without radiation it is within 6%, as can be observed in Table 4.9. Therefore,

radiation modelling can be applied to analyse the evaporation process of oil droplets under representative bearing chamber conditions.

**Table 4.9. Comparison of linear regression slopes to validate the radiation modelling**

<b>Case</b>	<b>Slope</b>	<b>Error</b>
Nomura	0.3545	-
Radiation	0.3553	0.2%
No radiation	0.3749	6%

Despite the error difference of 5.8% between the cases with and without radiation, which is minimal, it is important to observe the radiation effects inside the bearing chamber in order to predict whether there will be a higher rate of droplet evaporation under bearing chamber conditions.

Moreover, the droplet diameters are in the range of 14  $\mu\text{m}$  to 500  $\mu\text{m}$ , as discussed in Section 2.1.3, and the experiment uses a larger droplet diameter (600  $\mu\text{m}$ ) which shows a heating-up period of 0.0971 s; this is longer than the oil droplet's journey in a bearing chamber, as mentioned by Weinstock and Heister (2004).

However, the methodology presented in this validation is useful to observe the droplet evaporation process under the bearing chamber conditions. Section 5 will analyse and discuss the heating-up period of oil droplets and the time it takes oil droplets with different diameters to travel from the bearings to the bearing chamber walls. It is important to consider the initial droplet temperature after they are released from the bearings, as well as the oil temperature of saturation. The oil inlet temperature can be considered to be from 303.15 K to 403.15 K (Kanike et al., 2012) and the temperature of saturation to be 334 K for an oil base stock used in jet engines (Razzouk et al., 2007).

## 4.6 Guidelines and recommendations

This section will give some recommendations and guidelines for analysing the droplet evaporation process using a different model to the one specified in ANSYS Fluent. The UDF was programmed using two macros written for this work: `DEFINE_ADJUST` and `DEFINE_MASS_TRANSFER`. The first macro is to calculate the VOF and species gradients, which then should be saved in a UDM macro to allocate the values in each cell (`C_UDMI`). These values will be used in the computation of the mass transfer given in equation 3.22, as shown in Section 8.7. The computation of the mass transfer is called by the macro `DEFINE_MASS_TRANSFER` to add the corresponding source terms into the flow equations. It is important to highlight that the `DEFINE_ADJUST` macro should be inserted in the UDF Hooks to allocate the VOF and species gradients in the memory and to avoid possible errors such as “Segmentation fault” (Radwan, 2015). In the same way, it is important to initialise the mass transfer rate manually for the first iteration (Radwan, 2018). This initialisation can be done from the phase interaction mechanisms and selecting the constant rate mechanism. The initial value should be calculated based on the method of Abramzon and Sirignano (1989) and, once the species are initialised, the user-defined mechanism should be enabled. However, the residuals should be reduced to avoid numerical errors in the droplet’s interior.

Furthermore, in the fluid materials section, the temperature of reference of the gas phase should be the temperature of the saturation and the standard state enthalpy corresponds to the enthalpy of the evaporation at the temperature of the reference. Regarding the liquid properties, the standard state enthalpy of the liquid phase should be zero (Punekar, 2015).

Moreover, another important point to consider is to set the mass diffusivity of the mixture; it is recommended to set this as a multi-component and the coefficient can be constant or variable according to the temperature. Additionally, the order of the species on the mass diffusion coefficients should be according to the species that the user needs to calculate or monitor.

## 4.7 Summary

This chapter describes the validation modelling that is performed for customizing ANSYS to compute the evaporation using the VOF technique. The accuracy of the model was validated against experimental data (Daïf et al., 1998) to analyse the evaporation process for two fuels with different volatilities. To perform this validation, the CFD model was set up as explained in Section 4.3, detailing the geometry and boundary conditions, solution methods and meshing. The mesh sizing was defined based on a mesh independence study where the non-dimensional temporal evolution of droplets' squared diameter was monitored to ensure the accuracy of the results. Three levels of refinement were studied, where the last mesh sizing was compared with the experimental data (Daïf et al., 1998).

The predictions of droplet diameter reduction presented in this chapter were shown to match very well the experimental data available and were found to be within an error of 3% (see Section 4.4). Therefore, this numerical methodology can be used in further, more speculative, bearing chamber simulations.

The internal circulation, temperature, vapour mass fraction and wake length were also analysed and compared with previous numerical predictions (Strotos et al., 2016), and the results were discussed presenting the effects of convective flow over a suspended droplet in Section 4.4. It was noted that a wake is formed at the rear part of the droplet, enhancing the heat and mass transfer. Additionally, it was observed that the internal circulation favoured the internal droplet heating.

Section 4.6 provides guidelines and recommendations to customise ANSYS Fluent to analyse the droplet evaporation process, where there are some important tips for avoiding possible errors and progressing successfully with numerical predictions.

Overall, this chapter validates the methodology in Chapter 3 with good agreement against experiments. For this reason, the evaporation model can be applied to analyse droplets under simulated bearing chamber conditions to quantify the evaporation rate, mass fraction of oil vapour and temporal evolution of the droplet diameter, as well as to assist with the visualisation of the droplet's internal circulation, all of which is presented in Chapter 5.

## **5 Modelling oil droplet heat and mass transfer in aero-engine bearing chamber conditions**

The validated model presented in Chapter 4 is now applied to smaller representative droplets of an oil base stock used in bearing chambers of jet engines. This chapter (up to Section 5.2.2) and alongside Chapter 4 constitutes the base material for the paper presented by the author at ASME Turbo Expo 2019.

The oils used for gas turbine applications are synthetic and have a large range of operating temperatures. The composition of these oils is such that they have a base stock of synthetic ester, such as neopentyl polyol ester (MIL-PRF-23699F, 1997). The literature reports that neopentyl polyol ester can be assumed to be 80% pentaerythritol tetrapentanoate (PEC5) and 20% pentaerythritol tetranonanoate (PEC9) (Urness et al., 2016).

The approach outlined in the previous section that was used for validating purposes was also used in the work on oil droplet evaporation at bearing chamber temperature conditions.

The liquid properties of the oil are listed previously in Table 3.5. However, the oil vapour properties from experimental data are difficult to find in the literature. Therefore, the thermophysical properties of PEC5 in the gas phase are estimated theoretically based on the kinetic theory considering the gas as an ideal gas. The detailed calculation is laid out in Section 3.3.3.

In the validated model, a suspender is used to keep the droplet stationary. In this study, the role of the suspender is accounted for by using an MFR. The use of an MFR allows the droplet to remain stationary within the mesh and therefore stay within the refined zone. This approach is implemented via a UDF, where the velocity is obtained from equation 3.53.

The drag coefficient is calculated according to the correlation for the ‘standard drag curve’ for a solid sphere (Faeth, 1977), which is recommended for a range of Reynolds numbers ( $1 < Re < 800$ ) (Michaelides, 2006). The Reynolds number and the drag coefficient are computed from equation 3.54.

The equation 3.53 was solved and the droplet’s velocity was plotted in Figure 5.1, keeping the air velocity constant at 5 m/s and varying the droplet diameter. The droplet’s velocity presents an asymptotic trending, showing that droplets with larger diameters tend to travel for a shorter period than those with smaller diameters.

Furthermore, droplets with smaller diameters reach higher velocities than those with larger diameters. Therefore, it is recommended to use the MFR to keep the droplet’s position stationary for the variation of the droplet’s velocity during the evaporation process. Thus, the MFR follows the asymptotic trending according to the droplet radius reduction.

In addition, the use of an MFR avoids the secondary effects that the suspender has on the droplet’s heat transfer and it allows us to represent the dynamics of droplets inside the bearing chambers where, according to previous reports (Farrall et al., 2007), the motion of droplets with diameters less than 200  $\mu\text{m}$  is governed by air velocity.

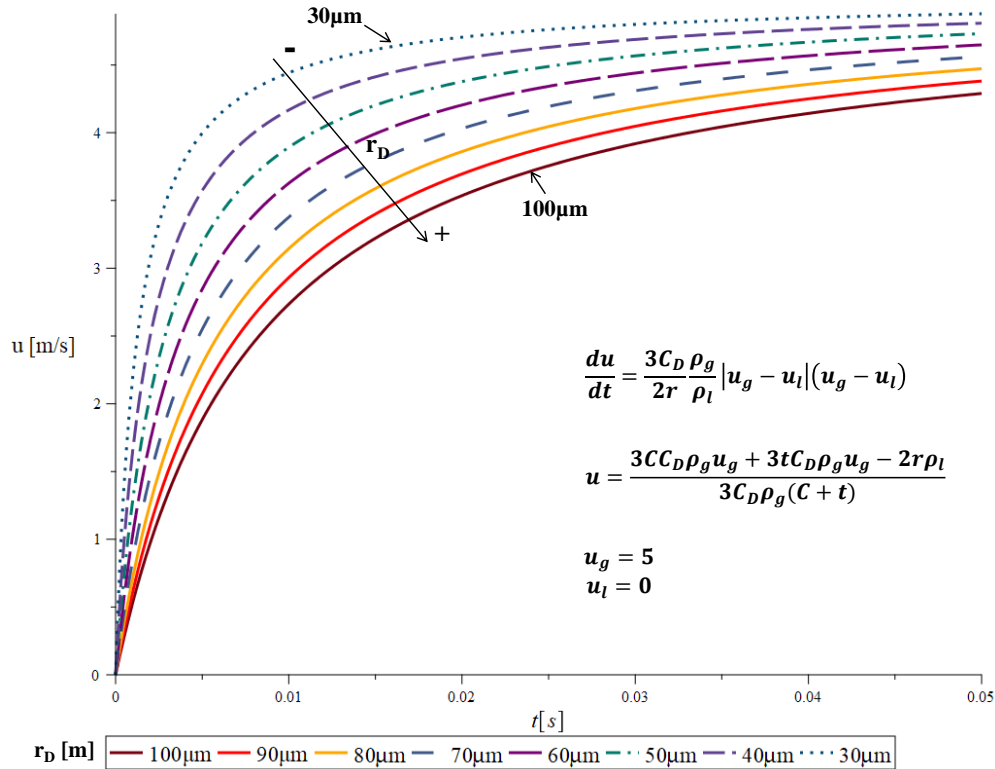


Figure 5.1. Variation of droplet velocity with droplet radius

## 5.1 Case setup

### 5.1.1 Analysis with a non-adaptive mesh

A parametric study was conducted using the values given in

Table 5.1 to understand the droplet evaporation process under representative bearing chamber conditions. The parametric study included two stages: the heating-up period and the phase-change period. Both periods are included in this section. The heating up is included to obtain the amount of time that the droplet takes to reach the temperature of saturation. Thus, if the temperature of the injected droplet is known, this research will predict whether the droplet is evaporating and for how long it will be evaporating during

its journey. Similar to the validation cases, the evaporation model computes the phase change once the liquid droplet reaches the saturation point.

The mesh used for the oil cases has three sections of refinement, as in the validation case. However, the size is scaled according to the droplet diameter to retain proportionality. A parametric study is proposed using the values in

Table 5.1, aiming to understand the evaporation process of a single oil droplet immersed in a convective flow. The main parameters to analyse are the air temperature, air inlet velocity and droplet diameter. The stationary droplets have an initial diameter of 200  $\mu\text{m}$ , which is the size of droplets that can be either in the airflow core or travelling from the bearings to the walls (see e.g. Farrall et al., 2007, Simmons et al., 2002).

The range of Reynolds numbers for oil droplets inside bearing chambers is  $0 < \text{Re} < 1400$ . For droplets with a  $D_0 < 200 \mu\text{m}$ , the Reynolds number is  $0 < \text{Re} < 580$ . These are the droplets that have the longest interaction with the hot convective flow. This analysis studied two air velocities, 1 m/s and 5 m/s, which are the velocities found in airflow recirculation zones inside bearing chambers (Aidarinis et al., 2011). For these velocities, the Reynolds numbers are 27 and 137, respectively. According to Clift et al. (2005), the transition from a laminar flow to a turbulent is from  $\text{Re} > 400$ . Therefore, the airflow is considered as laminar. The air temperatures take discrete values of 350 K, 450 K and 550 K, which are representative of the bearing chamber environment (Hashmi, 2012). The initial droplet temperature for all cases is 298 K and the saturation temperature is assumed to be 334 K (Razzouk et al., 2007).

**Table 5.1. Cases analysed with a non-adaptive mesh**

Case	$D_0$ [ $\mu\text{m}$ ]	Air			Droplet lifetime [s]
		T [K]	$u$ [m/s]	Re	
1	200	550	5	68	0.3
2			1	14	0.5
3		450	5	68	0.5
4			1	14	0.9
5		350	5	68	1.7
6			1	14	7.2

The CFD model setup is the same as described for the validation case, keeping values from 0.1 to 0.3 for the under-relaxation factors. Keeping these values low is very important to stabilise the simulation and obtain accuracy in the evaporation calculation. A variable time step from 1e-8 s to 1e-6 s targeting a Courant number of 0.25 was chosen. Keeping the Courant number below 0.25 is crucial to maintain the accuracy of the results. This is because the evaporation rate model is linked to the VOF gradients. If the Courant number is higher than this value, the volume fraction gradients diverge at the droplet's surface.

Moreover, the modelling of oil droplets under bearing chamber conditions presented issues to stabilising the simulation. Therefore, different schemes were tested to stabilise the computation. One of the main reasons for these instabilities might be the environment with a high temperature and, in consequence, a high evaporation rate.

In Figure 5.2 the options tested to stabilise the calculation are presented. The modifications to modelling the oil droplets are the addition of the MFR, the implementation of the time-step-changing factor and the use of the Pressure Implicit with Splitting of Operators (PISO) algorithm. This is because PISO provides more stability to the simulation and it is recommended for transient simulations (ANSYS, 2016c). The validation using PISO is presented in Section 4.5.5, which shows good agreement with the experimental results presented by Nomura et al. (1996). Therefore, this method is viable for the calculation of oil droplet evaporation in representative bearing chamber conditions.

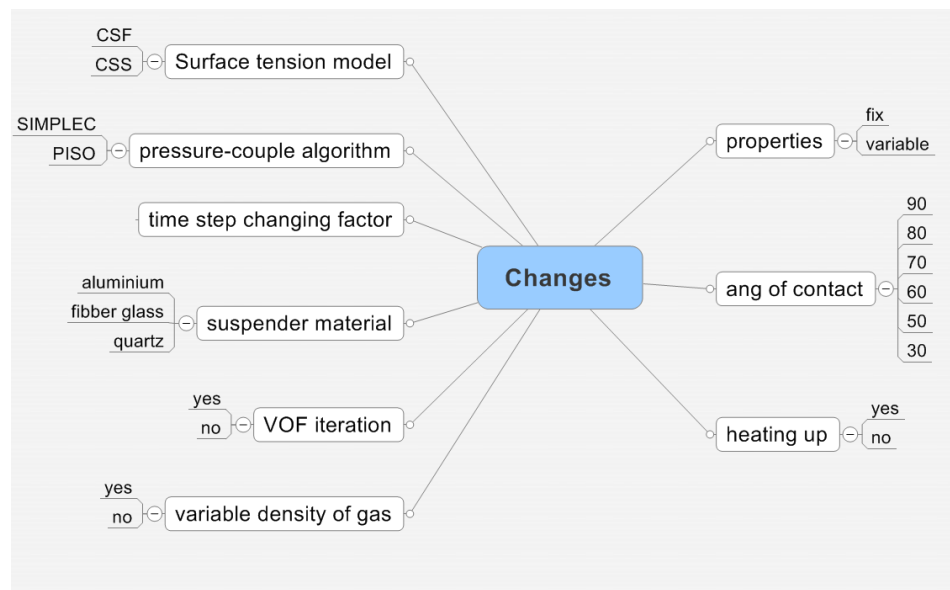


**Figure 5.2. Modifications to modelling droplets inside bearing chambers**

## 5.2 Results and discussions

### 5.2.1 Results of a single oil droplet under a convective environment

The heating and evaporation of a single droplet of PEC5 under aero-engine bearing chamber conditions was modelled. The parameters varied were the airflow velocity and the airflow temperature, to understand the effect of these parameters on droplet evaporation.

The temporal evolution of droplet diameter is presented in Figure 5.3 and Figure 5.4, where the droplet was exposed to different air temperatures and air velocities of 5 m/s and 1 m/s. Figure 5.3 shows Cases 1, 3 and 5 where the air velocity is 5 m/s and Figure 5.4 compares Cases 2, 4 and 6 with an air velocity of 1 m/s.

#### 5.2.1.1 Heating-up period

Referring to Figure 5.3 and Figure 5.4, the heating-up period for the air velocity of 5 m/s is shortest for Case 1, which is also the case with the highest temperature. The reason for this shorter heating-up period is because the heat transfer from the droplet's surface to the core is enhanced by the greater convective flow and the high air temperature. Similarly, in Figure 5.3 it can be observed that temperatures above 350 K considerably affect the oil droplet evaporation process.

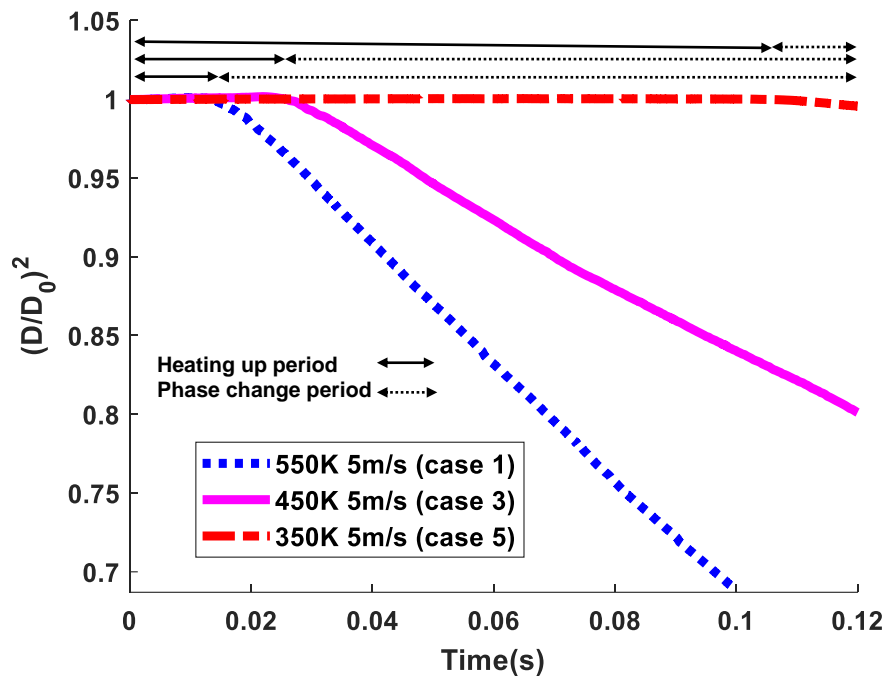


Figure 5.3. Temporal evolution of droplet diameter of PEC5 under convective airflow at 350 K, 450 K and 550 K, with an initial diameter of 200  $\mu\text{m}$  at 5 m/s

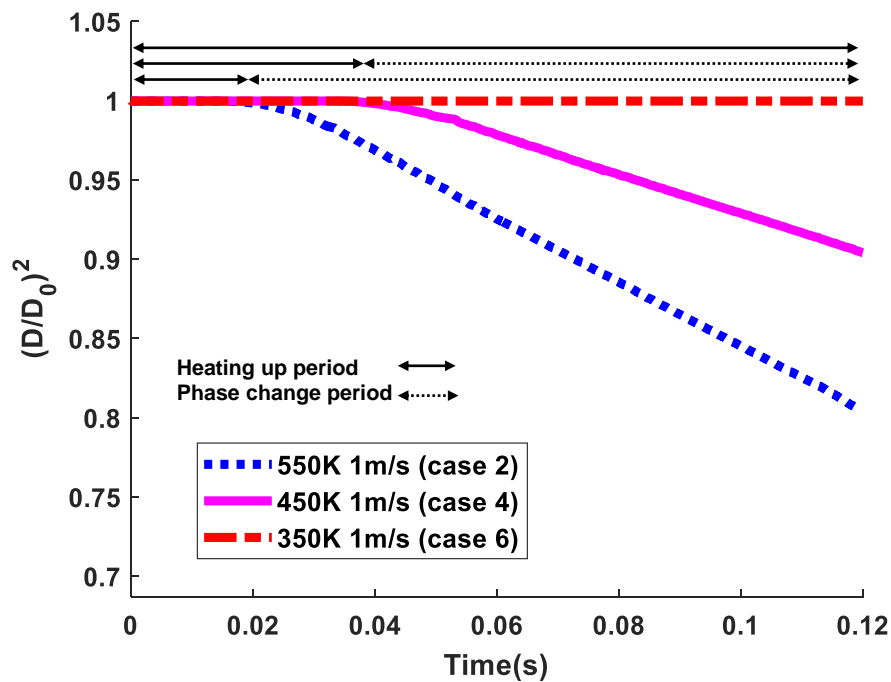


Figure 5.4. Temporal evolution of droplet diameter of PEC5 under convective airflow at 350 K, 450 K and 550 K, with an initial diameter of 200  $\mu\text{m}$  at 1 m/s

In contrast, Figure 5.4 presents Case 6, which has the longest heating-up period. This result was expected because aero-engine oils have a high boiling point to avoid evaporation at ambient temperatures, contrary to the requirements of fuels such as n-heptane, which has a boiling point of 371.53 K, and n-decane, which has a boiling point of 447.25 K. The boiling point of PEC5, which is the oil mixture base stock, is 608.85 K, as calculated from the Clausius–Clapeyron equation 3.35 with the experimental values of Razzouk et al. (2007). The boiling point of the multi-component mixture used in industrial lubricating oil is higher than PEC5 due to the additives. Therefore, modelling of a multi-component droplet is of interest for further studies, to observe the performance of the evaporation process of oil droplets in airflow with temperatures above 600 K.

The end of the heating-up period for Cases 1 and 2 is at 0.018 s and 0.019 s, respectively. Figure 5.5 shows these cases at 0.0178 s. Looking at Figure 5.5 a) and b), which show the oil vapour mass fractions, it can be seen that there is oil vapour present because the droplet's surface has reached the saturation temperature while the core is still increasing in temperature to reach this point. The oil mass fraction at the droplet's surface in Case 1 is 20% higher than for Case 2. Conversely, the oil vapour mass fraction is not present at this point in Cases 3, 4, 5 and 6 because the droplet's surface temperature is below 334 K and further time is needed to complete the heating-up period. The heating-up period is 0.027 s for Case 3 and 0.037 s for Case 4.

It is interesting to note that momentum transfer initiated by the velocity gradients between the gas and the liquid phases produces frictional forces, which form spherical vortices inside the liquid phase. This can be seen clearly in Figure 5.5 e) and f), Figure 5.6 c) and d), and Figure 5.7 c) and d). The toroidal flow is strongly related to the high air

velocities surrounding the droplet and it enhances heat and mass transfer from the surface to the core. There is a significant difference in the temperature field near the droplet for Cases 2, 4 and 6, where the air velocity is 1 m/s, compared to Cases 1, 3 and 5, where the air velocity is 5 m/s, as Figure 5.5 c) and d), Figure 5.6 a) and b), and Figure 5.7 a) and b) reveal.

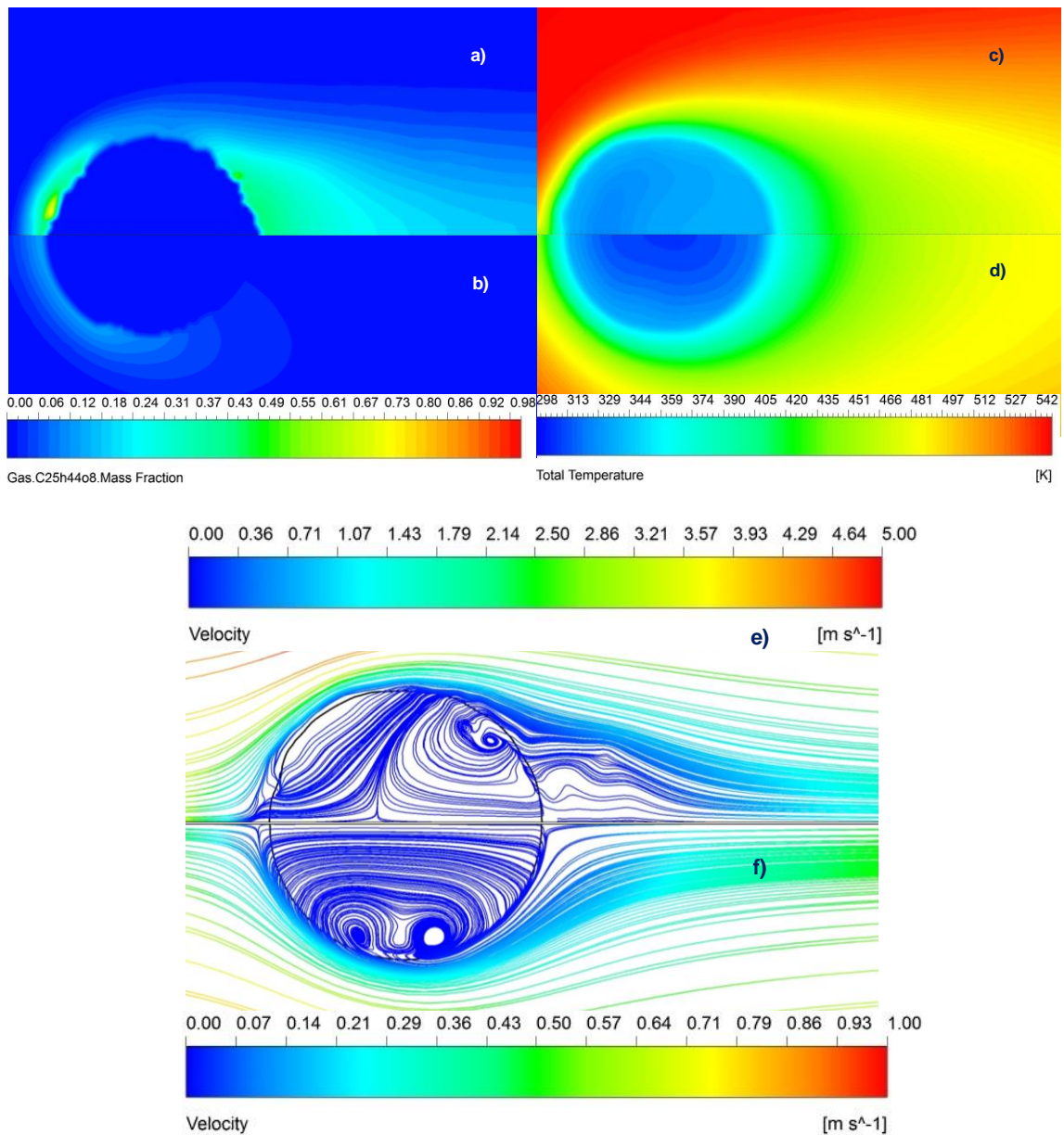


**Figure 5.5. Contours at 0.017 s of oil vapour mass fraction: a) Case 1, b) Case 2; temperature: c) Case 1, d) Case 2; velocity streamlines: e) Case 1, f) Case 2**

In addition, in all cases, the temperature distribution inside the droplet follows the pattern of the droplet's internal flow. The main vorticity for all cases is located from  $0.34 y/D$  to  $0.46 y/D$  along the radial direction, which means that the vorticity area is nearer to the surface than the core. Case 2 is interesting in that there are two main vortices (see Figure 5.5 f)). The main division of these two vortices is located at  $0.17 x/D$  and, following out from this division to the droplet's surface, it can be seen in Figure 5.5 b) that there is enhanced mass transfer from the liquid phase to the gas phase in this region. The vorticity affects heat distribution within the droplet, with low-velocity regions (vortex centres) being areas of reduced internal heat transfer.

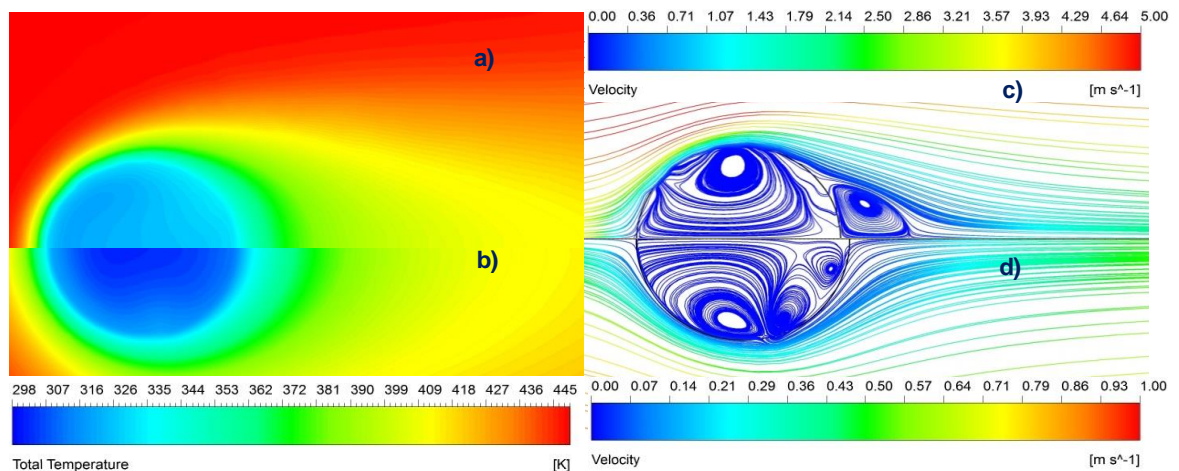


**Figure 5.6. Contours at 0.017 s of temperature: a) Case 3, b) Case 4; velocity streamlines: c) Case 3, d) Case 4**

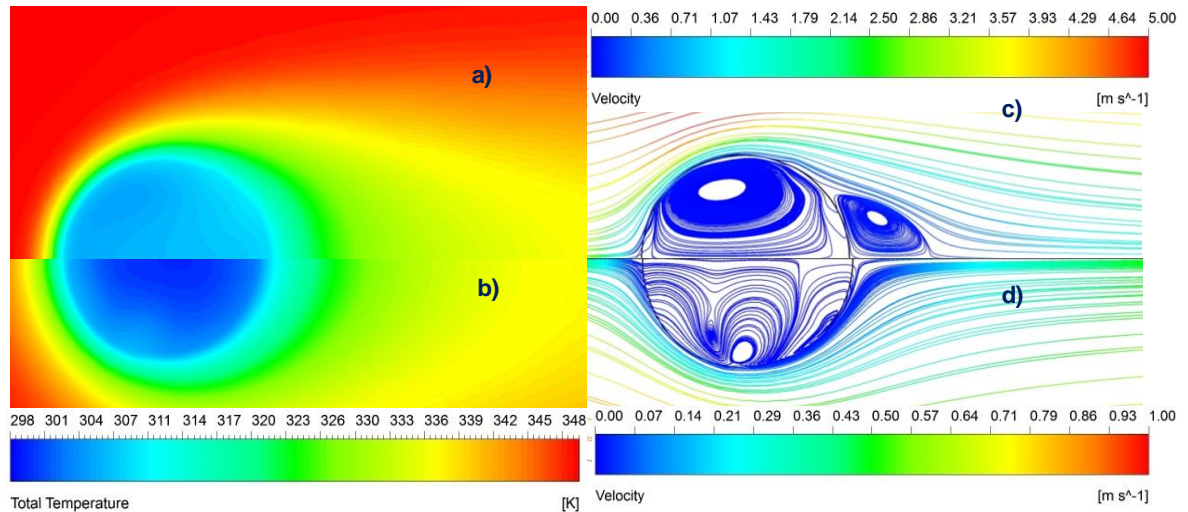


**Figure 5.7. Contours at 0.017 s of temperature: a) Case 5, b) Case 6; velocity streamlines: c) Case 5, d) Case 6**

### 5.2.1.2 Phase-change period

The instantaneous droplet diameter was normalised with the initial droplet diameter. The droplet diameter ratio is squared and, according to the  $D^2$ -law, this ratio presents a linear regression versus time after the initial heating-up period. This is observed in Figure 5.3 and Figure 5.4 and corresponds to the phase-change period. A higher evaporation rate is present in Case 1, where there is a steep gradient of droplet size reduction. Thus, in this case, the droplet's lifetime under high air temperature and high-velocity conditions is shorter than the other cases. This effect can be observed in Figure 5.9, where the droplet in Case 1 showed a diameter reduction of around 10% compared with Case 2. However, Case 6 at 0.1 s is still in the heating-up process, as Figure 5.4 shows.

Figure 5.9 and Figure 5.10 show the contours of oil vapour mass fraction, temperature and velocity streamlines for all cases at 0.09 s. At this stage, the droplet is at the phase-change period, except for Cases 5 and 6. Consequently, for Cases 5 and 6 there is no oil vapour present at the droplet's surface and the temperature continues increasing

until saturation. Nevertheless, the maximum oil vapour mass fraction of Case 1 is 10% higher than that of Case 2, as can be observed in Figure 5.9 a) and b).

Cases 3 and 4 present a similar oil vapour mass fraction, with a maximum of 80% of oil vapour at the droplet's surface. The difference between Cases 3 and 4 is the position of the maximum vapour mass fraction, which for Case 3 is at the top of the droplet but for Case 4 it is at the front part of the droplet, as Figure 5.10 a) and b) show, respectively. Additionally, the contours of oil vapour mass fraction show that there is a formation of bubbles inside the liquid phase. The bubbles are formed by oil vapour, as observed in Figure 5.9 a) for Case 1, Figure 5.9 b) for Case 2 and Figure 5.10 a) and b) for Cases 3 and 4, respectively.

Figure 5.9 e) and f) show that the formation of gas bubbles inside the droplet favours the internal flow and the formation of internal vortices, which are different to the flow pattern presented during the heating-up period (Figure 5.6 c)). These small vortices are observed around and inside the bubbles, as Figure 5.9 e) and f) show for Cases 1 and 2, respectively, and Figure 5.10 e) and f) show for Cases 3 and 4, respectively. Thus, it is noticed that there is heat and mass transfer between the internal bubbles and the liquid phase.

Previously, the formation of bubbles has been observed experimentally in the study of the evaporation of multi-component fuel droplets at low ambient pressure where the bubble absorbs heat from the droplet (Ghassemi et al., 2006). According to the literature, there are two scenarios in the growth and collapse of the bubble. In the first scenario, the bubble remains trapped inside the liquid phase due to surface tension and keeps growing before collapsing due heat absorption finish (Ghassemi et al., 2006, Wang et al., 2018). In

the second scenario, the bubble grows because it coalesces with other bubbles until it collapses due to the high internal circulation inside the droplet (Zhang et al., 2018, Shinjo et al., 2014, Rao et al., 2018).

After the bubble collapses, there is the formation of secondary droplets, as can be seen in Figure 5.9 c). The bubble collapse can cause a droplet to break up and this can disintegrate the droplet either completely or incompletely. When the droplet is disintegrated completely into many secondary droplets, this is called a micro-explosion and a partial break-up of the parent droplet is called puffing (Zhang et al., 2018, Shinjo et al., 2014). The puffing phenomena is observed in this research, as shown in Figure 5.9. The puffing and micro-explosion processes are consequence of the bubble rupture process.

The bubble rupture process starts with the bubble formation and growth; once the bubble collapses, there is a cavity formation. Cavity formation is due to the release of vapour from the bubble; this cavity generates instability and the droplet's inertial forces form a ligament. This ligament might break-up forming secondary droplets, as observed in Figure 5.8 (Avulapati et al., 2016). There are two types of ligament break-up: the ligament tip break-up and the ligament tip-base break-up. These mechanisms depend on the ligament aspect ratio, which consists of the ligament length versus the ligament diameter (Avulapati et al., 2016).

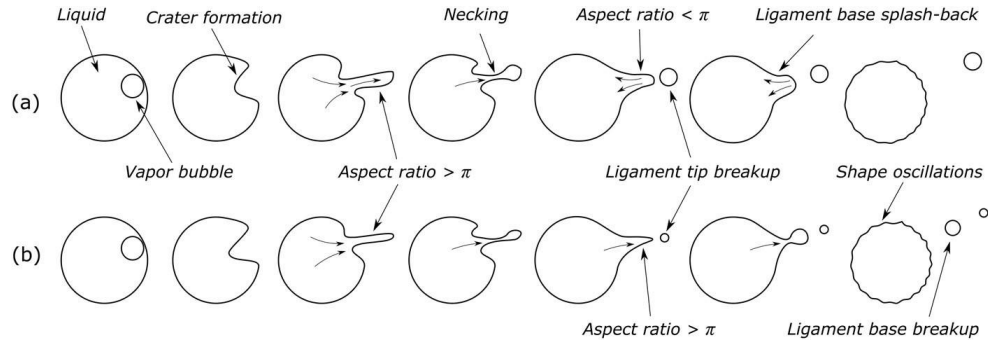


Figure 5.8. Bubble rupture process and ligament formation (Avulapati et al., 2016)

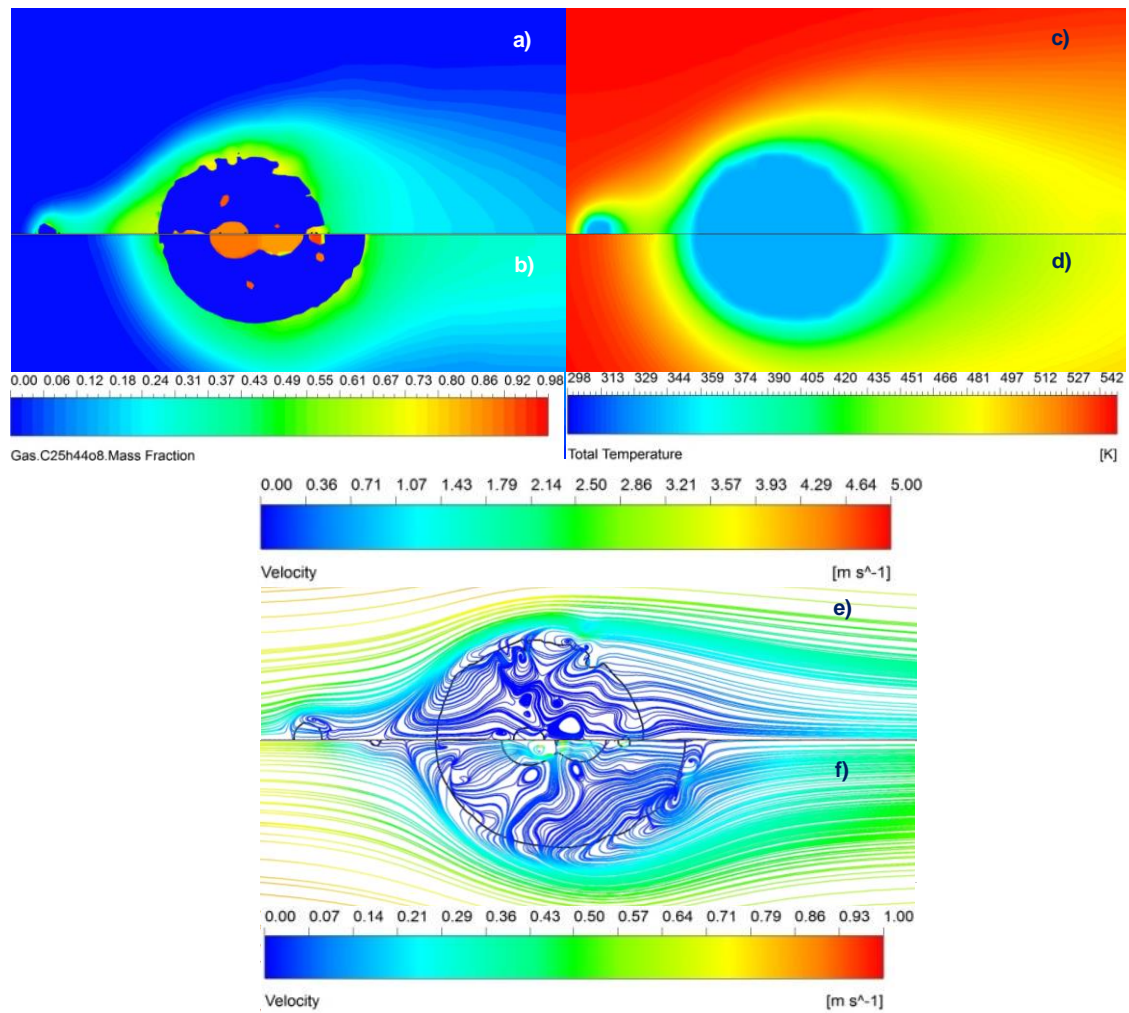
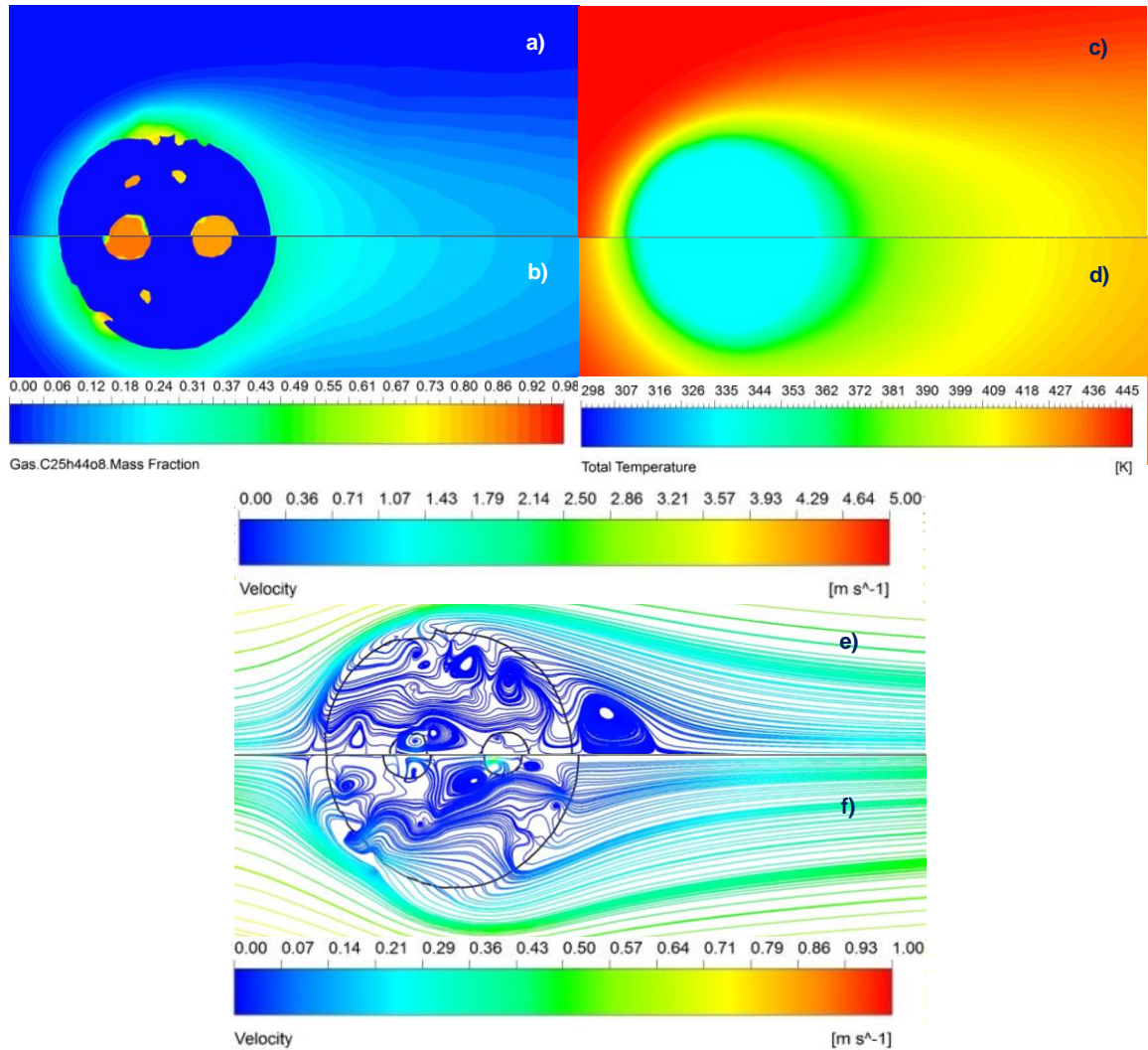


Figure 5.9. Contours at 0.09 s of oil vapour mass fraction: a) Case 1, b) Case 2; temperature: c) Case 1, d) Case 2; velocity streamlines: e) Case 1, f) Case 2



**Figure 5.10. Contours at 0.09 s of oil vapour mass fraction: a) Case 3, b) Case 4; temperature: c) Case 3, d) Case 4; velocity streamlines: e) Case 3, f) Case 4**

The temperature gradients between the droplet's surface and interior for Cases 5 and 6 are shown in Figure 5.11. It can clearly be seen in Figure 5.11 a) that the cold region of the droplet is displaced to the front part of the droplet and this corresponds to the position at which the formation of the main vortex of Case 5 occurs (Figure 5.12 c)). Here, the droplet's surface temperature is 1 K below the saturation point and this suggests that the droplet's surface might evaporate soon. The cold part facing the rear of the droplet with a

temperature of 319 K while the droplet's surface has a value of 326 K can be seen for Case 6 in Figure 5.11 b).

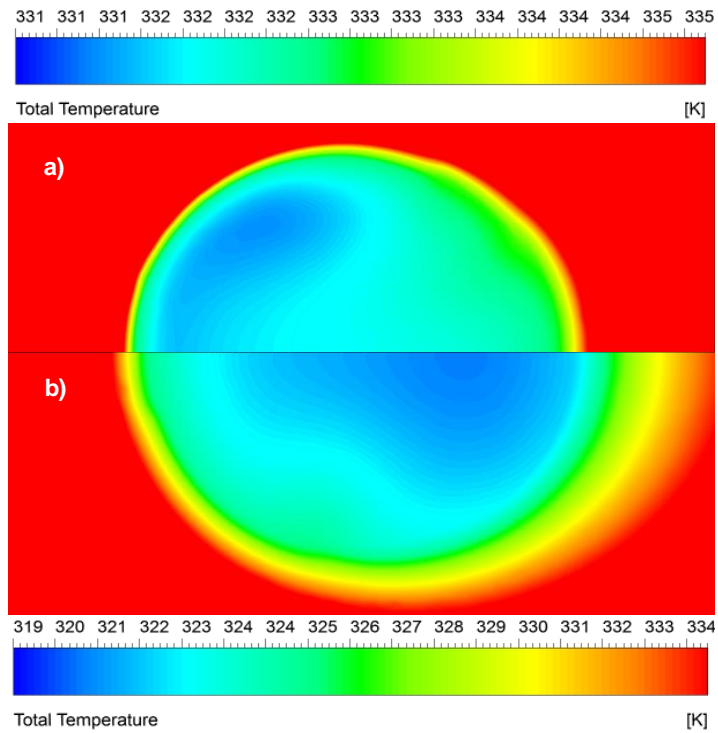


**Figure 5.11. Contours of temperature of the droplet's interior at 0.09 s: a) Case 5, b) Case 6**

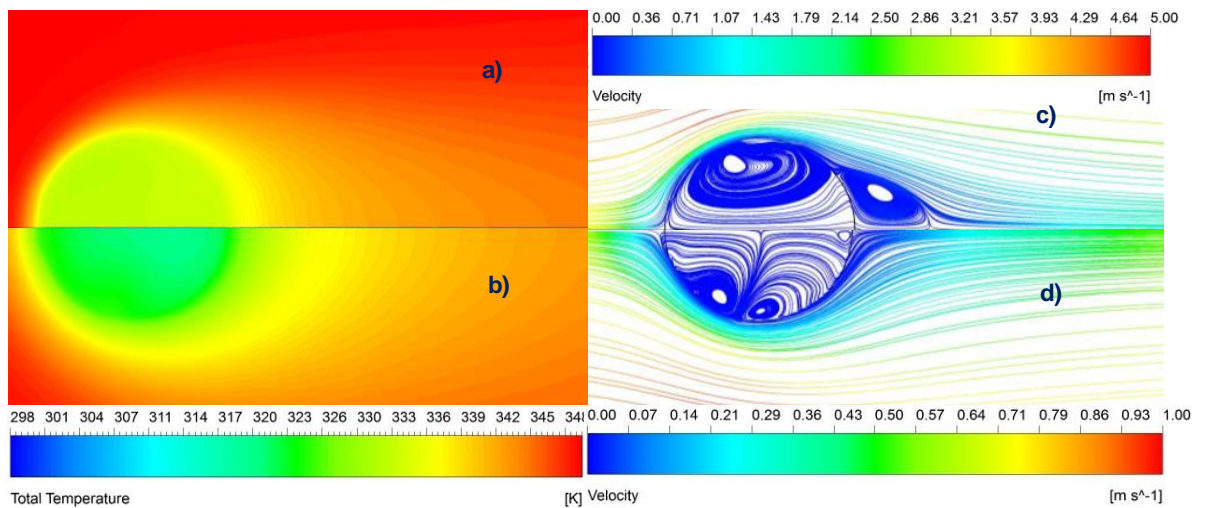


**Figure 5.12. Contours at 0.09 s of temperature: a) Case 5, b) Case 6; velocity streamlines: c) Case 5, d) Case 6**

These effects were observed in previous droplet evaporation analysis (Abramzon and Sirignano, 1989), where the heat transfer by the droplet's internal flow is dominant over the heat transfer by conduction at the later stages of the heating-up process.

Two vortices are observed for Case 6 at 0.09 s and they join at the top part of the droplet where it might start to evaporate (Figure 5.12 d)). Furthermore, a vortex is observed at the rear part of the droplet in the high convection cases. This recirculation may enhance the evaporation process and the vortex is usually observed in droplets held under intermediate Reynolds numbers (Clift et al., 2005).

Altogether, considering that high-velocity airflow enhances the droplet's internal circulation, heat and mass transfer and consequently the evaporation rate, it might be said that for air velocities above 5 m/s and droplets with a diameter around 200  $\mu\text{m}$ , it is expected that over 5% of the oil-liquid mass might have evaporated at 0.017 s. It can be suggested that this is likely to happen in core flow regions in bearing chambers as the droplets travel from the bearings to the wall at typical velocities of 5 m/s to 35 m/s (Chen et al., 2011a, Sun et al., 2016b). Additionally, the droplets that are travelling with the core flow have a range of velocities from 1 m/s to 16 m/s (Sun et al., 2016b). Moreover, from previous investigations it is known that inside bearing chambers the core air velocity increases with rotational speed (Aidarinis et al., 2011, Gorse et al., 2003), and the droplet's velocity and formation from the bearings are also a function of rotational speed (Gorse et al., 2005). With this in mind and taking into account the velocities and bearing chamber geometry reported previously (Chen et al., 2011a, Sun et al., 2016b), it is observed that the journey duration from the bearings to the bearing chamber walls of droplets with a

diameter of 200  $\mu\text{m}$  can vary from 0.001 s to 0.003 s, depending on the droplet and air velocities, which is reported in Section 8.6.

Therefore, we suggest that there might be more droplet evaporation and greater oil vapour flow with a higher rotational speed. However, with a higher shaft rotational speed, the droplets' journey from the bearings to the walls might be shorter for diameters above 200  $\mu\text{m}$  and droplets with diameters less than 100  $\mu\text{m}$  can keep travelling with the airflow (Chen et al., 2014, Glahn et al., 2000, Sun et al., 2016b). Furthermore, based on the  $D^2$ -law, it is possible to predict the droplet's lifetime from the linear equation of Figure 5.3 and Figure 5.4. Therefore, the droplets' lifetimes are presented in

Table 5.1, which shows that the shortest droplet lifetime is for Case 1 at 0.3 s.

Thus, the droplets that recirculate with the airflow for more than 0.3 s might evaporate completely, in contrast to the droplets that travel from the bearings to the walls. Regarding this, further investigation is needed to compute the lifetime of droplets with a diameter  $<200$   $\mu\text{m}$  travelling in the recirculation zones, which are more prone to generating higher vapour concentrations (Rosenlieb, 1978).

It is reported that the  $D^2$ -law can accurately model droplet vaporisation up to 700 K for an n-decane droplet under gravity and microgravity conditions (Chauveau et al., 2011). Therefore, the  $D^2$ -law is suitable to predict the evaporation rate for the conditions applied in this study. Moreover, it was noticed that for airflow temperatures  $>700$  K the  $D^2$ -law can accurately predict the droplet evaporation process if the model includes thermal expansion due to density variation during the heating-up period (Abou Al-Sood and Birouk, 2007); otherwise, the evaporation rate may be underestimated (Nayagam et al.,

2018). Given these points, this study provides the basis and best practices to model oil droplet evaporation, assuming constant thermophysical properties.

### **5.2.2 Analysis with an adaptive mesh refinement**

It was noticed that after 0.1 s the droplet would not remain in the same location even with an MFR technique. The reason for this is that the MFR velocity is associated with the evaporation rate and this rate is computed from the slope of the straight line shown in Figure 5.3 and Figure 5.4. However, as observed in Figure 5.9 and Figure 5.10, there are bubbles forming inside the droplet. These bubbles escape from the liquid phase and can be formed again at a later time. Thus, the pattern of the droplet's diameter reduction does not follow a straight line in practice. On account of this, it was observed that the droplet moves away from the mesh refinement zone. This is not an optimum condition to analyse the evaporation process and therefore a dynamic adaptive mesh refinement (AMR) technique has been applied.

The AMR technique allows us to follow the droplet's interface with a different refinement than the droplet's surroundings, as well as to follow the small particles of liquid detached from the droplet's surface due to the evaporation process. The AMR allows a refined mesh at the interface, while the droplet vicinity is discretised with a coarse mesh (ANSYS, 2016b).

The mesh adaption approach used in this analysis is based on tracking the gradient of the liquid volume fraction with a "Coarsen Threshold" and "Refine Threshold" (see FLUENT manual) of 0.05 and 0.01, respectively. These thresholds were chosen according to the volume iso-surface variation to surround the liquid interface with a finer mesh and the gas phase marked for coarsening.

It is important to stabilise the numerical case before mesh adaption is switched on. This ensures that the progression of the solution runs with higher time steps; otherwise if the adaption is applied too early, the solution takes longer to stabilise, the time steps will be short and the solution will be more expensive in terms of computational time. This is viable for our case because the initial state corresponds to the heating-up period when there is no mass fraction of oil vapour. This facilitates the stabilisation process, keeping a long dynamic adaption interval for the first 1000 time steps. The initial dynamic adaption interval was 100. After the stabilisation, the dynamic adaption interval should be changed to 2 for all cases in order to correctly catch the evaporation process.

The gradient adaption approach is based on the Euclidean norm of the gradient of the selected function and, in this case, the function is the volume fraction which is observed as follows (ANSYS, 2016b):

$$|e_{i1}| = (A_{cell})^{\frac{g_w}{2}} |\nabla f| \quad 5.1$$

where  $e_{i1}$  is the error indicator,  $g_w$  is the gradient volume weight and  $\nabla f$  is the Euclidian norm of the gradient of the desired field variable. In equation 5.1, the adaption is based on gradients, which needs a memory allocation in the same way as the interfacial mass transfer calculation in equation 3.22. Therefore, it is important to disable the option of “keep temporary solver memory” because this is not compatible with the gradient adaption meshing approach. Furthermore, the allocation of the new mesh gradients needs to free the memory of the UDF to compute the interfacial mass transfer.

The mesh has four refinement levels where each size becomes finer as it is approaches the interface, as can be observed in Figure 5.13.

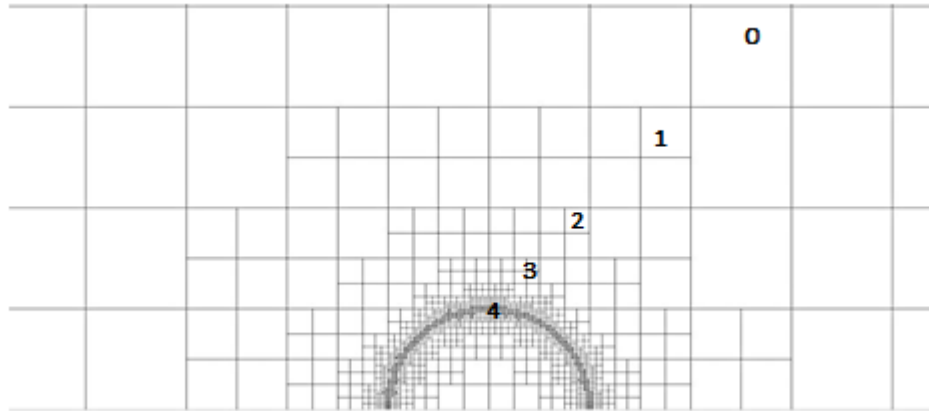


**Figure 5.13. Levels of refinement with the gradient adaptive meshing approach**

The mesh refinement will adapt all the volume fraction interface gradients and with this the mesh can follow all the small droplets that are detached due to the evaporation process, as shown in Figure 5.14. Figure 5.14 a) presents the mesh refinement at 0.0017 s for Case 7, while Figure 5.14 b) shows how the mesh refinements are adapting according to the quantity of liquid or gas in the domain.

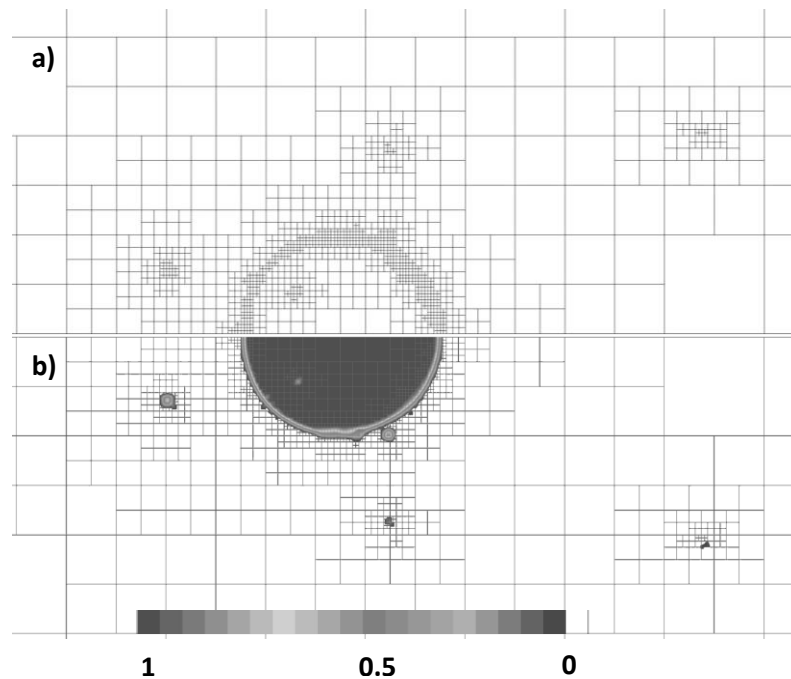


**Figure 5.14. Gradient adaptive meshing approach after 0.0017 s in Case 7: a) levels of refinement, b) mesh refinement with volume fraction contours**

Each refinement section was restricted to a minimum cell area of  $4e-12 \text{ m}^2$  and the cell was not refined if the area is less than this threshold value (ANSYS, 2016c).

The adaptive mesh approach was used to analyse the effects of different parameters on the evaporation process, in a similar fashion to the study performed for non-adaptive mesh. The parametric study with a non-adaptive mesh presented the effects of different gas flow temperatures and velocities. However, it was difficult to capture the effect of the diameter variation because for droplets with diameters less than  $50 \text{ }\mu\text{m}$ , they move faster than the reference frame movement (as can be observed in Figure 5.1). This means that the droplet moves out of the refinement region. Thus, for good droplet tracking, it is recommended to use the adaptive meshing technique coupled with the MFR. Otherwise, if the MFR is not implemented, a long domain is needed and this vastly increases the computational cost.

Consequently, the adaptive meshing approach allows tracking of the effects of changes in the droplet's diameter on the evaporation process. Hence, the cases analysed with the AMR approach are presented in Table 5.2.

**Table 5.2. Cases analysed with adaptive mesh refinement**

Case	Air				
	$D_0$ [ $\mu\text{m}$ ]	T [K]	$u$ [m/s]	Re	Droplet lifetime [s]
1	200	550	5	68	0.3
2			1	14	0.6
3		450	5	68	0.4
4			1	14	1.0
5	100	350	5	68	5.8
6			1	14	9.8
7	500	550	5	34.23	0.146
8	500	550	5	171.15	4.8

A comparison of the temporal evolution of droplet diameter for Case 1 is presented in Figure 5.15 a) for a non-adaptive mesh and b) for an adaptive mesh. The intercept should be  $4e-8$ , which is the squared diameter. Thus, it can be seen that the closest intercept is for the computation with the adaptive mesh. This might be because this analysis was performed with a finer mesh at the droplet's interface. The linear equation predicts that the lifetime for Case 1 with the non-adaptive mesh is 0.3 s; however, for the calculation with the adaptive mesh, the droplet lifetime is 0.4 s.

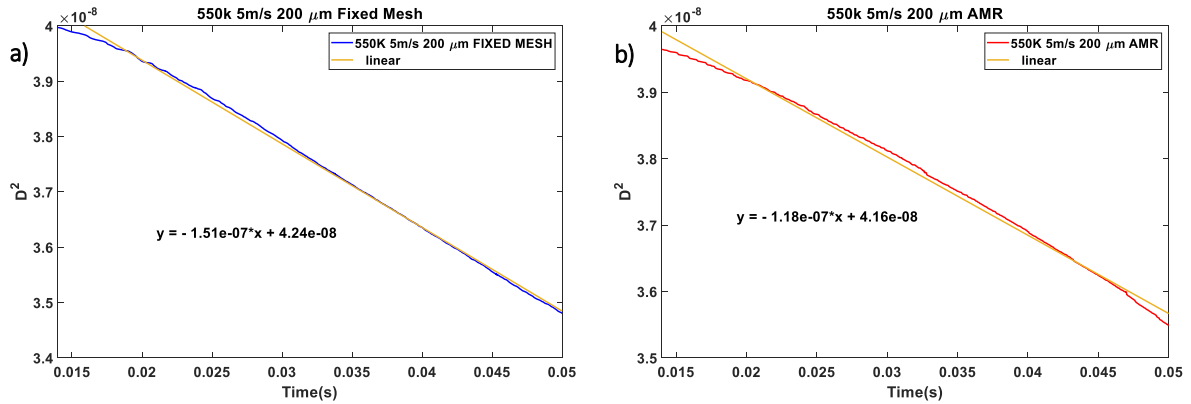


**Figure 5.15. Comparison of temporal evolution of droplet diameter computed with a) non-adaptive mesh and b) adaptive mesh**

It can be noted that both analyses are similar; however, the adaptive mesh allows the capture at the interface even if the droplet presents break-up. The mesh refinement at the interface for both analyses can be observed in Figure 5.16.

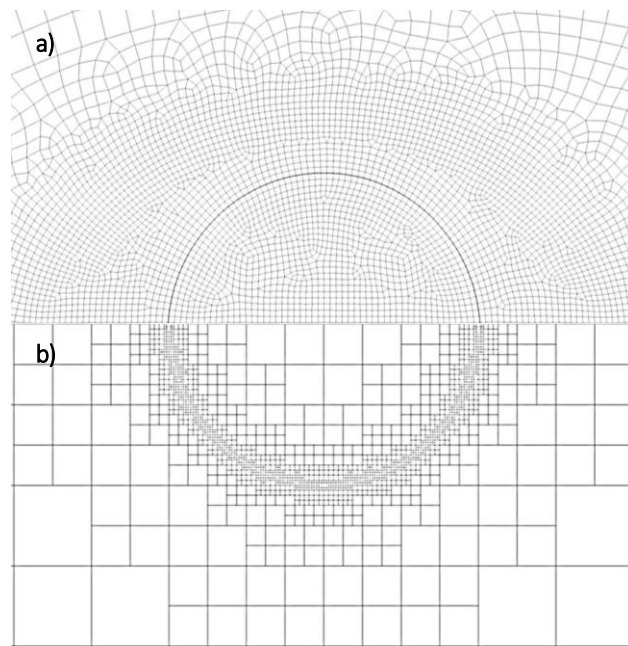


**Figure 5.16. Comparison of a) non-adaptive mesh and b) adaptive mesh at the droplet's interface**

Following the advantages using the adaptive mesh mentioned above, a parametrical study was conducted to analyse the change on the droplet evaporation rate when varying

the initial droplet diameter, the ambient temperature, the air velocity and a radiative environment.

### 5.2.3 Effect of varying initial droplet diameter

#### 5.2.3.1 Effect of varying initial droplet diameter on evaporation rate

The initial droplet diameter was varied to observe the evaporation rate under convective flow, keeping the same ambient conditions for all cases. The inlet velocity was fixed at 5 m/s with an air temperature of 550 K for all cases. Three different diameters were analysed, namely 100  $\mu\text{m}$ , 200  $\mu\text{m}$  and 500  $\mu\text{m}$ , which are the sizes that can be found in the bearing chamber core region, either travelling from the bearings to the walls or recirculating in the core flow as discussed in Section 2.1.

The droplets with smaller sizes tend to present higher evaporation rates because they have a greater surface area exposed to the surrounding environment per volume portion, as observed in Table 5.3. Figure 5.17 shows the average evaporation rate per surface area, where this rate for different ranges of droplet size can be estimated and approximated from a linear regression.

**Table 5.3. Comparison of initial droplet diameters, evaporation rates and surface area per volume ratios**

$D_0$ [ $\mu\text{m}$ ]	Average evaporation rate [ $\text{kg}/\text{m}^2\cdot\text{s}$ ]	A [ $\text{m}^2$ ]	V [ $\text{m}^3$ ]	A/V [ $\text{m}^{-1}$ ]
100	0.2	3.14159E-08	5.23599E-13	60,000
200	0.155	1.25664E-07	4.18879E-12	30,000
500	0.0174	7.85398E-07	6.54498E-11	12,000

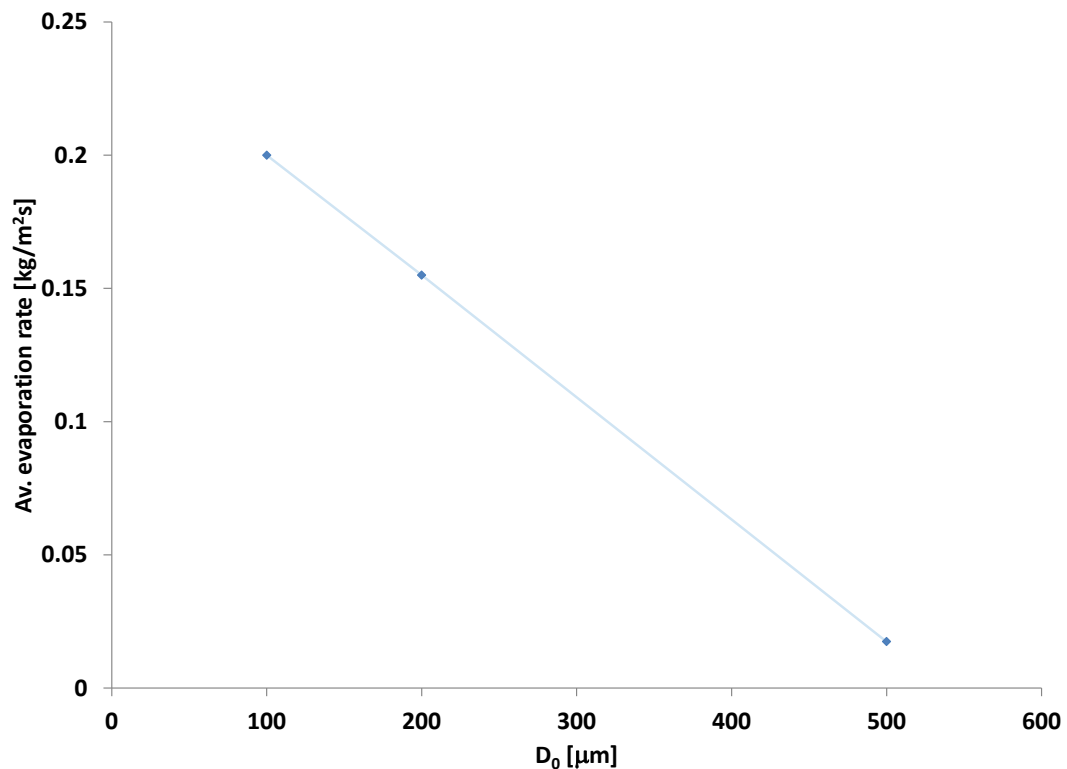


**Figure 5.17. Comparison of initial droplet diameter versus average evaporation rate per surface area**

The results of these three cases show that the evaporation rate tends to increase with the reduction of initial droplet diameter, as can be seen in Figure 5.18.

Figure 5.18 shows the temporal evolution of the non-dimensional squared diameter for the three cases mentioned above and reveals that the heating-up period is reduced for smaller droplet sizes.

Figure 5.19 shows the variation of the evaporation rate over the droplet's surface area for the same cases mentioned above. The data presents an oscillatory performance which was fitted, with a moving average regression with a range of 32 values, to compare the trending of each case. The time was normalised with the initial evaporation time to compare the evaporation rates of each case as in Figure 5.19.

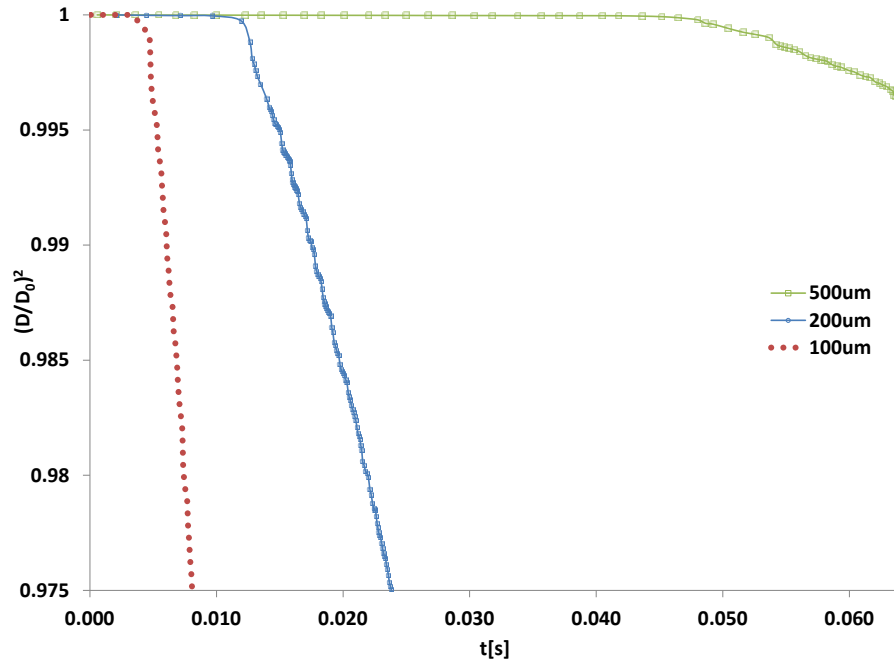


Figure 5.18. Non-dimensional squared diameter evolution for different initial droplet diameters, with air at 5 m/s and 550 K

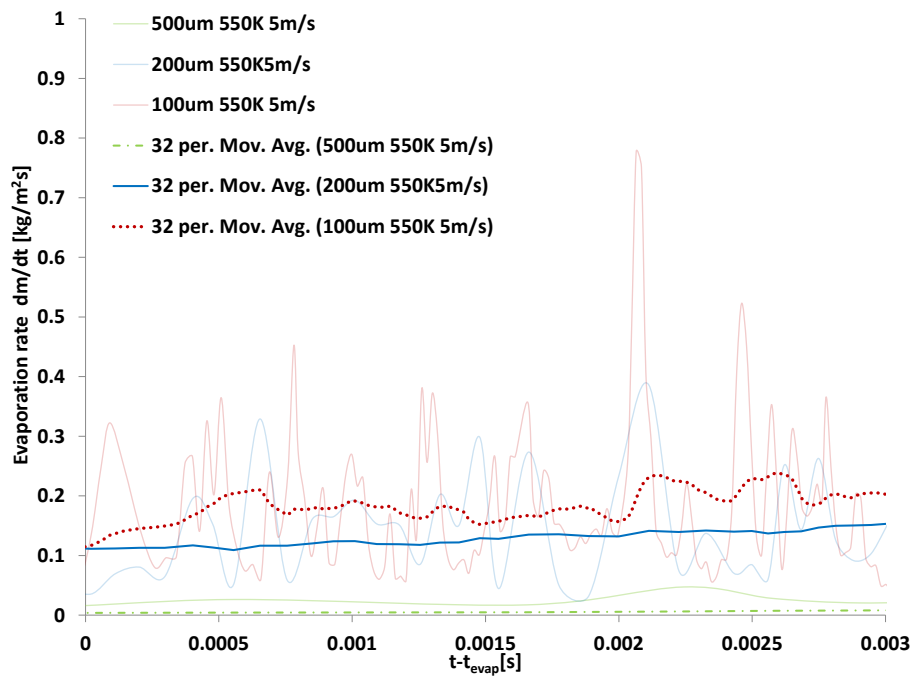


Figure 5.19. Variation of evaporation rate over droplet surface area for different initial droplet diameters

In Figure 5.19, it is shown from the average evaporation rates that the case with an initial droplet diameter of 100  $\mu\text{m}$  is 22% higher than the case with an initial diameter of 200  $\mu\text{m}$  and 91% higher than the case with an initial diameter of 500  $\mu\text{m}$ . The oscillatory performance of the average evaporation rate might be due to bubble collapse and the formation of secondary droplets.

### 5.2.3.2 *Effect of varying initial droplet diameter on heat transfer at the droplet's surface*

The heat transfer from the environment to the droplet's surface was analysed to predict the effect of the initial droplet diameter. Heat is transferred from the exterior to the droplet's surface and from this surface to the core by convection, as given by:

$$Q_g = h_g(T_g - T_s) \quad 5.2$$

$$Q_l = h_l(T_s - T_{int}) \quad 5.3$$

The heat transfer mechanism from the droplet's surface to the core can be considered to be convective since there is a presence of internal circulation, as shown in Figure 5.6. According to (Abramzon and Sirignano, 1989, Aggarwal et al., 1984), this internal circulation can be treated as a convective flow and can be approximated by the Hill's vortex model.

As the droplet's surface is a boundary with no thickness (see Figure 4.8), the heat flux from the environment to the surface and from the surface to the droplet core is the same ( $Q_g = Q_l$ ); therefore, the heat transfer ratio is given by:

$$\frac{h_l}{h_g} = \frac{T_s - T_{int}}{T_g - T_s} \quad 5.4$$

Figure 5.20 indicates that heat transfer from the droplet's surface to the core has a similar trend for all cases, which increases gradually to a peak value when the evaporation starts. After the curve reaches the peak, the droplet's internal temperature gradient decreases towards zero when the droplet's core reaches the saturation temperature. The case with  $D_0$  at 100  $\mu\text{m}$  presents the greatest heat transfer, which corresponds to 7% of the total heat flux.

Therefore, the heat transfer coefficient ratio indicates that during the heating-up period, the maximum heat transfer ratio from the droplet's surface to the core can increase by 1% with the reduction of the initial droplet diameter.

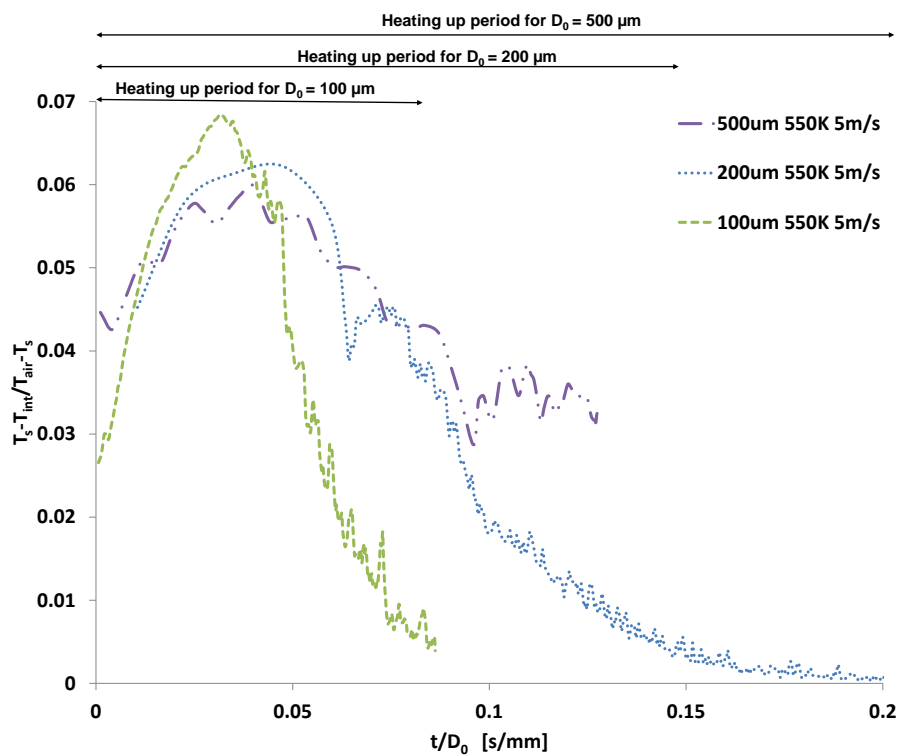


**Figure 5.20. Heat transfer ratio varying the initial droplet diameter, with air at 550 K and 5 m/s**

### ***5.2.3.3 Effect of varying initial droplet diameter on internal circulation***

Previous studies have analysed the evaporation rate of droplets and noted that, apart from diffusion, there is another important mechanism to consider when accurately calculating the evaporation rate, which is the internal circulation. The droplet's internal circulation might depend on the shear forces at the droplet's surface, the variation of temperature, the variation of the surface tension (Mandal and Bakshi, 2012) and the difference in viscosity between two fluids (Mohammadi et al., 2016). The difference in viscosity might be between two fluids in the liquid phase or one fluid in the liquid phase and other in the gas phase. In this research the difference in viscosity is between the gas and liquid phases at the droplet's interface, which creates the shear forces (Bergeles et al., 2018). Convection due to surface tension is known as Marangoni convection, where the surface tension might change due to differences in temperature and concentration; however, in this research the effects of Marangoni convection are excluded.

Therefore, in this analysis the internal circulation is dominated by the shear forces around the interface and the temperature at the droplet's surface, which enhances and controls the evaporation rate (Prakash and Sirignano, 1978). The droplet's internal motion presents three main regimes, namely spherical vortex, internal wake and the liquid boundary layer, as can be observed in Figure 5.21.

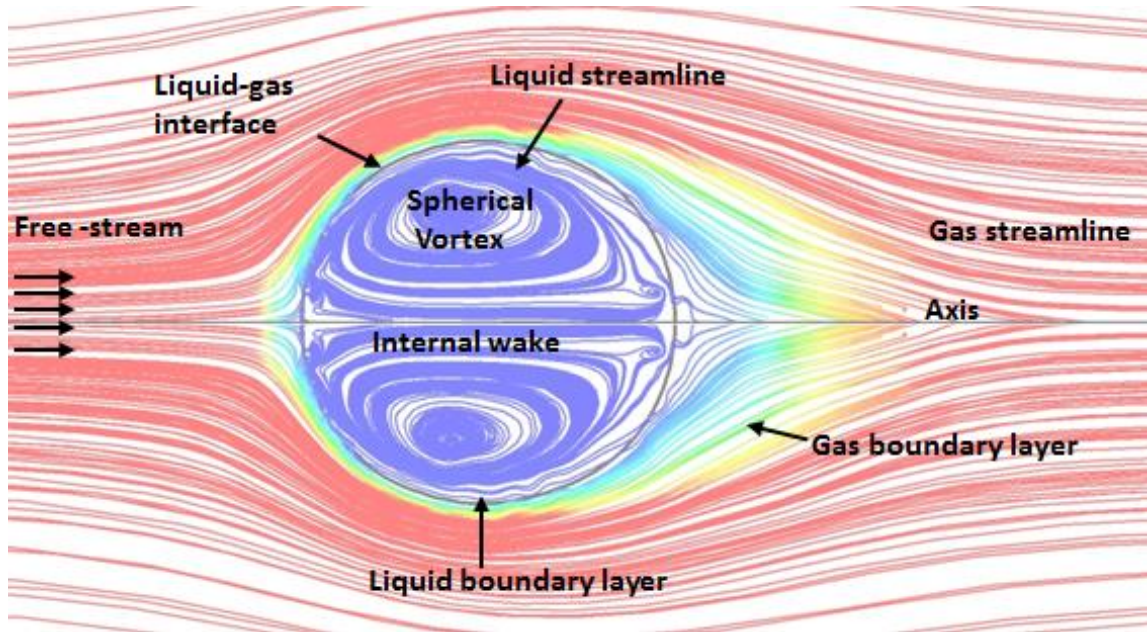


**Figure 5.21. Axisymmetric flow field of the internal circulation of a vaporising droplet; schematic reproduced for a droplet with initial diameter of 100  $\mu\text{m}$ , at 550 K and 5 m/s (adapted from Sirignano, 2010)**

Figure 5.21 shows the streamlines of the internal circulation of a droplet immersed in a convective flow at 550 K and 5 m/s with an initial diameter of 100  $\mu\text{m}$ , as well as the flow pattern that is similar to the one described by Sirignano (2010) and presents the Hill's spherical vortex (Hill, 1894, Scase and Terry, 2018).

The internal circulation is quantified by measuring the average of the velocity magnitude, which was calculated at the droplet's interior through a surface created within the VOF range from 0.8 to 1 to make sure that the region of interest was liquid. Figure 5.22 shows the region selected to compute the liquid phase just before the droplet's interface, which is the line at  $\text{VOF} = 1$ .

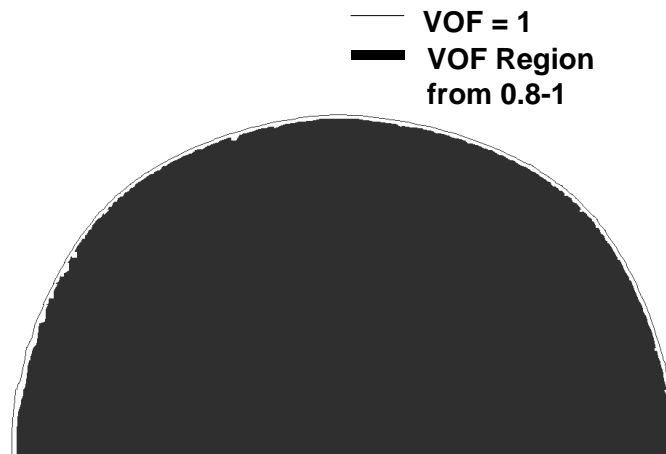


**Figure 5.22. Region of interest to compute the average velocity magnitude at the droplet's interior**

It is expected that the internal velocity presents fluctuations due to the temperature variation along the droplet's interior. This is in addition to the effect of the shear stresses around the droplet's surface due to convective airflow, which removes the vapour and allows the circulation of air at the interface (Mandal and Bakshi, 2012, Kumar et al., 2018). Figure 5.23 shows the oscillations of the oil vapour around the droplet's interface due to the effect of the air which removes this vapour.

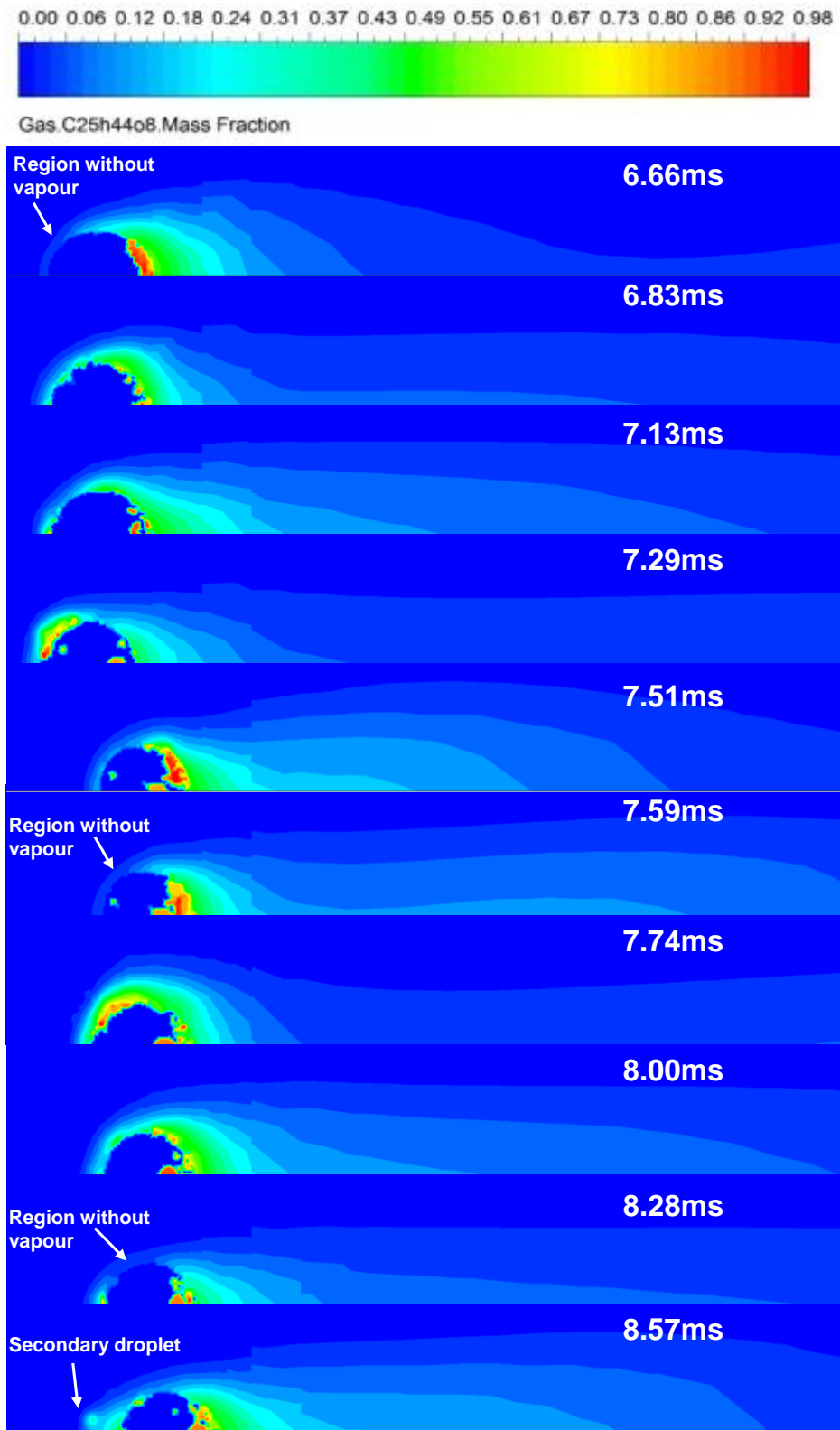


Figure 5.23. Oscillation of oil vapour mass fraction around the droplet's interface.

$$D_0 = 100 \mu\text{m}, T = 550 \text{ K}, V_{\text{air}} = 5 \text{ m/s}$$

Oil vapour removal is common at the front of the droplet, thereby increasing the oil vapour at the rear part of the droplet. In addition, the internal circulation is affected by the oil vapour produced by the secondary droplet formed by the evaporation process, as observed at 0.00857 s in Figure 5.23; therefore, it is expected that the droplet's internal velocity presents oscillations.

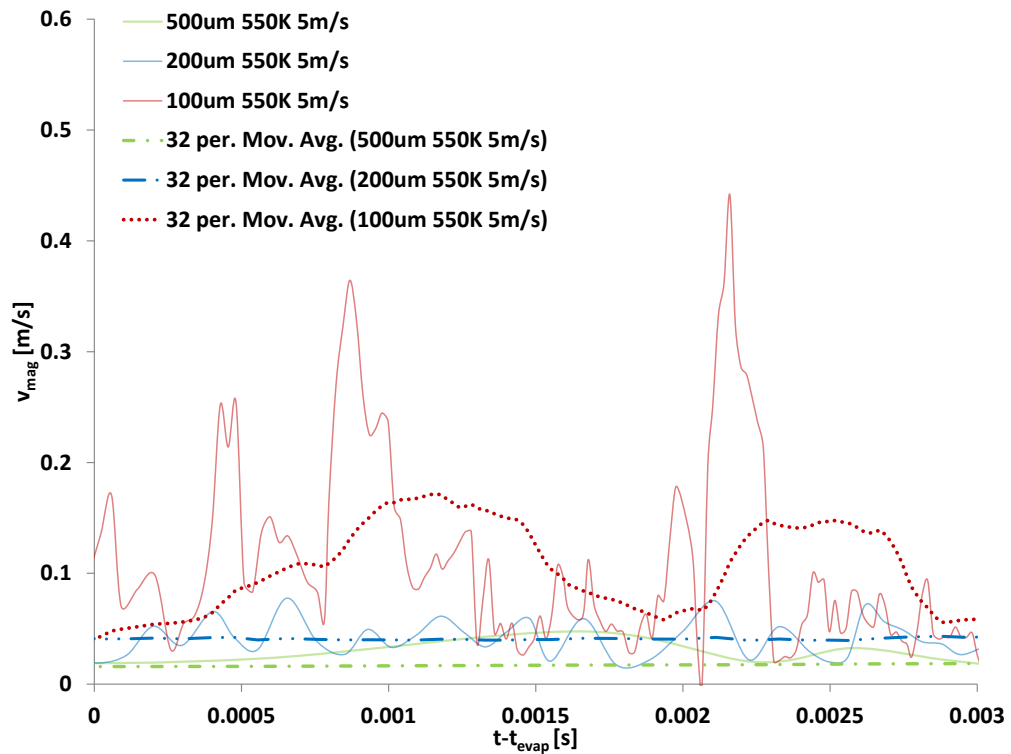
#### *5.2.3.3.1 Quantitative analysis of the effect of varying initial droplet diameter on internal circulation*

Figure 5.24 shows the oscillations of the droplet's internal velocity, which was fitted, with a moving average regression with a range of 32 values, to compare the three cases with different initial droplet diameters. This method was considered before comparing the oscillatory performance of droplets of various fuels from low to high volatility, where it was concluded that the evaporation rate enhances the internal circulation and the oscillations increase in concentration with high volatility (Mandal and Bakshi, 2012, Kumar et al., 2018, Kumar and Mandal, 2018). Therefore, this method is used in this research to evaluate the influences of initial diameter, air velocity and air temperature on droplet evaporation.

Figure 5.24 shows that the velocity magnitude of droplets with an initial diameter of 100  $\mu\text{m}$  shows a higher amplitude than the other two cases. This might be due to the higher evaporation rate that the smallest droplet diameter shows in comparison with the other two cases (with initial droplet diameters of 200  $\mu\text{m}$  and 500  $\mu\text{m}$ ). This is shown in Figure 5.24 where it can be seen that the peak velocity magnitude in the case of a droplet with an initial diameter of 100  $\mu\text{m}$  might be due to the peak of the evaporation rate, as presented in Figure 5.19 for the same initial droplet diameter.

Despite the calculation of the average velocity for the three cases, the case with the initial diameter of  $100\ \mu\text{m}$  has a fluctuation, as shown by the red dotted line in Figure 5.24, with a maximum value of  $0.15\ \text{m/s}$  and a minimum of  $0.05\ \text{m/s}$ . Therefore, in order to compare this with the other two cases, the intermediate value of  $0.1\ \text{m/s}$  is taken for the initial droplet diameter of  $100\ \mu\text{m}$ .

Therefore, the average velocity of each case is  $0.1\ \text{m/s}$ ,  $0.04\ \text{m/s}$  and  $0.02\ \text{m/s}$  for the initial droplet diameters of  $100\ \mu\text{m}$ ,  $200\ \mu\text{m}$  and  $500\ \mu\text{m}$ , respectively. Keeping these values in mind, this means that the case with  $D_0 = 100\ \mu\text{m}$  has a velocity magnitude that is 60% higher than the case with  $D_0 = 200\ \mu\text{m}$  and 80% higher than the case with  $D_0 = 500\ \mu\text{m}$ . From this, it can be said that the internal circulation might increase with a reduction of the initial droplet diameter.



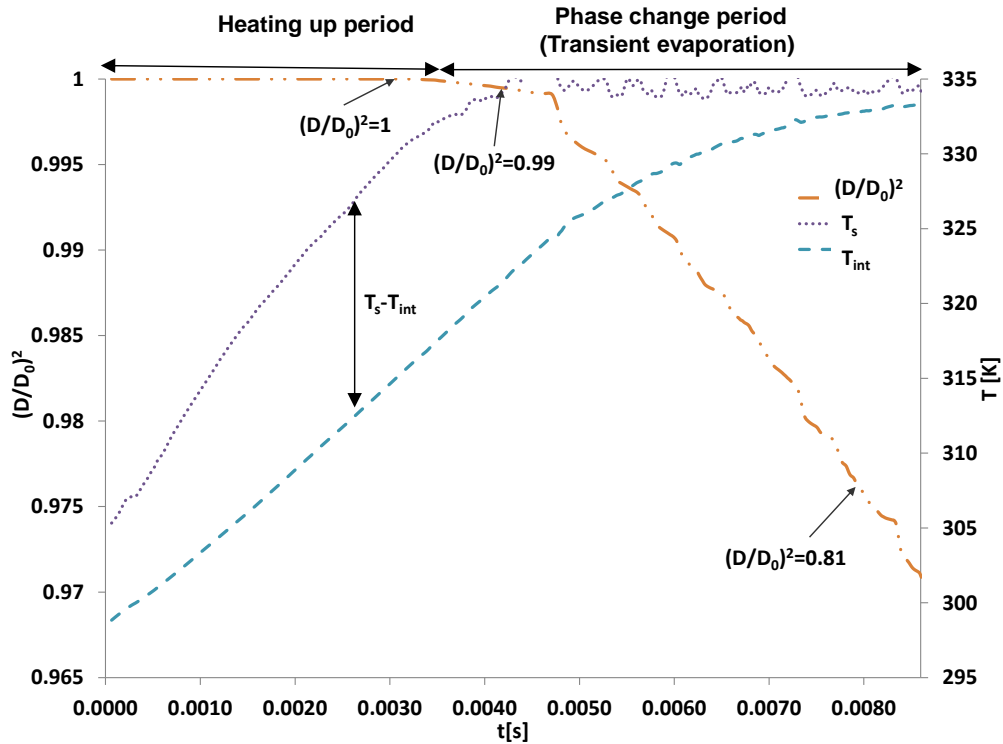
**Figure 5.24. Comparison of the average velocity at the droplet's interior varying the initial droplet diameter**

### 5.2.3.3.2 *Qualitative analysis of the effect of varying initial droplet diameter on internal circulation*

In this section, the internal circulation is analysed with the temperature and oil vapour mass fraction contours, as well as the streamlines of the velocity inside and outside the droplet. The evaporation process has been divided into three stages based on the droplet's surface and core temperatures. The stages are the heating-up period and the phase-change period, with the latter subdivided into transient evaporation and steady evaporation.

Figure 5.25, Figure 5.29 and Figure 5.34 show the three stages of the evaporation process. The heating-up period is when the droplet's surface temperature increases until reaching saturation at 334 K; transient evaporation occurs when the phase change has started and the droplet's surface temperature is saturated but the core temperature is still increasing; and, finally, steady evaporation is when the droplet's surface temperature and the droplet core have reached saturation and the diameter is still decreasing at a constant temperature.

The internal circulation was analysed for the heating-up period and transient evaporation for three initial droplet diameters, namely 100  $\mu\text{m}$ , 200  $\mu\text{m}$  and 500  $\mu\text{m}$  at 5 m/s and 550 K. The contours and velocity streamlines were analysed for the heating-up period and for transient evaporation. Transient evaporation was studied at two points – one at the beginning of this stage and one at the end – when the core is approaching the temperature of saturation, as shown in Figure 5.25, Figure 5.29 and Figure 5.34 for the initial droplet diameters of 100  $\mu\text{m}$ , 200  $\mu\text{m}$  and 500  $\mu\text{m}$ , respectively.



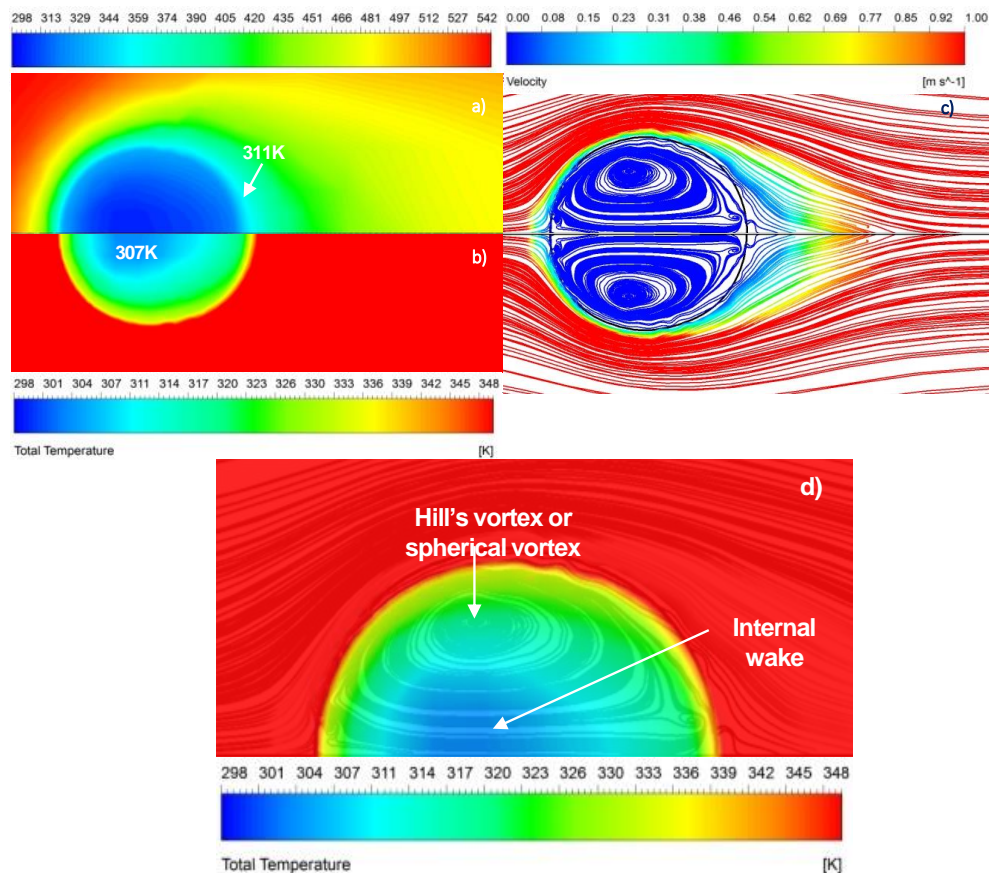
**Figure 5.25. Temporal evolution of the droplet normalised square diameter versus temperature evolution at the droplet surface  $T_s$  and the droplet core  $T_{int}$  for an initial diameter of  $100\ \mu\text{m}$ , with air at  $550\ \text{K}$  and  $5\ \text{m/s}$**

Figure 5.26 a), b) and c) show the contours of interior and exterior droplet temperature and velocity streamlines, respectively, for a droplet of  $100\ \mu\text{m}$  that is in the heating-up period with a  $\left(\frac{D}{D_0}\right)^2 = 1$  and  $0.0031\ \text{s}$ , as shown in Figure 5.25.

Figure 5.26 a) and b) show the temperature of the droplet's surroundings and the temperature at the droplet's interior, respectively. Figure 5.26 a) shows that the exterior temperature at the droplet's surface is still around  $311\ \text{K}$  and has not reached the saturation temperature, which is  $334\ \text{K}$ . Figure 5.26 b) shows the core temperature at  $307\ \text{K}$ . The internal vortices of a droplet with an initial diameter of  $100\ \mu\text{m}$  are shown in Figure 5.26 c), which presents a similar internal flow field to the one mentioned by (Prakash and

Sirignano, 1978, Sirignano, 2010) where the spherical internal vortex displays a counter-clockwise direction.

The internal vortex matches with the region that is around 323 K; moreover, the region with the lowest temperature is the core of the droplet at approximately 307 K, which corresponds to the internal wake zone, as shown in Figure 5.26 d). Thus, at 0.0031 s the region with high vorticity, where there is the Hill's vortex, is where the temperature has distributed fastest, contrary to the region of the internal wake, which is the coldest zone.



**Figure 5.26. Contours and streamlines for a droplet with an initial diameter of  $100 \mu\text{m}$  at  $(\frac{D}{D_0})^2 = 1$ , 0.0031 s: a) external droplet temperature, b) internal droplet temperature, c) velocity streamlines, d) warm and cold zones at the droplet's interior due to internal circulation**

Figure 5.27 a), b), c), d) and e) show the contours of oil vapour mass fraction, liquid volume fraction, external droplet temperature, internal droplet temperature and velocity streamlines, respectively, for a droplet with an initial diameter of  $100\ \mu\text{m}$  at  $\left(\frac{D}{D_0}\right)^2 = 0.99$  and  $0.0042\ \text{s}$ . The contours and streamlines indicate the evolution of the evaporation process at the initial stage, which is the beginning of transient evaporation.

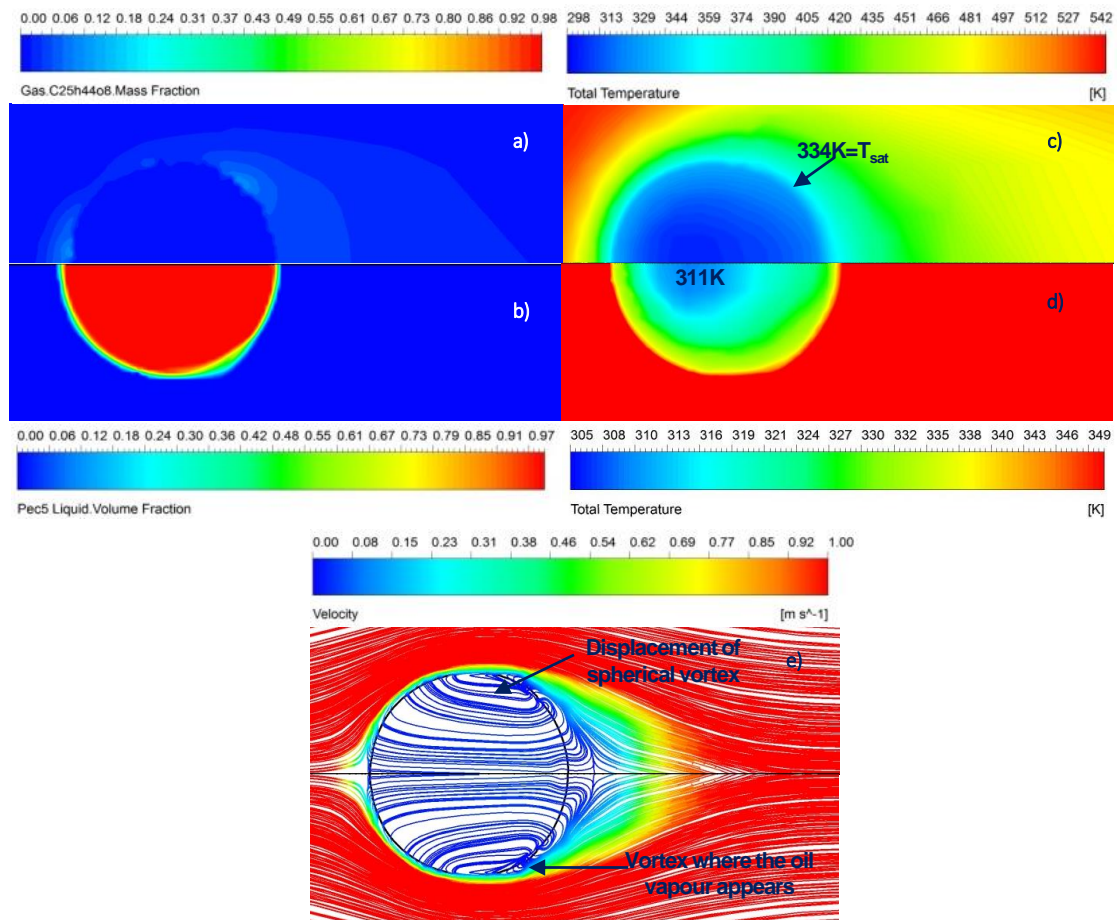


**Figure 5.27. Contours and streamlines for a droplet with an initial diameter of  $100\ \mu\text{m}$  at  $\left(\frac{D}{D_0}\right)^2 = 0.99$  and  $0.0042\ \text{s}$ : a) oil vapour mass fraction, b) liquid volume fraction, c) external temperature, d) internal temperature, e) velocity streamlines**

Figure 5.27 a) indicates that at  $0.0042\ \text{s}$ , the evaporation starts and there is an oil vapour mass fraction of around 10%. The droplet core's temperature is  $311\ \text{K}$ , but the

surface has reached the saturation temperature and the start of transient evaporation is observed with the core temperature still increasing and the surface temperature at 334 K.

The spherical vortex has been displaced, showing the main recirculation at the top of the droplet's surface, mainly where the oil vapour is seen, as shown in Figure 5.27 a) and e). It might be said that the Hill's vortex practically disappears due to the beginning of the evaporation process and the internal wake is larger during transient evaporation than in the heating-up period.

Figure 5.28 a), b), c), d) and e) show the contours and streamlines at the end of transient evaporation with  $\left(\frac{D}{D_0}\right)^2 = 0.81$  and 0.0081 s for a droplet with an initial diameter of 100  $\mu\text{m}$ .

At  $\left(\frac{D}{D_0}\right)^2 = 0.81$  and 0.0081 s the flow pattern described by (Prakash and Sirignano, 1978, Sirignano, 2010) and shown in Figure 5.21 has changed due to evaporation at the rear part of the droplet and the bubble forming inside the droplet. The vorticity at the rear part of the droplet is expected due to the external flow presented, which is a mixture of oil vapour and air, and also due to the stagnation point at the rear part of the droplet enhancing the mass transfer in this zone, as presented in Figure 5.28 a) and e).

At this point, the droplet's surface is at the saturation temperature and the oil vapour mass fraction is 42%. The temperature of the droplet's core is around 1 K below the saturation temperature; however, some regions in the droplet's interior, mainly at the rear part, have reached the saturation temperature and show a bubble formation, as indicated in Figure 5.28 a), b) and e).

Inside the bubble there is the presence of an 85% oil vapour mass fraction and a 15% fraction of air. The formation of the bubble might be due to a homogeneous nucleation generated by the liquid saturation and it can probably go on absorbing heat from the liquid and keep evaporating as has been observed previously (Rao et al., 2018, Wang et al., 2018). The bubble can be trapped due to viscosity and surface tension forces; however, the droplet's internal convection moves the bubble to the front of the droplet and the bubble then collapses, forming secondary droplets as shown in Figure 5.28 e).

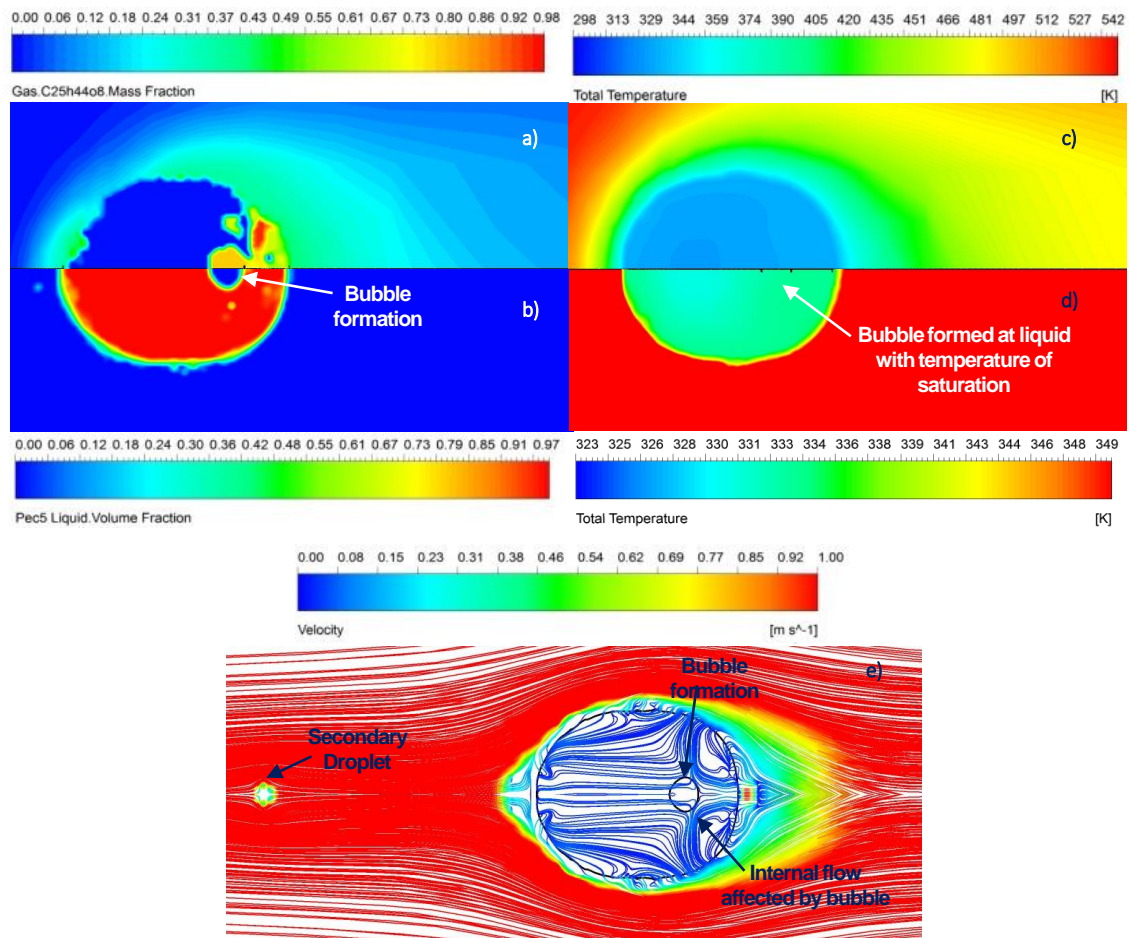
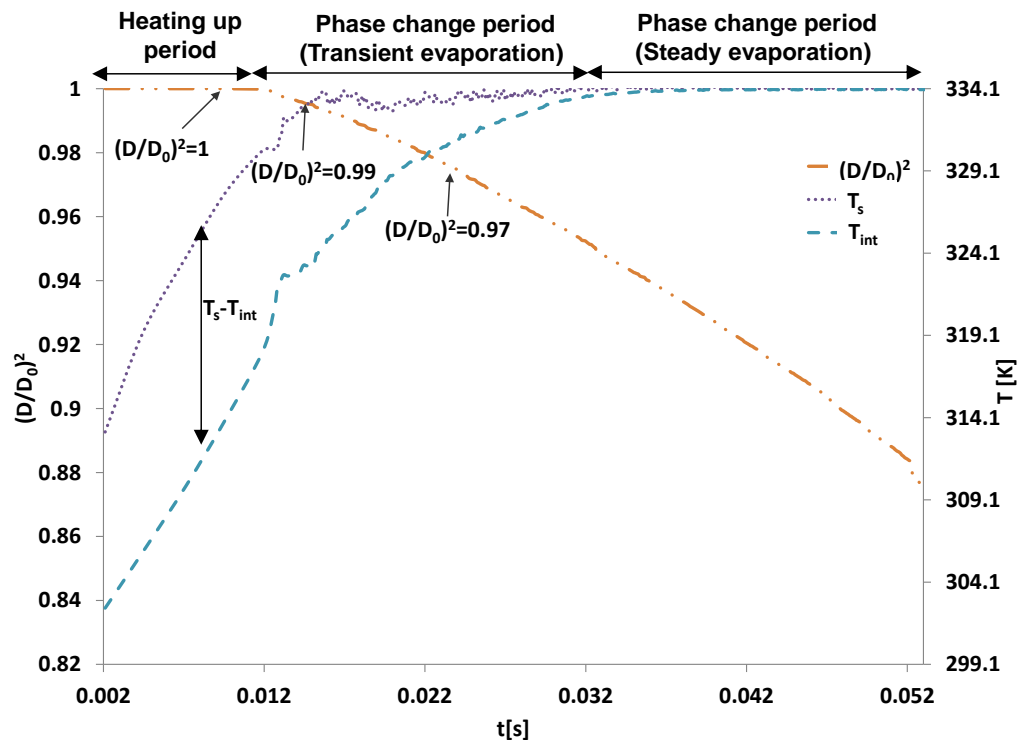


Figure 5.28. Contours and streamlines for a droplet with an initial diameter of  $100 \mu\text{m}$  at  $\left(\frac{D}{D_0}\right)^2 = 0.81$  and  $0.0081$  s: a) oil vapour mass fraction, b) liquid volume fraction, c) external temperature, d) internal temperature, e) velocity streamlines

Figure 5.28 e) indicates the streamlines at the droplet's surface that are due to the momentum exchange from the release of oil vapour at the surface and downstream of the droplet. In addition, Figure 5.28 e) shows the influence of the bubble formation on the droplet's internal flow field due to mass transfer at the bubble's surface and at the rear part of the droplet.

The internal circulation is analysed for a droplet with an initial diameter of  $200\ \mu\text{m}$  at  $\left(\frac{D}{D_0}\right)^2 = 1$ ,  $\left(\frac{D}{D_0}\right)^2 = 0.99$  and  $\left(\frac{D}{D_0}\right)^2 = 0.97$ , which corresponds to the heating-up period, the beginning of transient evaporation and the end of transient evaporation, respectively, as indicated in Figure 5.29.



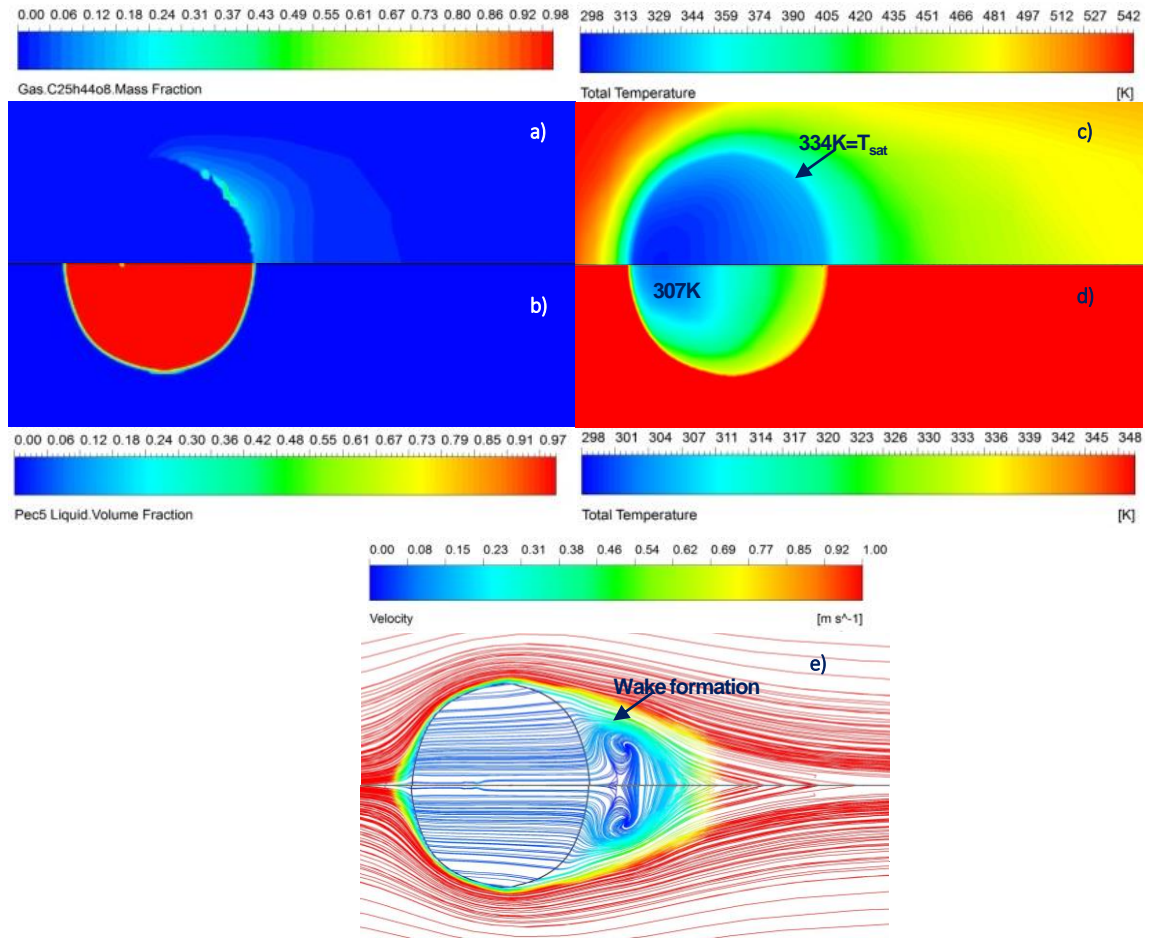
**Figure 5.29. Temporal evolution of a droplet normalised square diameter versus temperature evolution at the droplet surface  $T_s$  and the droplet core  $T_{int}$  for an initial diameter of  $200\ \mu\text{m}$ , with air at  $550\ \text{K}$  and  $5\ \text{m/s}$**

Figure 5.29 indicates the difference in temperature between the droplet's surface  $T_s$  and the droplet's core  $T_{int}$  which is a characteristic of transient evaporation. This gradient reduces as the  $T_{int}$  reaches the saturation temperature; at this point, steady evaporation starts.

The contours of oil vapour mass fraction, liquid volume fraction, temperature at the droplet's surroundings and temperature at the droplet's core are presented in Figure 5.30 a), b), c) and d) and the velocity streamlines are shown in Figure 5.30 e) for  $\left(\frac{D}{D_0}\right)^2 = 1$  and 0.01 s. In Figure 5.30 a) it can be seen that at 0.01 s part of the droplet's surface has started to evaporate downstream. Figure 5.30 b) shows that there is no presence of oil vapour in the droplet's interior, which means that there is no bubble formation at this stage. In Figure 5.30 c) and d) the droplet's interior presents a high gradient in temperature, with the coldest zone at the front of the droplet's interior where there is the lowest temperature of 307 K. At the rear of the droplet's interior, the temperature is around 315 K and the temperature downstream of the droplet's surface is 334 K.

Furthermore, by analysing the internal flow field of a droplet with an initial diameter of 200  $\mu\text{m}$ , it can be noted (see Figure 5.30 e)) that at 0.1 s the internal flow field does not present the spherical vortex, as occurs in the droplet with an initial diameter of 100  $\mu\text{m}$  (see Figure 5.26 c)). However, in the external flow there is the formation of a wake at the rear part of the droplet, which matches with the presence of oil vapour.

Thus, the wake at the rear enhances the evaporation and the heat transfer from the droplet's surface to the core; this explains why the temperature of the droplet's interior is higher at the rear part of it than at the front part (Figure 5.30 c) and d)).

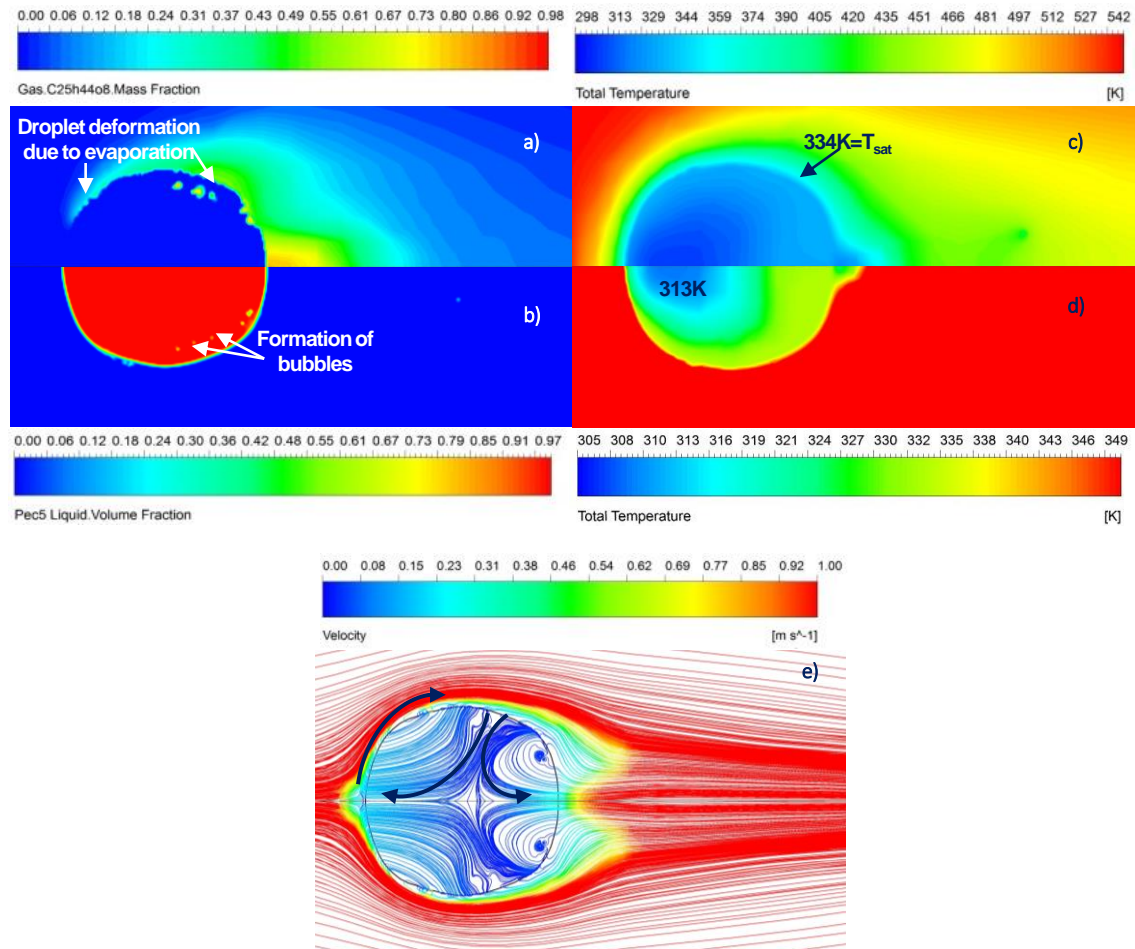


**Figure 5.30. Contours and streamlines for a droplet with an initial diameter of 200  $\mu\text{m}$  at  $\left(\frac{D}{D_0}\right)^2 = 1$  and 0.01 s: a) oil vapour mass fraction, b) liquid volume fraction, c) external temperature, d) internal temperature, e) velocity streamlines**

Figure 5.31 a), b), c) and d) shows the contours of oil vapour mass fraction, liquid volume fraction, and internal and external droplet temperature, respectively. Figure 5.31 e) shows the velocity streamlines; all figures are for  $\left(\frac{D}{D_0}\right)^2 = 0.99$  and 0.015 s and an initial droplet diameter of 200  $\mu\text{m}$ .

Figure 5.31 a) and b) indicate that there is the formation of small bubbles, a deformation of the droplet's surface due to evaporation and the droplet-surface's oil vapour covers more surface area at 0.15 s than at the previous stage at 0.1 s (see Figure

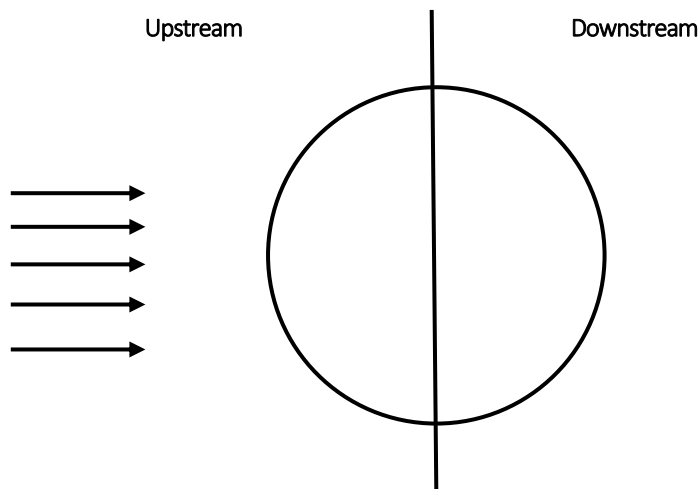
5.30 a)). However, Figure 5.31 c) and d) show that the droplet's interior is still heating up, with the coldest region at 313 K.



**Figure 5.31. Contours and streamlines for a droplet with an initial diameter of 200  $\mu\text{m}$  at  $\left(\frac{D}{D_0}\right)^2 = 0.99$  and 0.015 s: a) oil vapour mass fraction, b) liquid volume fraction, c) external temperature, d) internal temperature, e) velocity streamlines**

Figure 5.31 e) shows the formation of two vortices following opposite directions; the flow is divided, which separates the droplet into two regions. These vortices distribute the temperature in the two regions, upstream and downstream, as represented in Figure 5.32. Figure 5.31 c) and d) indicate that the upstream region is the cold zone and the downstream region is the warm zone; therefore, it is clear that the internal flow field

distribution favours heat transfer inside the droplet. Thus, it is important to include internal circulation in the calculation of droplet evaporation.



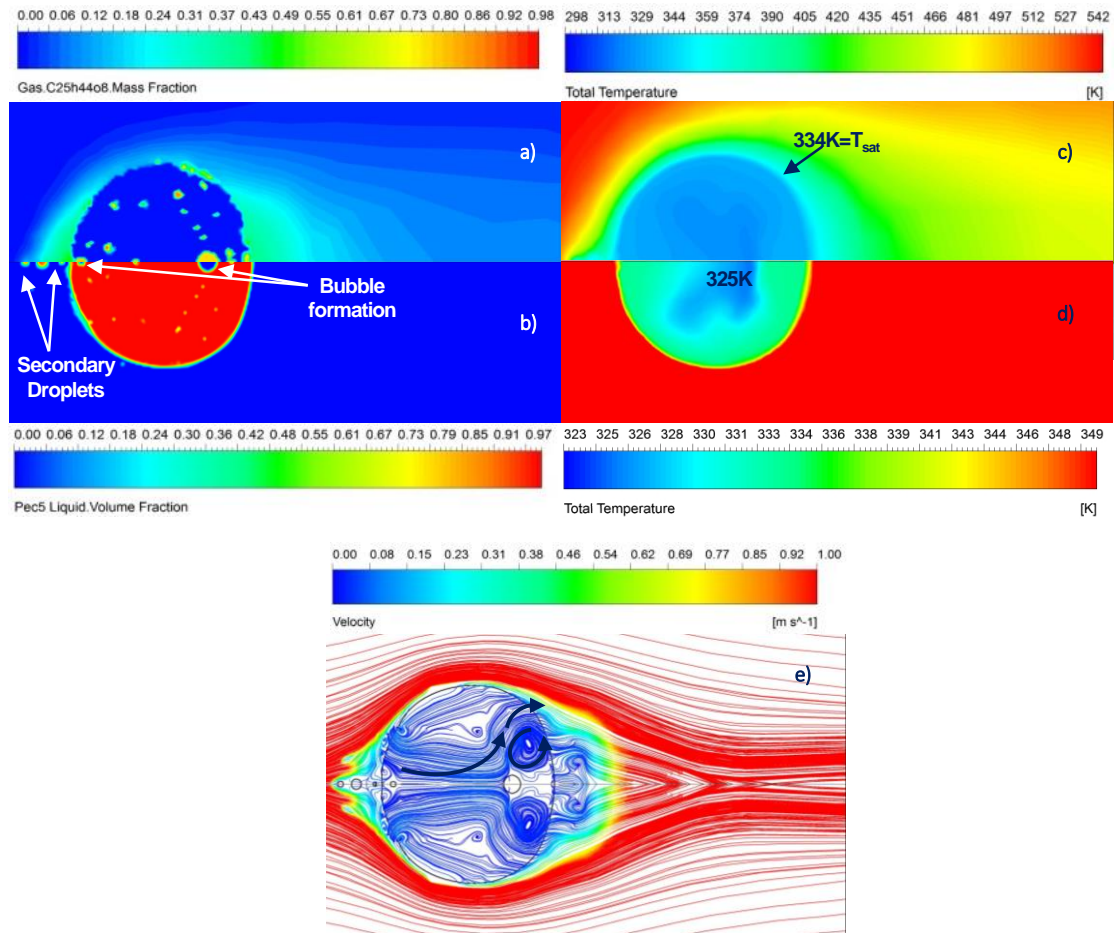
**Figure 5.32. Droplet representation of the two regions formed by the internal flow**

Figure 5.33 a), b), c) and d) show the contours of oil vapour mass fraction, liquid volume fraction, and external and internal droplet temperature, respectively. Figure 5.33 e) presents the velocity streamlines; all of these are presented at  $\left(\frac{D}{D_0}\right)^2 = 0.97$  and  $0.024$  s, which is almost at the end of the transient evaporation (see Figure 5.29).

Figure 5.33 a) and b) show the formation of a bubble downstream of the droplet, similar to Figure 5.28 e). Moreover, Figure 5.33 a) and b) indicate that small droplets have detached due to the evaporation process modifying the flow field at the front of the droplet. This means that small particles of oil might be travelling in the core flow of the bearing chamber and that the droplet break-up might also be due to the evaporation process and not only because of body forces.

The droplet's surface presents an oil vapour mass fraction while the core is still in the heating-up period, as can be observed in Figure 5.33 d). It shows that the bubble is

located in the limit of the main internal vortex, as seen in Figure 5.33 e). Figure 5.33 c) and d) indicate that the limit of the internal vortex matches the limit of the two zones with different temperatures and the bubble is trapped in the two regions, as indicated in Figure 5.33 e).



**Figure 5.33. Contours and streamlines for a droplet with an initial diameter of 200  $\mu\text{m}$  at  $\left(\frac{D}{D_0}\right)^2 = 0.97$  and 0.024 s: a) oil vapour mass fraction, b) liquid volume fraction, c) external temperature, d) internal temperature, e) velocity streamlines**

Moreover, contours and streamlines of a droplet with an initial diameter of 500  $\mu\text{m}$  are analysed during the heating-up period  $\left(\frac{D}{D_0}\right)^2 = 1$  and the transient evaporation  $\left(\frac{D}{D_0}\right)^2 = 0.99$  as shown in Figure 5.34.

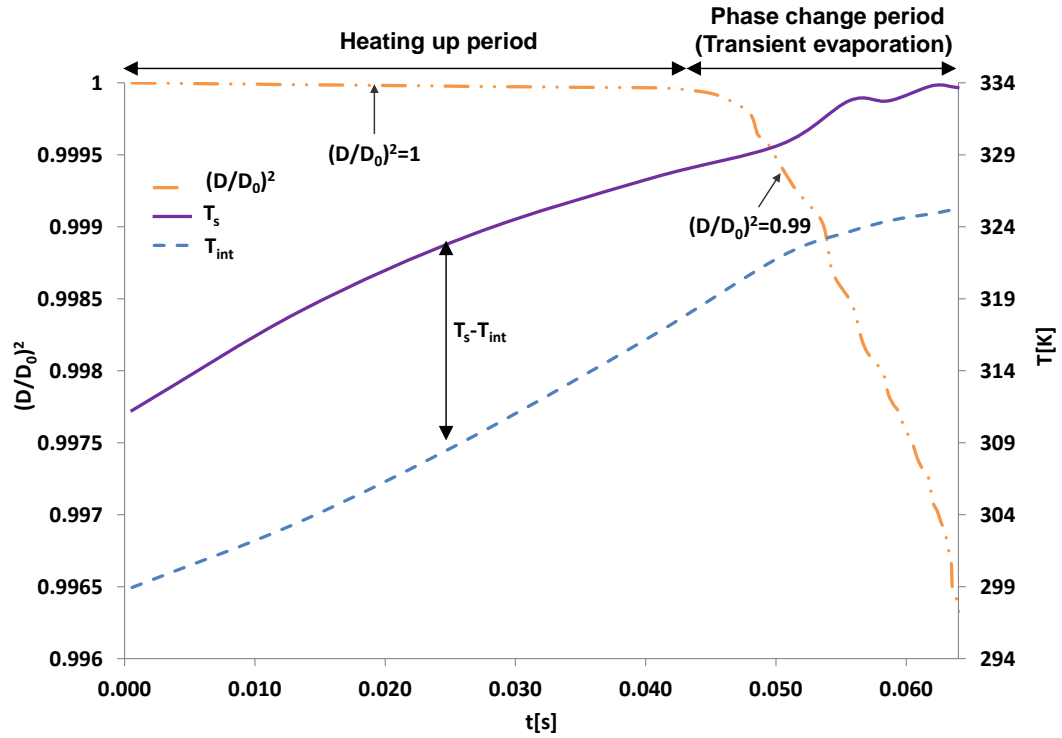


**Figure 5.34. Temporal evolution of droplet normalised square diameter versus temperature evolution at the droplet surface  $T_s$  and the droplet core  $T_{int}$  for an initial diameter of  $500\ \mu\text{m}$ , with air at  $550\ \text{K}$  and  $5\ \text{m/s}$**

By analysing a droplet with an initial diameter of  $500\ \mu\text{m}$  in Figure 5.35 c) at  $0.02\ \text{s}$ , the flow field is shown to be similar to that of a droplet with an initial diameter of  $100\ \mu\text{m}$  at  $0.003\ \text{s}$  (Figure 5.26 c)), with a spherical vortex being presented. In addition, the liquid boundary layer of the droplet with an initial diameter of  $500\ \mu\text{m}$  shows a small recirculation at the downstream region inside the droplet, which has a momentum exchange with the external wake at the rear part of the droplet. This external wake enhances the heat transfer from the droplet's surface to the core, as can be observed in Figure 5.35 b). Thus, if the droplet is divided into halves (see Figure 5.32), it shows that downstream of the droplet the temperature is around  $20\ \text{K}$  higher than the upstream half.

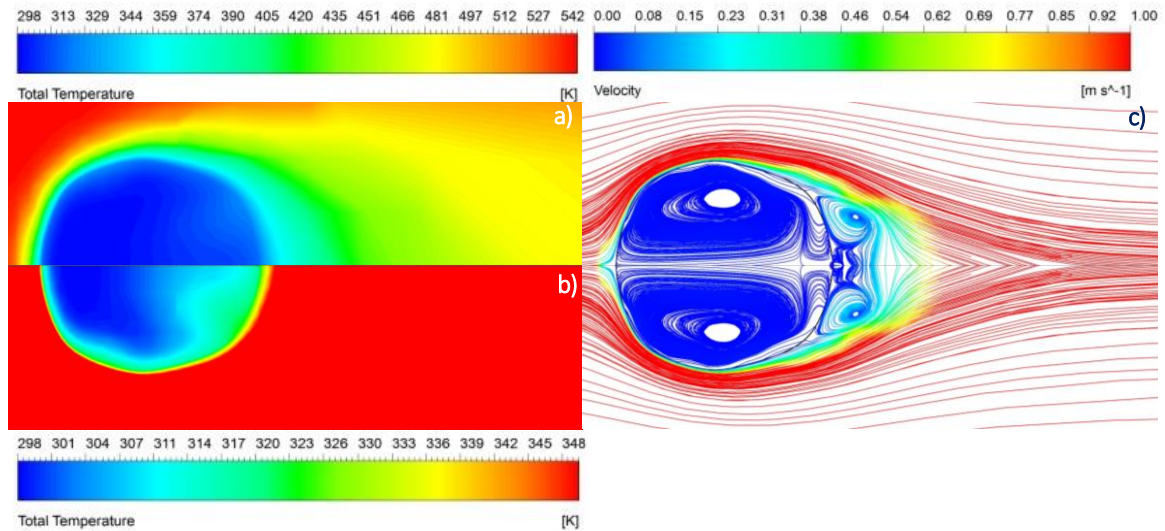


**Figure 5.35. Contours and streamlines for a droplet with an initial diameter of 500  $\mu\text{m}$  at  $\left(\frac{D}{D_0}\right)^2 = 1$  and 0.02 s: a) external temperature, b) internal temperature, c) velocity streamlines**

Figure 5.36 e) indicates that the internal wake is extended and the main vortex has been displaced to the top part of the droplet, which is the same position as the oil vapour with the highest concentration (5%) at 0.05 s, as shown in Figure 5.36 a).

In Figure 5.36 c) and d) the second part of the droplet reaches the saturation temperature while upstream of the droplet is still in the heating-up period. The cooling difference in temperatures inside the droplet might affect oil degradation and effectiveness inside the bearing chamber; this could be investigated in further studies.

In general, the droplet's internal circulation increases with the reduction of initial diameter. Hence, the droplet's internal temperature distribution takes the longest for droplets with an initial diameter of 500  $\mu\text{m}$ , which might have higher temperature gradients and might affect the oil degradation.

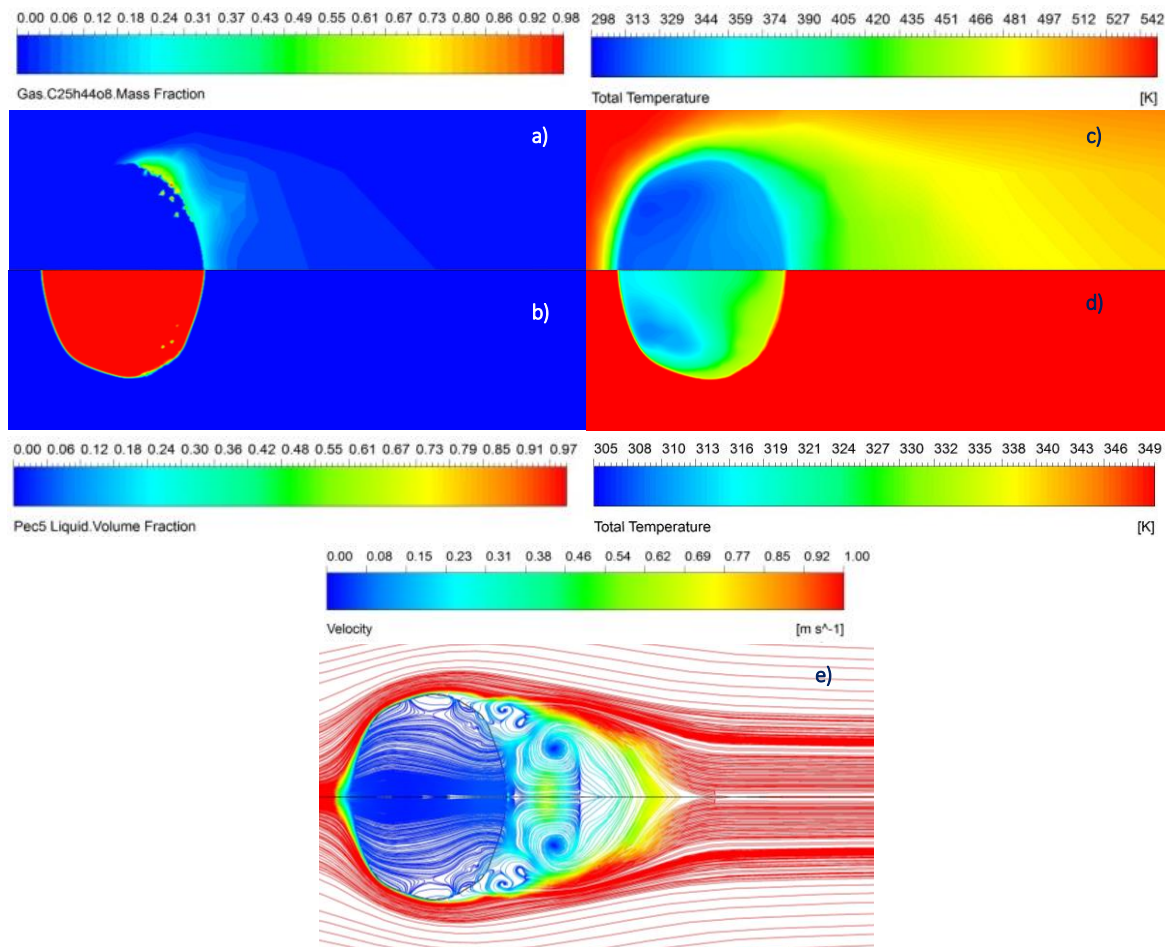


Figure 5.36. Contours and streamlines for a droplet with an initial diameter of  $500 \mu\text{m}$  at  $\left(\frac{D}{D_0}\right)^2 = 0.99$  and  $0.05 \text{ s}$ : a) oil vapour mass fraction, b) liquid volume fraction, c) external temperature, d) internal temperature, e) velocity streamlines

## 5.2.4 Effect of air velocity

### 5.2.4.1 Effect of varying air velocity on evaporation rate

Inside bearing chambers, we can find different air velocities which depend on the shaft speed. As aforementioned in Section 5.2.1.2, the core flow has a range of velocities from  $5 \text{ m/s}$  to  $35 \text{ m/s}$ , which influences the droplet's motion.

The droplet's motion can be classified into two categories. First, there are the droplets that travel from the bearings to the walls, which have a range of velocities from  $5 \text{ m/s}$  to  $35 \text{ m/s}$ . Second, there are the droplets with a diameter less than  $200 \mu\text{m}$  that travel

with the core flow. Based on this, for the first scenario, the relative droplet velocity is calculated and for the CFD case setup, the relative velocity is represented in the inlet airflow with a droplet at zero velocity. For the second scenario, the droplet travels with the core flow; thus, the droplet's velocity depends on the balance of body forces (drag force and droplet weight). As reported before, the droplets with a diameter smaller than 200  $\mu\text{m}$  are governed by airflow conditions (Farrall et al., 2007).

The droplet evaporation rate was analysed to predict the effect of the air velocity variation for both scenarios mentioned above. Two inlet air velocities were proposed, namely 5 m/s and 1 m/s, keeping the ambient temperature at 550 K and the initial droplet diameter at 200  $\mu\text{m}$ .

Analysing these two scenarios, Figure 5.37 shows a larger reduction in droplet diameter for those under high-velocity core flow. Comparing both cases at 0.047 s, the case with airflow at 5 m/s had lost 10% of its initial diameter, which is a 6% greater reduction than the case with an air velocity of 1 m/s. Therefore, the larger reduction in the droplet diameter under the effects of airflow at 5 m/s might be due to the greater shear stress forces at the droplet's surface, which enhances the evaporation.

Figure 5.38 indicates that the maximum evaporation rate over the droplet's surface for airflow at 5 m/s is around 0.1  $\text{kg}/\text{m}^2\text{s}$  higher than the case with airflow at 1 m/s. In addition, from the slope of the linear regression of the equation 3.30 and applied to the two cases in Figure 5.37, the evaporation rate for the case with air at 5 m/s is 0.140  $\text{mm}^2/\text{s}$  and for the case with air at 1 m/s it is 0.07  $\text{mm}^2/\text{s}$ , which means that for the former case the evaporation rate is twice as high as the latter case which correlates with Figure 5.38.

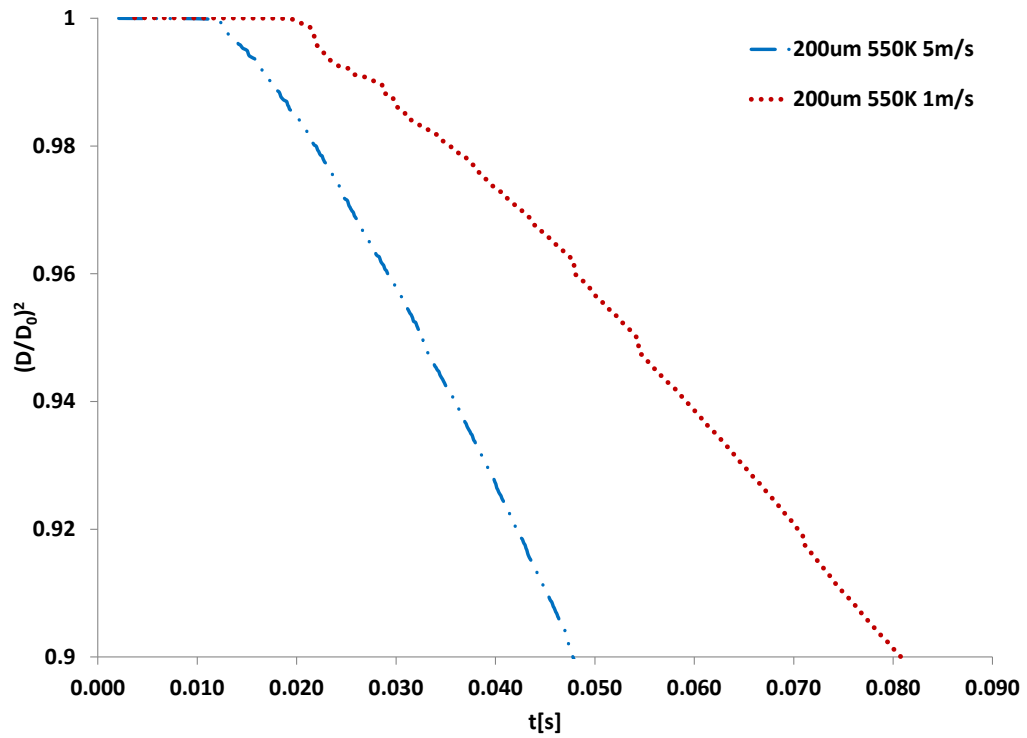


Figure 5.37. Non-dimensional squared diameter evolution for an initial droplet diameter of 200  $\mu\text{m}$ , varying the air inlet velocity (5 m/s and 1 m/s)

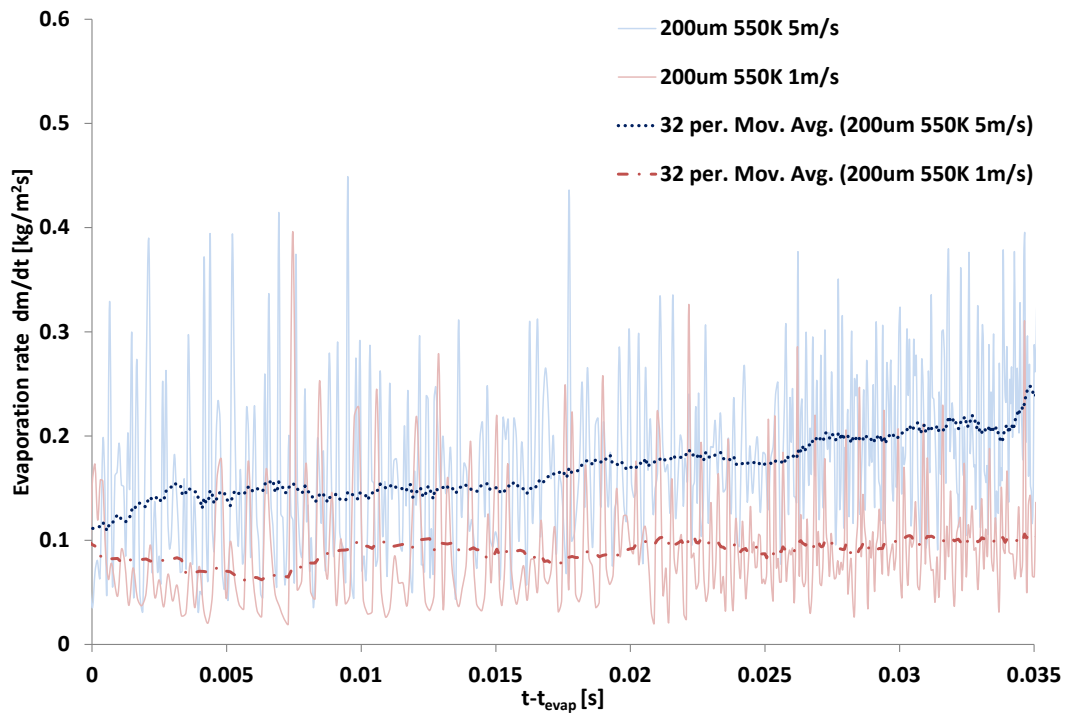
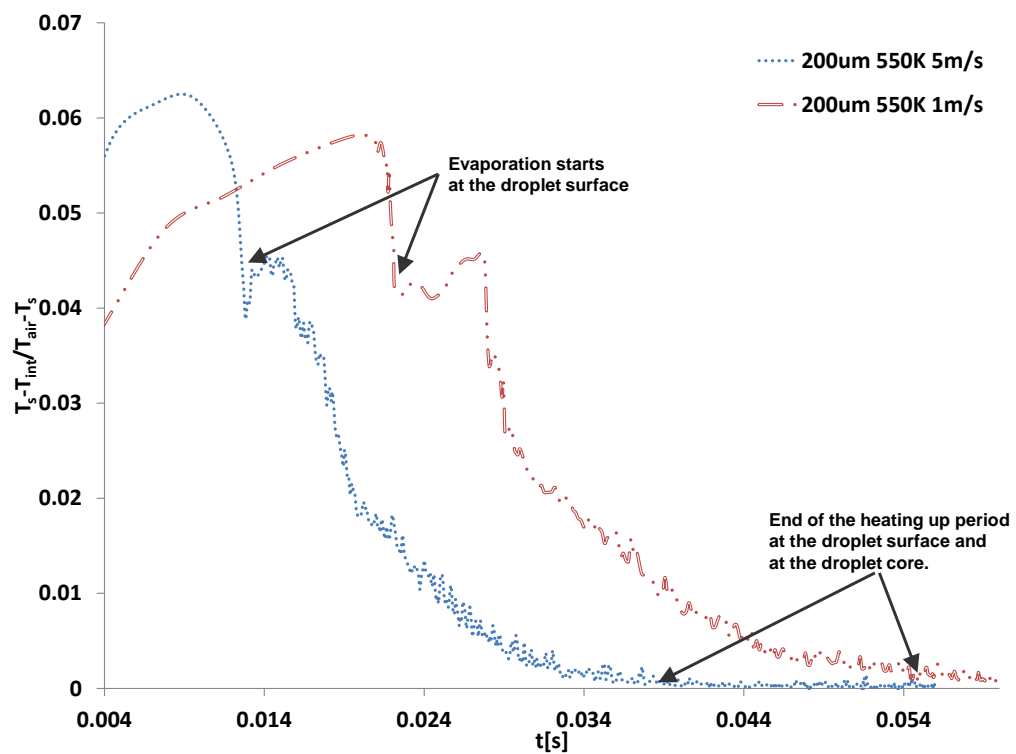


Figure 5.38. Variation of evaporation rate over a droplet's surface area for different air inlet velocity (5 m/s and 1 m/s)

### 5.2.4.2 Effect of varying air velocity on heat transfer at the droplet's surface

Following the explanation presented in Section 5.2.3.2, the ratio of the heat transfer at the droplet's surface was studied by varying the ambient air velocity for two different values, 5 m/s and 1 m/s, while keeping the same initial diameter and air temperature for both cases. In Figure 5.39, the variation in air velocity shows that the maximum value of the heat transfer ratio is only affected slightly. The maximum value for the case with an air velocity of 5 m/s is just 0.4% higher than the case with airflow of 1 m/s. The case with the higher air velocity reaches the peak value 0.01 s faster than the case with the low velocity, which is due to the extended heating-up period for the latter case.



**Figure 5.39. Heat transfer ratio varying the inlet air velocities and with air at 550 K and  $D_0 = 200 \mu\text{m}$**

Moreover, there is a transition section, which is when evaporation starts at the droplet's surface which means that the heating-up period at the surface has finished while

it is still in process at the core (see Figure 5.29). The heating process completely ends both on the surface and in the core of the droplet when the heat transfer ratio is zero, as can be observed in Figure 5.39.

### ***5.2.4.3 Effect of varying air velocity on internal circulation***

#### ***5.2.4.3.1 Quantitative analysis of the effect of varying air velocity on internal circulation***

In this section, the fluctuations of the average velocity magnitude at the droplet's interior are evaluated, similar to Section 5.2.3.3.2. The average velocity magnitude is measured in the area with a VOF from 0.8 to 1, as presented in Figure 5.22.

The droplet's internal circulation flow field might vary if the droplet is subjected to a gaseous field at different velocities. The internal circulation was analysed for a droplet with an initial diameter of 200  $\mu\text{m}$  with a surrounding airflow at 550 K and two different velocities, namely 5 m/s and 1 m/s. The fluctuations were fitted with a moving average regression with a range of 32 values in order to compare both cases.

Figure 5.40 indicates that at the beginning of the evaporation process, the droplet subjected to an air velocity of 1 m/s shows large fluctuations of average velocity magnitude and temperature at the droplet's surface (see Figure 5.41 for fluctuations of temperature at the droplet's surface). However, after some time, the curve for the case with air velocity of 1 m/s decreases gradually until reaching the average value of the fit curve of internal velocity magnitude of around 0.04 m/s, which is similar to the case with air velocity of 5 m/s. In addition, it is noted that both best-fit curves follow the same trend.

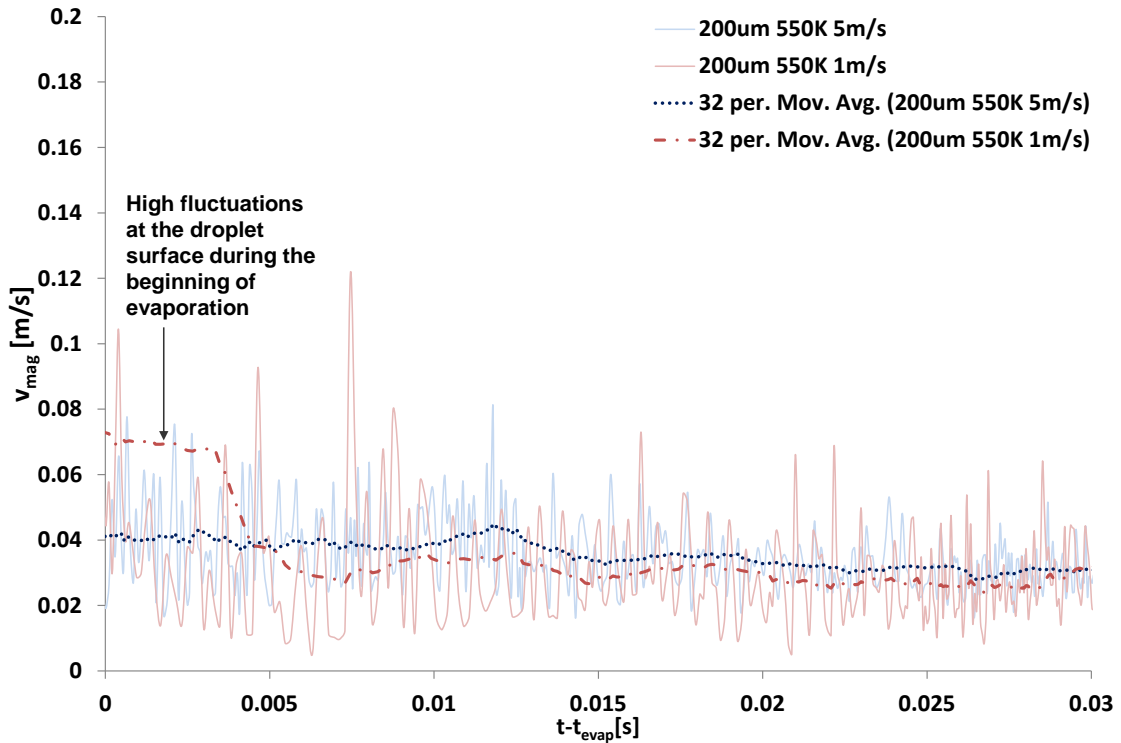


**Figure 5.40. Comparison of the velocity magnitude at the droplet's interior varying the velocity of air**

#### 5.2.4.3.2 Qualitative analysis of the effect of varying air velocity on internal circulation

In this section, the effect of air velocity on internal circulation is analysed. This analysis is performed by taking the contours of oil vapour mass fraction, liquid volume fraction, and the internal and external temperatures into account. In addition, the internal flow pattern is observed with the velocity streamlines. Both the contours and streamlines are presented for the separate stages of the evaporation process, namely during the heating-up period,  $\left(\frac{D}{D_0}\right)^2 = 1$  and 0.021 s, and transient evaporation,  $\left(\frac{D}{D_0}\right)^2 = 0.99$  and 0.023 s and  $\left(\frac{D}{D_0}\right)^2 = 0.97$  and 0.039 s, as shown in Figure 5.41, similar to Section 5.2.3.3.2.

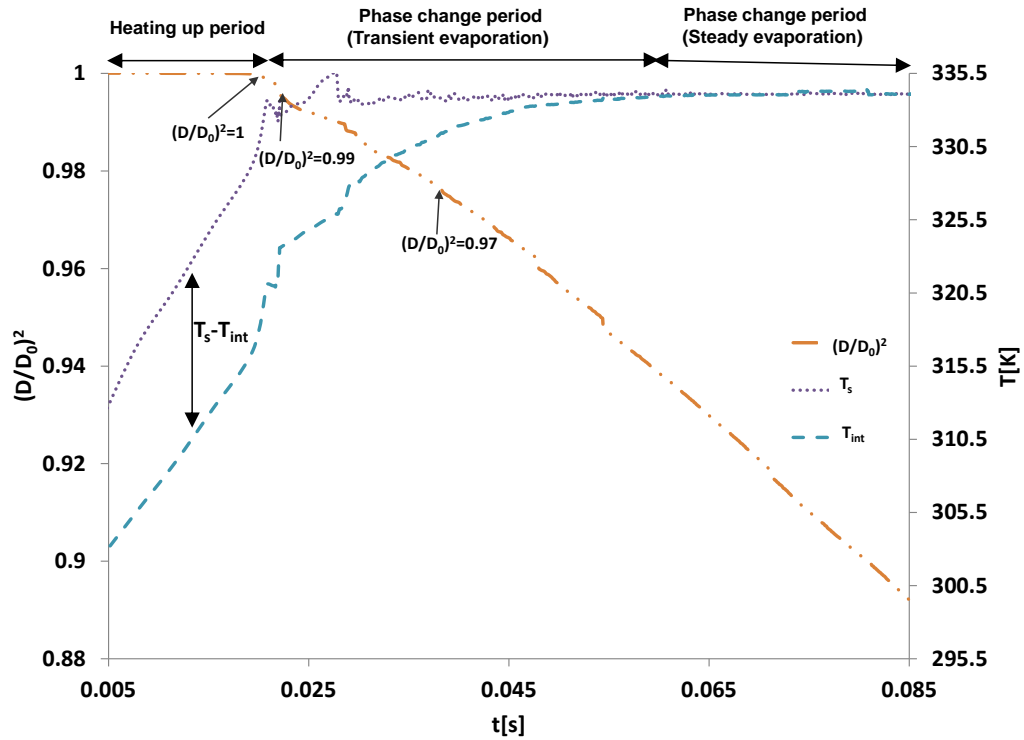


**Figure 5.41. Temporal evolution of a droplet normalised square diameter versus temperature evolution at the droplet surface  $T_s$  and the droplet core  $T_{int}$  for an initial diameter of 200  $\mu\text{m}$ , with air at 550 K and 1 m/s**

The contours and velocity streamlines at  $\left(\frac{D}{D_0}\right)^2 = 1$  are shown in Figure 5.42 a) and b). Figure 5.42 a) indicates that the evaporation starts at the front of the droplet for the case with air at 1 m/s, which is different to the case with air at 5 m/s as presented in Figure 5.42 b). This might be due to the wake formed at the front of the droplet, as observed in Figure 5.42 b) and Figure 5.43 e) where the internal vortex can be seen at the top of the droplet's surface. The coldest part of the droplet has a temperature of around 310 K, while the surface has reached the saturation temperature at 334 K (see Figure 5.43 c) and d)).

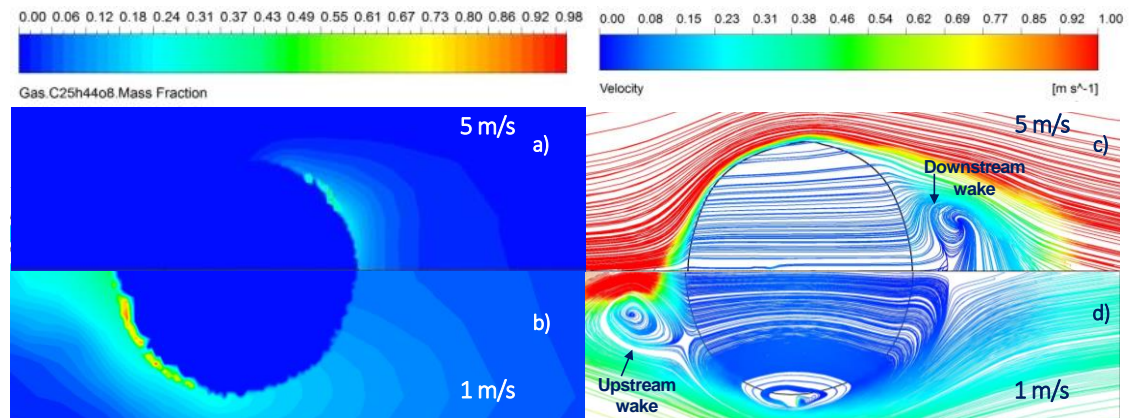


**Figure 5.42. Comparison of contours and streamlines for two cases varying the air velocity with an initial droplet diameter of 200  $\mu\text{m}$  and air at 550 K at  $\left(\frac{D}{D_0}\right)^2 = 1$ : a) oil vapour mass fraction for the case at 5 m/s, b) oil vapour mass fraction for the case at 1 m/s, c) streamlines of internal velocity for the case at 5 m/s, d) streamlines of internal velocity for the case at 1 m/s**

Figure 5.43 e) shows that the internal flow pattern is divided into two directions: the main direction is counter-clockwise for the Hill's vortex and the second direction is from downstream to upstream of the droplet forming an external wake at the front. The Hill's vortex, or spherical vortex, and the internal wake were shown previously in Figure 5.21. This flow pattern distributes the temperature in such a way that the core of the droplet is the cold region, as observed in Figure 5.43 c) and d), contrary to the case with air velocity of 5 m/s where the cold region is in the upstream half of the droplet.

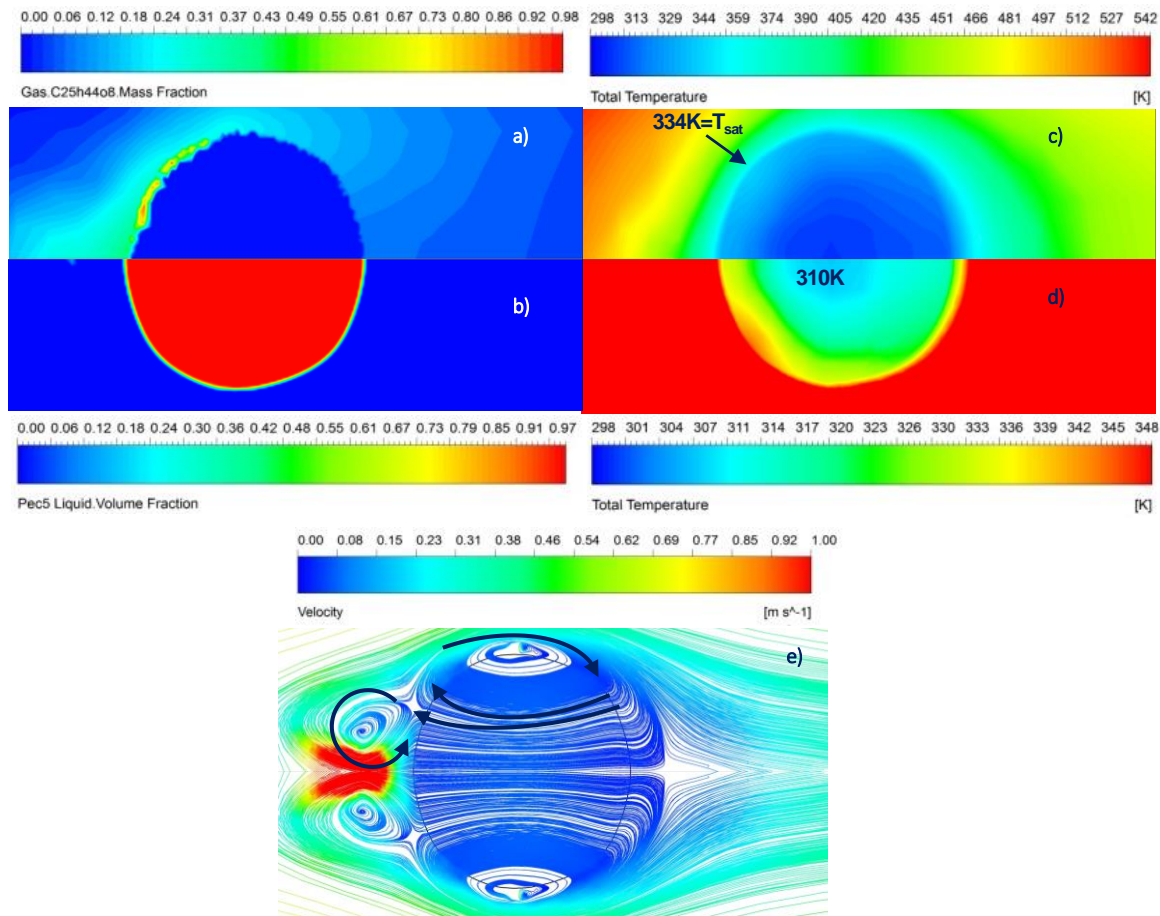


**Figure 5.43. Contours and streamlines at  $\left(\frac{D}{D_0}\right)^2 = 1$  and 0.021 s for a droplet with an initial diameter of 200  $\mu\text{m}$  under airflow at 1 m/s: a) oil vapour mass fraction, b) liquid volume fraction, c) external temperature, d) internal temperature, e) velocity streamlines**

Figure 5.44 a) and b) indicate the formation of a bubble at the front of the droplet, which is probably due to the high recirculation at the front which might favour the entrance of gas to the liquid phase. The bubble observed in Figure 5.44 e) presents a high velocity at the bubble's centre and mass and momentum interchanges with the internal wake; part of the flow of the internal wake goes around the bubble and the other part interacts with the flow coming from the bubble. Additionally, the external wake formed in  $\left(\frac{D}{D_0}\right)^2 = 1$  presents distortion due to the small secondary droplets upstream of the parent droplet, as

shown in Figure 5.44 b). These secondary droplets show momentum and mass interchanges with the parent droplet because the secondary droplets are also evaporating, as shown in Figure 5.44 a), b) and e).

Figure 5.44 d) shows that the bubble is formed where the droplet has reached the saturation temperature at the liquid phase and the core is heating up while the droplet's surface is at the saturation point.

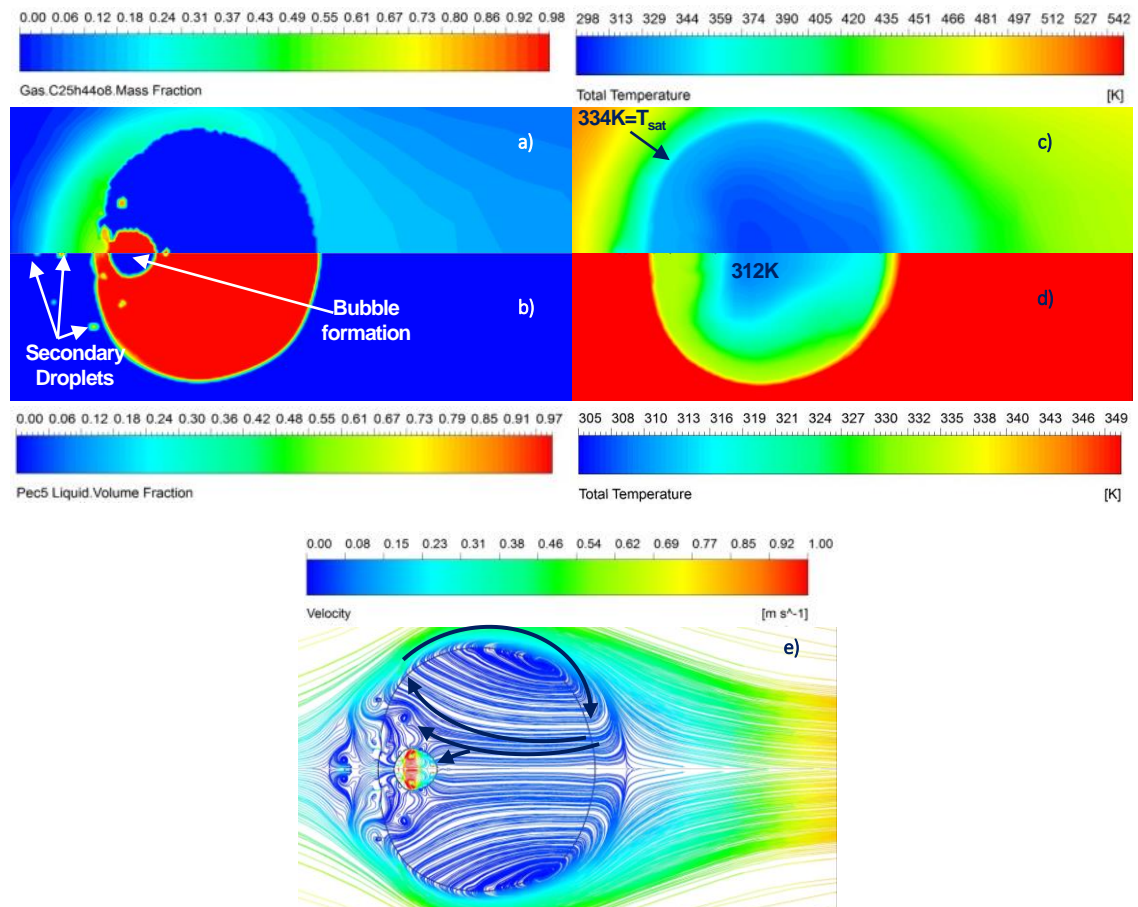


**Figure 5.44. Contours and streamlines at  $\left(\frac{D}{D_0}\right)^2 = 0.99$  and  $0.023$  s for a droplet with an initial diameter of  $200 \mu\text{m}$  under airflow at  $1 \text{ m/s}$ : a) oil vapour mass fraction, b) liquid volume fraction, c) external temperature, d) internal temperature, e) velocity streamlines**

Figure 5.45 a) and b) show a comparison of the velocity streamlines of both the cases, where it shows that the flow patterns change for each case. The case with an external

velocity of 5 m/s presents two vortices dividing the droplet in half, contrary to the case with an external velocity of 1 m/s where the flow pattern is still formed by a spherical vortex and an internal wake. In addition, for the case at 1 m/s there is the formation of a bubble and secondary droplets that is not observed for the case at 5 m/s. The formation of the external wake is disintegrated with the generation of the secondary droplets, which creates small vortices around them.

In summary, the droplet's surrounding velocity might affect the internal flow pattern and consequently the heat transfer distribution; however, the evaporation rate is higher for the case with a higher velocity around the droplet (i.e. 5 m/s).

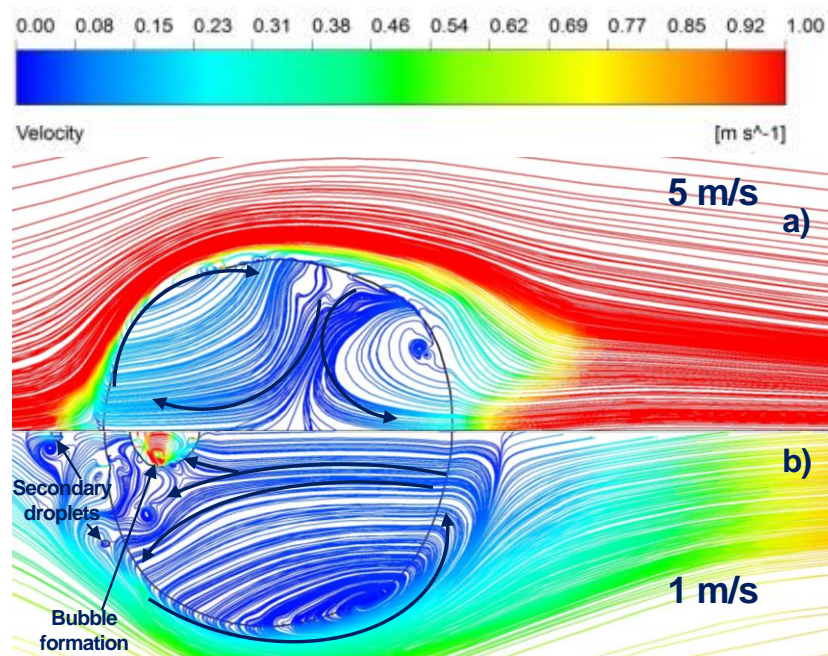


**Figure 5.45. Comparison of velocity streamlines of two cases varying the air velocity with an initial droplet diameter of 200  $\mu\text{m}$  and air at 550 K at  $\left(\frac{D}{D_0}\right)^2 = 0.99$ : a) streamlines of internal velocity for the case at 5 m/s, b) streamlines of internal velocity for the case at 1 m/s**

Figure 5.46 a) and b) indicate that the oil vapour distribution is extended over the droplet's entire surface, with a higher concentration at the rear of approximately 48%. This means that the interface has reached the saturation temperature around the droplet, but the core is still 10 K colder than the surface, as observed in Figure 5.46 c) and d). This thermal distribution is mainly due to the flow field, which divides the droplet into two with an internal wake in each half as shown in Figure 5.46 e).

Figure 5.46 a) and b) indicate the formation of a second bubble. Each bubble is located in each half of the droplet and both bubbles are in the regions where the internal temperature has reached the saturation temperature. Figure 5.46 e) indicates recirculation inside the bubbles. This phenomena has been observed before where the recirculation inside the bubble might enlarge it, creating internal instability and generating vorticity pairs with opposite directions due to mass and momentum interchanges at the bubble's surface (Zhang et al., 2018).

The droplet's internal circulation is influenced by the bubble formation and the associated recirculation causes distortion due to the viscous shear at the gas-liquid interface between bubbles and droplet. In addition, the mass and momentum interchanges at the bubble's interface might form a chaotic motion, which has previously been observed experimentally in burning droplets (Miglani et al., 2014). This chaotic motion is observed in Figure 5.46 e) next to the bubbles with small vortices in opposite directions at the bubble's interface, as mentioned before by (Zhang et al., 2018).

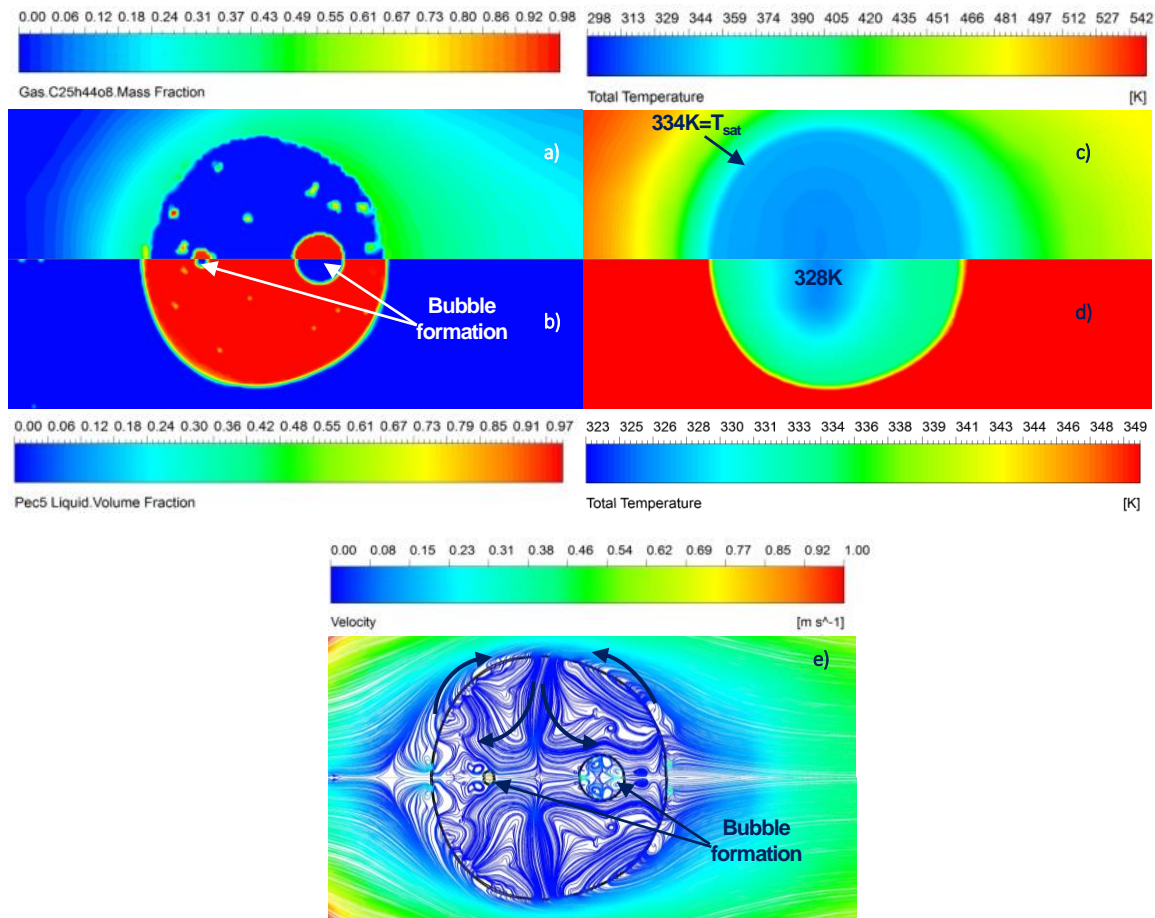


**Figure 5.46. Contours and streamlines at  $\left(\frac{D}{D_0}\right)^2 = 0.97$  and  $0.039$  s for a droplet with an initial diameter of  $200 \mu\text{m}$  under airflow at  $1 \text{ m/s}$ : a) oil vapour mass fraction, b) liquid volume fraction, c) external temperature, d) internal temperature, e) velocity streamlines**

Figure 5.47 a) and b) show a comparison of the velocity streamlines to observe the influence on the droplet's internal circulation at  $\left(\frac{D}{D_0}\right)^2 = 0.97$  of varying the air velocity with one case at  $5 \text{ m/s}$  and the other at  $1 \text{ m/s}$ , respectively. Figure 5.47 a) indicates that the case with air velocity of  $5 \text{ m/s}$  has a vortex formation in the downstream half of the droplet, which might be associated with the bubble being formed. Moreover, the droplet is not divided into two main halves as is the case in Figure 5.47 b); this is probably due to the temperature being more uniform at the droplet's interior for the case at  $5 \text{ m/s}$ , while

the temperature distribution in the case with air at 1 m/s shows the core being 10 K cooler than in other droplet regions (see Figure 5.46 d)). The case with air at 5 m/s in Figure 5.47 a) shows secondary droplets detached from the parent droplet at the front, contrary to the case in Figure 5.47 b). The case with an air velocity of 1 m/s is given in Figure 5.47 b) which shows two bubbles, one of which is located in the downstream half, similar to the case with a velocity of 5 m/s in Figure 5.47 a).

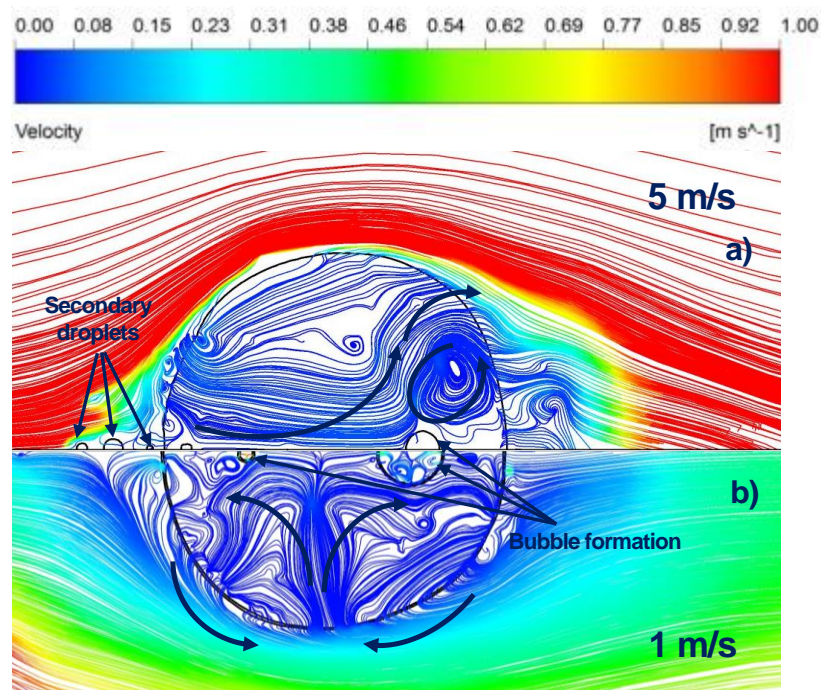


**Figure 5.47. Comparison of velocity streamlines of two cases varying the air velocity with an initial droplet diameter of 200  $\mu\text{m}$  and air at 550 K at  $\left(\frac{D}{D_0}\right)^2 = 0.97$ : a) streamlines of internal velocity for the case at 5 m/s, b) streamlines of internal velocity for the case at 1 m/s**

In general, for low air velocities, the formation of bubbles occurs sooner due to the temperature distribution taking a long time to reach uniformity and, as a consequence, there are high-temperature gradients inside the droplet, and it was noted that the bubbles are formed where there are two regions with high-temperature gradients.

## 5.2.5 Effect of bearing chamber ambient temperature

### 5.2.5.1 *Effect of varying bearing chamber ambient temperature on evaporation rate*

The effect of ambient temperature on evaporation rate was studied by varying this parameter for three different values, namely 550 K, 450 K and 350 K. These three values can be found in the bearing chamber conditions, as discussed in Section 2.1.5.1 and summarised in Table 2.2.

The initial droplet temperature is 298 K in all cases; this is to observe the heating-up period and its duration, which is important in terms of bearing chamber application because the droplets could be injected from the bearings with temperatures from 303.15 K to 403.15 K (Kanike et al., 2012). Consequently, some droplets might be travelling in the core flow during the heating-up period and others might be travelling during the phase-change stage due to the saturation temperature of PEC5 being 334 K (Razzouk et al., 2007).

The initial droplet diameter was kept at 200  $\mu\text{m}$  and the air velocity kept at 5 m/s to analyse the evaporation rate combining high ambient velocity and high ambient temperature. Thus, the combination of high ambient velocity and high ambient temperature enhanced the evaporation rate and reduced the droplet diameter considerably faster than the cases with temperatures of 450 K and 350 K, as shown in Figure 5.48.

Figure 5.48 shows that the droplet diameter reduces sharply for the case at 550 K. When the droplet diameter has diminished by 7% of its initial diameter, the other two cases are still in the heating-up period. Conversely, the case with an ambient temperature of 350 K holds a longer heating-up period, which finished at 0.12 s, starting the droplet diameter reduction at a rate of 0.007  $\text{mm}^2/\text{s}$ .

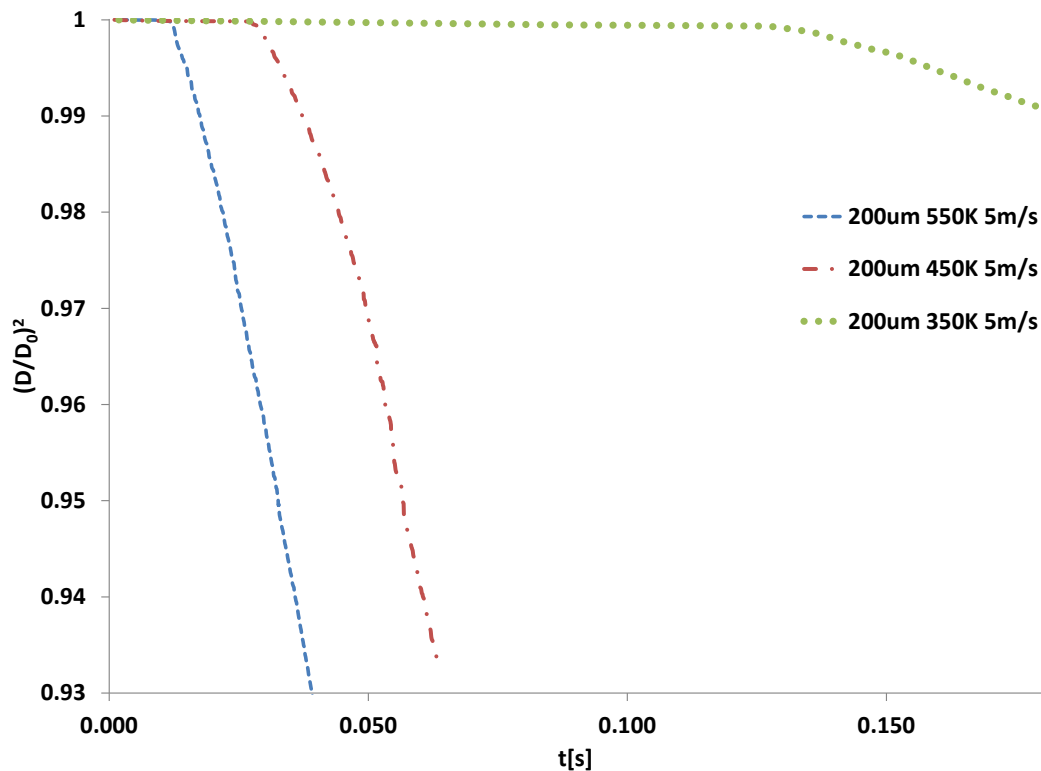


**Figure 5.48. Non-dimensional squared diameter evolution for an initial droplet diameter of 200  $\mu\text{m}$  varying the air inlet temperature**

Figure 5.49 reveals that the evaporation rate increases with the increase in air temperature. From the average values for each case, the evaporation rate in the case with air at 550 K is around 30% higher than the case with air at 450 K and 90% higher than the case with air at 350 K.

Generally speaking, the evaporation constants (obtained from equations 3.29 and 3.30) for the cases with air at 550 K, 450 K and 350 K are  $0.140 \text{ mm}^2/\text{s}$ ,  $0.109 \text{ mm}^2/\text{s}$  and  $0.007 \text{ mm}^2/\text{s}$ , respectively. This means that the evaporation constant in the case with air temperature of 550 K is around 22% higher than the case with air at 450 K and 95% higher than the case with air at 350 K, which is roughly similar to the values of the best-fit curve discussed above for Figure 5.49.

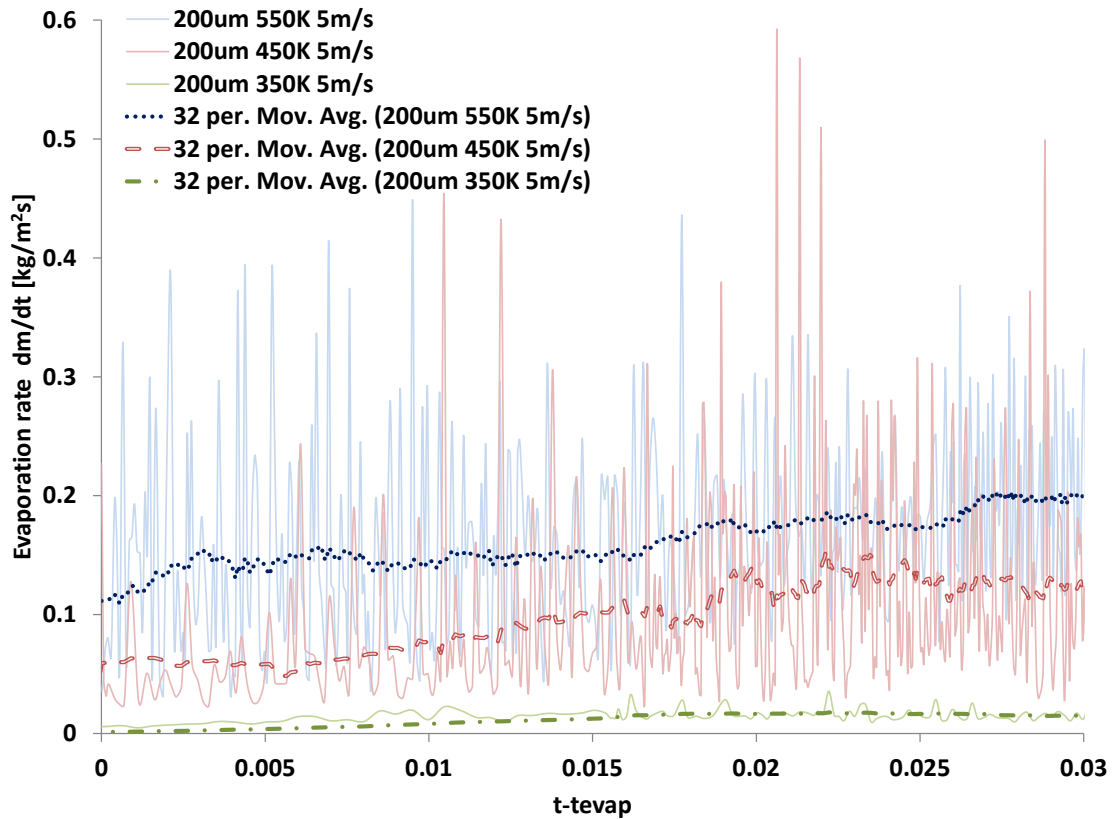


**Figure 5.49. Variation of evaporation rate over a droplet's surface area for different ambient temperatures**

Therefore, the average values can be used to predict the evaporation rates at different air temperatures (from 350 K to 550 K), as shown in Figure 5.50 where the trend is approximated to a linear regression. The trend shows us that the evaporation rate increases with the ambient temperature and for this reason it is recommended to study higher temperatures than 550 K to observe whether the trend still follows a linear regression.

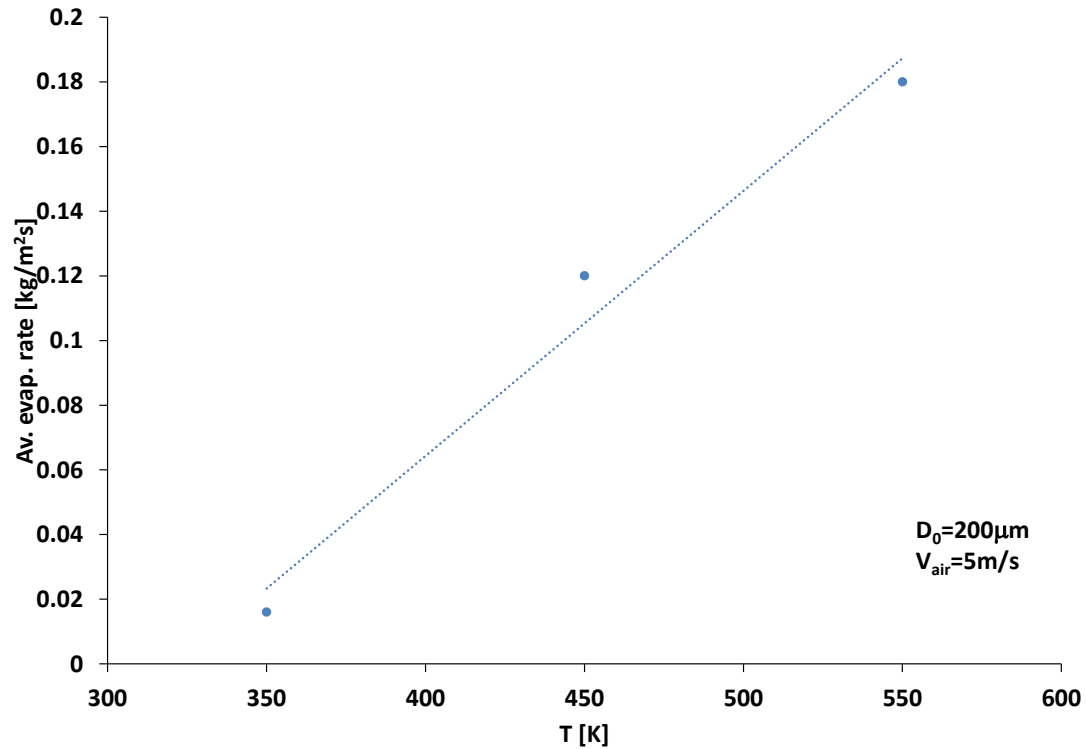


**Figure 5.50. Effects of air temperature on the average evaporation rate per surface area for a droplet with an initial diameter of 200  $\mu\text{m}$  and air velocity of 5 m/s**

#### 5.2.5.2 *Effect of varying bearing chamber ambient temperature on heat transfer at the droplet's surface*

The heat transfer ratio, which evaluates the heat transferred from the droplet's surface to the core and the heat transferred from the environment to the droplet's surface, was analysed for three different ambient temperatures, namely 550 K, 450 K and 350 K, while keeping the initial droplet diameter and air velocity constant for the three cases mentioned. As can be seen in Figure 5.51, the heat transfer ratio shows similar peak values for the cases with air temperatures of 450 K and 350 K. Additionally, analysing the maximum values of the three cases, it is noted that the case with an ambient temperature of 550 K has a heat transfer ratio that is 0.4% lower than the other two cases, which means that for this case the temperature gradient from the environment to the droplet's surface is greater than the gradient from the droplet's surface to the core.

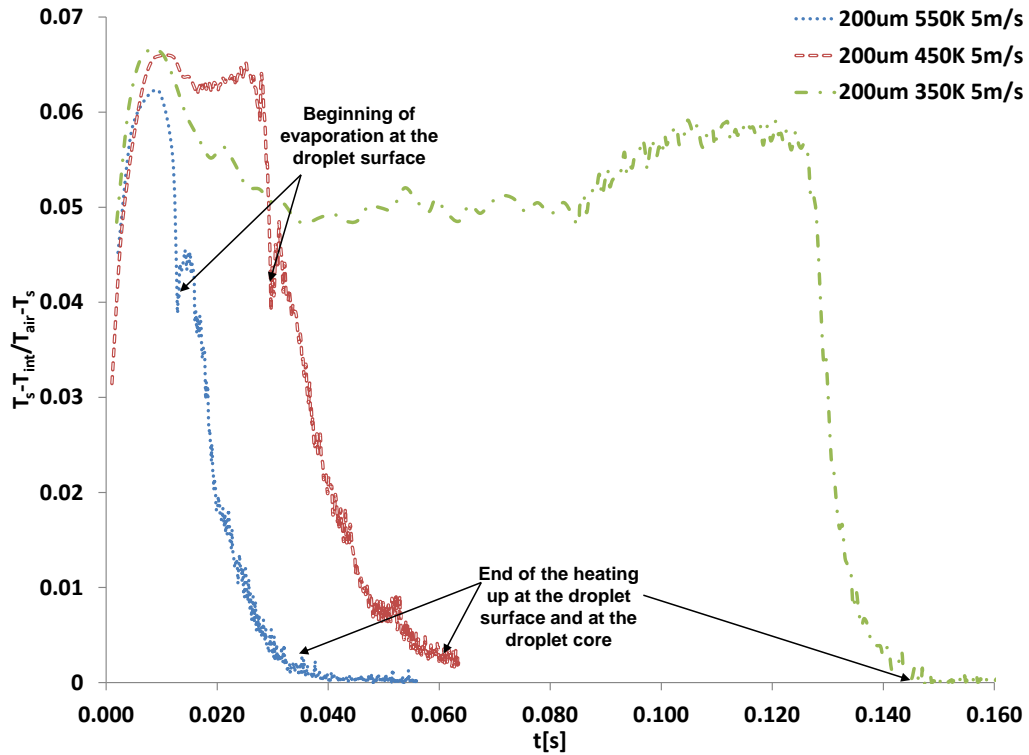


**Figure 5.51. Heat transfer ratio for different ambient temperatures**

### 5.2.5.3 *Effect of varying bearing chamber ambient temperature on internal circulation*

#### 5.2.5.3.1 *Quantitative analysis of the effect of varying bearing chamber ambient temperature on internal circulation*

In this section, the fluctuations of the average velocity magnitude in the droplet's interior by varying the temperature of the surroundings are evaluated. These fluctuations are evaluated similarly to the method described in Section 5.2.4.3.1 and Section 5.2.3.1, where the average velocity magnitude is measured in the area with a VOF from 0.8 to 1 as presented in Figure 5.22.

In previous sections it was discussed that the thermal gradients within the droplet drive the flow field and create the vortex formation within the droplet. Based on that, it is interesting to analyse the effects of airflow temperature on the droplet's internal

circulation. Hence, three air temperatures were studied, namely 550 K, 450 K and 350 K. Each case had the same initial droplet diameter of 200  $\mu\text{m}$  and the same air velocity of 5 m/s.

With this in mind, the average velocity magnitude within the droplet was compared in Figure 5.52, which indicates that in all cases the velocity magnitude increases with an increase in air temperature. The average values of the velocity magnitude are 0.04 m/s, 0.03 m/s and 0.01 m/s for the cases with air temperatures at 550 K, 450 K and 350 K respectively, where the case with air temperature at 550 K is 25% higher than the case with air at 450 K and 75% higher than the case with air at 350 K. Therefore, the temperature gradient at the droplet's interface might affect the droplet's internal velocity magnitude.

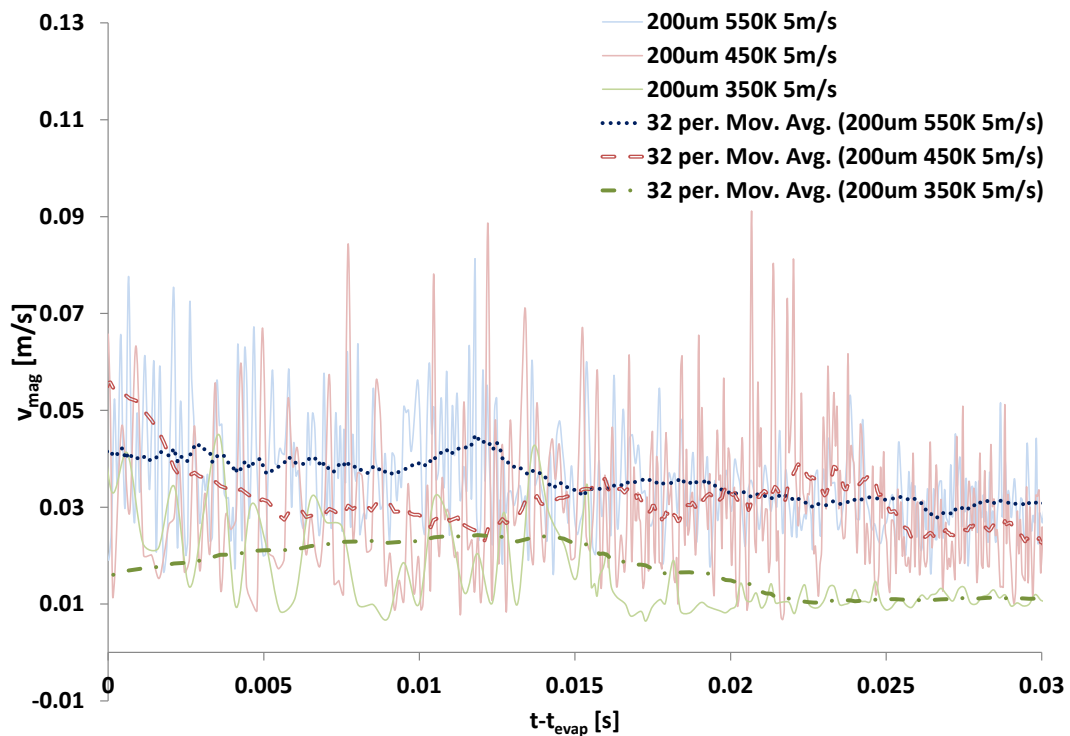


**Figure 5.52. Comparison of the velocity magnitude at the droplet's interior varying the temperature of air**

### 5.2.5.3.2 Qualitative analysis of the effect of varying bearing chamber ambient temperature on internal circulation

This section analyses the effect of varying the bearing chamber ambient temperature on the internal circulation for different stages of the evaporation process, namely  $\left(\frac{D}{D_0}\right)^2 = 1$ ,  $\left(\frac{D}{D_0}\right)^2 = 0.99$  and  $\left(\frac{D}{D_0}\right)^2 = 0.97$ . Figure 5.53 indicates that the values mentioned above correspond to the heating-up period and transient evaporation. In comparison with the case with an external temperature of 550 K in Figure 5.29, the difference between the temperatures at the droplet's surface and at the core is around 5 K lower for the case with an external temperature of 450 K.

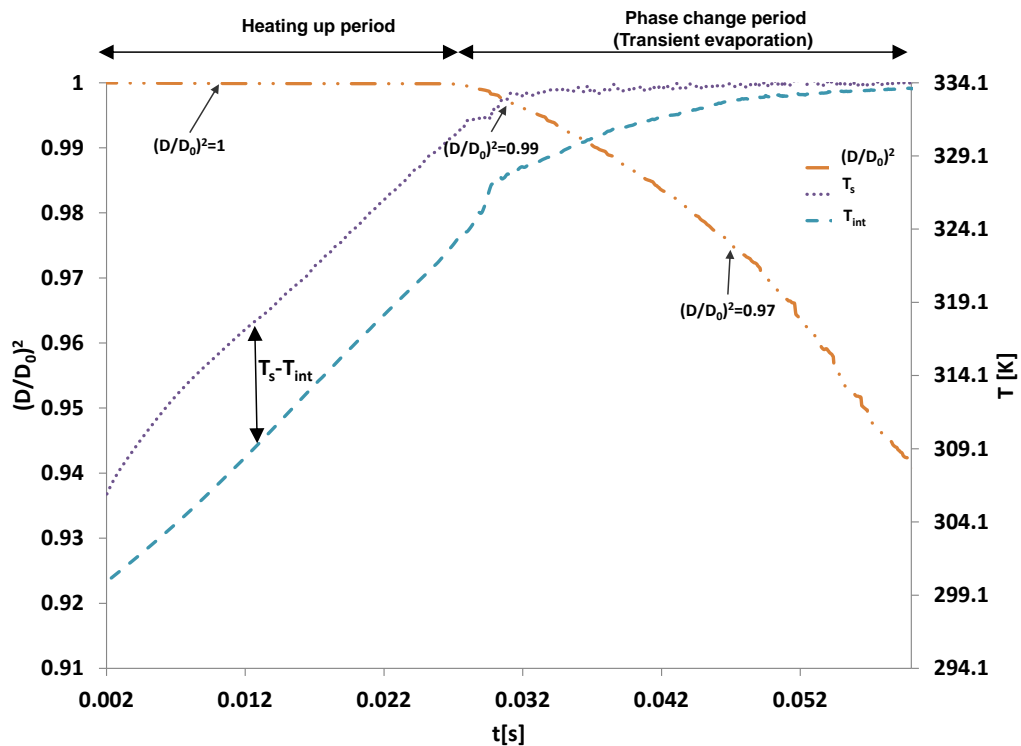
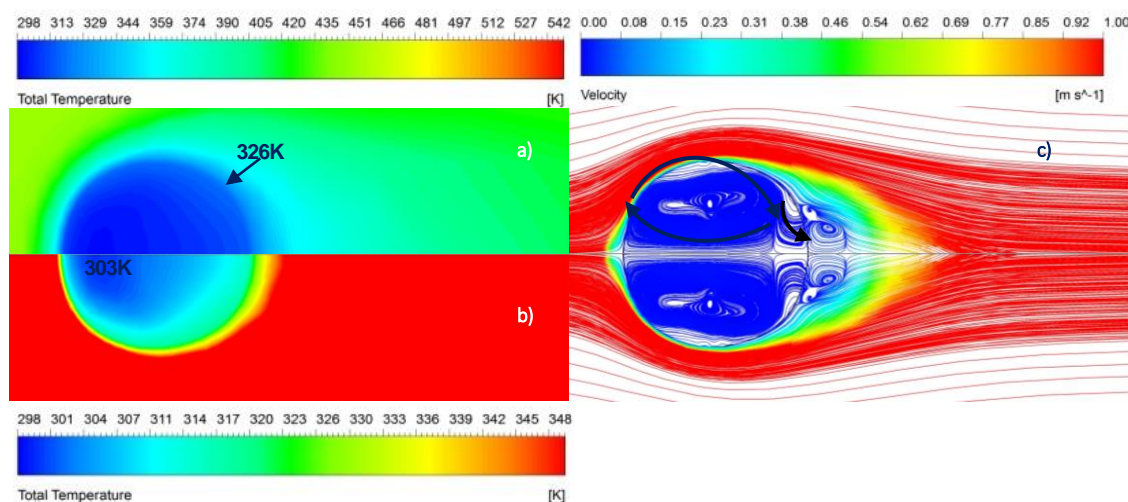


**Figure 5.53. Temporal evolution of droplet normalised square diameter versus temperature evolution at the droplet surface  $T_s$  and the droplet core  $T_{int}$  for an initial diameter of 200  $\mu\text{m}$ , with air at 450 K and 5 m/s**

In this section, the contours of oil mass fraction, liquid volume fraction and the temperature at the droplet's exterior and core are presented, as well as the velocity streamlines. The contours and the streamlines are analysed at  $\left(\frac{D}{D_0}\right)^2 = 1$ ,  $\left(\frac{D}{D_0}\right)^2 = 0.99$  and  $\left(\frac{D}{D_0}\right)^2 = 0.97$  for the cases with air temperatures at 450 K and 350 K and compared with the case at 550 K, which is presented in Section 5.2.3.3.2.

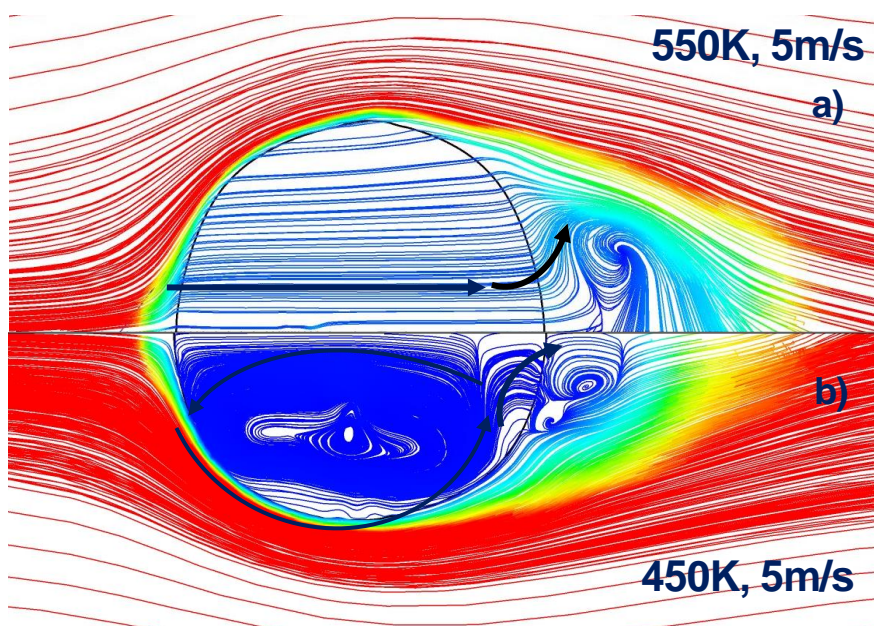
Figure 5.54 a) and b) show the contours of temperature, where it can be seen that the saturation point has not been reached and evaporation has not yet started. Figure 5.54 b) indicates that the temperature distribution in the droplet's interior shows the coldest region in the upstream half of the droplet, similar to the case with a temperature of 550 K as discussed earlier in Section 5.2.3.3.2.

Figure 5.54 c) shows the velocity streamlines where the Hill's vortex is clearly distinguished. Additionally, part of the internal flow is linked with the external wake formed at the rear part of the droplet.



**Figure 5.54. Contours and streamlines at  $\left(\frac{D}{D_0}\right)^2 = 1$  and 0.01 s for a droplet with an initial diameter of 200  $\mu\text{m}$  under airflow at 450 K: a) external temperature, b) internal temperature, c) velocity streamlines**

Figure 5.55 a) and b) show a comparison of varying the air temperature with a case at 550 K and the other at 450 K, respectively, both at  $\left(\frac{D}{D_0}\right)^2 = 1$ . The internal flow pattern for the first case (Figure 5.55 a)) does not present vorticity at the droplet's interior; however, there is the formation of an external wake, which is physically longer than in the second case Figure 5.55 b).



**Figure 5.55. Comparison of velocity streamlines of two cases varying the air velocity with an initial droplet diameter of 200  $\mu\text{m}$  and air at 5 m/s at  $\left(\frac{D}{D_0}\right)^2 = 1$ : a) streamlines of internal velocity for the case at 550 K, b) streamlines of internal velocity for the case at 450 K**

Figure 5.56 a), b), c) and d) show the contours of oil vapour mass fraction, liquid volume fraction, and the droplet's external and internal temperatures, respectively, at  $\left(\frac{D}{D_0}\right)^2 = 0.99$  and 0.031 s.

Figure 5.56 a) depicts the droplet's surface evaporating with the highest value of 73% of oil vapour mass fraction over air mass fraction. The evaporation is mainly at the

rear side of the droplet, which consequently shows a deformation on the surface. In the same way, Figure 5.56 b) shows the formation of small bubbles near to the surface, which are located in the region where the liquid is saturated.

Figure 5.56 e) shows the velocity streamlines, where the flow pattern has a displaced spherical vortex and a small vortex in the downstream half of the droplet with mass and momentum interchanges with the external wake.

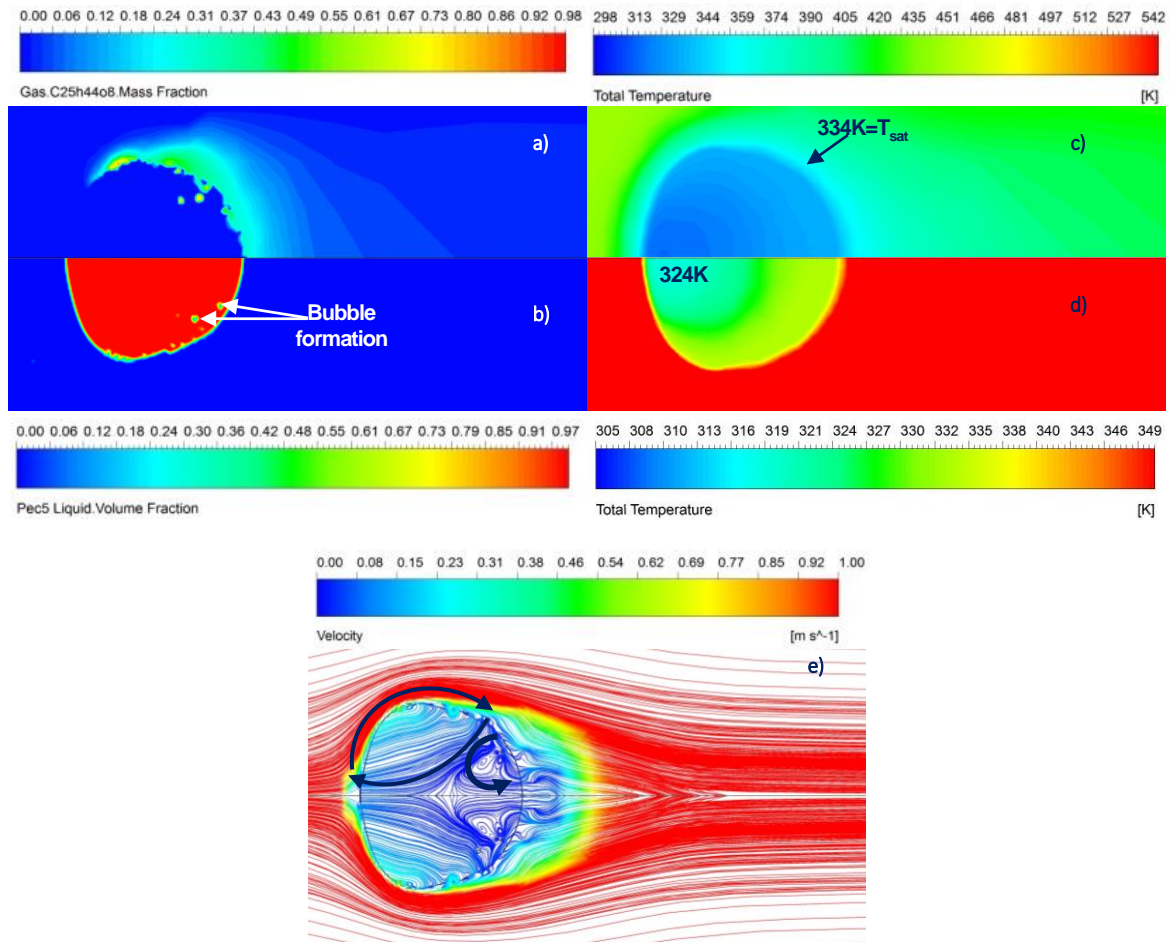
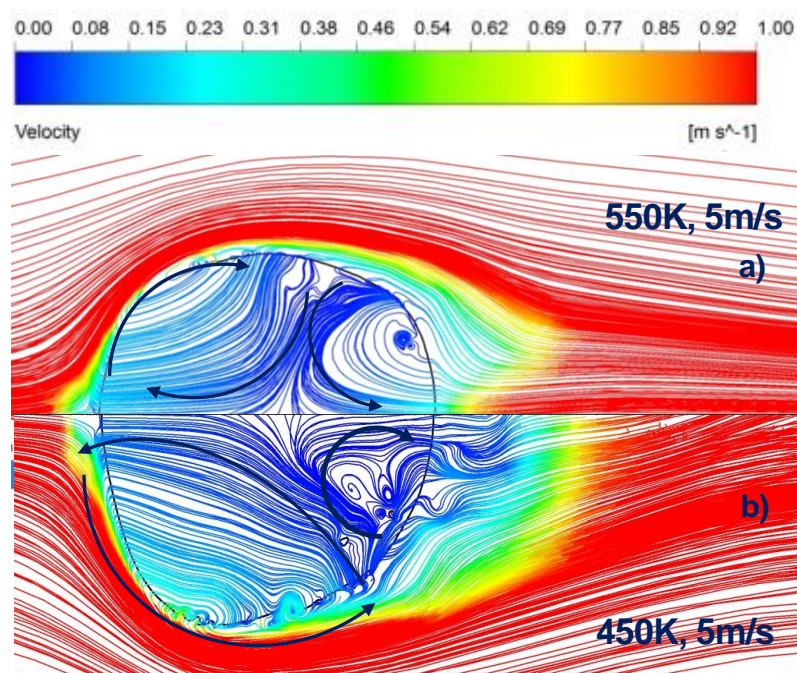


Figure 5.56. Contours and streamlines at  $\left(\frac{D}{D_0}\right)^2 = 0.99$  and  $0.031$  s for a droplet with an initial diameter of  $200 \mu\text{m}$  under airflow at  $450 \text{ K}$ : a) oil vapour mass fraction, b) liquid volume fraction, c) external temperature, d) internal temperature, e) velocity streamlines

Figure 5.57 a) and b) display a comparison of the cases with air temperatures at 550 K and 450 K, respectively, at  $\left(\frac{D}{D_0}\right)^2 = 0.99$ , where both cases show a similar flow pattern with the droplet divided into two halves. However, in Figure 5.57 b) the main vortex looks longer for the case with airflow at 450 K than for the case with airflow at 550 K (see Figure 5.57 a)). In addition, Figure 5.57 b) shows droplet deformation at the rear; this might be due to the temperature of the droplet's surface reaching saturation in the region where the deformation is found.



**Figure 5.57. Comparison of velocity streamlines of two cases varying the air velocity with an initial droplet diameter of 200  $\mu\text{m}$  and air at 5 m/s at  $\left(\frac{D}{D_0}\right)^2 = 0.99$ : a) streamlines of internal velocity for the case at 550 K, b) streamlines of internal velocity for the case at 450 K**

Figure 5.58 a) and b) depict that the oil vapour mass fraction has surrounded the droplet's surface with bubbles inside the liquid phase at  $\left(\frac{D}{D_0}\right)^2 = 0.97$  and 0.047 s. Figure

5.58 c) and d) show that the core is heating up to 331 K, but the temperature of the surface is saturated; in other words, the transition period is finishing.

Additionally, the internal flow pattern direction is from the front to the rear side of the droplet, as seen in Figure 5.58 e). There are some vortices due to the bubble mass flux at the interface and the external wake is formed downstream of the droplet. As a difference from the previous cases analysed, there are small bubbles formed behind the main bubble, which might mean that all of them will coalesce to generate a large bubble due to the high convective flow at the droplet's interior.

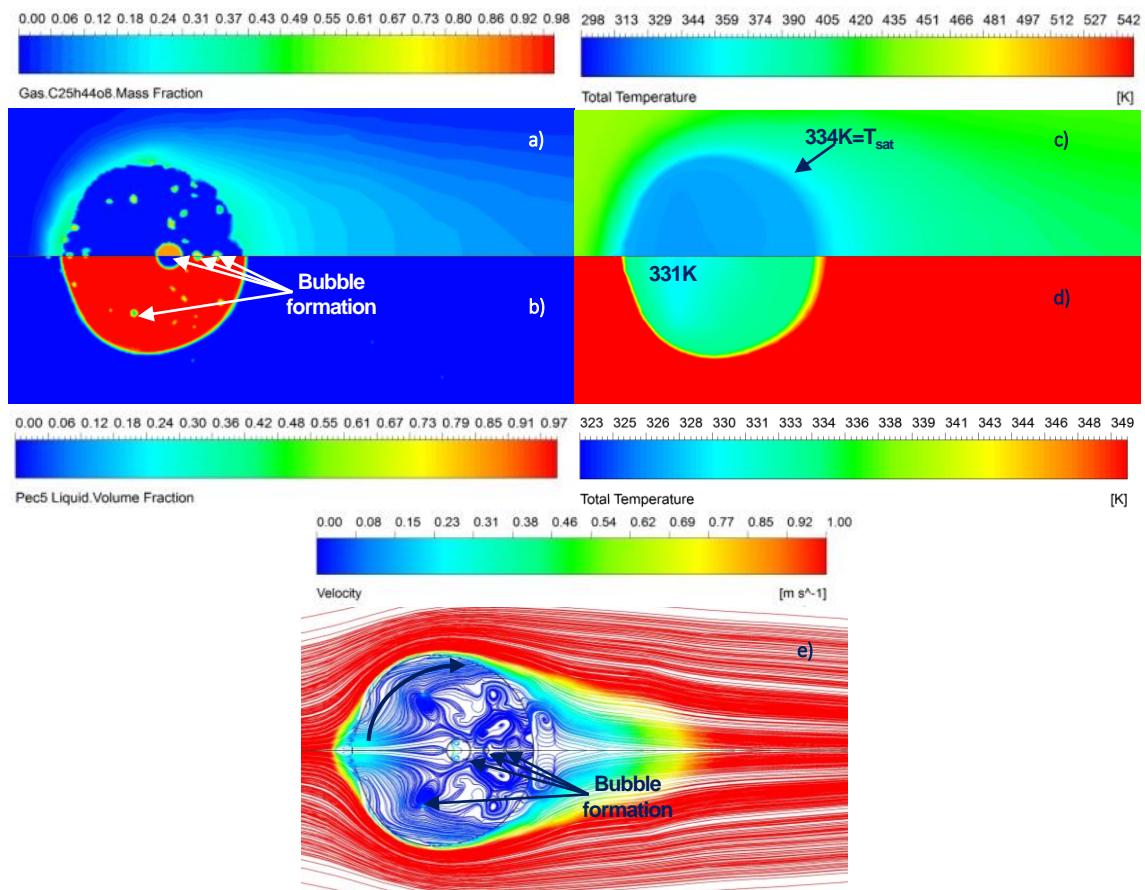
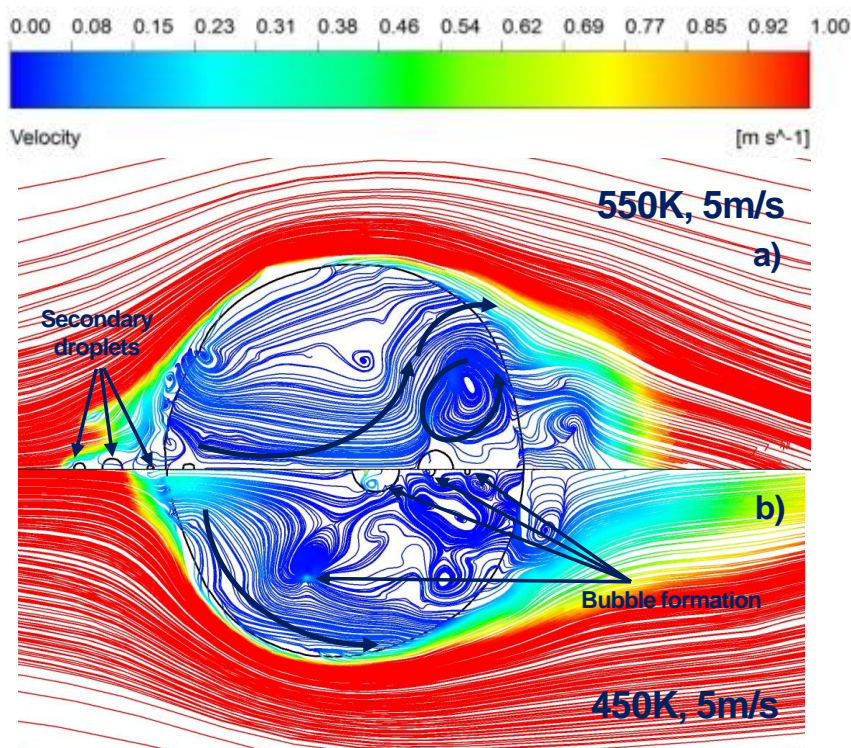


Figure 5.58. Contours and streamlines at  $\left(\frac{D}{D_0}\right)^2 = 0.97$  and  $0.047$  s for a droplet with an initial diameter of  $200 \mu\text{m}$  under airflow at  $450 \text{ K}$ : a) oil vapour mass fraction, b) liquid volume fraction, c) external temperature, d) internal temperature, e) velocity streamlines

Figure 5.59 a) and b) compare the velocity streamlines when the air is at 550 K and 450 K, respectively, at  $\left(\frac{D}{D_0}\right)^2 = 0.97$ . The first case in Figure 5.59 a) shows a formation of secondary droplets at the rear of the droplet and a small vortex generated at the back. The external wake is larger than the second case; this is because the first case has a higher evaporation rate, which is mixed with the air at higher velocity, than the second case. In Figure 5.59 b) the second case shows the formation of bubbles in the downstream half of the droplet, which influences the flow pattern.



**Figure 5.59. Comparison of velocity streamlines of two cases varying the air velocity with an initial droplet diameter of 200  $\mu\text{m}$  and air at 5 m/s at  $\left(\frac{D}{D_0}\right)^2 = 0.97$ : a) streamlines of internal velocity for the case at 550 K, b) streamlines of internal velocity for the case at 450 K**

Furthermore, for the case with an air temperature of 350 K, the internal flow pattern, oil mass fraction, liquid volume fraction, and external and internal droplet temperatures

are analysed during the heating-up period and at the end of the phase-change period, namely  $\left(\frac{D}{D_0}\right)^2 = 1$  and  $\left(\frac{D}{D_0}\right)^2 = 0.99$ . Figure 5.60 shows the stages mentioned, where the transient evaporation is shorter than the cases with air at 550 K and 450 K and the average temperature gradient difference between the droplet's surface and core is just 2 K.

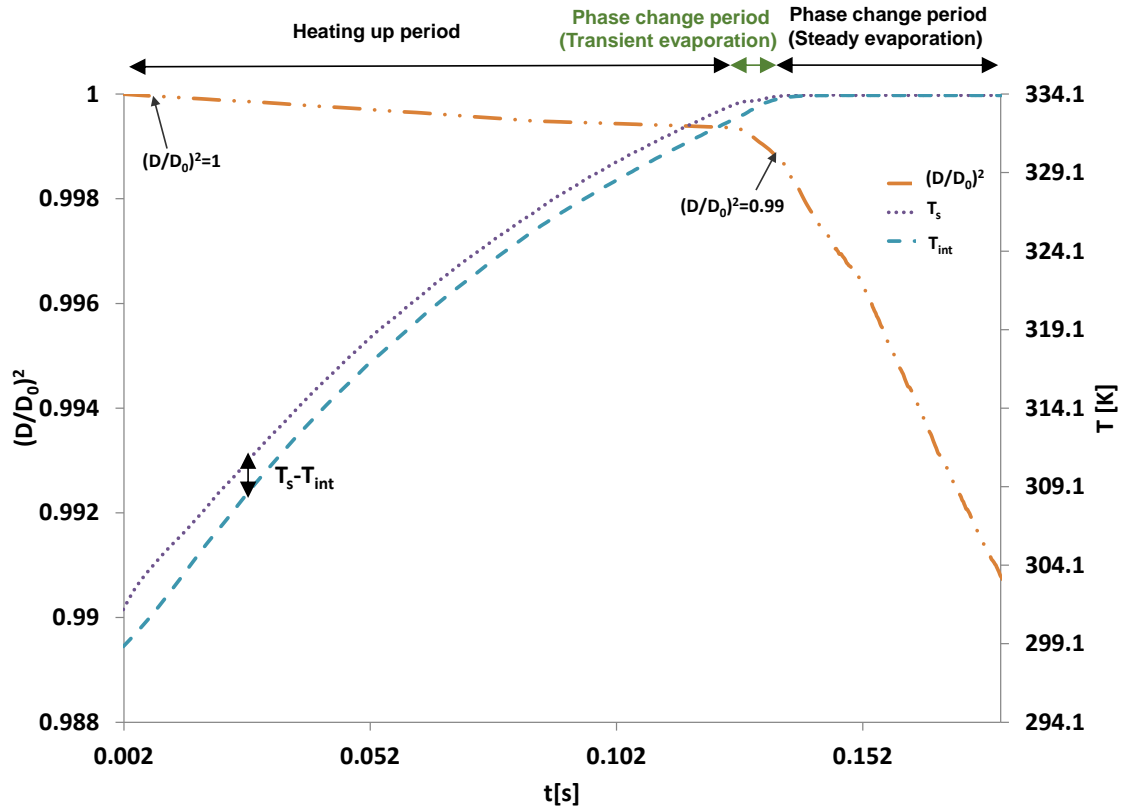
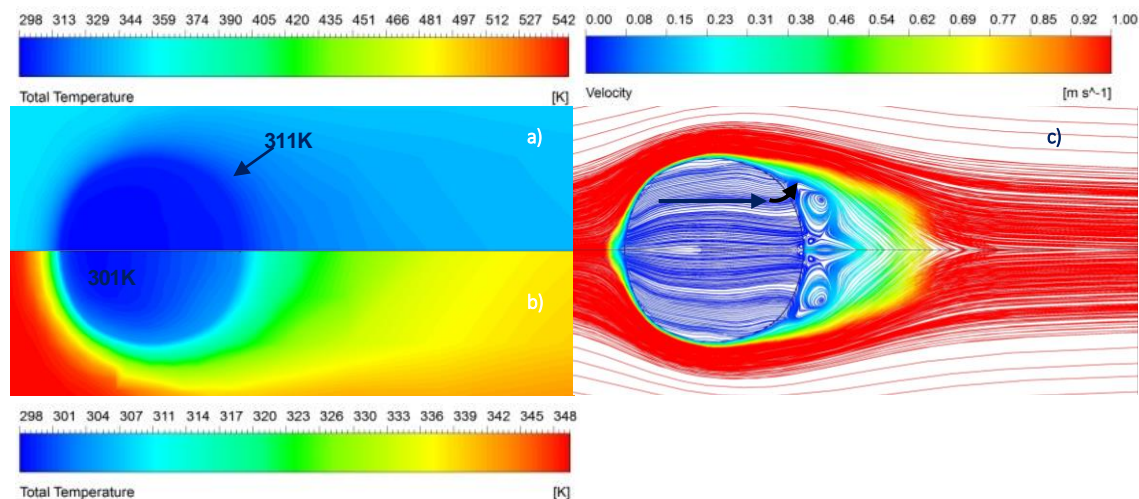


**Figure 5.60. Temporal evolution of droplet normalised square diameter versus temperature evolution at the droplet surface  $T_s$  and the droplet core  $T_{int}$  for an initial diameter of 200  $\mu\text{m}$ , with air at 350 K and 5 m/s**

Figure 5.61 a) and b) depict the droplet's internal and external temperatures and Figure 5.61 c) shows the velocity streamlines, all at  $\left(\frac{D}{D_0}\right)^2 = 1$  and 0.008 s. Similarly, in the cases at 550 K and 450 K, the coldest region of the liquid phase is located in the upstream half of the droplet. Conversely, the case at 350 K shows lower temperature gradients than the other two cases mentioned above; for instance, at 0.008 s, the droplet's

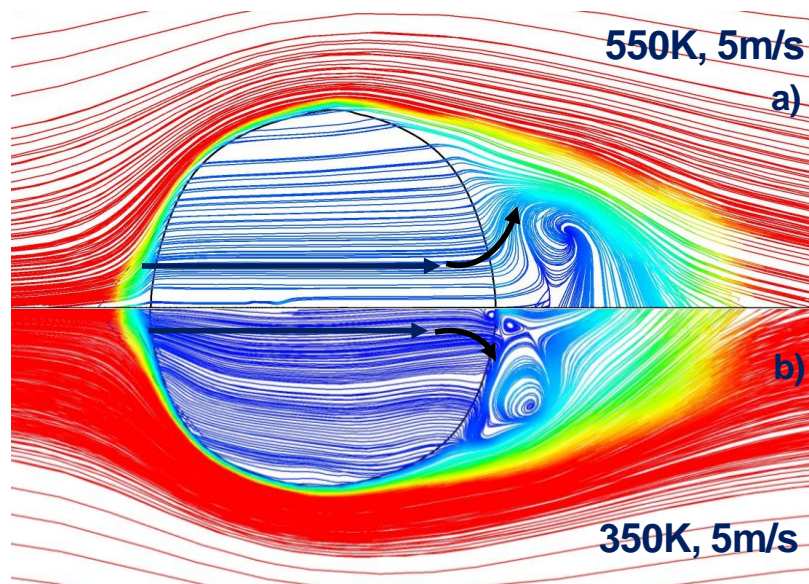
core has a temperature of 301 K, the surface has a temperature of 311 K, the heating-up period is still in process and the oil vapour mass fraction is zero at the droplet's surface.

Figure 5.61 c) indicates that there is no spherical vortex and the internal wake is extended along the droplet. Furthermore, the external wake is present at the rear of the droplet, as in all the cases with an air velocity of 5 m/s.



**Figure 5.61. Contours and streamlines at  $\left(\frac{D}{D_0}\right)^2 = 1$  and 0.008 s for a droplet with an initial diameter of 200  $\mu\text{m}$  under airflow at 350 K: a) external temperature, b) internal temperature, c) velocity streamlines**

Comparing the case with air at 550 K and the case with air at 350 K in Figure 5.62 a) and b) it can be seen that the latter case has an external wake shorter than the former and the internal spherical vortex is not formed in either case at  $\left(\frac{D}{D_0}\right)^2 = 1$ . This is because it is the beginning of the heating-up period and the heat transfer from the droplet's surface to the core is only at the surface and has not extended yet. However, for the case at 550 K, the external wake looks longer than the case at 350 K because the heat transfer rate is higher for the former case.



**Figure 5.62. Comparison of velocity streamlines of two cases varying the air velocity with an initial droplet diameter of 200  $\mu\text{m}$  and air at 5 m/s at  $\left(\frac{D}{D_0}\right)^2 = 1$ : a) streamlines of internal velocity for the case at 550 K, b) streamlines of internal velocity for the case at 350 K**

Additionally, the case with an air temperature of 350 K was analysed in Figure 5.63 a), b), c), d) and e) for  $\left(\frac{D}{D_0}\right)^2 = 0.99$  and 0.135 s. Figure 5.63 a) shows that the oil vapour mass fraction is only present in the downstream half of the droplet and there are no bubbles formed in the liquid phase, as seen in Figure 5.63 b). Moreover, Figure 5.63 c) and d) show that the internal temperature is just 1 K lower than the surface temperature; therefore, the transient evaporation is almost finished.

Figure 5.63 e) shows the Hill's vortex formed along the droplet with a small wake at the rear, which links with the external wake. This pattern was observed in the cases discussed previously and it is more common during the heating-up period and when the transient evaporation has just started.

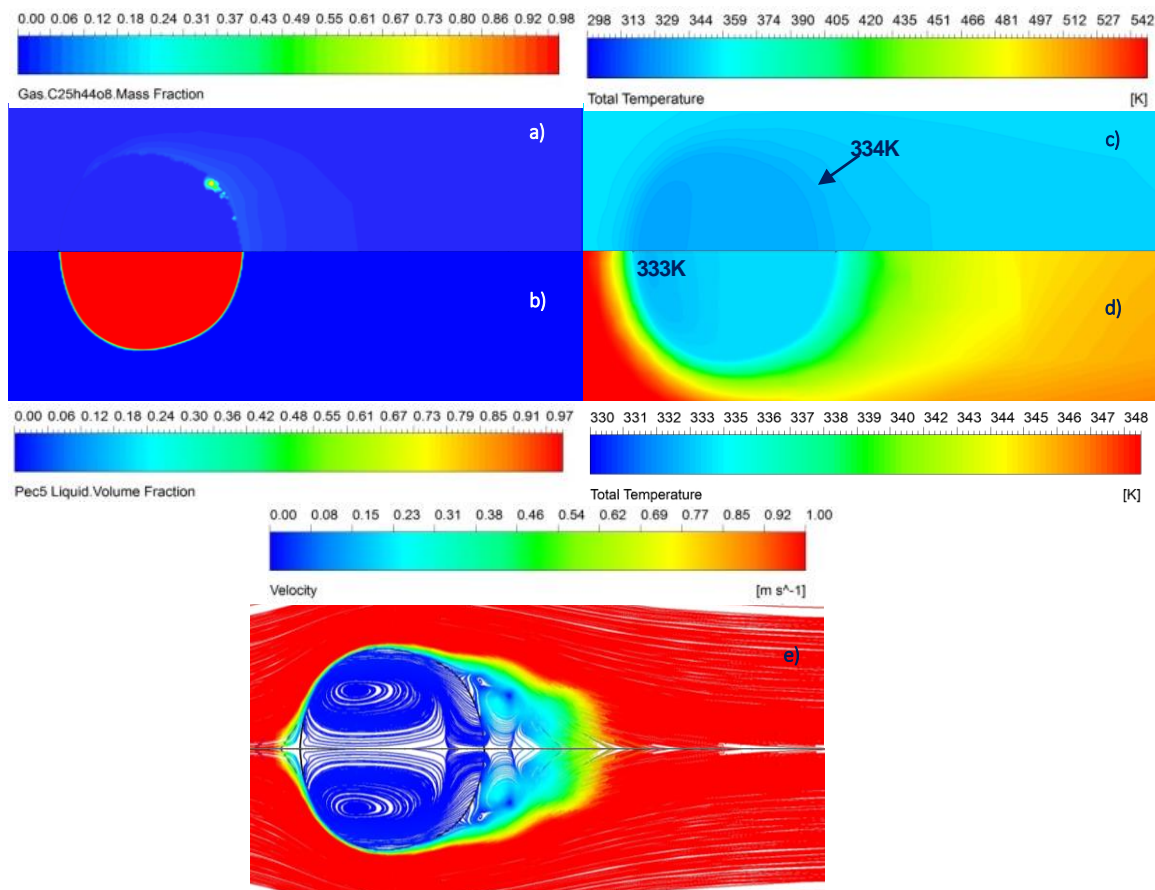


**Figure 5.63. Contours and streamlines at  $\left(\frac{D}{D_0}\right)^2 = 0.99$  and  $0.135$  s for a droplet with an initial diameter of  $200 \mu\text{m}$  under airflow at  $350 \text{ K}$ : a) oil vapour mass fraction, b) liquid volume fraction, c) external temperature, d) internal temperature, e) velocity streamlines**

Figure 5.64 a) and b) show a comparison between both cases varying air temperature of  $550 \text{ K}$  and  $350 \text{ K}$ , respectively. When the air is at  $550 \text{ K}$ , two vortices form and circulate in opposite directions. The vortex centre, which is in the upstream half of the droplet, is displaced to the droplet's surface, contrary to the centre of the Hill's vortex for the case at  $350 \text{ K}$ . This phenomenon might be because the heat transfer takes longer for the case at  $350 \text{ K}$  than the case at  $550 \text{ K}$  and consequently the velocity inside the droplet is slightly lower for the case at  $350 \text{ K}$ . Therefore, the air temperature influences the internal flow

distribution, with the internal velocity favouring the internal temperature uniformity when the droplet's external temperature is high.

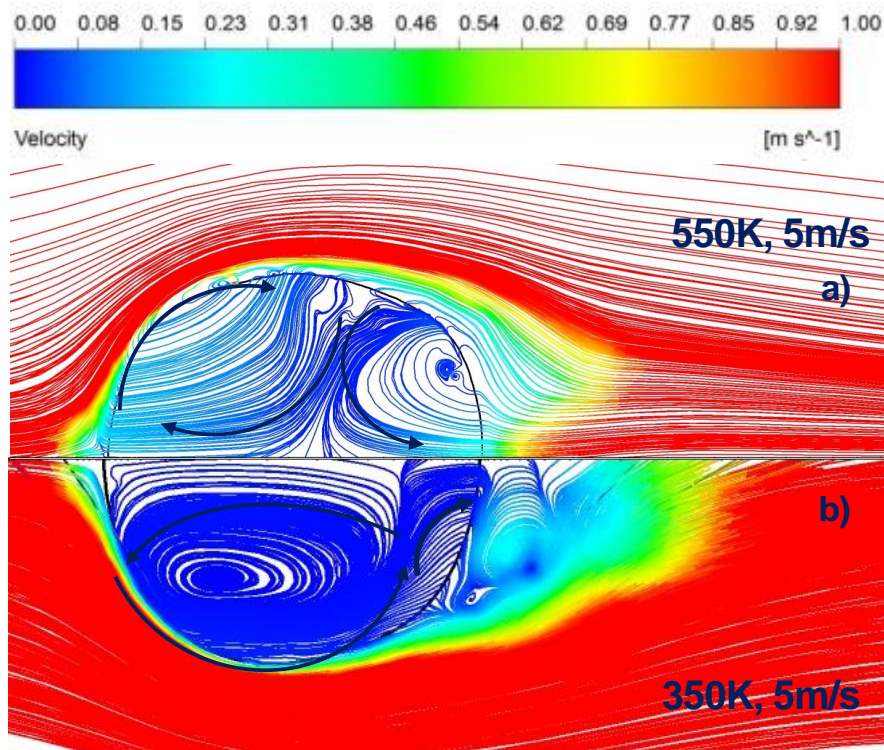
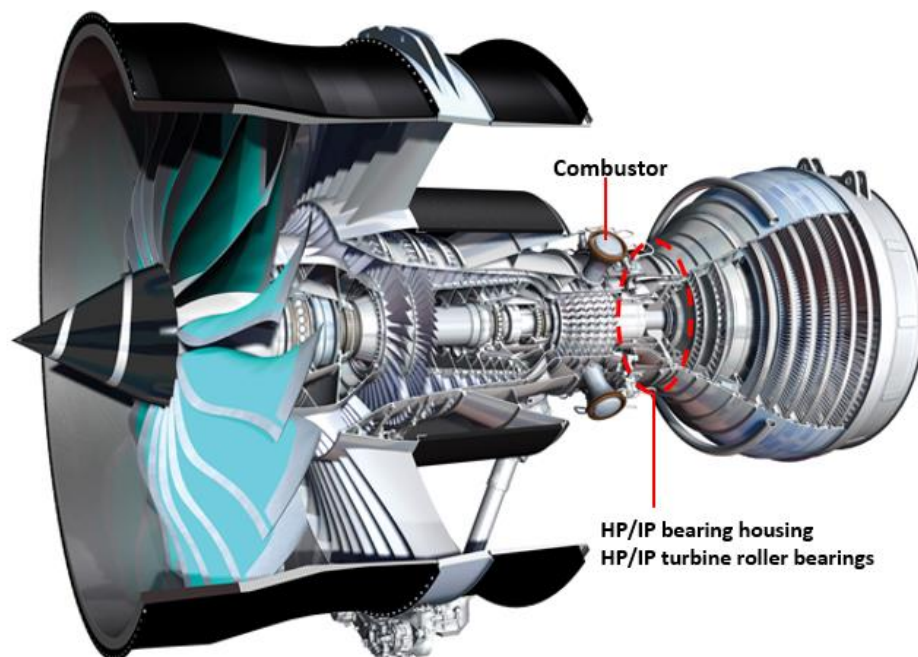


Figure 5.64. Comparison of velocity streamlines of two cases varying the air velocity with an initial droplet diameter of  $200\ \mu\text{m}$  and air at  $5\ \text{m/s}$  at  $\left(\frac{D}{D_0}\right)^2 = 0.99$ : a) streamlines of internal velocity for the case at  $550\ \text{K}$ , b) streamlines of internal velocity for the case at  $350\ \text{K}$

### 5.2.6 Effect of radiation

The intermediate pressure HP/IP bearing chamber is located near to the combustor (see Figure 5.65), which holds a range of temperatures above 1000°C. Hence, it is important to know if the heat transfer from the combustor to the bearing chamber influences the droplet evaporation rate. Thus, the radiation heat transfer was analysed from a parametric study to observe whether the radiation affects the heat and mass transfer from the environment to the droplet, which is travelling in the core flow.



**Figure 5.65. Combustor and HP/IP bearing chamber locations on the Ultrafan engine (Adapted from Rolls-Royce, 2016)**

The parameters were the initial droplet diameter and the temperature at the walls. Three diameters and two wall temperatures were studied, as can be observed in Table 5.4. The two temperatures were proposed according to the operating conditions discussed in Section 2.2.2.1.

**Table 5.4. Cases analysed considering heat transfer by radiation**

Case	$D_0$ [ $\mu\text{m}$ ]	Air		Wall
		T [K]	$u$ [m/s]	T [K]
9	100	550	5	550
10			5	850
11	200	550	5	550
12			5	850
13	500	550	5	550
14			5	850

#### **5.2.6.1 Effect of radiation on evaporation rate**

In Section 5.2.3, it was noted that the evaporation rate increases with a reduction in initial diameter, which is shown in Figure 5.66. This can be observed in the slopes of each case, where the slopes for droplets with an initial diameter of 100  $\mu\text{m}$  are less inclined than others and this means that these droplets have a shorter lifetime than droplets with initial diameters of 200  $\mu\text{m}$  and 500  $\mu\text{m}$ . Therefore, in this section it is discussed whether the heat transfer by radiation increases the evaporation rate for different initial droplet diameters.

A comparison of the cases with an initial droplet diameter of 100  $\mu\text{m}$  shows that radiation affects the heating-up period and the first part of the droplet diameter reduction. Figure 5.66 indicates that the heating-up period is shorter for the cases with an initial diameter of 100  $\mu\text{m}$  exposed to radiation effects. Moreover, after 0.006 s, the evaporation rate of the case without radiation is similar to the case with radiation at 550 K and 1% higher than the case with radiation at 850 K.

For droplets with an initial diameter of 200  $\mu\text{m}$ , the cases with radiation show a heating-up period that is approximately 0.005 s shorter than case without radiation. Furthermore, the cases with radiation show a similar evaporation rate between them but this is higher than case without radiation until 0.018 s. After 0.018 s, the trend for all cases is similar, as shown in Figure 5.66. Therefore, after the heating-up period, radiation presents less of an effect on droplets with an initial diameter of 200  $\mu\text{m}$ . This means that it is convection that affects the evaporation of droplets with an initial diameter of 200  $\mu\text{m}$ , rather than radiation. Figure 5.66 illustrates that the cases with an initial droplet diameter of 500  $\mu\text{m}$  are in the heating-up period, while the cases with diameters of 100  $\mu\text{m}$  and 200  $\mu\text{m}$  are in the phase-change period.

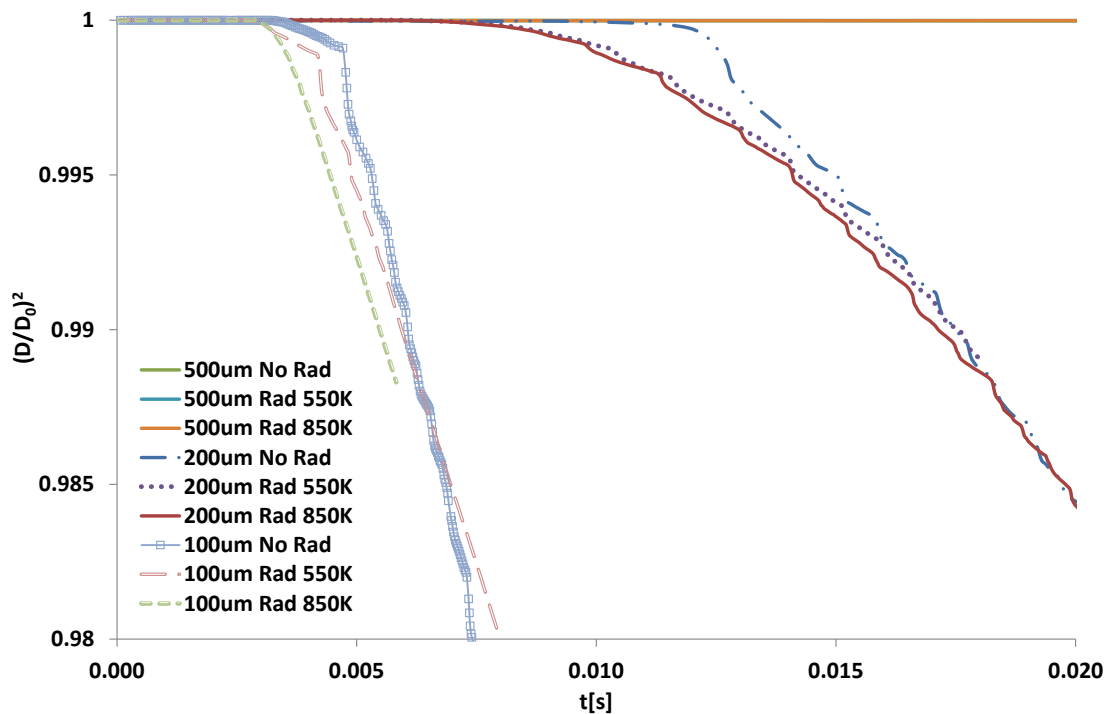


**Figure 5.66. Effect of radiation on temporal evolution of droplet diameter for different initial diameters, with air at 5 m/s and 550 K**

As a result, the cases of droplets with an initial diameter of 500  $\mu\text{m}$  were compared and presented in Figure 5.67. The main differences between the cases with and without radiation are the heating-up period, which is 0.02 s shorter for the cases with radiation, and the evaporation rate, which is higher for the cases with radiation.

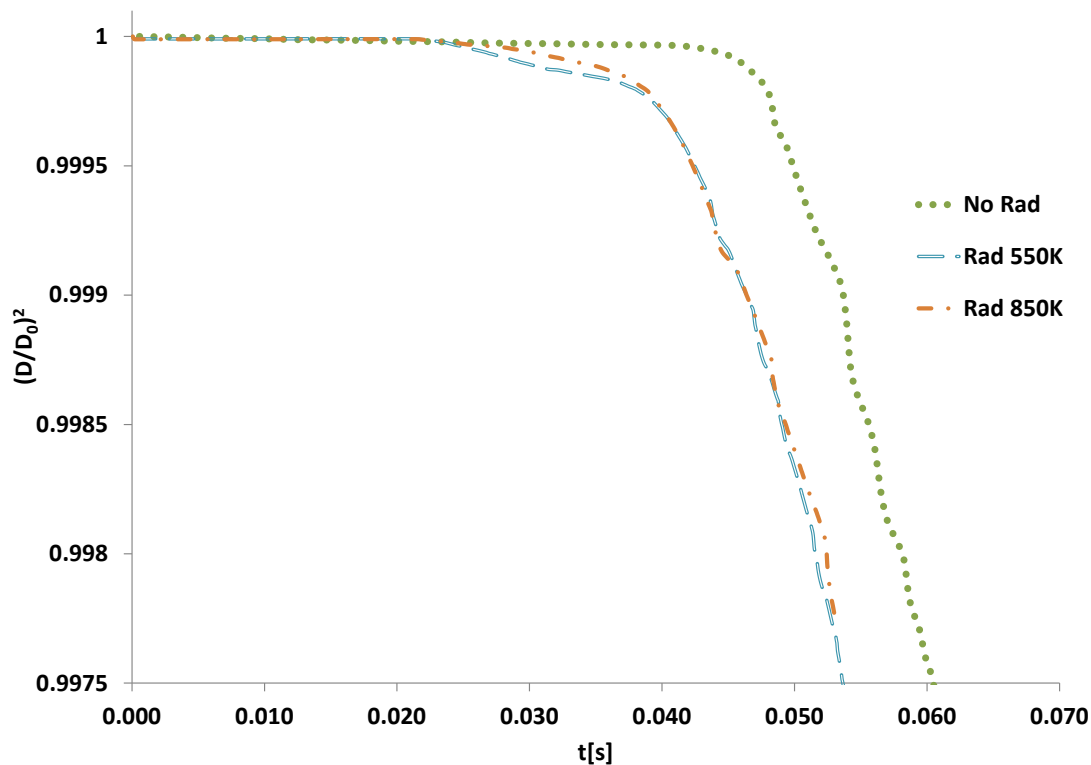


**Figure 5.67. Effect of radiation on temporal evolution of droplet diameter for an initial diameter of 500  $\mu\text{m}$ , with air at 5 m/s and 550 K**

The evaporation rate over a droplet's surface area is evaluated by varying the initial droplet diameter. The evaporation rate over a droplet's surface area shows fluctuations because in some parts of the surface the evaporation rate is higher than in other regions, as observed previously in the contours of oil vapour mass fraction (see Figure 5.69). These fluctuations were fitted with a moving average regression with a range of 32 values, as seen in Figure 5.68.

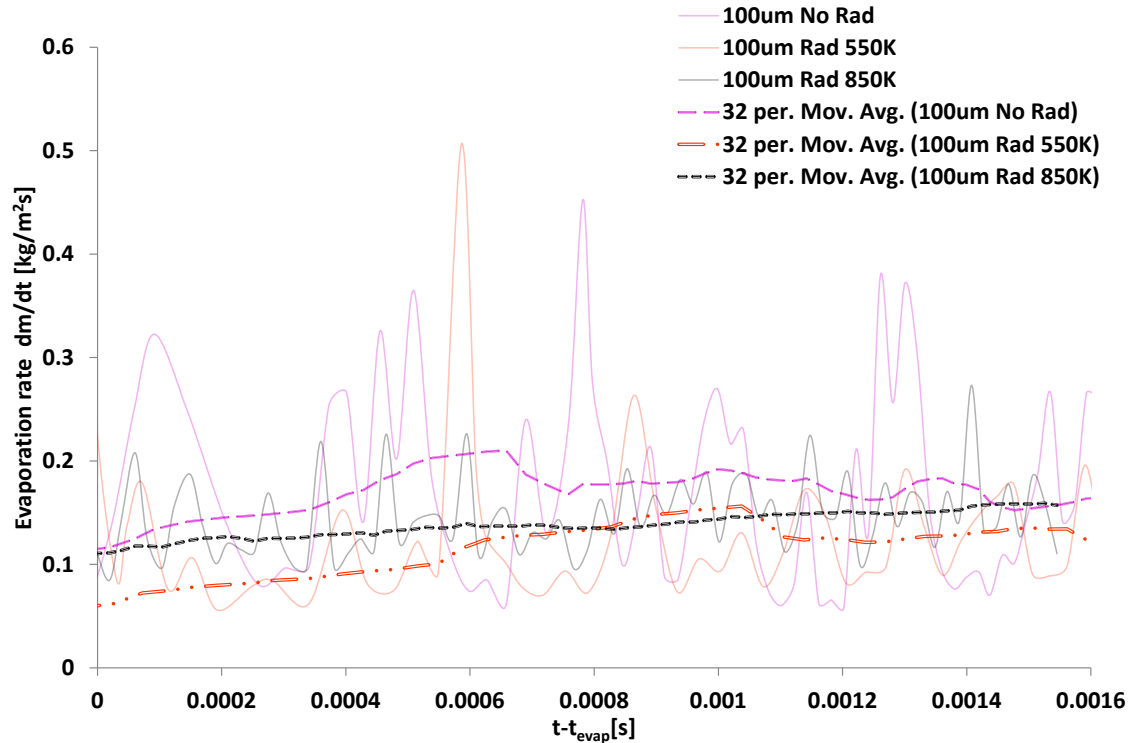


**Figure 5.68. Comparison of the evaporation rate over a droplet's surface area for an initial diameter of 100  $\mu\text{m}$ , with airflow at 5 m/s**

Figure 5.68 shows a comparison of the evaporation rate for the cases with an initial diameter of 100  $\mu\text{m}$ . The radiation cases show a reduction of the evaporation rate, which is probably because the concentration of oil vapour at the droplet's surface is higher for these cases, as observed in Figure 5.69, which might reduce heat transfer from the air to the droplet's surface. The oil vapour film might reduce the difference in temperature between the environment and the droplet's surface.

Figure 5.69 shows a comparison of the oil vapour mass fraction for the cases with an initial droplet diameter of 100  $\mu\text{m}$  at 0.004 s. From this it is noted that the higher concentration of oil vapour mass fraction is for the case with a radiative environment and a wall at 850 K.

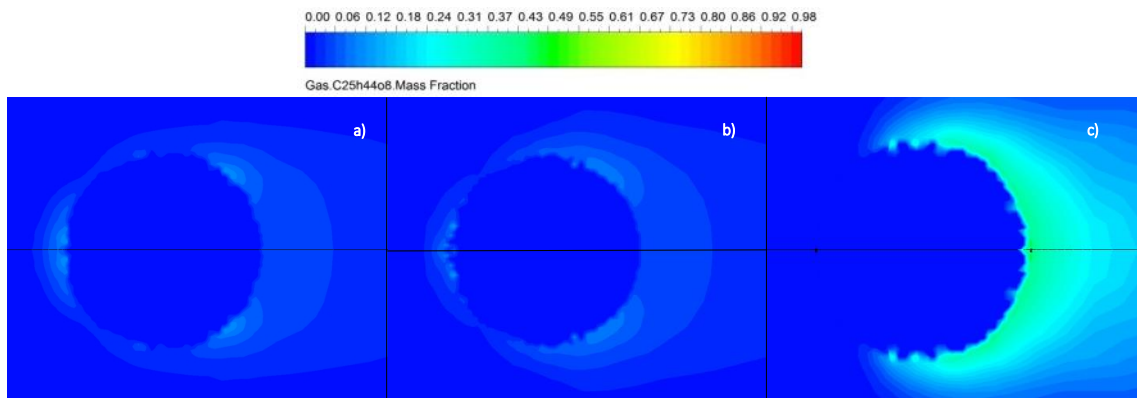


**Figure 5.69. Comparison of oil vapour mass fraction for an initial droplet diameter of 100  $\mu\text{m}$ , with airflow of 5 m/s at 0.004 s: a) no radiative environment, b) a radiative environment with a wall at 550 K, c) a radiative environment with a wall at 850 K**

Figure 5.70 shows the evaporation rate over the droplet's surface area for the cases with and without the influence of radiation for initial droplet diameters of 200  $\mu\text{m}$ , where the cases with radiation are at the beginning of the evaporation process. In Figure 5.70, the fitted curve indicates that evaporation increases progressively for the cases with radiation and it is expected to reach a similar value to the case without radiation. Likewise, in the graph plotted for the reduction of the normalised squared diameter in Figure 5.66.

Figure 5.71 compares the three cases of droplets with an initial diameter of 500  $\mu\text{m}$ . From the average evaporation rates, the case with the wall temperature at 850 K is 20% higher than the case with the wall temperature at 550 K and 60% higher than the case without radiation. The three cases show the same trend and increase progressively because they are all at the beginning of the evaporation process, when the droplet's surface is evaporating and the core is in the heating-up process, as discussed in Section 5.2.6.3.

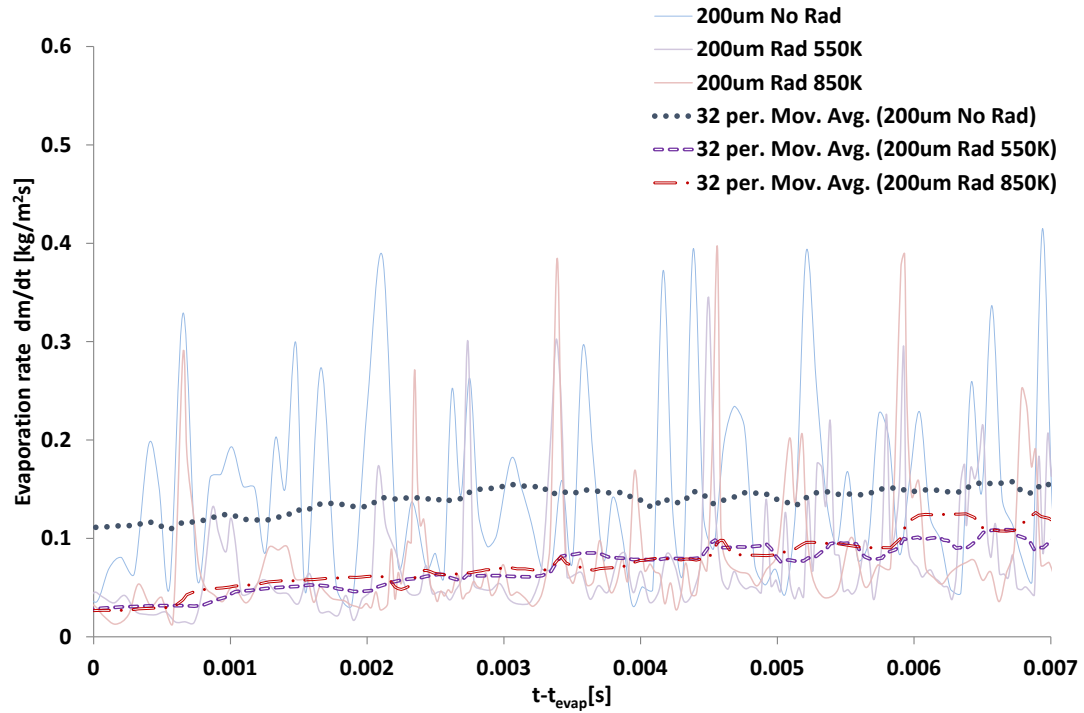


Figure 5.70. Comparison of the evaporation rate over a droplet's surface area for an initial droplet diameter of 200  $\mu\text{m}$ , with airflow of 5 m/s

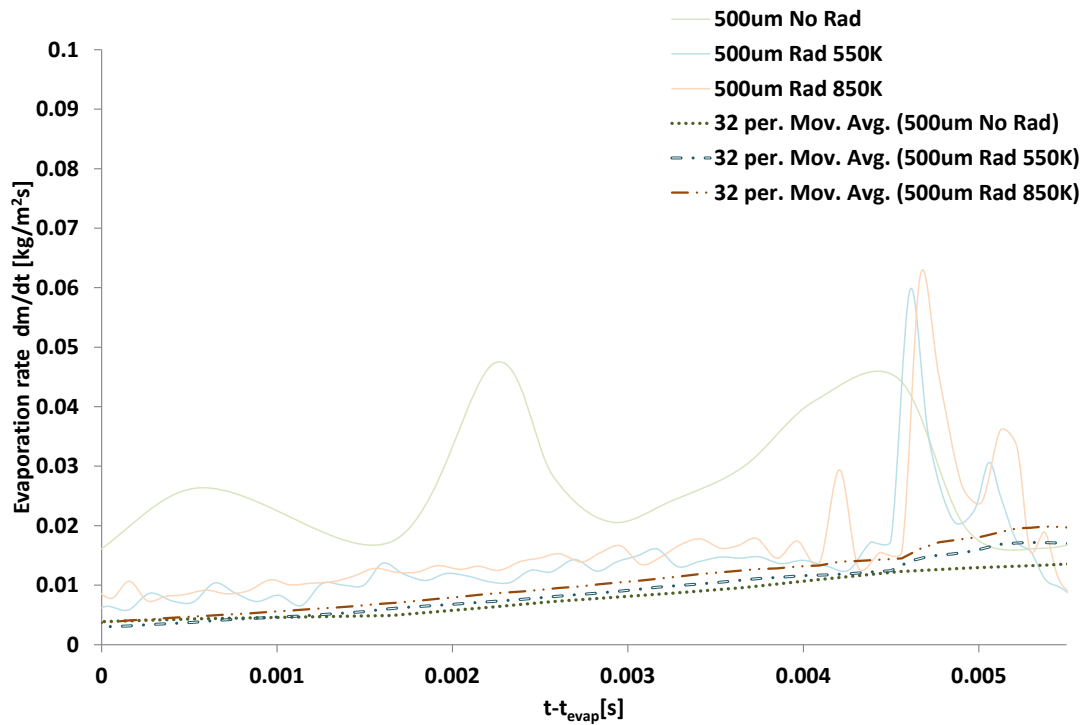


Figure 5.71. Comparison of the evaporation rate over a droplet's surface area for an initial droplet diameter of 500  $\mu\text{m}$ , with airflow of 5 m/s

### 5.2.6.2 *Effect of radiation on heat transfer at the droplet's surface*

The heat transfer coefficient  $h_g$  is a parameter that relates the quantity of heat transferred from the air to the droplet's surface and the variation of temperature at the droplet's surface. The heat transfer coefficient was estimated to quantify the effects of the initial diameter and airflow velocity, and it was calculated from:

$$h_g = \frac{Nu_g k_g}{D} \quad 5.5$$

which is a function of the Nusselt number that follows the correlation given in equation 5.6. The Nusselt number correlation includes the effects of radiation and convection, as presented in the equation 5.6 (Renksizbulut and Yuen, 1983):

$$Nu(1 + B_H)^{0.7} = 2 + 0.57Re^{1/2}Pr^{1/3} \quad 5.6$$

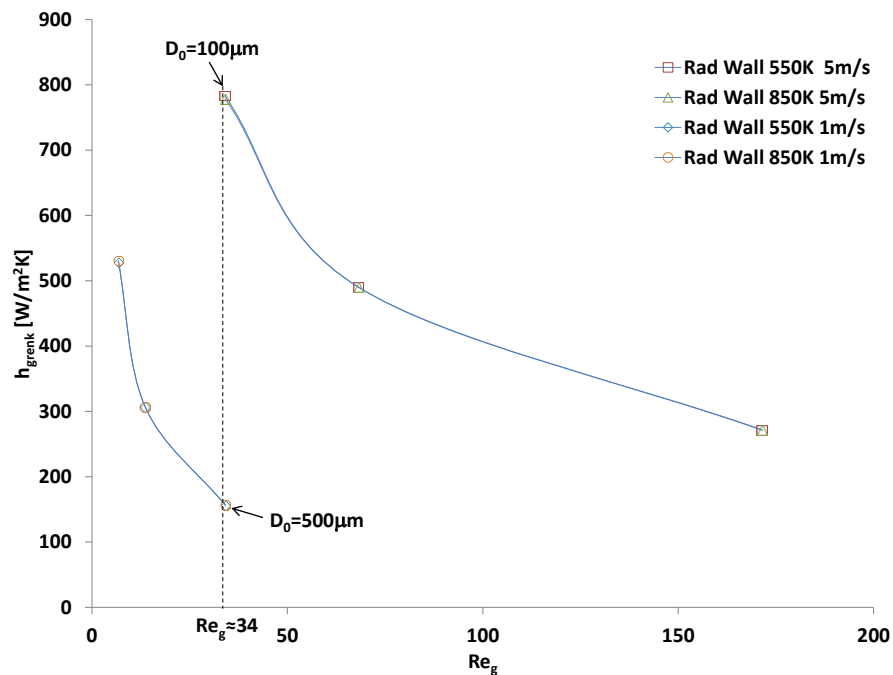
The Nusselt correlation is explained in more detail in Section 5.2.8.

Figure 5.72 presents the variation of heat transfer coefficient at the droplet's surface for different Reynolds numbers, where the highest value of  $h_g$  is for the cases with an initial droplet diameter of 100  $\mu\text{m}$ , air at 5 m/s and 550 K. The heat transfer coefficient increases with the reduction in the droplet diameter, as well as with the increase in the airflow velocity.

For the same Reynolds number, e.g.  $Re = 34$ , the heat transfer coefficient can be reduced by 20% if the initial droplet diameter is increased from 100  $\mu\text{m}$  to 500  $\mu\text{m}$  and the air velocity is decreased from 5 m/s to 1 m/s. Therefore, the initial droplet diameter and airflow velocity are key parameters to reduce the heat transfer between the airflow and the droplet's surface. In terms of application to aero-engine bearing chambers, it is recommended to have droplets with a large diameter that are travelling at low velocity,

which will reduce the heat transfer coefficient and avoid the formation of secondary droplets if the droplet splashes onto the oil film.

Additionally, heat transfer by radiation from the environment and from a wall were considered. Two possible conditions were analysed. The first condition is that the air and wall have the same temperature (550 K). The second condition is that the air has a temperature of 550 K and the wall is at 850 K. Both conditions present similar heat transfer coefficients, as observed in Figure 5.72. The similarities in heat transfer coefficients for both conditions show that the radiation might not have an effect on the analysed temperatures and it is recommended to study higher ambient temperatures than 850 K to observe the influence of radiation from walls.



**Figure 5.72. Variation of heat transfer coefficient at the droplet's surface for different Reynolds numbers**

Besides the analysis above, which talks about the variation of the heat transfer coefficient with the Reynolds number, comparisons of the heat transfer ratio are shown in Figure 5.73 and Figure 5.74 and discussed below.

First, the heat transfer ratio for a droplet with an initial diameter of 500  $\mu\text{m}$  is presented in Figure 5.73, where, comparing the cases with and without radiation, it is observed from the maximum value that radiation increases the heat transfer from the droplet's surface to the core by 2%. Moreover, from the maximum values, the heat transfer from the droplet's surface to the core shows a negligible increment (around 0.1%) when the wall temperature is at 850 K compared with the case with a wall temperature of 550 K.

Second, the heat transfer ratio for a droplet with an initial diameter of 200  $\mu\text{m}$  is presented in Figure 5.74. From the maximum values of each case it is noted that the heat transfer ratio presents an increment of 2% when the radiation is included in the calculation. Additionally, comparing the cases with radiation and varying the temperature of the wall, it is seen that the wall at 850 K increases the heat transfer from the droplet's surface to the core by 0.2%.

Third, the heat transfer ratio for a droplet with an initial diameter of 100  $\mu\text{m}$  is presented in Figure 5.74. From the maximum values, an increment of 2% in the heat transfer ratio is seen when the radiation is included in the calculation. Moreover, the heat transfer ratio between the cases with radiation increases gradually with similar values until the evaporation starts. However, after reaching the peak value of the heat transfer ratio at 0.07, the curve for the case with a wall at 850 K presents a heat transfer ratio that is 0.5% higher than the case with a wall at 550 K.

Overall, radiation increases the heat transfer coefficient from the droplet's surface to the core by 2% for all the initial diameters considered. Additionally, for the two cases with radiation, the increment in the wall temperature increases the heat transfer ratio by around 0.2%. This is because the effects of the heat transfer by convection on the droplet evaporation process are more significant than the effects of the heat transfer by radiation. The effects of heat transfer by radiation will probably be significant of the evaporation process if the temperature of the environment is higher than 850 K.

From Figure 5.73 and Figure 5.74, the maximum value of the heat transfer ratio is seen to be similar (around 0.8) between the cases with initial droplet diameters of 500  $\mu\text{m}$  and 200  $\mu\text{m}$ . However, the heat transfer ratio for the case with an initial diameter of 100  $\mu\text{m}$  is 1% less than the other two diameters. Therefore, the heat transfer between the droplet's surface and the core increases with an increment in the initial droplet diameter and with a radiative environment.

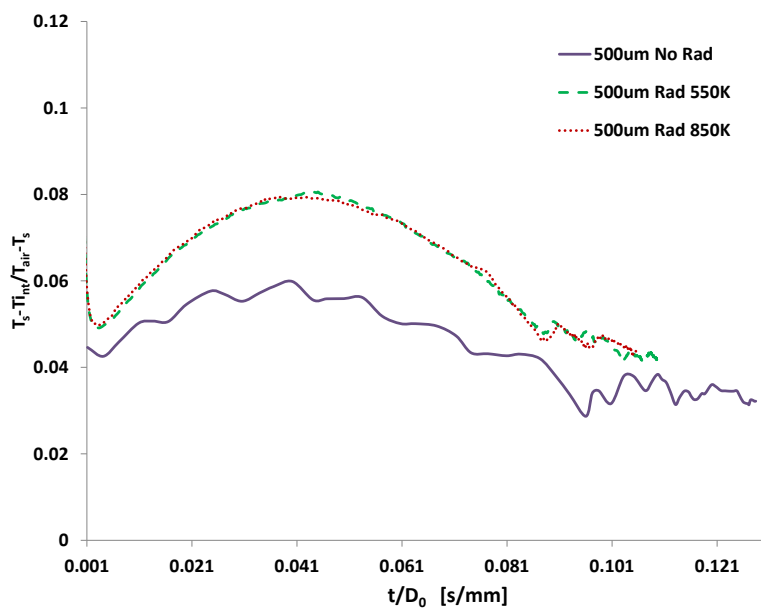


**Figure 5.73. Heat transfer ratio for different radiative ambient conditions at 5 m/s, surrounding a droplet with an initial diameter of 500  $\mu\text{m}$**

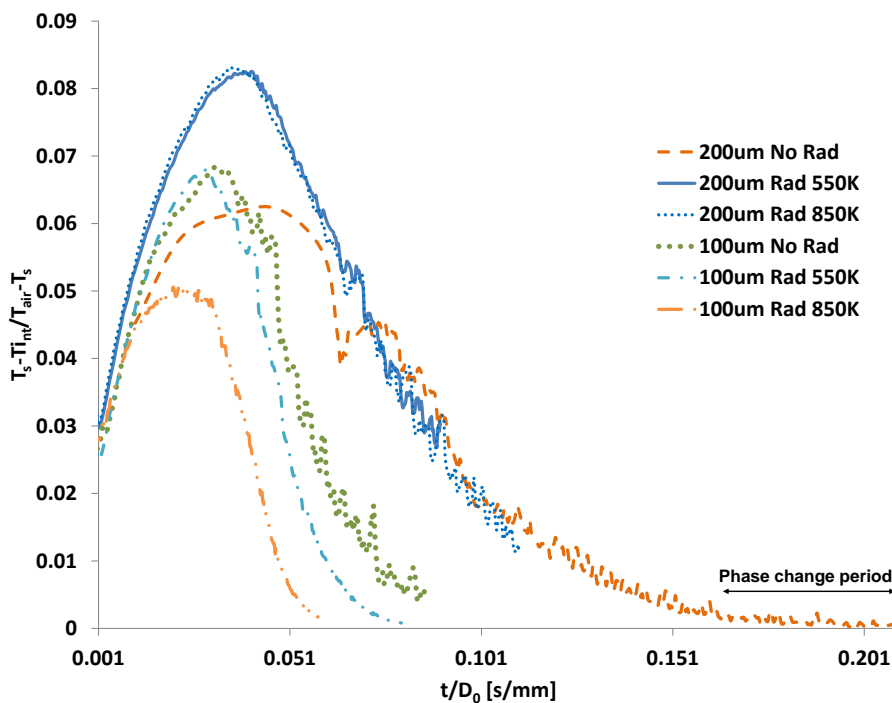


**Figure 5.74. Heat transfer ratio for different radiative ambient conditions at 5 m/s, surrounding droplets with initial diameters of 200  $\mu\text{m}$  and 100  $\mu\text{m}$**

### 5.2.6.3 Effect of radiation on internal circulation

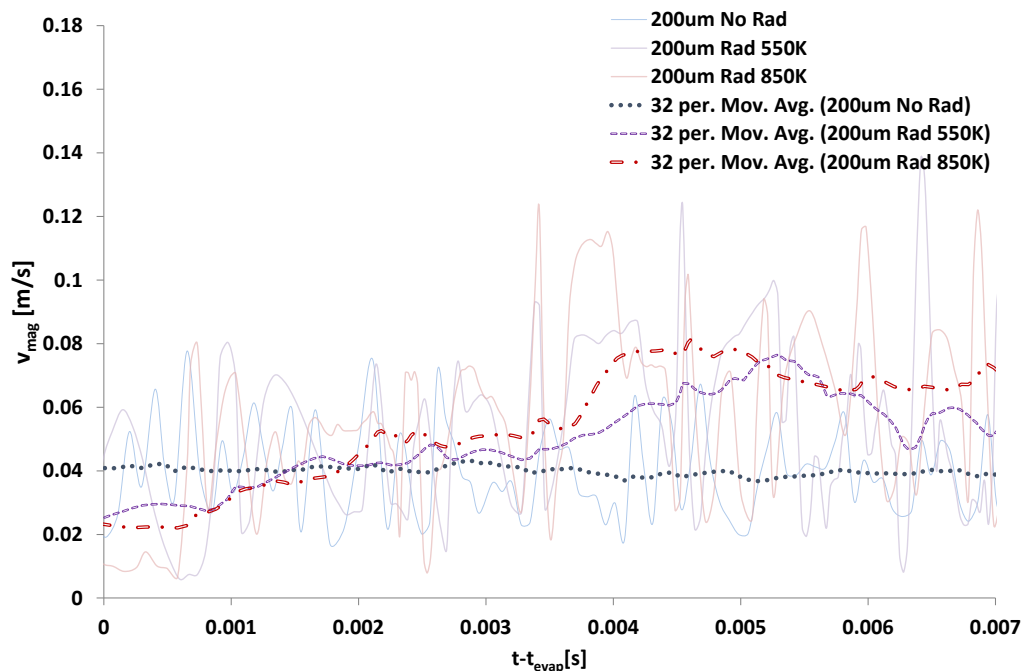
#### 5.2.6.3.1 Quantitative analysis of the effect of radiation on internal circulation

As analysed in Section 5.2.6.1, radiation in the environment might increase the evaporation rate by around 30% for the cases proposed. Therefore, it is of interest to analyse whether the internal circulation is affected by radiation in the environment. Thus, the velocity magnitude was quantified for three different initial droplet diameters (100  $\mu\text{m}$ , 200  $\mu\text{m}$  and 500  $\mu\text{m}$ ) and three conditions (no radiation, radiation with a wall at 550 K and radiation with a wall at 850 K). The air was at 550 K and 5 m/s for all cases.

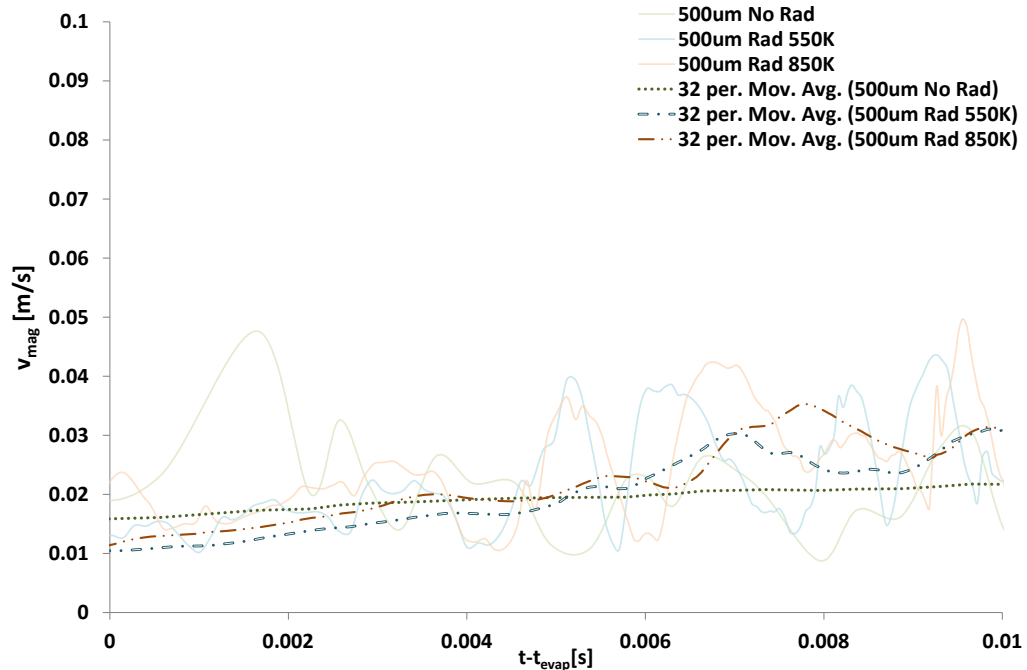
Figure 5.75 indicates that the internal circulation increases with radiation for a droplet with an initial diameter of 200  $\mu\text{m}$ , which, in the case with a wall at 850 K, is around 15% higher than the case with a wall at 550 K and 40% than the case without radiation. In other words, external radiation increases the droplet's internal velocity.

Figure 5.76 shows the internal velocity magnitude of the cases with an initial diameter of 500  $\mu\text{m}$ , in which a slight difference in values between the cases can be noted. The internal velocity magnitude in the case with a wall temperature of 850 K is around 12% higher than the case with a wall temperature of 550 K and 20% higher than the case without radiation.

However, the cases with radiation and a droplet with an initial diameter of 100  $\mu\text{m}$  present a different trend in the velocity magnitude; therefore, these are not included because, from the point of view of the author, the internal circulation is not calculated properly for the cases with radiation or with an initial diameter of 100  $\mu\text{m}$ . The author recommends using a different radiation model for droplets with an initial diameter of 100  $\mu\text{m}$ , such as the discrete ordinates model (DOM).



**Figure 5.75. Comparison of the velocity magnitude for different radiative ambient conditions at 5 m/s, surrounding a droplet with initial diameter of 200  $\mu\text{m}$**



**Figure 5.76. Comparison of the velocity magnitude for different radiative ambient conditions at 5 m/s, surrounding a droplet with initial diameter of 500  $\mu\text{m}$**

#### 5.2.6.3.2 Qualitative analysis of the effect of radiation on internal circulation

In this section, the internal circulation is analysed qualitatively for an initial droplet diameter of 200  $\mu\text{m}$  to investigate the effect of radiation with walls at 550 K and 850 K.

Two stages of the evaporation process are proposed to investigate, specifically  $\left(\frac{D}{D_0}\right)^2 = 1$

and  $\left(\frac{D}{D_0}\right)^2 = 0.99$ , as shown in Figure 5.77 and Figure 5.80. These figures illustrate that

both stages correspond to the heating-up period and the phase-change period. Moreover, the temperature evolution at the droplet's surface and core and the gradient are observed in the temperature contours.

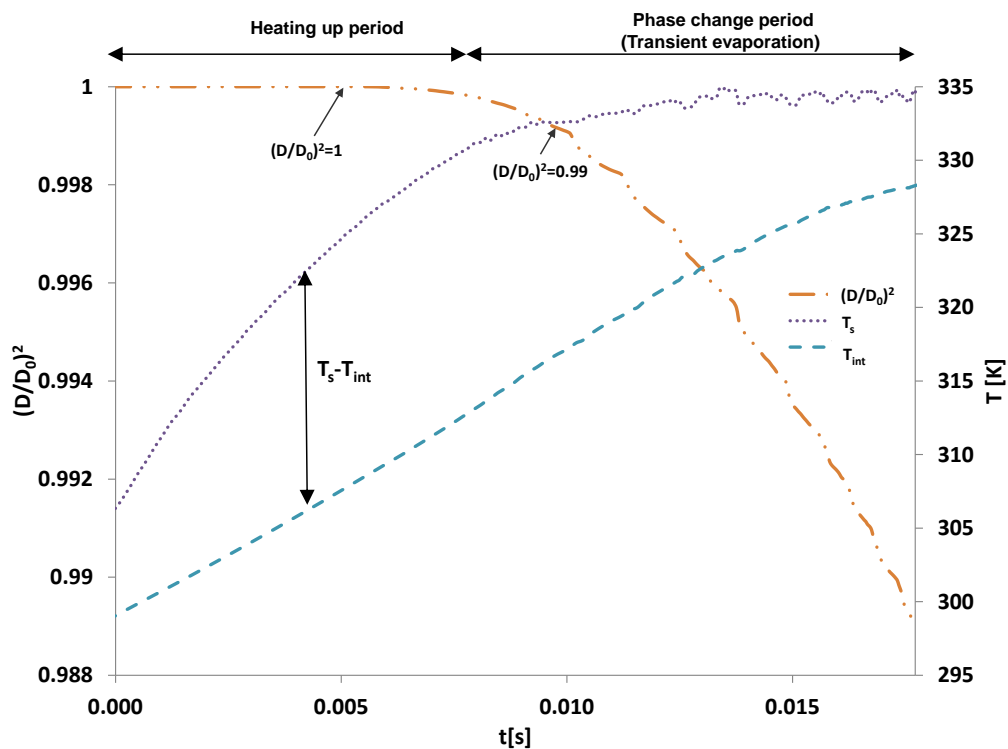


**Figure 5.77. Temporal evolution of droplet normalised square diameter versus temperature evolution at the droplet surface  $T_s$  and the droplet core  $T_{int}$  for an initial diameter of  $200\ \mu\text{m}$  with a radiative environment and a wall at  $550\ \text{K}$**

The contours of the oil vapour mass fraction, liquid volume fraction, internal and external temperatures, and internal flow streamlines are presented for a droplet with an initial droplet diameter of  $200\ \mu\text{m}$  with a radiative environment and a wall at  $550\ \text{K}$  in Figure 5.78 a), b), c), d) and e) respectively. The flow pattern is similar in all cases, with and without radiation. The main difference is that the heating-up period is shorter for cases with radiation.

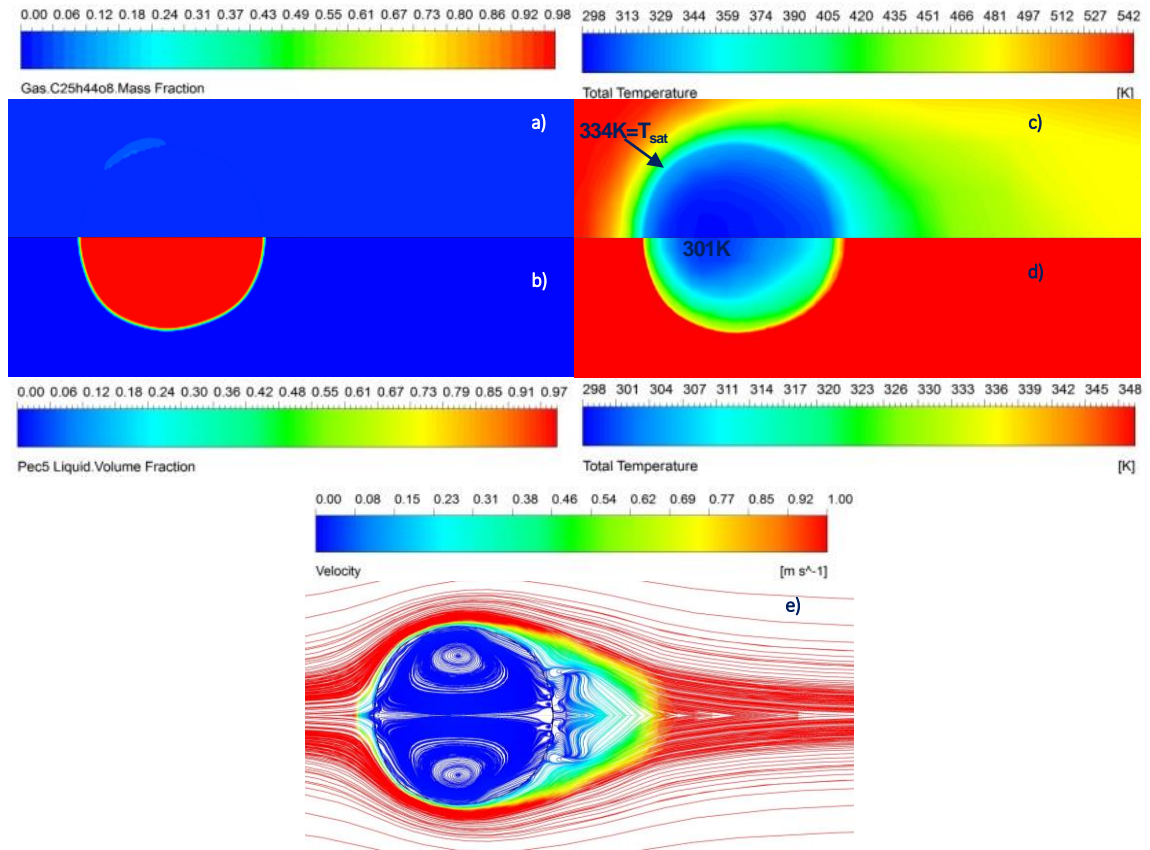


**Figure 5.78. Contours and streamlines at  $\left(\frac{D}{D_0}\right)^2 = 1$  and 0.007 s for a droplet with an initial diameter of 200  $\mu\text{m}$  with a radiative environment and a wall at 550 K: a) oil vapour mass fraction, b) liquid volume fraction, c) external temperature, d) internal temperature, e) velocity streamlines**

Figure 5.79 a), b), c) and d) display the contours of oil vapour mass fraction, liquid volume fraction, temperature at the droplet's surroundings and at the droplet's core, respectively, at  $\left(\frac{D}{D_0}\right)^2 = 0.99$  and 0.010 s. Figure 5.79 a) illustrates that at  $\left(\frac{D}{D_0}\right)^2 = 0.99$  the droplet's surface has more evaporation than the case at  $\left(\frac{D}{D_0}\right)^2 = 1$ . Figure 5.79 d) shows that the temperature at the droplet's core has increased by 9 K more than the case at  $\left(\frac{D}{D_0}\right)^2 = 1$ . Figure 5.79 e) shows that the spherical vortex has not appeared probably

because the evaporation is stronger at the droplet's surface than in the previous case (i.e.

$$\left(\frac{D}{D_0}\right)^2 = 1).$$

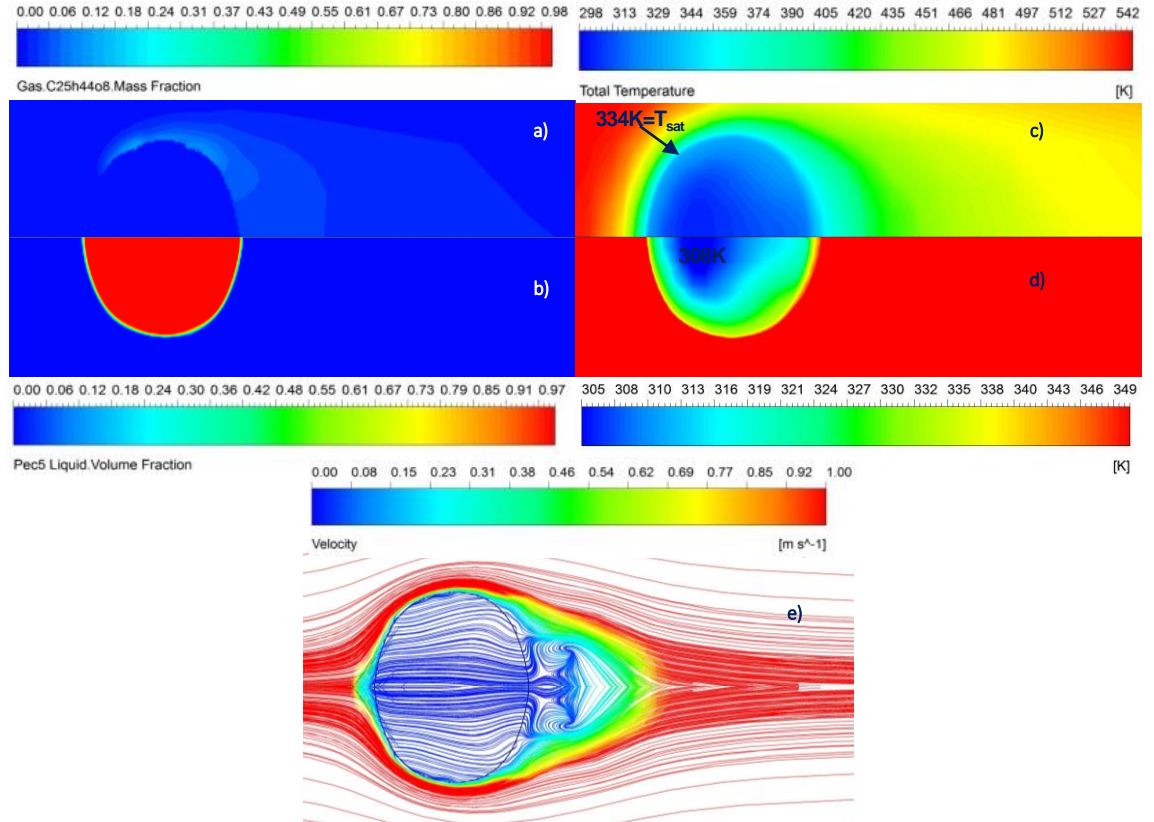


**Figure 5.79. Contours and streamlines at  $\left(\frac{D}{D_0}\right)^2 = 0.99$  and  $0.010$  s for a droplet with an initial diameter of  $200 \mu\text{m}$  with a radiative environment and a wall at  $550 \text{ K}$ : a) oil vapour mass fraction, b) liquid volume fraction, c) external temperature, d) internal temperature, e) velocity streamlines**

Similar to above, the case with a wall temperature of  $850 \text{ K}$  is analysed during the heating-up period with  $\left(\frac{D}{D_0}\right)^2 = 1$  and  $0.007$  s and during transient evaporation with

$\left(\frac{D}{D_0}\right)^2 = 0.99$  and  $0.10$  s, as shown in Figure 5.80.

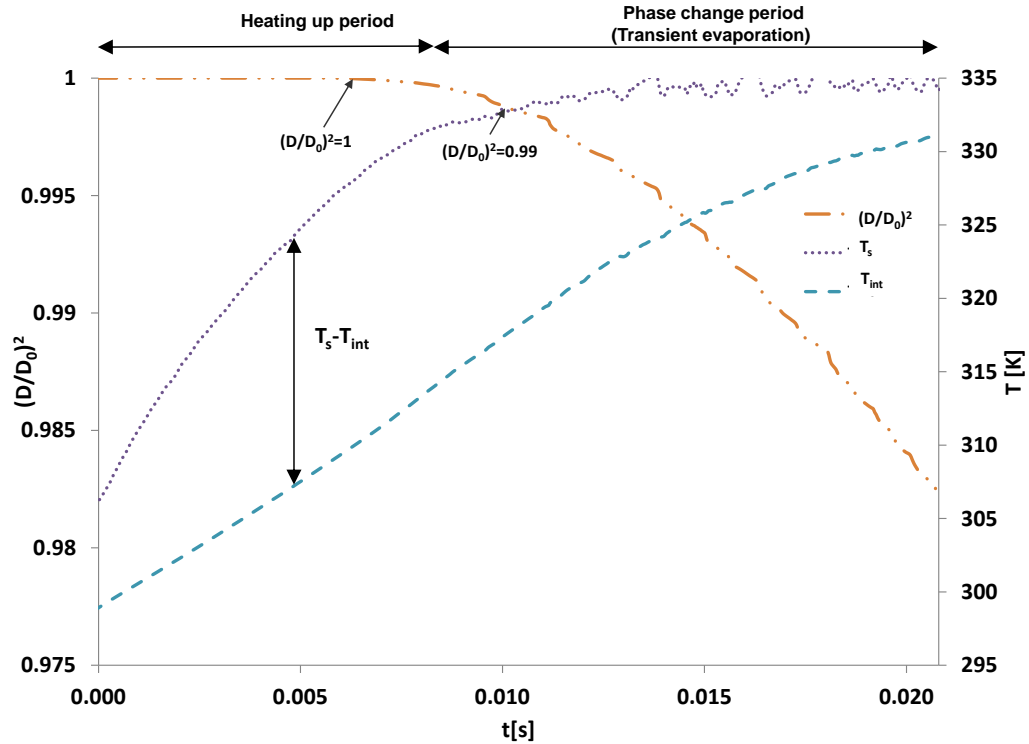


**Figure 5.80. Temporal evolution of droplet normalised square diameter versus temperature evolution at the droplet surface  $T_s$  and the droplet core  $T_{int}$  for an initial diameter of  $200\ \mu\text{m}$  with a radiative environment and a wall at  $850\ \text{K}$**

The contours of oil vapour mass fraction, liquid volume fraction, and external and internal temperatures for both stages (i.e.  $\left(\frac{D}{D_0}\right)^2 = 1$  and  $\left(\frac{D}{D_0}\right)^2 = 0.99$ ) show a similar performance to the case with a wall at  $550\ \text{K}$ , as observed in Figure 5.81 a), b), c) and d) respectively.

These similarities that were observed in both cases, namely the cases with wall temperatures of  $550\ \text{K}$  and  $850\ \text{K}$ , were expected because in the temporal evolution of droplet diameter depicted previously in Figure 5.66, the reduction in the droplet diameter shows the same trending and matches perfectly for both.

Figure 5.81 e) shows the velocity streamlines during the heating-up period (i.e.  $\left(\frac{D}{D_0}\right)^2 = 1$ ), when the spherical vortex is observed, contrary to Figure 5.82 e) which

shows vorticity at the droplet's surface due to the beginning of the evaporation process as well as an external vortex formation at the rear part of the droplet. In summary, the evaporation process affects the internal flow pattern and radiation influences the internal circulation as a consequence of increasing the evaporation rate.

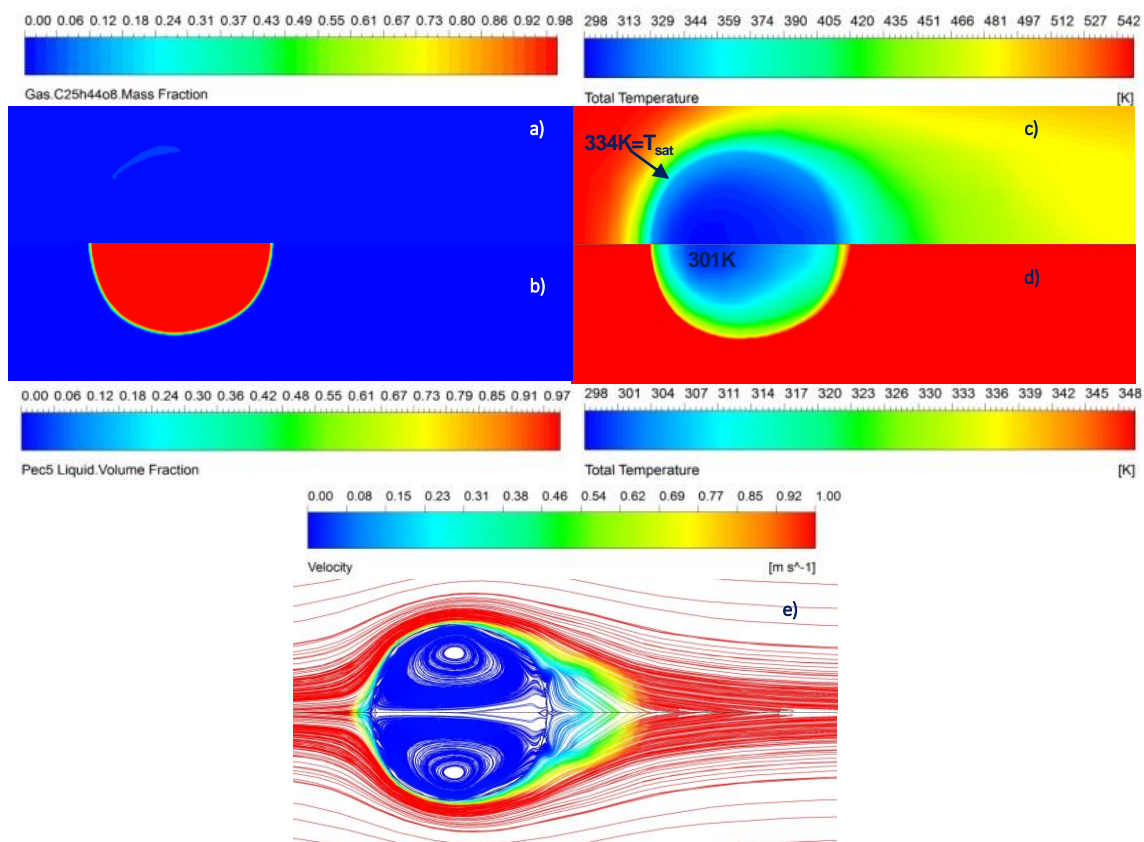


Figure 5.81. Contours and streamlines at  $\left(\frac{D}{D_0}\right)^2 = 1$  and  $0.007$  s for a droplet with an initial diameter of  $200 \mu\text{m}$  with a radiative environment and a wall at  $850 \text{ K}$ : a) oil vapour mass fraction, b) liquid volume fraction, c) external temperature, d) internal temperature, e) velocity streamlines

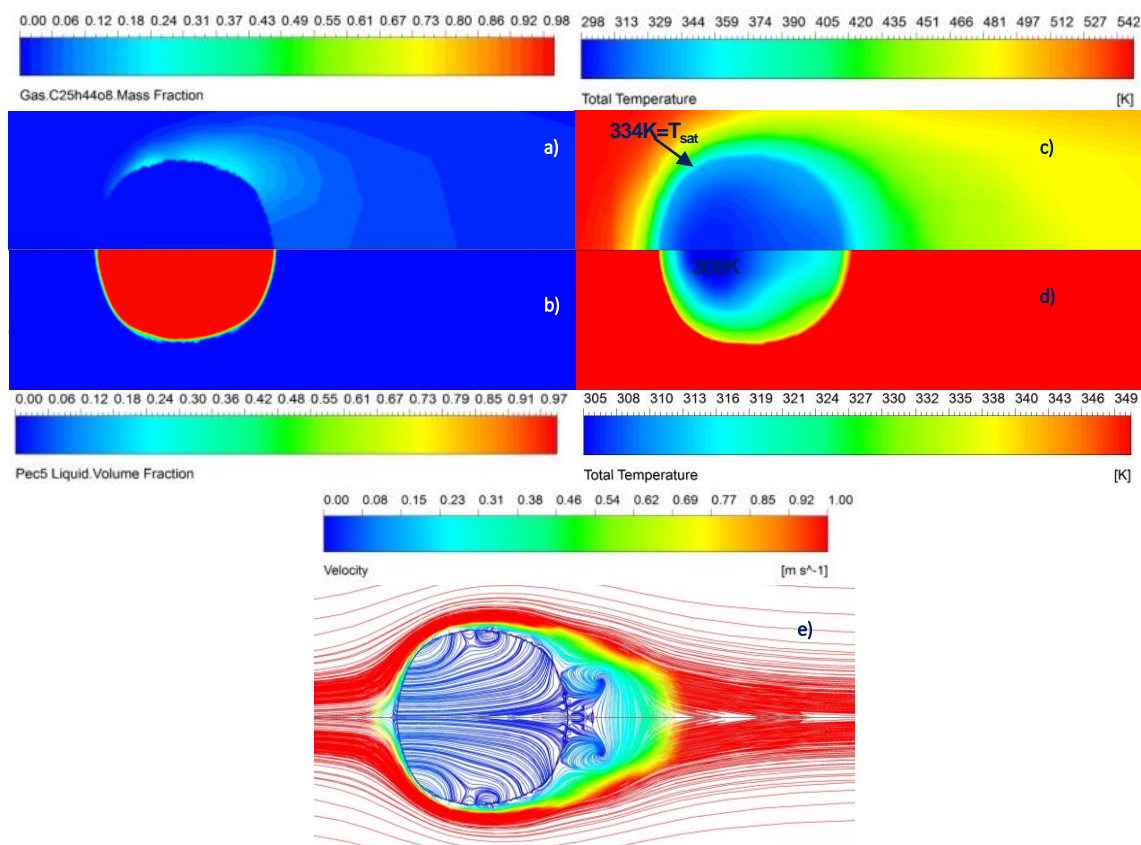
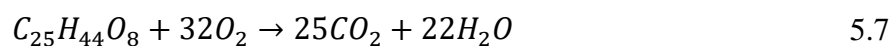


Figure 5.82. Contours and streamlines at  $\left(\frac{D}{D_0}\right)^2 = 0.99$  and  $0.010$  s for a droplet with an initial diameter of  $200 \mu\text{m}$  with a radiative environment and a wall at  $850 \text{ K}$ : a) oil vapour mass fraction, b) liquid volume fraction, c) external temperature, d) internal temperature, e) velocity streamlines

## 5.2.7 Vapour mass fraction

### 5.2.7.1 Flammability limits

The flammability limits provide the range where the oil vapour concentration might ignite. The flammability limits were calculated according to equations 2.19–2.22. The upper and lower limits are based on the stoichiometric ratio of a molecule of  $\text{C}_{25}\text{H}_{44}\text{O}_8$  (PEC5), which is the molecular formula of an oil base stock used in jet engines. The balanced equation assuming a complete oxidation is obtained as follows:



where the molar ratio at the stoichiometric point is  $1/32$  which means that for 1 molecule of  $C_{25}H_{44}O_8$  we need 32 molecules of  $O_2$  to produce a complete reaction and the oxidation. Moreover, when the  $O_2$  is combined with air, the molar ratio is  $1/5$  (Rosenlieb, 1978). Therefore, the total stoichiometric ratio is  $1/5 \times 1/32 = 0.0063 = 0.63\%$  of oil vapour to air by volume.

Thus, the upper and lower limits are given as follows in volume percentage of oil vapour concentration:

$$LL_{297K} = 0.00346 = 0.346\%$$

$$UL_{297K} = 0.0302 = 3.024\%$$

and the flammability range, considering a temperature of 550 K, is:

$$LL_{550K} = 0.0028 = 0.28\%$$

$$UL_{550K} = 0.0035 = 3.57\%$$

Therefore, for the sake of clarity in terms of post-processing the flammability limits and the stoichiometric ratio, they are converted to mass fraction oil vapour concentrations as follows:

$$\text{Stoichiometric ratio} = 0.83 = 84\%$$

$$LL_{297K} = 0.742 = 74.2\%$$

$$UL_{297K} = 0.963 = 96.3\%$$

$$LL_{550K} = 0.701 = 70.1\%$$

$$UL_{550K} = 0.968 = 96.8\%$$

As a result, the oil vapour mass fraction for a bearing chamber case is calculated, extrapolating from a single droplet to the total number of droplets travelling in the core flow of the bearing chamber.

As mentioned previously in Section 2.1.3, the distribution of droplet diameters might be from 14  $\mu\text{m}$  to 500 $\mu\text{m}$  (Glahn et al., 1996), as shown in Figure 5.83. Using a Phase Doppler Particle Analyzer (PDPA) technique, Glahn et al. (1996) took 3000 samples and plotted a diameter histogram for an oil volume flow of 100 l/h and air mass flow of 10 g/s with a shaft speed of 12,000 rpm.

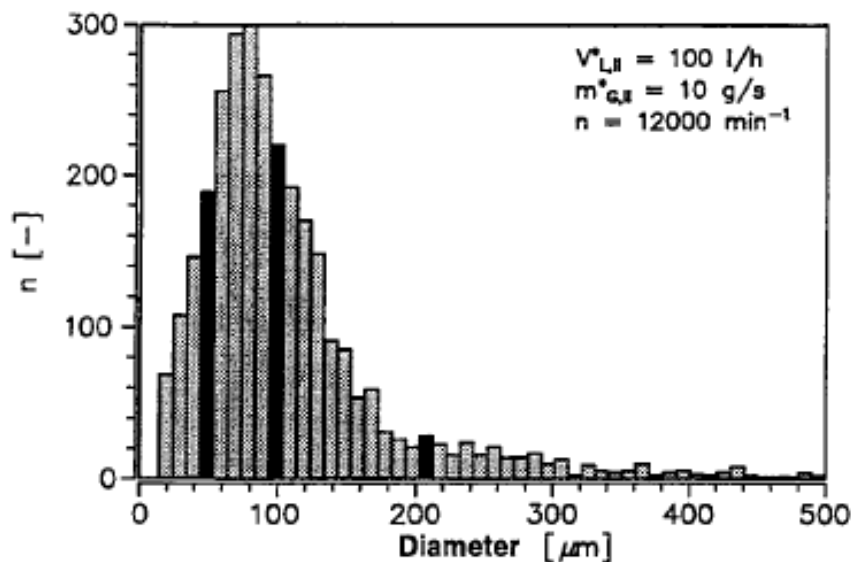


**Figure 5.83. Diameter histogram at 12,000 rpm (see Glahn et al., 1996)**

The analysis of the oil vapour mass fraction in a bearing chamber is based on the histogram in Figure 5.83, which in turn is based on the Rosin–Rammler distribution. The extrapolation was done as follows.

The number of droplets was reproduced by Glahn et al.(1996), as in Figure 5.84. From this, the cumulative number of droplets was calculated and consequently the probability of the number of droplets per diameter and the probability of the cumulative number of droplets (Figure 5.85). The mass of oil associated with each diameter of droplet was calculated and then the cumulative mass of oil associated with each diameter of droplet, as shown in Figure 5.86 and the probabilities in Figure 5.87.

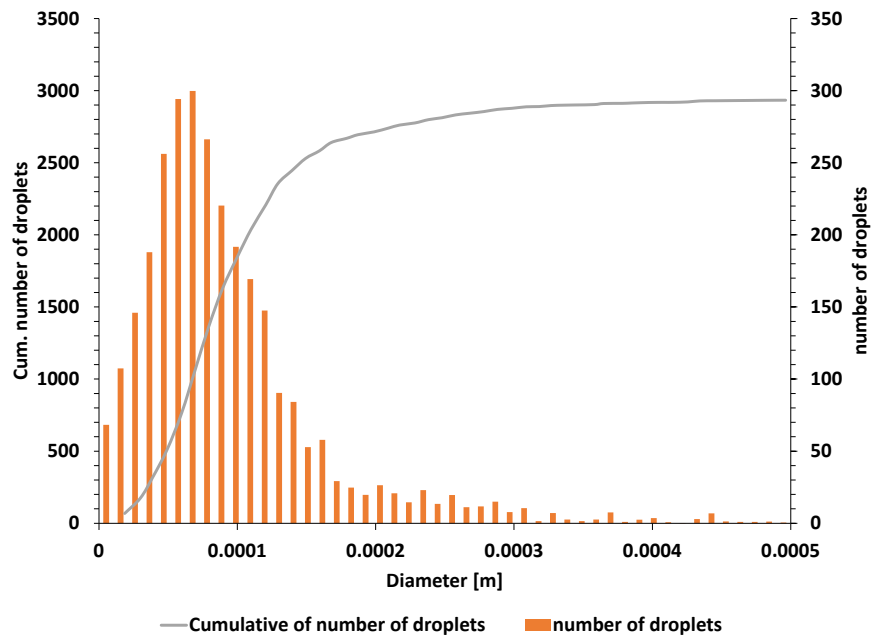


Figure 5.84. Cumulative number of droplets and number of droplets per diameter in the population (see Glahn et al., 1996)

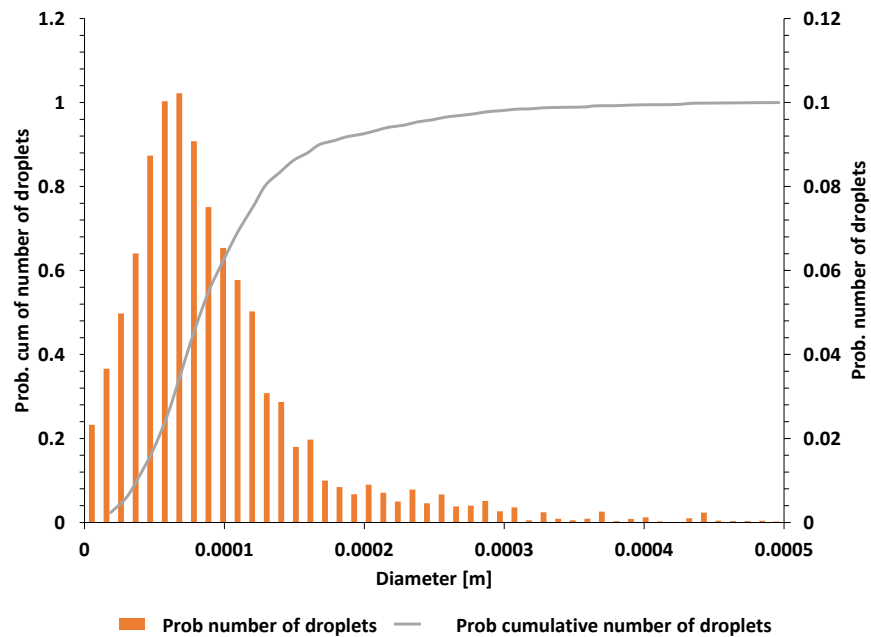


Figure 5.85. Probability of cumulative number of droplets and probability of number of droplets per diameter in the population

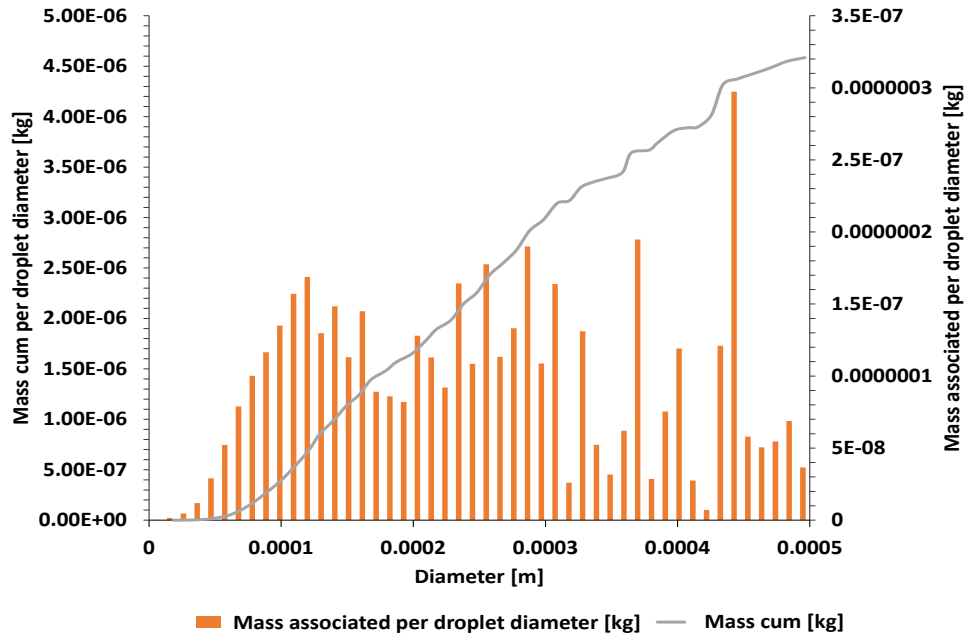


Figure 5.86. Mass associated per droplet diameter and cumulative mass of oil per droplet diameter

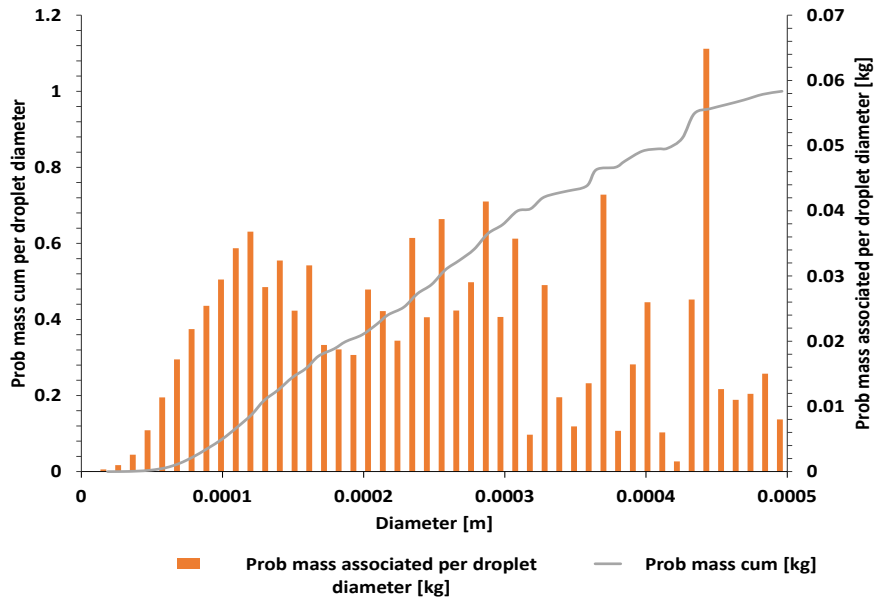
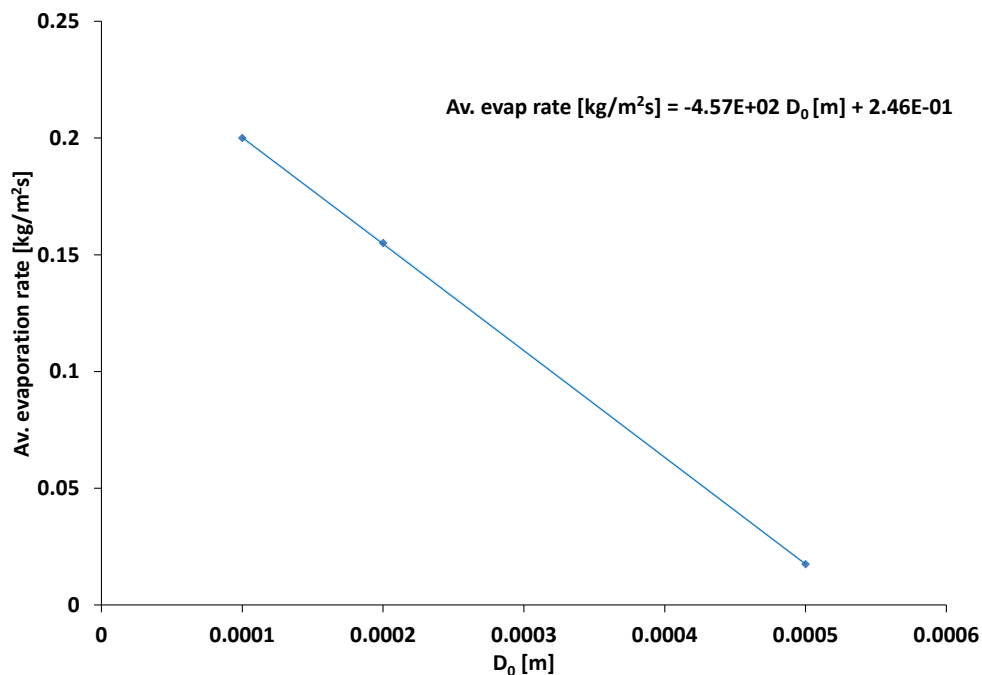


Figure 5.87. Probability of mass associated per droplet diameter and probability of cumulative mass of oil per droplet diameter

The average evaporation rate was retrospectively predicted for each droplet diameter from the linear regression of the average evaporation rate of the cases discussed in 5.2.3.1 and presented in Figure 5.88.

Figure 5.88 shows that the evaporation rate increases with the reduction in initial droplet diameter because for small diameters there is more surface area exposed to the airflow conditions, which favours evaporation at the droplet's surface as well as heat transfer from the environment to the droplet's surface and from the droplet's surface to the core.

Thus, from Figure 5.88 and the linear regression equation, the evaporation rate for each droplet diameter was predicted, assuming that the air velocity in the chamber is the same for all the geometry and the air temperature in the chamber is uniform at 550 K.



**Figure 5.88. Linear regression of the average evaporation rate per surface area for each droplet diameter with an air temperature of 550 K**

The time of residence of each droplet diameter is calculated from the solution to the equation 2.7, which represents the droplet dynamics travelling in the core flow and is reproduced for clarity as follows:

$$\frac{du}{dt} = \frac{3C_D \rho_g}{2r \rho_l} |u_g - u_l|(u_g - u_l) \quad 5.8$$

Figure 5.89 shows the time of residence of a droplet travelling from the bearings to the walls for the geometry of the experiment presented by Glahn et al. (1996).

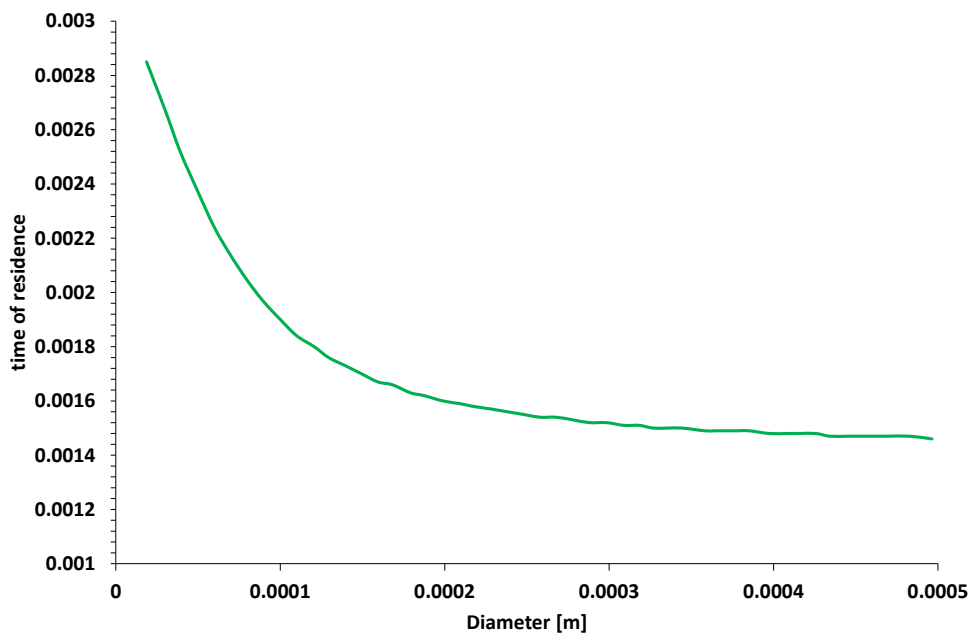


**Figure 5.89. Time of residence of droplets travelling from the bearings to the walls**

As a result, the time of residence of the radial droplet displacement (from bearings to wall) and the area per droplet diameter were calculated to consequently obtain the fraction of vapour per droplet from the linear regression equation displayed in Figure 5.88. Then, this fraction was extrapolated to a bearing chamber case from the probability of mass associated per droplet diameter (Figure 5.87), from which 2% of oil is converted to vapour in total. This 2% is just for the droplets that are travelling in the core flow from

the bearings to the walls; therefore, these droplets do not evaporate completely. However, it is important to analyse the droplets that are kept trapped in the recirculation regions.

Assuming that 30% of the oil in the chamber is converted into droplets travelling in the core flow of the bearing chamber, the oil flow is 100 l/h and the airflow is 10 g/s, the mass fraction of oil vapour concentration in the gas phase in a bearing chamber is 0.01, which is below the flammability limits. This assumption of 30% is based on the estimations of previous researchers who analysed the two-phase flow in bearing chambers as members of the G2TRC (Bristot, 2019, Adeniyi, 2019).

The vapour concentration in the bearing chamber is calculated considering that a range of the oil from 5% to 100% is converted into droplets travelling in the core flow, as observed in Table 5.5. Thus, considering all the conditions mentioned above, the oil vapour concentration does not reach the flammability limits.

**Table 5.5. Vapour concentration per the fraction of oil converted into droplets in the bearing chamber**

Fract. of oil to droplets [%]	5%	10%	30%	50%	75%	100%
Mass flow oil droplets [kg/s]	0.001	0.003	0.008	0.014	0.021	0.028
Evap. fract.	2%	2%	2%	2%	2%	2%
Mass flow vapour [kg/s]	0.00002	0.00005	0.00014	0.00024	0.00036	0.00048
Vap. concentration into gas	0	0	0.014	0.02	0.04	0.05

### 5.2.8 Correlations

The present method of the calculation of the heat and mass transfers between the droplet's surface and the surrounding air was validated by comparing each case with the reported heat and mass transfer correlations. These correlations were obtained from

experiments on droplet evaporation at high air temperatures and with laminar flow. The fluids analysed were water, methanol and n-heptane, and the correlations proposed by (Renksizbulut and Yuen, 1983) evaluate the diffusivity from the droplet's surface to the environment with the Sherwood number given by:

$$Sh(1 + B_M)^{0.7} = 2 + 0.57Re^{1/2}Sc^{1/3} \quad 5.9$$

where the Sherwood number  $Sh$  correlates with the Schmidt number  $Sc$  and is the ratio of momentum diffusivity and mass diffusivity, as expressed in equation 2.18.

In addition, the Sherwood number is a function of the Spalding mass transfer number  $B_M$  and the droplet's Reynolds number defined by equations 2.10 and 2.11, respectively. Each one of these non-dimensional parameters was calculated individually for each time step and the average values of each case plotted in Figure 5.90. The values obtained follow the trending of Renksizbulut and Yuen's (1983) correlation; therefore, the computation of the mass transfer from the droplet's surface to the environment is validated and matches the correlation very well.

Furthermore, Figure 5.90 shows that the mass transfer rate at the droplet's surface increases with the velocity of the air and it also increases with the initial droplet diameter; in other words, the Sherwood number increases as the Reynolds number increases.

As discussed earlier in Section 5.2.6.2, the Reynolds number is the same for cases with (i) an initial diameter of 500  $\mu\text{m}$  and airflow at 1 m/s, and (ii) an initial diameter of 100  $\mu\text{m}$  and airflow at 5 m/s; however, the heat transfer coefficient is higher for the case with a droplet diameter of 100  $\mu\text{m}$  and airflow at 5 m/s. It is difficult to visualise the effect of air temperature on mass transfer at the droplet's surface with the correlations of

Renksizbulut and Yuen (1983) and therefore the effect of the temperature was analysed separately in Section 5.2.5.3.

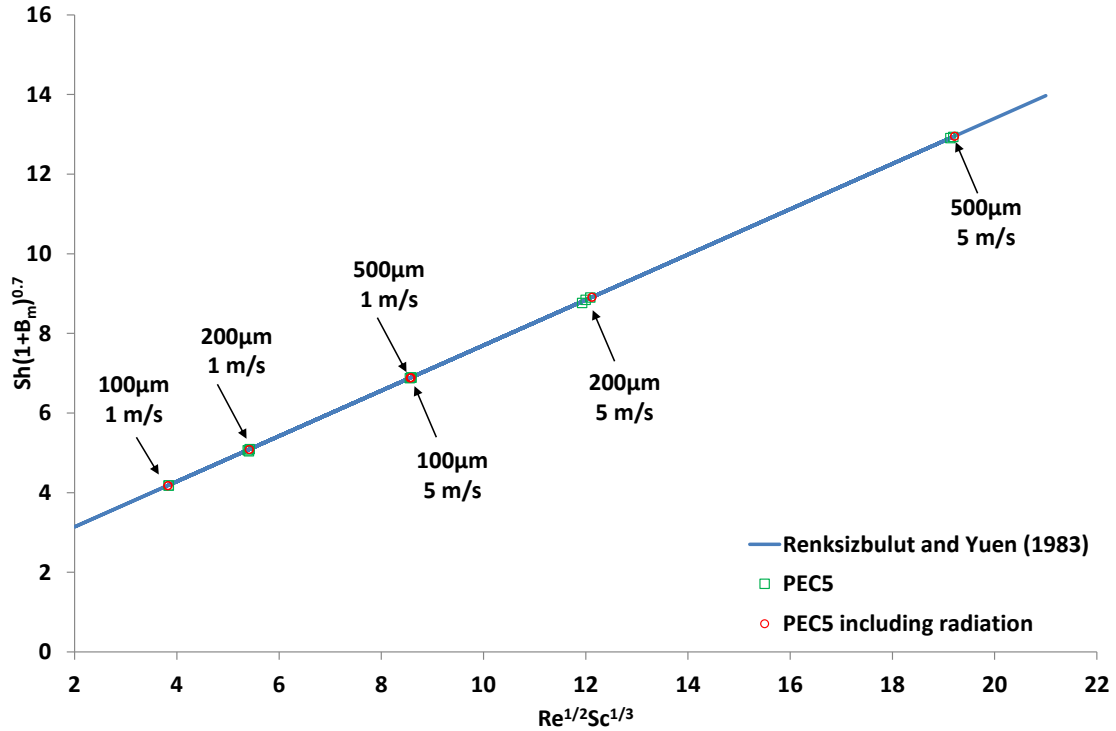


**Figure 5.90. Comparison of mass transfer results with the correlation presented by Renksizbulut and Yuen (1983)**

The heat transfer from the environment to the droplet's surface was validated using the following correlation (Renksizbulut and Yuen, 1983):

$$Nu(1 + B_H)^{0.7} = 2 + 0.57Re^{1/2}Pr^{1/3} \quad 5.10$$

where the analogue parameter to the Schmidt number is the Prandtl number, which is the ratio of momentum diffusivity and thermal diffusivity, as expressed in equation 2.17. The analogue parameter to the Spalding mass transfer number is the Spalding heat transfer number  $B_H$  given by:

$$B_H = \frac{Cp_g(T_g - T_s)}{L_s} \quad 5.11$$

Similar to the mass transfer evaluation, the heat transfer evaluation was obtained, first, from the calculation of each parameter for all the time steps of each case and then by plotting the averages of these parameters on Figure 5.91. Hence, a comparison of the heat transfer calculation of the present research with the correlation of Renksizbulut and Yuen (1983) shows a good agreement, as shown in Figure 5.91.

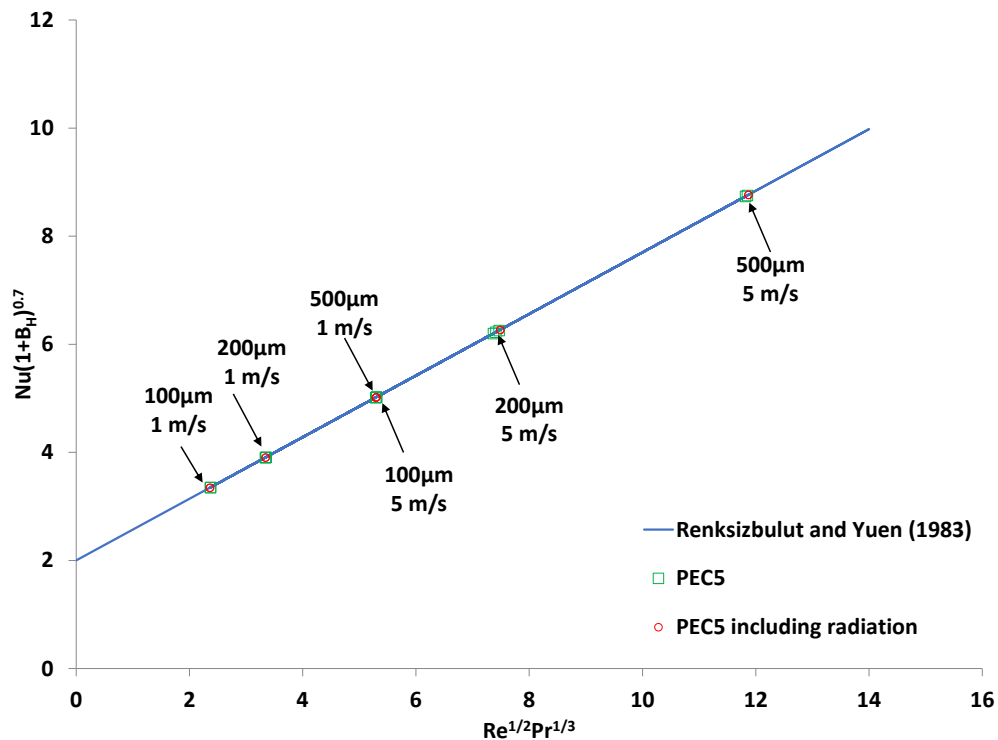


**Figure 5.91. Comparison of heat transfer results with the correlation presented by Renksizbulut and Yuen (1983)**

Figure 5.91 shows that the heat transfer by convection increases with both the air velocity and the initial droplet diameter; this means that the Nusselt number increases with the Reynolds number.

Under these circumstances, the cases with a low air velocity and small initial droplet diameter have reduced heat transfer at the droplet's surface, and the highest Nusselt number is for the case with the largest initial droplet diameter and highest air velocity (i.e.

500  $\mu\text{m}$  and 5 m/s, respectively). As discussed earlier in Section 5.2.7.1, the probability of finding droplets with a diameter of 500  $\mu\text{m}$  in the bearing chamber is less than 0.1%; thus, it is recommended to focus the analysis on droplets with an initial diameter of 100  $\mu\text{m}$  and high air velocities.

Moreover, from these correlations we can validate that the calculations of the temperature and the oil vapour mass fraction at the droplet's surface are correct. Additionally, these correlations allow the calculation of the Nusselt number to obtain the heat transfer coefficient, as discussed in Section 5.2.6.2.

Overall, the present method correlates well with the heat and mass transfer correlations presented in the literature by Renksizbulut and Yuen (1983).

## 6 Conclusions

The research presented in this work has aimed to understand the heat and mass transfer of droplets in the core flow region of the bearing chamber. Thus, in this thesis, a numerical methodology applicable to aero-engine bearing chambers has been developed and tested to quantify the evaporation rate, the temporal evolution of droplet diameters, the heat transfer at the droplet's surface and the droplet's internal velocity magnitude.

Furthermore, a parametrical study has been presented varying the initial droplet diameter, air velocity, air temperature and the influence of external radiation on droplet evaporation. In this section, the main findings of the work are summarised and the contributions to knowledge and recommendations for future work are also given.

### 6.1 Main achievements

The main achievements of this research are summarised as follows.

- The evaporation model was validated against previous experiments and numerical analysis from the research of Banerjee (2013), Daïf et al. (1998) and Strotos et al. (2016), which were performed using suspended fuel droplets immersed in airflows with higher temperatures than the fuel and at different air velocities. The non-dimensional squared variation was quantified to compare the present results with the experimental data. As a consequence, the numerical results were validated within the 3% RMSD against the experimental data.

- The validated model was then applied to representative droplets of an oil base stock used in jet engine bearing chambers. The oil base stock used was pentaerythritol tetrapentanoate (PEC5), which can be assumed to be 80% of the composition of the oils used in aero-engines. Therefore, the calculation of the thermos-physical properties of PEC5 in the gas phase were estimated theoretically, based on the kinetic theory considering the gas phase as an ideal gas.
- A parametrical study was conducted varying the initial droplet diameter, air temperature and air velocity, as well as including the radiation in the environment. This parametric study provided the average evaporation rate per droplet diameter, the temporal evolution of the droplet diameter, the temperature of the gas phase mixture near to the droplet's surface, the oil vapour concentration and the velocity of the droplet's internal flow.

The effects on the evaporation rate of varying the initial droplet diameter are summarised below.

- The evaporation rate might increase by around 90% if the initial droplet diameter is reduced from 500  $\mu\text{m}$  to 100  $\mu\text{m}$ , and it can increase by around 20% if the diameter is reduced from 200  $\mu\text{m}$  to 100  $\mu\text{m}$ . The droplet's internal velocity magnitude might increase by more than 50% with a reduction of the initial droplet diameter. The evaporation rate is higher for droplets with a small diameter (<200  $\mu\text{m}$ ), which are quicker to evaporate completely if they are suspended in the core flow of the bearing chamber for more than 0.15 s for droplets with a diameter of 100  $\mu\text{m}$  and 0.3 s for droplets with a diameter of 200  $\mu\text{m}$ .

- The evaporation rate increases with a reduction in initial droplet diameter because, for small diameters, there is more surface area exposed to the airflow conditions, which favours evaporation at the droplet's surface as well as heat transfer from the environment to the droplet's surface and from the droplet's surface to the core. In addition, the probability of finding droplets with a diameter less than 200  $\mu\text{m}$  inside the bearing chamber is 93%; therefore, the evaporation of the 93% of the population of droplets increases the oil vapour concentration inside the bearing chamber.

Findings related to the time of residence of droplets and the evaporation rate are summarised below.

- According to the analysis in this research and based on previous experimental reports by Glahn et al. (1996), the most common droplets inside the bearing chamber are those with a diameter of 100  $\mu\text{m}$  and the population of droplets with diameters less than 100  $\mu\text{m}$  is 60%. Therefore, some droplets travel from the bearings to the walls and others stay in the core flow.
- The time of residence of droplets that travel radially (from the bearings to the walls) was calculated, where the droplets with a diameter less than 100  $\mu\text{m}$  were found to have a residence time of around 0.002 s and released 2% of their initial mass to vapour. The results of this research indicate that this time is not sufficient for enough vapour to be produced from the droplets that travel radially from the bearings to the walls to cause ignition.

- There would need to be a vapour mass fraction concentration of 0.7 to 0.9 to reach the required vapour levels for ignition, but, for the radial time of residence and the distribution of vapour calculated, this limit is not reached. However, it is of interest for further studies to determine the percentage of droplets that stay in the core region for a long time, as well as to determine the vapour mass fraction concentration produced from these droplets in order to determine whether the concentration of droplets that stay travelling in the core region reaches the ignition limits.

Findings related to the effects on the evaporation rate of varying the air velocity are summarised below.

- The air velocities of 1 m/s and 5 m/s are found in the recirculation regions of the bearing chamber, and they can also be assumed to be the relative velocities of the droplets and the air, which provides an estimation of the evaporation rate in two scenarios in the bearing chamber. One scenario is the droplets travelling in the recirculation regions and the other is the droplets' radial journey from the bearings to the wall. Therefore, these velocities were used for the purposes of the evaporation rate calculation.
- An increase in the air velocity shows higher reduction on the droplet diameter, which is due to the higher shear stress forces at the droplet's surface which enhances evaporation. Moreover, the evaporation rate for the case with an initial diameter of 200  $\mu\text{m}$  and air at 5 m/s is 0.140  $\text{mm}^2/\text{s}$ , and for the case with air at 1 m/s it is 0.07  $\text{mm}^2/\text{s}$ , which means that for the case with air at 5 m/s the evaporation

rate is twice as high as with air at 1 m/s. Therefore, an increase in air velocity inside the bearing chamber causes an increase in the oil vapour concentration in the core flow.

- The velocity magnitude in the droplet's interior was calculated, where, for a droplet with an initial diameter of 200  $\mu\text{m}$  and air at 550 K, the evaporation rate might increase by 50% if the air velocity is increased from 1 m/s to 5 m/s. Also, the droplet's velocity magnitude increases by 23% when the evaporation process reaches a steady state.
- As a summary, an increase in air velocity increases the droplet's internal circulation and consequently the heat transfer from the droplet's surface to the core, which increases the evaporation rate. However, at the same time, an increase in the heat transfer from the surroundings to the droplet increases the cooling of the core flow inside the bearing chamber.

Findings related to the effects on the evaporation rate of varying the ambient temperature are summarised below.

- The temperature in the bearing chamber is in the range of 350 K to 850 K and it might vary due to the geometry and operation conditions. Consequently, in this study the air temperature was analysed for three different temperatures, namely 350 K, 450 K and 550 K, for a droplet with an initial diameter of 200  $\mu\text{m}$ .
- The initial droplet temperature was considered to be 298 K in all cases; this is to observe the heating-up period and its duration, which is important in terms of bearing chamber application because the droplets might be injected from the

bearings with oil temperatures from 303.15 K to 403.15 K. Consequently, some droplets might be travelling in the core flow during the heating-up period and others might be travelling during the phase-change stage due to the saturation temperature of PEC5 being 334 K. Therefore, this research provides the duration of the heating-up period and this can be used as a reference if further analysis is needed to predict different stages of the evaporation process, knowing the specific oil droplet temperature inside the bearing chamber.

- The results show that the evaporation rate increases by 22% if the air temperature increases from 450 K to 550 K and by 95% if the air temperature increases from 350 K to 550 K. Moreover, the droplet's internal velocity magnitude is similar between the cases with air temperatures of 450 K and 550 K, but it can increase by around 60% if the air temperature increases from 350 K to 550 K. Therefore, the regions that are at 550 K inside the core flow of the bearing chamber might show higher concentrations of oil vapour.

Findings related to the effects on the evaporation rate of radiation are summarised below.

- Radiation effects were analysed, with the results showing that radiation in the environment has different effects on droplet evaporation and this mainly depends on the initial droplet diameter.
- The evaporation rate for the case without radiation might be 32% higher than with radiation for droplets with an initial diameter of 100  $\mu\text{m}$ . This might be because the concentration of oil vapour at the droplet's surface is higher for the cases with radiation, which might reduce the heat transfer from the air to the droplet's surface.

The oil vapour film might reduce the difference in temperature between the environment and the droplet's surface.

- It is noted that the radiation is not significant for droplets with an initial diameter of 200  $\mu\text{m}$ . However, radiation might increase the evaporation rate by 32% for droplets with an initial diameter of 500  $\mu\text{m}$ . According to the histogram presented by Glahn et al. (1996), the probability of the mass associated per droplet diameter for droplets with an initial diameter of 500  $\mu\text{m}$  in the bearing chamber is 1%. Therefore, radiation might affect only 1% of the oil associated with the droplets with an initial diameter of 500  $\mu\text{m}$  in the bearing chamber. In addition, radiation in the environment increases the droplet's internal velocity magnitude by around 36% in droplets with an initial diameter of 200  $\mu\text{m}$ .

Findings related to the droplet's internal circulation are summarised below.

- A qualitative analysis was performed to observe the droplet's internal circulation, the droplet's temperature gradients and the oil vapour mass fraction. In general, the droplet's internal flow field follows the patterns predicted by the Hill's vortex model, which includes a spherical vortex, or Hill's vortex, an internal wake and a liquid boundary layer.
- The spherical vortex is displaced to the droplet's surface when the evaporation starts, creating a recirculation at the droplet's interface. Moreover, while the droplet core is closer to the saturation temperature, the formation of bubbles can be seen inside the droplet in the regions of higher temperature gradients. In some

cases, the bubble collapses and releases liquid, causing the formation of a small secondary droplet.

- The droplet's internal circulation is influenced by the bubble formation and the associated recirculation causes distortion due to the viscous shear at the gas–liquid interface between the bubbles and the droplet. In addition, the mass and momentum interchange at the bubble interface might form a chaotic motion, which has been experimentally observed previously in burning droplets (Miglani et al., 2014). This chaotic motion is observed next to the bubbles with small vortices in opposite directions at the bubble's interface, which agrees with the study of Zhang et al. (2018). Moreover, vorticity with opposite directions is also seen in the bubble's interior in this study.
- The implication of bubble formation inside droplets travelling in the core flow of the bearing chamber arises from the formation of secondary droplets due to the collapse of a bubble. The secondary droplets formed by the bubble break-up have diameters less than 10  $\mu\text{m}$ , which might increase the oil vapour concentration.
- In the literature, it is noted that during the evaporation of high viscosity droplets, there is a formation of bubbles and the bubble interface precipitates the formation of a shell structure, which increases the pressure on the bubble until it causes a complete disintegration of the droplet (Miglani et al., 2014). The shell formation is a subject for further studies to analyse the thermal degradation of oil droplets inside bearing chambers and to observe how the thermal degradation of oil droplets affects the evaporation process inside the chamber.

Findings related to the heat transfer coefficient are summarised below.

- The heat transfer coefficient from the environment to the droplet's surface was calculated. This showed that the droplet's initial diameter and the airflow velocity are key parameters to reduce the heat transfer between the airflow and the droplet's surface.
- The results show that the heat transfer coefficient can be reduced by 20% if the initial droplet diameter is increased from 100  $\mu\text{m}$  to 500  $\mu\text{m}$  and the air velocity is decreased from 5 m/s to 1 m/s. Therefore, droplets with large diameters travelling at low velocity reduce the heat transfer coefficient.
- The heat and mass transfer coefficients were calculated based on the correlations of Renksizbulut and Yuen (1983). Therefore, the present method correlates well with the heat and mass transfer correlations reported in the literature.

## 6.2 Contributions to knowledge

This research presented a detailed analysis of droplet heat and mass transfers in representative bearing chamber conditions. The analysis provides an estimation of the droplet evaporation rate, the droplet's lifetime and the oil vapour mass fraction of a single droplet under different ambient conditions.

This research presented the methodology of the estimation of the oil properties to analyse the evaporation rate of droplets, which can be extrapolated to the simulations in all the oil flow patterns found in the bearing chamber (i.e. ligaments and thin film). It also provides guidance and recommendations to model the evaporation of oil droplets, including the MFR, adaptive meshing and a radiative environment.

This work estimated the vapour concentration needed to reach the flammability limits for droplets of PEC5 travelling in the core flow of bearing chambers. It found that the vapour concentration in the bearing chamber is lower than the flammability range, assuming that all the droplets travel from the bearings to the wall. Additionally, it provided a calculation of the amount of vapour produced by different sized droplets of oil in bearing chamber conditions, as well as an estimation of the lifetime of oil droplets in bearing chamber conditions.

Moreover, the analysis extrapolated the evaporation rate and amount of vapour from one droplet to the proportion of oil in droplets by size in the bearing chamber. As a result, the time of residence and a prediction of the evaporation rates for droplets with initial diameters between  $18\mu\text{m}$  and  $500\mu\text{m}$  were calculated.

The methodology used to extrapolate the findings for one droplet to a bearing chamber case can be used in further analysis as a design tool to estimate the vapour concentrations for a variety of operational conditions not considered here. Therefore, the outcome of this research might be to contribute to the design of the bearing chambers of the new generation of aero-engines.

### **6.3 Future work**

Further work is needed to add a turbulent flow and observe the effects on the evaporation rate; the turbulence model can include the damping factor to avoid divergence at the droplet's interface.

It is important to know the number of droplets travelling in the core flow inside the bearing chamber, as well as the residence time of the droplets travelling in the core flow region, in order to determine whether there are droplets that will evaporate completely.

It is recommended to implement the methodology of this research, including the large variation of air velocities and temperatures, in the whole bearing chamber in order to estimate the oil vapour concentration. The present methodology can be included in the simulation of the whole bearing chamber using the Lagrangian–Eulerian approach, similar to the research of Adeniyi (2015), including the evaporation model and analysing the regions with a high concentration of vapour and the temperatures in the core flow, as well as localising the confined regions where the vapour can reach the flammability limits.

Furthermore, in this research the effect of radiation might be overestimated due to the assumptions of non-thermal expansion during the heating-up period, as well as the consideration that the droplet is opaque and has a black body absorption which is the maximum absorption that the droplet can have. However, this investigation can provide conservative data for the risk assessment of new designs of bearing chambers. This study can be extended, adding to the variation of the thermophysical properties in the gas and liquid phases. The oil can be considered as semi-transparent and the radiation in the environment can be considered as non-grey radiation, which means accounting for the emissivity dependence of the wavelength media. However, this can be computationally expensive for calculations regarding the whole bearing chamber.

It is important to include in further numerical analysis the variation of the liquid's thermophysical properties, which might help to predict whether there will be the formation of bubbles inside the evaporative droplets. One important property to observe with the

formation of bubbles is the variation of the liquid's viscosity with time, as well as the surface tension, because both properties might lead to bubble formation. Surface tension is reduced when the temperature increases, which might influence the droplet's internal circulation and bubble generation inside the droplets.

Consequently, if the effect of temperature variations on the thermophysical properties is included, the heat transfer might be faster from the droplet's surface to the core and therefore the evaporation rate might increase. Therefore, it is important to include the variation of these properties according to the temperature.

In addition, it is recommended to include the whole composition of the aero-engine oil, which means studying the evaporation of multi-component droplets inside bearing chamber conditions. This will give a better estimation of the evaporation rates and the amount of oil in the bearing chamber.

The parametrical study should be extended, varying the ambient pressure and increasing the ambient temperature and airflow velocity. The variation of the ambient pressure might give different evaporation rates to those estimated in this study, which is important to analyse to determine the vapour concentration in the core flow.

Furthermore, it is recommended to study the evaporation rate under different pressures inside the bearing chamber, because previous studies have noted that droplet evaporation increases in high-pressure and high-temperature conditions and the size of droplets is small in high-pressure environments, which might increase the oil vapour concentration in the bearing chamber's core flow. Moreover, the air-oil vapour mixture might be quicker to ignite in high-pressure environments because the high pressure

produces variations in the oil's AIT, which can be decreased and thereby produce exothermic reactions that are not observed at ambient pressure.

## 7 References

- ABOU AL-SOOD, M. M. & BIROUK, M. 2007. A numerical study of the effect of turbulence on mass transfer from a single fuel droplet evaporating in a hot convective flow. *International Journal of Thermal Sciences*, 46, 779-789.
- ABRAMZON, B. & SAZHIN, S. 2005. Droplet vaporization model in the presence of thermal radiation. *International Journal of Heat and Mass Transfer*, 48, 1868-1873.
- ABRAMZON, B. & SAZHIN, S. 2006. Convective vaporization of a fuel droplet with thermal radiation absorption. *Fuel*, 85, 32-46.
- ABRAMZON, B. & SIRIGNANO, W. A. 1989. Droplet vaporization model for spray combustion calculations. *International Journal of Heat and Mass Transfer*, 32, 1605-1618.
- ADENIYI, A. A. 2015. *A coupled Lagrangian-Eulerian framework to model droplet to film interaction with heat transfer*. PhD Thesis. University of Nottingham, 2015.
- ADENIYI, A. A. 2019. Private communication.
- ADENIYI, A. A., MORVAN, H. P., SIMMONS, K. A. & ASME 2014. A transient CFD simulation of the flow in a test rig of an aeroengine bearing chamber. *Proceedings of the ASME Turbo Expo: Turbine Technical Conference and Exposition, Jun 16-20, 2014, Düsseldorf, Germany*, 5C: Heat Transfer, V05CT16A030.
- AGGARWAL, S. K., SIRIGNANO, W. A. & TONG, A. Y. 1984. A comparison of vaporization models in spray calculations. *AIAA Journal*, 22, 1448-1457.
- AIDARINIS, J., MISSIRLIS, D., YAKINTHOS, K. & GOULAS, A. 2011. CFD Modeling and LDA Measurements for the Air-Flow in an Aero Engine Front Bearing Chamber. *Journal of Engineering for Gas Turbines and Power*, 133, 082504-082504-8.
- ALBERNAZ, D. L., AMBERG, G. & DO-QUANG, M. 2016. Simulation of a suspended droplet under evaporation with Marangoni effects. *International Journal of Heat and Mass Transfer*, 97, 853-860.
- ANSYS 2016a. #2039870, How to stabilize VOF simulation with Geo-Reconstruct scheme? In: ANSYS FLUENT, K. R. S. (ed.). ANSYS, Inc.
- ANSYS 2016b. ANSYS Fluent Theory Guide. Canonsburg, PA 15317: ANSYS, Inc.
- ANSYS 2016c. ANSYS Fluent Users Guide. Canonsburg, PA 15317: ANSYS, Inc.
- AROSSI, A., ISHAQ, G. & MENACER, M. 2003. Measurement of Gas/Liquid Flow Velocities in Rapidly Rotating Annular Systems. *Proceedings of the ASME/JSME 2003 4th Joint Fluids Summer Engineering Conference, July 6-10, 2003, Honolulu, Hawaii, USA*, 1: Fora, Parts A, B, C, and D., 1805-1809.
- AVIATION, B. 2019. *Rolls-Royce's Alan Newby Talks The Future Of Aircraft Engines* [Online]. Published by ITP Media Group. Available: <https://www.aviationbusinessme.com/19018-rolls-royces-alan-newby-talks-the-future-of-aircraft-engines> [Accessed 24/09/2019].
- AVULAPATI, M. M., GANIPPA, L. C., XIA, J. & MEGARITIS, A. 2016. Puffing and micro-explosion of diesel-biodiesel-ethanol blends. *Fuel*, 166, 59-66.

- BANERJEE, R. 2007. A Numerical Study of Combined Heat and Mass Transfer in an Inclined Channel Using the VOF Multiphase Model. *Numerical Heat Transfer, Part A: Applications*, 52, 163-183.
- BANERJEE, R. 2013. Numerical investigation of evaporation of a single ethanol/iso-octane droplet. *Fuel*, 107, 724-739.
- BANERJEE, R. & GOPINATH, R. 2011. CFD analysis to study evaporation of a single ETHANOL/ISO-octane binary mixture droplet. *Proceedings of the ASME-JSME-KSME 2011 Joint Fluids Engineering Conference, July 24–29, 2011, Hamamatsu, Japan*, 1, Symposia – Parts A, B, C, and D, 2571-2578.
- BANERJEE, R. & ISAAC, K. M. 2004. An algorithm to determine the mass transfer rate from a pure liquid surface using the volume of fluid multiphase model. *International Journal of Engine Research*, 5, 23-37.
- BAUMGARTEN, C. 2006. *Mixture formation in internal combustion engines*, Springer Science & Business Media.
- BERGELES, K., HARDALUPAS, Y. & TAYLOR, A. M. K. P. 2018. On the transient flow inside and around a deforming millimetre class oil droplet falling under the action of gravity in stagnant air. *Physics of Fluids*, 30, 013305.
- BRACKBILL, J. U., KOTHE, D. B. & ZEMACH, C. 1992. A continuum method for modeling surface tension. *Journal of Computational Physics*, 100, 335-354.
- BRISTOT, A. 2019. Private communication.
- BRISTOT, A., MORVAN, H. P. & SIMMONS, K. A. 2016. Evaluation of a Volume of Fluid CFD methodology for the oil film thickness estimation in an aero-engine bearing chamber. *Proceedings of the ASME Turbo Expo 2016: Turbomachinery Technical Conference and Exposition, June 13–17, 2016, Seoul, South Korea*, 2C: Turbomachinery, V02CT39A007.
- BUSAM, S., GLAHN, A. & WITTIG, S. 2000. Internal Bearing Chamber Wall Heat Transfer as a Function of Operating Conditions and Chamber Geometry. *Journal of Engineering for Gas Turbines and Power*, 122, 314-320.
- CHANDRA, B. & SIMMONS, K. 2017. Experimental investigation on aeroengine shallow sump performance. *Proceedings of the 1st Global Power and Propulsion Forum, January 16-18, Zurich, Switzerland*.
- CHAUVEAU, C., BIROUK, M. & GÖKALP, I. 2011. An analysis of the d2-law departure during droplet evaporation in microgravity. *International Journal of Multiphase Flow*, 37, 252-259.
- CHEN, B., CHEN, G. D. & SHEN, X. L. 2011a. Oil Droplet Motion Considering Breakup in an Aeroengine Bearing Chamber. *Advances in Mechanical Design, Pts 1 and 2*, 199-200, 638-645.
- CHEN, B., CHEN, G. D., SUN, H. C. & ZHANG, Y. H. 2014. Effect of oil droplet deformation on its deposited characteristics in an aeroengine bearing chamber. *Proceedings of the Institution of Mechanical Engineers, Part G: Journal of Aerospace Engineering*, 228, 206-218.
- CHEN, G., SUN, H. & WANG, J. 2011b. Research into Configuration and Flow of Wall Oil Film in Bearing Chamber Based on Droplet Size Distribution. *Chinese Journal of Aeronautics*, 24, 355-362.

- CHEN, J.-N., OUYANG, X.-L., ZHANG, Z. & JIANG, P.-X. 2016. A numerical model for simulating the droplet flow and evaporation. *Journal of Engineering Thermophysics*, 37, 637-642.
- CHEW, J. W. 1996. Analysis of the oil film on the inside surface of an aero-engine bearing chamber housing. *Proceedings of the ASME 1996 International Gas Turbine and Aeroengine Congress and Exhibition, June 10–13, 1996, Birmingham, United Kingdom*, 1: Turbomachinery, V001T01A082.
- CHUNG, T. H., AJLAN, M., LEE, L. L. & STARLING, K. E. 1988. Generalized multiparameter correlation for nonpolar and polar fluid transport properties. *Industrial & Engineering Chemistry Research*, 27, 671-679.
- CHUNG, T. H., LEE, L. L. & STARLING, K. E. 1984. Applications of kinetic gas theories and multiparameter correlation for prediction of dilute gas viscosity and thermal conductivity. *Industrial & Engineering Chemistry Fundamentals*, 23, 8-13.
- CLIFT, R., GRACE, J. R. & WEBER, M. E. 2005. *Bubbles, drops, and particles*, Mineola, New York, Dover Publications, Inc.
- CROUCHEZ-PILLOT, A. & MORVAN, H. P. 2014. CFD simulation of an aeroengine bearing chamber using an enhanced volume of fluid (VOF) method: An evaluation using adaptive meshing. *Proceedings of the ASME Turbo Expo 2014: Turbine Technical Conference and Exposition, June 16–20, 2014, Düsseldorf, Germany*, 5C: Heat Transfer, V05CT16A033.
- DAÏF, A., BOUAZIZ, M., CHESNEAU, X. & ALI CHÉRIF, A. 1998. Comparison of multicomponent fuel droplet vaporization experiments in forced convection with the Sirignano model. *Experimental Thermal and Fluid Science*, 18, 282-290.
- DEEPU, P., BASU, S. & KUMAR, R. 2013. Vaporization dynamics of functional droplets in a hot laminar air jet. *International Journal of Heat and Mass Transfer*, 56, 69-79.
- DENNER, F. & VAN WACHEM, B. G. M. 2015. Numerical time-step restrictions as a result of capillary waves. *Journal of Computational Physics*, 285, 24-40.
- DIMIAN, A. C., BILDEA, C. S. & KISS, A. A. 2014. Chapter 16 - Health, Safety and Environment. In: DIMIAN, A. C., BILDEA, C. S. & KISS, A. A. (eds.) *Computer Aided Chemical Engineering*. Elsevier.
- DONG, Q., WANG, Z., ZHANG, Y. & WANG, J. 2014. Numerical Simulation of Interior Flow in Evaporation Droplet. *Proceedings of the ASME 2014 4th Joint US-European Fluids Engineering Division Summer Meeting collocated with the ASME 2014 12th International Conference on Nanochannels, Microchannels, and Minichannels, August 3–7, 2014, Chicago, Illinois, USA*, 1D, Symposia: Transport Phenomena in Mixing; Turbulent Flows; Urban Fluid Mechanics; Fluid Dynamic Behavior of Complex Particles; Analysis of Elementary Processes in Dispersed Multiphase Flows; Multiphase Flow With Heat/Mass Transfer in Process Technology; Fluid Mechanics of Aircraft and Rocket Emissions and Their Environmental Impacts; High Performance CFD Computation; Performance of Multiphase Flow Systems; Wind Energy; Uncertainty Quantification in Flow Measurements and Simulations, V01DT31A003.
- EXXONMOBIL. 2016. *Mobil Jet Oil II Aircraft-Type Gas Turbine Lubricant* [Online]. Spring Texas: Exxon Mobil Corporation. Available:

[http://pds.exxonmobil.com/USA-English/Aviation/PDS/GLXXENAVIEMMobil\\_Jet\\_Oil\\_II.aspx](http://pds.exxonmobil.com/USA-English/Aviation/PDS/GLXXENAVIEMMobil_Jet_Oil_II.aspx) [Accessed].

- FAETH, G. M. 1977. Current status of droplet and liquid combustion. *Progress in Energy and Combustion Science*, 3, 191-224.
- FANG, L. & CHEN, G. 2018. The study of droplet deformation and droplet volume fraction in an aero-engine bearing chamber. *Proceedings of the Institution of Mechanical Engineers, Part G: Journal of Aerospace Engineering*, 233(6), 2264–2277.
- FARRALL, M., HIBBERD, S. & SIMMONS, K. 2000. Computational modelling of two-phase air/oil flow within an aero-engine bearing chamber. *Proceedings of the 2000 ASME Fluids Engineering Division Summer Meeting, June 11-15, 2000, Boston Massachusetts*, 677-684.
- FARRALL, M., HIBBERD, S. & SIMMONS, K. 2007. The Effect of Initial Injection Conditions on the Oil Droplet Motion in a Simplified Bearing Chamber. *Journal of Engineering for Gas Turbines and Power*, 130, 012501-012501.
- FARRALL, M., HIBBERD, S., SIMMONS, K. & GIDDINGS, D. 2006. Prediction of air/oil exit flows in a commercial aero-engine bearing chamber. *Proceedings of the Institution of Mechanical Engineers Part G-Journal of Aerospace Engineering*, 220, 197-202.
- FARRALL, M. B. 2000. *Numerical modelling of two-phase flow in a simplified bearing chamber*. Thesis (Ph.D.)--University of Nottingham, 2000.
- FEI, W., CHEN, G., FU, Y. & TAO, W. 2017. Transient Analysis of Air/Oil Two-Phase Flow in Bearing Chamber under the Periodic Boundary Conditions. *The 3rd International Conference on Mechatronics and Mechanical Engineering (ICMME 2016), MATEC Web of Conferences*, 95, 1-4.
- FLAGAN, R. C. 1988. *Fundamentals of air pollution engineering / Richard C. Flagan, John H. Seinfeld*, Englewood Cliffs, N.J., Englewood Cliffs, N.J. : Prentice Hall.
- FLAGAN, R. C. & SEINFELD, J. H. 2013. *Fundamentals of air pollution engineering*, Courier Corporation.
- FLOUROS, M., IATROU, G., YAKINTHOS, K., COTTIER, F. & HIRSCHMANN, M. 2015. Two-Phase Flow Heat Transfer and Pressure Drop in Horizontal Scavenge Pipes in an Aero-engine. *Journal of Engineering for Gas Turbines and Power*, 137, 081901-081901.
- FULLER, E. N., ENSLEY, K. & GIDDINGS, J. C. 1969. Diffusion of halogenated hydrocarbons in helium. The effect of structure on collision cross sections. *The Journal of Physical Chemistry*, 73, 3679-3685.
- FULLER, E. N. & GIDDINGS, J. C. 1965. A Comparison of Methods for Predicting Gaseous Diffusion Coefficients. *Journal of Chromatographic Science*, 3, 222-227.
- FULLER, E. N., SCHETTLER, P. D. & GIDDINGS, J. C. 1966. New Method for Prediction of Binary Gas-Phase Diffusion Coefficients. *Industrial & Engineering Chemistry*, 58, 18-27.
- GHASSEMI, H., BAEK, S. W. & KHAN, Q. S. 2006. Experimental study on binary droplet evaporation at elevated pressures and temperatures. *Combustion Science and Technology*, 178, 1031-1053.

- GLAHN, A., BUSAM, S., BLAIR, M. F., ALLARD, K. L. & WITTIG, S. 2000. Droplet Generation by Disintegration of Oil Films at the Rim of a Rotating Disk. *Journal of Engineering for Gas Turbines and Power*, 124, 117-124.
- GLAHN, A., BUSAM, S. & WITTIG, S. 1997. Local and mean heat transfer coefficients along the internal housing walls of aero engine bearing chambers. *Proceedings of the ASME 1997 International Gas Turbine and Aeroengine Congress and Exhibition, June 2–5, 1997, Orlando, Florida, USA*, 3: Heat Transfer; Electric Power; Industrial and Cogeneration, V003T09A050.
- GLAHN, A., KURRECK, M., WILLMANN, M. & WITTIG, S. 1996. Feasibility Study on Oil Droplet Flow Investigations Inside Aero Engine Bearing Chambers—PDPA Techniques in Combination With Numerical Approaches. *Journal of Engineering for Gas Turbines and Power*, 118, 749-755.
- GLAHN, A. & WITTIG, S. 1996. Two-Phase Air/Oil Flow in Aero Engine Bearing Chambers: Characterization of Oil Film Flows. *Journal of Engineering for Gas Turbines and Power*, 118, 578-583.
- GLAHN, A. & WITTIG, S. 1999. Two-Phase Air/Oil Flow in Aero-Engine Bearing Chambers – Assessment of an Analytical Prediction Method for the Internal Wall Heat Transfer. *International Journal of Rotating Machinery*, 5, 155-165.
- GODSAVE, G. A. E. 1949. Combustion of Droplets in a Fuel Spray. *Nature*, 164, 708-709.
- GODSAVE, G. A. E. 1953. Studies of the combustion of drops in a fuel spray—the burning of single drops of fuel. *Symposium (International) on Combustion*, 4, 818-830.
- GORSE, P., BUSAM, S. & DULLENKOPF, K. 2004. Influence of Operating Condition and Geometry on the Oil Film Thickness in Aeroengine Bearing Chambers. *Journal of Engineering for Gas Turbines and Power*, 128, 103-110.
- GORSE, P., DULLENKOPF, K. & BAUER, H. J. 2005. The Effect of Airflow Across Aero-Engine Roller Bearing on Oil Droplet Generation. *17th International Symposium on Airbreathing Engines (ISABE), September 4-9, 2005, Munich, Germany*, ISABE-2005-1208, 1-9.
- GORSE, P., DULLENKOPF, K., BAUER, H. J., WITTIG, S. & ASME 2008. An Experimental Study on Droplet Generation in Bearing Chambers Caused by Roller Bearings. *Proceedings of the ASME Turbo Expo 2008: Power for Land, Sea, and Air, June 9–13, 2008, Berlin, Germany*, 4: Heat Transfer, Parts A and B, 1681-1692.
- GORSE, P., WILLENBORG, K., BUSAM, S., EBNER, J., DULLENKOPF, K. & WITTIG, S. 2003. 3D-LDA measurements in an aero-engine bearing chamber. *American Society of Mechanical Engineers, International Gas Turbine Institute, Turbo Expo (Publication) IGTI*, 5 A, 257-265.
- HANN, D. B., CHERDANTSEV, A. V., MITCHELL, A., MCCARTHY, I. N., HEWAKANDAMBY, B. N. & SIMMONS, K. 2016. A study of droplet impact on static films using the BB-LIF technique. *Experiments in Fluids*, 57, 1-12.
- HART, R. A. 2005. *Numerical modelling of tunnel fires and water mist suppression*. Thesis (PhD)--University of Nottingham, 2005.

- HASHMI, A. A. 2012. *Oil Film Dynamics in Aero Engine Bearing Chambers: Fundamental Investigations and Numerical Modelling*. Thesis (PhD)--Karlsruhe Institute of Technology, 2012.
- HEE, J. L. 2019. *Experimental and Computational Investigation into Oil Shedding from an Aeroengine Ball Bearing*. Thesis (PhD)--University of Nottingham, 2019.
- HILL, M. J. M. 1894. On a Spherical Vortex. *Philosophical Transactions of the Royal Society of London. A*, 185, 213-245.
- HUSTED, B. P., HOLMSTEDT, G. & HERTZBERG, T. 2004. The physics behind water mist systems. *Proceedings of International Water Mist Association Conference, October 6-8, Rome Italy*, 1-15.
- INCROPERA, F. P., DEWITT, D. P., BERGMAN, T. & S., L. A. 2007. *Fundamentals of heat and mass transfer*, Hoboken, N.J., Hoboken, N.J. : Wiley.
- JAKOBY, R., KIM, S. & WITTIG, S. 1999. Correlations of the Convection Heat Transfer in Annular Channels With Rotating Inner Cylinder. *Journal of Engineering for Gas Turbines and Power*, 121, 670-677.
- JINGYU, Z., ZHENXIA, L. & GUOZHE, R. 2016. The design and performance evaluation of axial ventilator with honeycomb in the turbofan engine lubrication system. *Proceedings of the Institution of Mechanical Engineers, Part G: Journal of Aerospace Engineering*, 230, 1397-1408.
- KAKIMPA, B., MORVAN, H. P. & HIBBERD, S. 2014. Report on a Validated Energy Equation as Part of a CFD-Based Film Solution, E-BREAK Deliverable 2.2.2.1, UTC Report FF117/BK/10.
- KAKIMPA, B., MORVAN, H. P. & HIBBERD, S. 2016. The numerical simulation of multi-scale oil films using coupled VOF and Eulerian thin-film models. *Proceedings of the ASME Turbo Expo 2016: Turbomachinery Technical Conference and Exposition, June 13–17, 2016, Seoul, South Korea*, V001T01A020.
- KANIKE, N., TALURU, D., NELANTI, K. & GUJAR, K. G. 2012. Thermal Analysis of Gas Turbine Bearing Compartment During Normal Operation Period. *Proceedings of the ASME 2012 Gas Turbine India Conference. ASME 2012 Gas Turbine India Conference, December 1, 2012, Mumbai, Maharashtra, India*, 505-511.
- KRUG, M. B., HOFLER, C., BAUER, H.-J. & KURZ, W. 2015. Evaluation of the Volume of Fluid Method for the Numerical Modelling of an Aero Engine Bearing Chamber. *22nd International Symposium on Air Breathing Engines (ISABE), October 25-30, 2015, Phoenix, Arizona, USA*, ISABE-2015-21284, 1-10.
- KUCHTA, J. M. & CATO, R. J. 1968. Ignition and Flammability Properties of Lubricants. *SAE International*, 77, 1008-1020.
- KUMAR, A. & MANDAL, D. K. 2018. Oscillatory circulation inside evaporating methanol–water drops. *International Journal of Multiphase Flow*, 102, 130-137.
- KUMAR, A., PRASAD, S., PAL, P., NARAYANAN, S. & MANDAL, D. K. 2018. Circulation Inside a Methanol – Water Drop Evaporating in a Heated Atmosphere. *Colloid and Interface Science Communications*, 24, 82-86.
- KURZ, W., BAUER, H.-J. & ASME 2014. An Approach for Predicting the Flow Regime in An Aero Engine Bearing Chamber. *Proceedings of the ASME Turbo Expo 2014: Turbine Technical Conference and Exposition, June 16–20, 2014, Düsseldorf, Germany*, 5C: Heat Transfer, V05CT16A037.

- KURZ, W., DULLENKOPF, K. & BAUER, H. J. 2013. Capacitive Film Thickness Measurements in a Ventless Aero-Engine Bearing Chamber-Influence of Operating Conditions and Offtake Design. *Journal of Engineering for Gas Turbines and Power-Transactions of the Asme*, 135.
- LAGE, P. L. C. & RANGEL, R. H. 1993. Single droplet vaporization including thermal radiation absorption. *Journal of Thermophysics and Heat Transfer*, 7, 502-509.
- LEE, W. H. 1979. A Pressure Iteration Scheme for Two-Phase Flow Modeling. Los Alamos, New Mexico.: Los Alamos Scientific Laboratory.
- LIU, H. 2000. *Science and Engineering of Droplets - Fundamentals and Applications*, Park Ridge, N.J.: Norwich, N.Y.: Noyes Publications; William Andrew Pub.
- LONG, W., YI, P., JIA, M., FENG, L. & CUI, J. 2015. An enhanced multi-component vaporization model for high temperature and pressure conditions. *International Journal of Heat and Mass Transfer*, 90, 857-871.
- MAGNINI, M. 2012. *CFD modeling of two-phase boiling flows in the slug flow regime with an interface capturing technique*. Thesis (PhD)--University of Bologna, 2012.
- MANDAL, D. K. & BAKSHI, S. 2012. Internal circulation in a single droplet evaporating in a closed chamber. *International Journal of Multiphase Flow*, 42, 42-51.
- MAQABLEH, A., SIMMONS, K., HIBBERD, S., POWER, H. & YOUNG, C. 2003. CFD modelling of three-component air/oil flow and heat transfer in a rotating annulus. *Proceedings, Eleventh annual conference of the CFD Society of Canada, May 28-30, Vancouver, Canada*, 39.
- MICHAELIDES, E. 2006. *Particles, bubbles & drops: their motion, heat and mass transfer*, Singapore ; London: World Scientific.
- MICHAILIDOU, E. K., ASSAEL, M. J., HUBER, M. L., ABDULAGATOV, I. M. & PERKINS, R. A. 2014. Reference Correlation of the Viscosity of n-Heptane from the Triple Point to 600 K and up to 248 MPa. *Journal of Physical and Chemical Reference Data*, 43, 023103.
- MIGLANI, A., BASU, S. & KUMAR, R. 2014. Insight into instabilities in burning droplets. *Physics of Fluids*, 26, 032101.
- MIL-PRF-23699F 1997. Lubricating oil, Aircraft Turbine Engine, Synthetic Base, NATO Code Number O-156. Department of Defense of United States of America.
- MITCHELL, A. J., SIMMONS, K. & HANN, D. 2016. Droplet Impingements upon Moving Films: An Examination of Secondary Droplet Production. *International Journal of Heat and Mass Transfer*, 1-17.
- MOHAMMADI, E., KING, A. & NARAYANASWAMY, R. A study on the Flow Field and Internal Circulation of a Single Moving Droplet. 20th Australasian Fluid Mechanics Conference, 5-8 December 2016 2016 Perth, Australia.
- MONSALVO, M. A. 2006. *Phase Behavior and Viscosity Modeling of Refrigerant-Lubricant Mixtures*. Thesis (PhD)--Technical University of Denmark.
- NASA. 2018. *A Tool to Evaluate the Dynamic Capability of Turbine Engines* [Online]. NASA. Available: <https://technology.nasa.gov/patent/LEW-TOPS-96> [Accessed 22/02/2018].
- NAYAGAM, V., DIETRICH, D. L. & WILLIAMS, F. A. 2018. Unsteady droplet combustion with fuel thermal expansion. *Combustion and Flame*, 195, 216-219.

- NOMURA, H., UJIIE, Y., RATH, H. J., SATO, J. I. & KONO, M. 1996. Experimental study on high-pressure droplet evaporation using microgravity conditions. *Symposium (International) on Combustion*, 26, 1267-1273.
- PEDUTO, D. 2015. *Oil droplet impact dynamics in aero-engine bearing chambers : correlations derived from direct numerical simulations / Davide Peduto*. Thesis (PhD)--University of Nottingham, 2015.
- POLING, B. E., PRAUSNITZ, J. M. & CONNELL, J. P. 2001. *The properties of gases and liquids* Singapore ; London, Singapore ; London : McGraw-Hill.
- PRAKASH, S. & SIRIGNANO, W. A. 1978. Liquid fuel droplet heating with internal circulation. *International Journal of Heat and Mass Transfer*, 21, 885-895.
- PRAKASH, S. & SIRIGNANO, W. A. 1980. Theory of convective droplet vaporization with unsteady heat transfer in the circulating liquid phase. *International Journal of Heat and Mass Transfer*, 23, 253-268.
- PUNEKAR, H. 2015. #2028458, What are the best practices to use Lee evaporation condensation model in Fluent? *In: ANSYS FLUENT*, K. R. S. (ed.). ANSYS, Inc.
- RADWAN, A. 2015. #2016316, How to access the reconstruction gradients of a UDS in Fluent by means of UDF? *In: ANSYS FLUENT*, K. R. S. (ed.). ANSYS, Inc.
- RADWAN, A. 2018. #2056261, Working with species gradients in ANSYS Fluent User-Defined Functions (UDF) for multiphase applications. *In: ANSYS FLUENT*, K. R. S. (ed.). ANSYS, Inc.
- RAGHURAM, S., RAGHAVAN, V., POPE, D. N. & GOGOS, G. 2013. Two-phase modeling of evaporation characteristics of blended methanol–ethanol droplets. *International Journal of Multiphase Flow*, 52, 46-59.
- RAO, D. C. K., KARMAKAR, S. & BASU, S. 2018. Bubble dynamics and atomization mechanisms in burning multi-component droplets. *Physics of Fluids*, 30, 067101.
- RAZZOUK, A., MOKBEL, I., GARCÍA, J., FERNANDEZ, J., MSAKNI, N. & JOSE, J. 2007. Vapor pressure measurements in the range 10–5Pa to 1Pa of four pentaerythritol esters: Density and vapor–liquid equilibria modeling of ester lubricants. *Fluid Phase Equilibria*, 260, 248-261.
- RENKSIZBULUT, M., NAFZIGER, R. & LI, X. 1991. A mass transfer correlation for droplet evaporation in high-temperature flows. *Chemical Engineering Science*, 46, 2351-2358.
- RENKSIZBULUT, M. & YUEN, M. C. 1983. Experimental Study of Droplet Evaporation in a High-Temperature Air Stream. *Journal of Heat Transfer*, 105, 384-388.
- ROLLS-ROYCE. 2016. *Civil Aerospace. Future Products*. [Online]. Available: <http://www.rolls-royce.com/products-and-services/civil-aerospace/products/future-products/advance.aspx> [Accessed 20/06/2016].
- ROLLS-ROYCE, L. 2005. *The jet engine*, Derby: Rolls-Royce.
- ROSENLIEB, J. W. 1978. Aircraft Engine Sump Fire Mitigation, Phase II. *NASA-CR-135379 Technical Report*. Cleveland, Ohio: National Aeronautics and Space Administration.
- SAZHIN, S. S. 2006. Advanced models of fuel droplet heating and evaporation. *Progress in Energy and Combustion Science*, 32, 162-214.
- SAZHIN, S. S., ABDELGHAFAR, W. A., SAZHINA, E. M. & HEIKAL, M. R. 2005. Models for droplet transient heating: Effects on droplet evaporation, ignition, and break-up. *International Journal of Thermal Sciences*, 44, 610-622.

- SAZHIN, S. S., KRISTYADI, T., ABDELGHAFAR, W. A., BEGG, S., HEIKAL, M. R., MIKHALOVSKY, S. V., MEIKLE, S. T. & AL-HANBALI, O. 2007a. Approximate Analysis of Thermal Radiation Absorption in Fuel Droplets. *Journal of Heat Transfer*, 129, 1246-1255.
- SAZHIN, S. S., KRISTYADI, T., ABDELGHAFAR, W. A. & HEIKAL, M. R. 2006. Models for fuel droplet heating and evaporation: Comparative analysis. *Fuel*, 85, 1613-1630.
- SAZHIN, S. S., KRISTYADI, T., HEIKAL, M. R., ABDELGHAFAR, W. A. & SHISHKOVA, I. N. 2007b. Fuel Droplet Heating and Evaporation: Analysis of Liquid and Gas Phase Models. *SAE International*, 2688-3627.
- SCASE, M. M. & TERRY, H. L. 2018. Spherical vortices in rotating fluids. *Journal of Fluid Mechanics*, 846, R4.
- SCHMIDT, J., HANK, W. K., KLEIN, A. & MAIER, K. 1982. The Oil/air System of a Modern Fighter Aircraft Engine. *Proceedings of the 59th Symposium of the AGARD Propulsion and Energetics Panel, May 31-June 3, 1982, Ottawa, Canada*, 323, Problems in Bearings and Lubrication, 93-112.
- SHINJO, J., XIA, J., GANIPPA, L. C. & MEGARITIS, A. 2014. Physics of puffing and microexplosion of emulsion fuel droplets. *Physics of Fluids*, 26, 103302.
- SIMMONS, K., HIBBERD, S., WANG, Y. & CARE, I. 2002. Numerical Study of the Two-Phase Air/Oil Flow Within an Aero-Engine Bearing Chamber Model Using a Coupled Lagrangian Droplet Tracking Method. *Proceedings of the ASME 2002 Pressure Vessels and Piping Conference. Computational Technologies for Fluid/Thermal/Structural/Chemical Systems With Industrial Applications, August 5-9, 2002, Vancouver, BC, Canada*, 1, 325-331.
- SIRIGNANO, W. A. 2010. *Fluid dynamics and transport of droplets and sprays / William A. Sirignano*, Cambridge, Cambridge : Cambridge University Press.
- SPALDING, D. B. 1953. The combustion of liquid fuels. *Symposium (International) on Combustion*, 4, 847-864.
- STROTOS, G., GAVAISES, M., THEODORAKAKOS, A. & BERGELES, G. 2011. Numerical investigation of the evaporation of two-component droplets. *Fuel*, 90, 1492-1507.
- STROTOS, G., GAVAISES, M., THEODORAKAKOS, A. P. & BERGELES, G. C. 2008. Evaporation of a suspended multicomponent droplet under convective conditions. *Proceedings of CHT-08 ICHMT International Symposium on Advances in Computational Heat Transfer, May 11-16, 2008, Marrakesh, Morocco*, 121, No. 4., 770-773.
- STROTOS, G., MALGARINOS, I., NIKOLOPOULOS, N. & GAVAISES, M. 2016. Predicting the evaporation rate of stationary droplets with the VOF methodology for a wide range of ambient temperature conditions. *International Journal of Thermal Sciences*, 109, 253-262.
- SUN, H., CHEN, G., WANG, L. N. & WANG, F. 2016a. Oil droplets fractions and oil droplets/air energy transfer analysis in bearing chamber. *Acta Aeronautica et Astronautica Sinica*, 3, 030.
- SUN, H., CHEN, G. & ZHANG, Y. 2016b. Theoretical and experimental studies on the motion and thermal states of oil droplet in a bearing chamber. *Proceedings of the*

- Institution of Mechanical Engineers, Part G: Journal of Aerospace Engineering*, 230(14), 2596–2614.
- SUN, H.-C., CHEN, G.-D., YOU, H. & CHEN, J.-Y. 2013. Effect of Sealing Air on Oil Droplet and Oil Film Motions in Bearing Chamber. *国际设备工程与管理 (英文版)*, 130-139.
- TKACZYK, P. 2011. *CFD simulation of annular flows through bends / Piotr Tkaczyk*. Thesis (PhD)--University of Nottingham, 2011.
- TKACZYK, P. M. & MORVAN, H. P. 2011. Film thickness prediction in an annular two-phase flow around C-shaped bend. *Journal of Computational Multiphase Flows*, 3, 27-39.
- TSENG, C. C. & VISKANTA, R. 2005. Effect of Radiation Absorption on Fuel Droplet Evaporation. *Combustion Science and Technology*, 177, 1511-1542.
- URNS, S. R. 2000. *An introduction to combustion : concepts and applications*, Boston, Mass. ; London, McGraw-Hill.
- URNESS, K. N., GOUGH, R. V., WIDEGREN, J. A. & BRUNO, T. J. 2016. Thermal Decomposition Kinetics of Polyol Ester Lubricants. *Energy & Fuels*, 30, 10161-10170.
- WANG, C., MORVAN, H. P., HIBBERD, S. & CLIFFE, K. A. 2011. Thin Film Modelling for Aero-Engine Bearing Chambers. *Proceedings of the ASME 2011 Turbo Expo: Turbine Technical Conference and Exposition, June 6-10, 2011, Vancouver, British Columbia, Canada*, 1: Aircraft Engine; Ceramics; Coal, Biomass and Alternative Fuels; Wind Turbine Technology, 277-286.
- WANG, J., WANG, X., CHEN, H., JIN, Z. & XIANG, K. 2018. Experimental study on puffing and evaporation characteristics of jatropa straight vegetable oil (SVO) droplets. *International Journal of Heat and Mass Transfer*, 119, 392-399.
- WEINSTOCK, V. D. & HEISTER, S. D. 2004. Modeling Oil Flows in Engine Sumps: Drop Dynamics and Wall Impact Simulation. *Journal of Engineering for Gas Turbines and Power*, 128, 163-172.
- WEN, C. S. 1996. *The fundamentals of aerosol dynamics / C. S. Wen*, Singapore, Singapore : World Scientific.
- WILLENBORG, K., BUSAM, S., ROCKAMP, H. & WITTIG, S. 2002. Experimental Studies of the Boundary Conditions Leading to Oil Fire in the Bearing Chamber and in the Secondary Air System of Aeroengines. *Proceedings of the ASME Turbo Expo 2002: Power for Land, Sea, and Air, June 3-6, 2002, Amsterdam, The Netherlands*, 3: Turbo Expo 2002, Parts A and B, 739-747.
- WILLIAMS, J. 2009. *Thin film rimming flow subject to droplet impact at the surface*. Thesis (PhD)--University of Nottingham, 2009.
- WITTIG, S., GLAHN, A. & HIMMELSBACH, J. 1994. Influence of High Rotational Speeds on Heat Transfer and Oil Film Thickness in Aero-Engine Bearing Chambers. *Journal of Engineering for Gas Turbines and Power*, 116, 395-401.
- WONG, S.-C. & LIN, A.-C. 2006. Internal temperature distributions of droplets vaporizing in high-temperature convective flows. *Journal of Fluid Mechanics*, 237, 671-687.
- YI, P., LONG, W., FENG, L., JIA, M. & TIAN, J. 2015. A Numerical Investigation of the Vaporization Process of Lubricating Oil Droplets under Gas Engine Conditions. *SAE International*, JSAE 20159274.

- YI, P., LONG, W., JIA, M., TIAN, J. & LI, B. 2016. Development of a quasi-dimensional vaporization model for multi-component fuels focusing on forced convection and high temperature conditions. *International Journal of Heat and Mass Transfer*, 97, 130-145.
- YOKOZEKI, A. 2005. Theoretical performances of various refrigerant-absorbent pairs in a vapor-absorption refrigeration cycle by the use of equations of state. *Applied Energy*, 80, 383-399.
- ZHANG, Y., HUANG, Y., HUANG, R., HUANG, S., MA, Y., XU, S. & WANG, Z. 2018. A new puffing model for a droplet of butanol-hexadecane blends. *Applied Thermal Engineering*, 133, 633-644.
- ÇENGEL, Y. A. 2011. *Thermodynamics : an engineering approach* / Yunus A. Çengel, Michael A. Boles, New York, New York : McGraw-Hill.

## 8 Annex

### 8.1 Literature review

#### 8.1.1 Two-phase flow in bearing chambers

The literature review is divided into three accounting the main contributors to study the two-phase flow in bearing chambers, as it is observed in Figure 8.1. The main contributors are the University Technology Centre and Gas Turbine and Transmissions Research Centre both in the section called UTC (Figure 8.2); the Karlsruhe Institute of Technology in the subsection of KIT (Figure 8.3) and in the subsection of others includes the studies made in others research institutes and universities such as the Northwestern Polytechnical University.

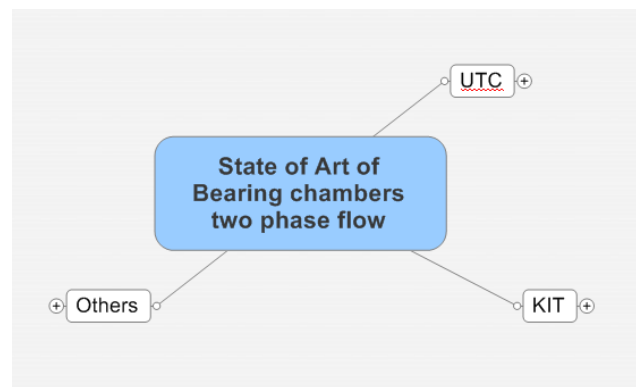


**Figure 8.1. Main contributors in the research on two-phase flow in bearing chambers**

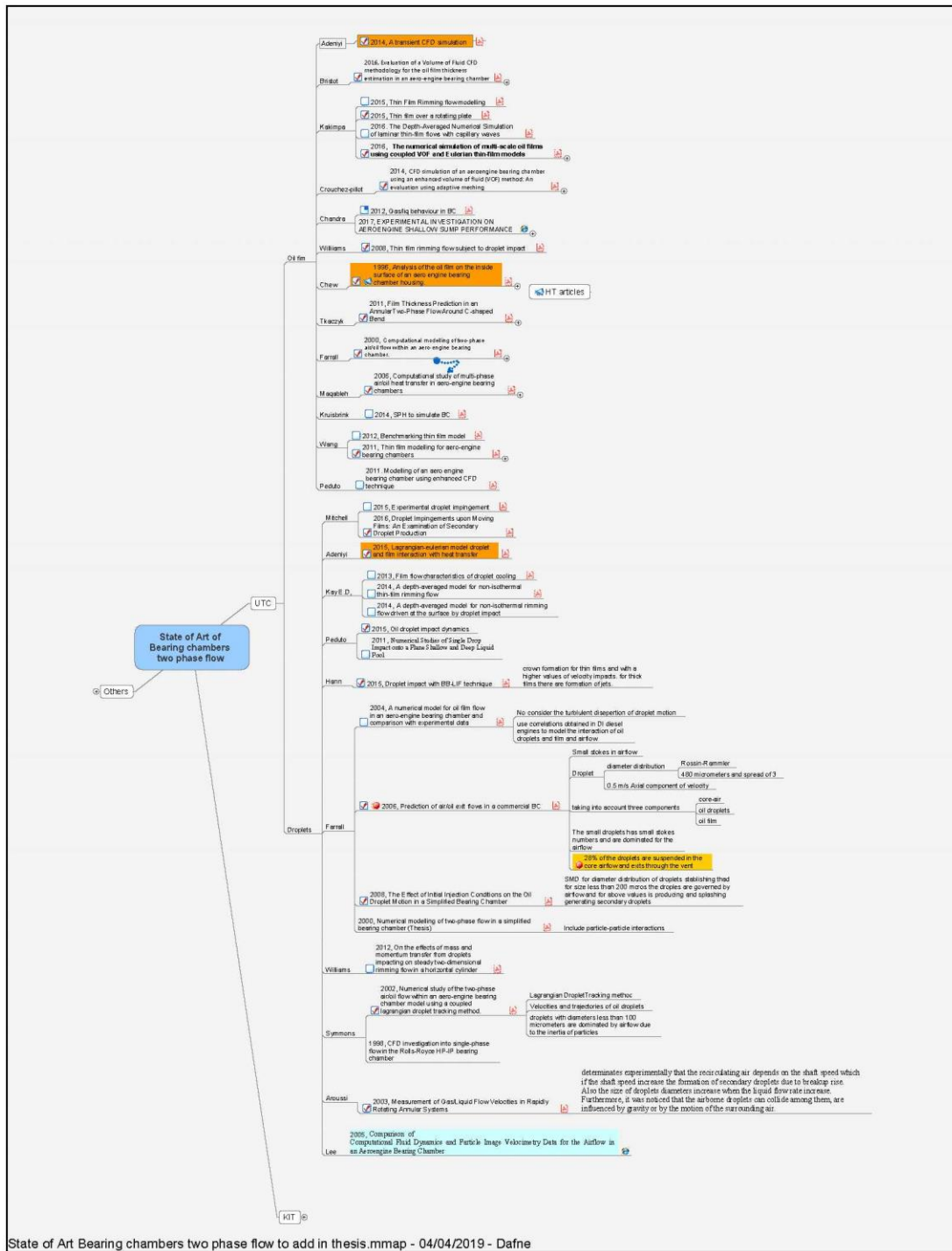


Figure 8.2. Overview of the literature review from the University Technology Centre and Gas Turbine and Transmissions Research Centre.

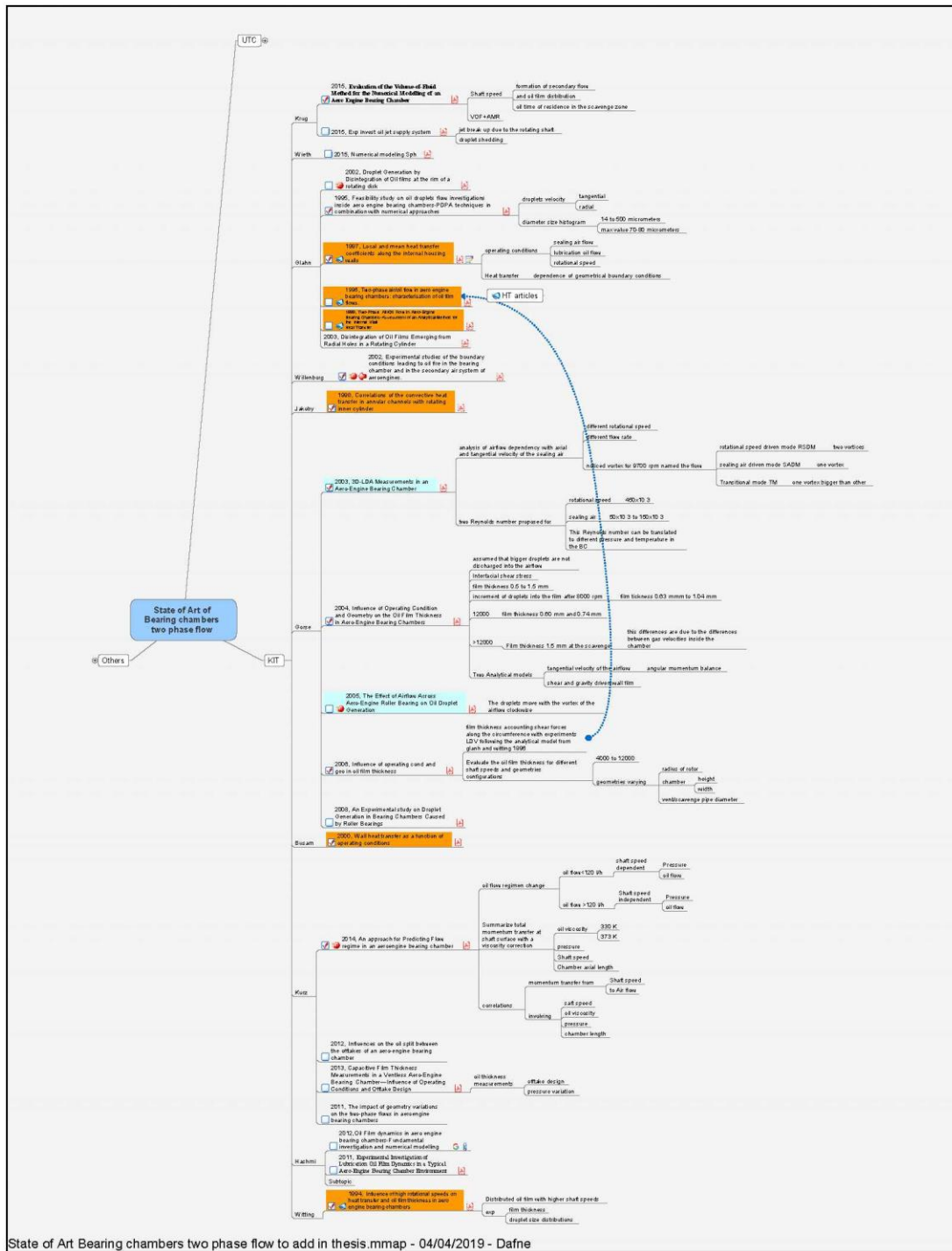


Figure 8.3. Overview of the literature review from the Karlsruhe Institute of Technology.

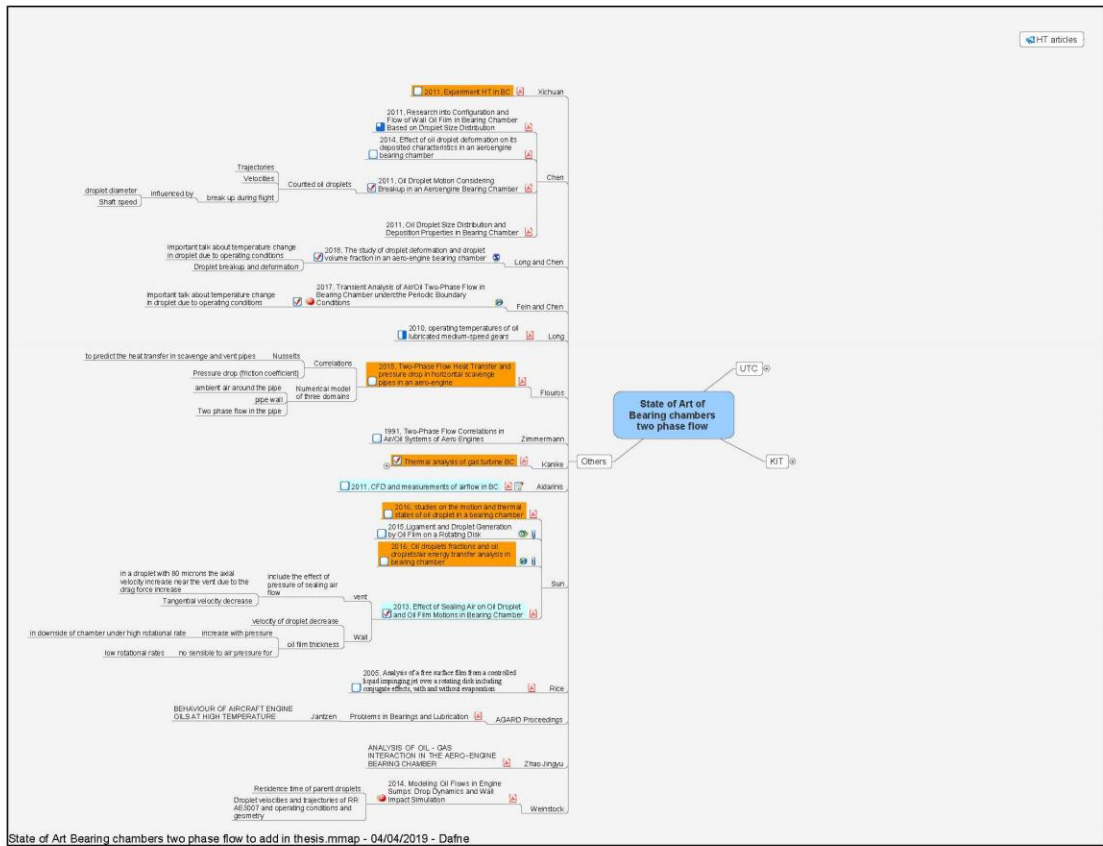


Figure 8.4. Overview of the literature review from others research institutes and universities such as the Northwestern Polytechnical University.

## 8.2 Modelling droplets inside bearing chambers-Case issues

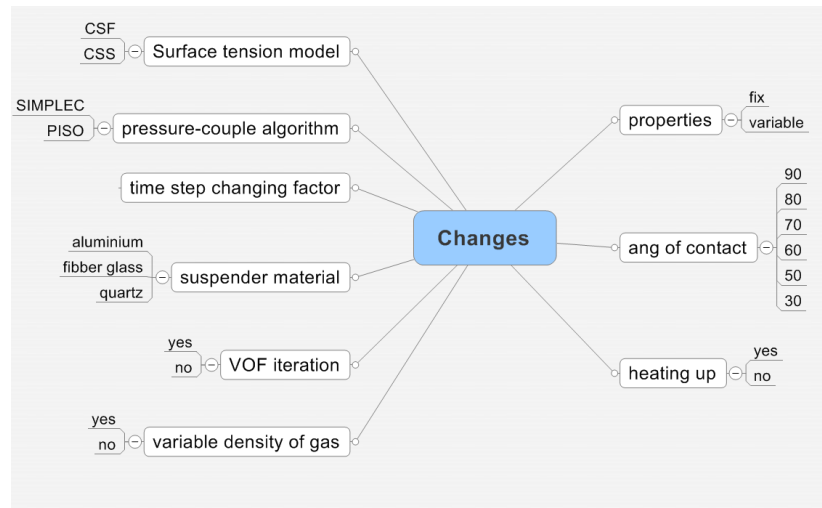


Figure 8.5. Modifications done to modelling droplets inside bearing chambers.

## 8.3 Radiation models advantages and limitations.

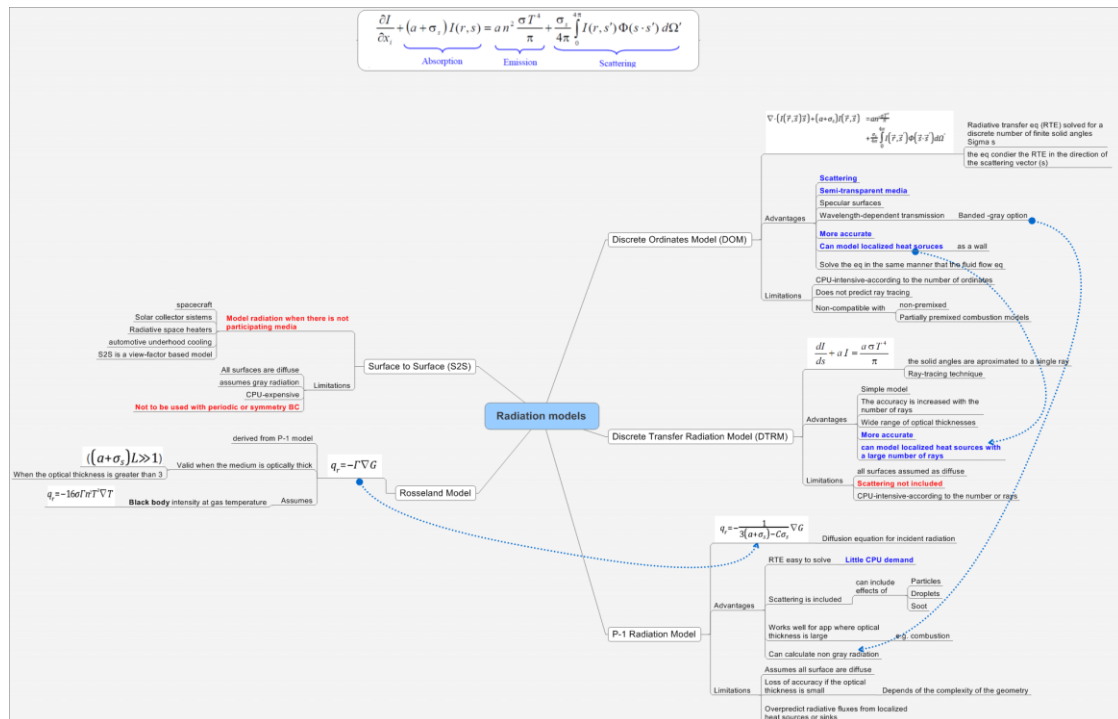


Figure 8.6. Available radiation models in ANSYS fluent.

## 8.4 Force balance analysis

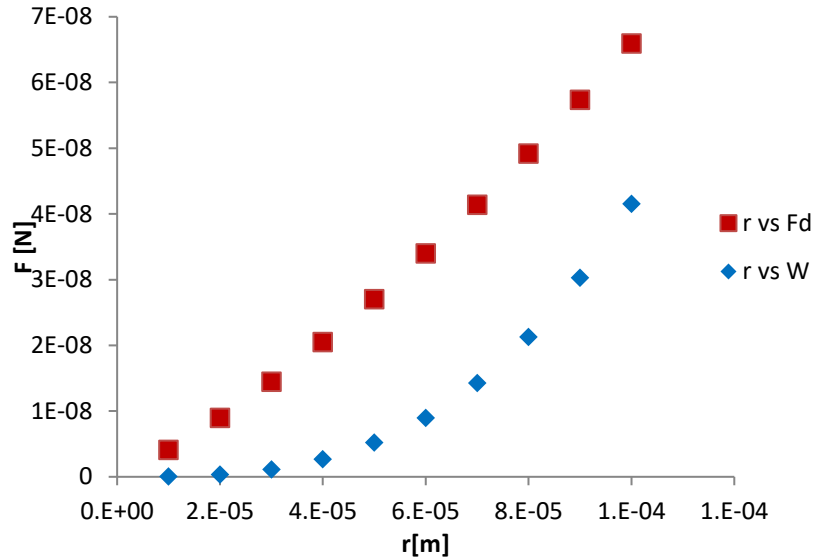


Figure 8.7 Drag force vs Weight for an oil droplet with 200 $\mu\text{m}$  of diameter under the airflow with velocity of 1m/s

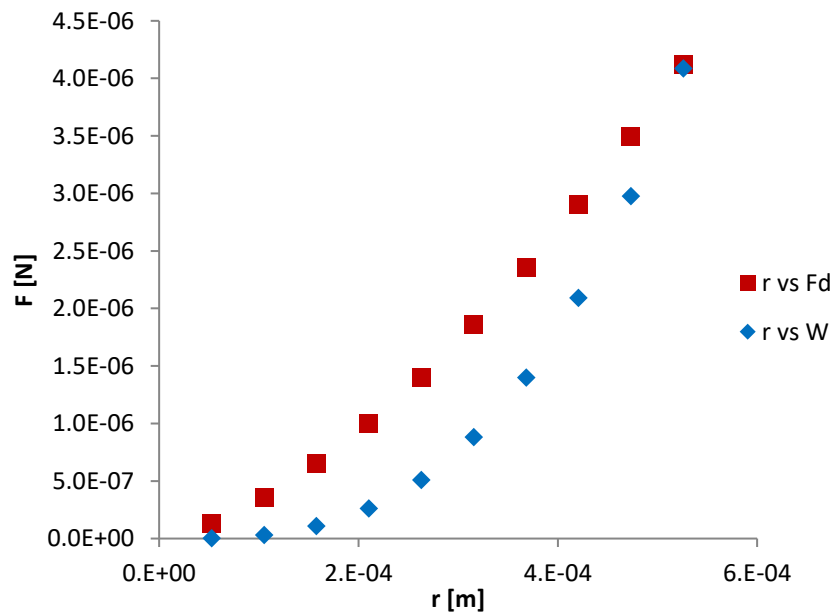


Figure 8.8 Drag force vs Weight for a heptane droplet with 1052  $\mu\text{m}$  of diameter under the airflow with velocity of 3.2m/s

## 8.5 Calculation of Reynolds numbers inside the bearing chamber.

bristol 2016 (-10 to 10 m/s) [Sun, 2014; sun, 2013; Glahn, 2002](#)

1m=1e6µm Re

ua	ud [m/s]		d [µm]	rd [m]	Re	We
10		14.21959265	1	5.00E-07	0.288867832	0.000592692
10		17.9760924			0.546032926	0.00211772
10		24.68105589			1.005046019	0.007174685
10		31.87672585			1.497652239	0.015931362
10		52.43147161			2.904803438	0.059932785
	ua-ud		10	5.00E-06	2.888678324	0.005926924
					5.460329264	0.021177204
					10.05046019	0.071746853
					14.97652239	0.159313625
					29.04803438	0.599327849
			20	1.00E-05	5.777356648	0.011853847
					10.92065853	0.042354408
					20.10092039	0.143493705
					29.95304478	0.318627249
					58.09606876	1.198655698
			50	2.50E-05	14.44339162	0.029634618
					27.30164632	0.105886021
					50.25230097	0.358734263
					74.88261194	0.796568124
					145.2401719	2.996639244
			100	5.00E-05	28.88678324	0.059269235
					54.60329264	0.211772041
					100.5046019	0.717468526
					149.7652239	1.593136247
					290.4803438	5.993278489
			150	7.50E-05	43.33017486	0.088903853
					81.90493895	0.317658062
					150.7569029	1.076202789
					224.6478358	2.389704371
					435.7205157	8.989917733
			200	1.00E-04	57.77356648	0.118538471
					109.2065853	0.423544082
					201.0092039	1.434937052
					299.5304478	3.186272494
					580.9606876	11.98655698
			300	1.50E-04	86.66034972	0.177807706
					163.8098779	0.635316123
					301.5138058	2.152405579
					449.2956717	4.779408741
					871.4410314	17.97983547
			400	2.00E-04	115.547133	0.237076941
					218.4131705	0.847088164
					402.0184077	2.869874105
					599.0608956	6.372544988
					1161.921375	23.97311395
			500	2.50E-04	144.4339162	0.296346176
					273.0164632	1.058860205
					502.5230097	3.587342631
					748.3261194	7.965681235
					1452.401719	29.96639244

Figure 8.9. Calculation of Reynolds numbers inside the bearing chamber taking into account the air velocity at 10 m/s.

bristot 2016 (-10 to 10 m/s) [Sun, 2014; sun, 2013; Glahn, 2002](#)

1m=1e6μm      Re

ua	ud [m/s]	d [μm]	rd [m]	Re	We	
5	ud	1	5.00E-07	0.631161339	0.002829513	
5				0.888326433	0.005605007	
5				1.347339526	0.012893923	
5				1.839945745	0.024045898	
5				3.247096944	0.074889593	
		ua-ud	10	5.00E-06	6.311613386	0.028295133
					8.883264326	0.056050066
					13.47339526	0.128939226
					18.39945745	0.240458976
					32.47096944	0.748895927
	20	1.00E-05	1.00E-05	12.62322677	0.056590265	
				17.76652865	0.112100132	
				26.94679051	0.257878452	
				36.7989149	0.480917951	
				64.94193888	1.497791854	
	50	2.50E-05	2.50E-05	31.55806693	0.141475664	
				44.41632163	0.28025033	
				67.36697628	0.644696131	
				91.99728725	1.202294878	
				162.3548472	3.744479634	
	100	5.00E-05	5.00E-05	63.11613386	0.282951327	
				88.83264326	0.56050066	
				134.7339526	1.289392262	
				183.9945745	2.404589757	
				324.7096944	7.488959269	
	150	7.50E-05	7.50E-05	94.67420079	0.424426991	
				133.2489649	0.84075099	
				202.1009288	1.934088393	
				275.9918618	3.606884635	
				487.0645416	11.2334389	
	200	1.00E-04	1.00E-04	126.2322677	0.565902655	
				177.6652865	1.12100132	
				269.4679051	2.578784524	
				367.989149	4.809179514	
				649.4193888	14.97791854	
	300	1.50E-04	1.50E-04	189.3484016	0.848853982	
				266.4979298	1.681501981	
				404.2018577	3.868176785	
				551.9837235	7.213769271	
				974.1290832	22.46687781	
	400	2.00E-04	2.00E-04	252.4645354	1.13180531	
				355.330573	2.242002641	
				538.9358102	5.157569047	
				735.978298	9.618359027	
				1298.838778	29.95583708	
	500	2.50E-04	2.50E-04	315.5806693	1.414756637	
				444.1632163	2.802503301	
				673.6697628	6.446961309	
				919.9728725	12.02294878	
				1623.548472	37.44479634	

Figure 8.10. Calculation of Reynolds numbers inside the bearing chamber taking into account the air velocity at 5 m/s.

bristol 2016 (-10 to 10 m/s) [Sun, 2014; sun, 2013; Glahn, 2002](#)  $1m=1e6\mu m$  Re

ua	ud [m/s]	d [ $\mu m$ ]	rd [m]	Re	We
1	14.21959265	1	5.00E-07	0.904996144	0.00581734
1	17.9760924			1.162161238	0.009593205
1	24.68105589			1.621174331	0.018667682
1	31.87672585			2.11378055	0.031735895
1	52.43147161			3.520931749	0.088053408
	ua-ud	10	5.00E-06	9.049961436	0.058173396
	-13.21959265			11.62161238	0.095932051
	-16.9760924			16.21174331	0.186676821
	-23.68105589			21.1378055	0.317358952
	-30.87672585			35.20931749	0.880534085
	-51.43147161	20	1.00E-05	18.09992287	0.116346792
				23.24322475	0.191864102
				32.42348661	0.373353641
				42.275611	0.634717904
				70.41863498	1.76106817
		50	2.50E-05	45.24980718	0.290866979
				58.10806188	0.479660256
				81.05871653	0.933384103
				105.6890275	1.586794761
				176.0465875	4.402670425
		100	5.00E-05	90.49961436	0.581733958
				116.2161238	0.959320512
				162.1174331	1.866768207
				211.378055	3.173589521
				352.0931749	8.80534085
		150	7.50E-05	135.7494215	0.872600937
				174.3241856	1.438980768
				243.1761496	2.80015231
				317.0670825	4.760384282
				528.1397624	13.20801127
		200	1.00E-04	180.9992287	1.163467916
				232.4322475	1.918641024
				324.2348661	3.733536414
				422.75611	6.347179043
				704.1863498	17.6106817
		300	1.50E-04	271.4988431	1.745201873
				348.6483713	2.877961536
				486.3522992	5.600304621
				634.134165	9.520768564
				1056.279525	26.41602255
		400	2.00E-04	361.9984574	2.326935831
				464.864495	3.837282048
				648.4697322	7.467072827
				845.51222	12.69435809
				1408.3727	35.2213634
		500	2.50E-04	452.4980718	2.908669789
				581.0806188	4.79660256
				810.5871653	9.333841034
				1056.890275	15.86794761
				1760.465875	44.02670425

Figure 8.11. Calculation of Reynolds numbers inside the bearing chamber taking into account the air velocity at 1 m/s.

## 8.6 Calculation of the time it takes for a drop to travel from the bearings to walls according to the literature review.

The time of the droplet journey from bearings to walls is calculated from the radial velocities reported in previous literature as follows:

According to the droplet trajectories presented by (Sun et al., 2016b),

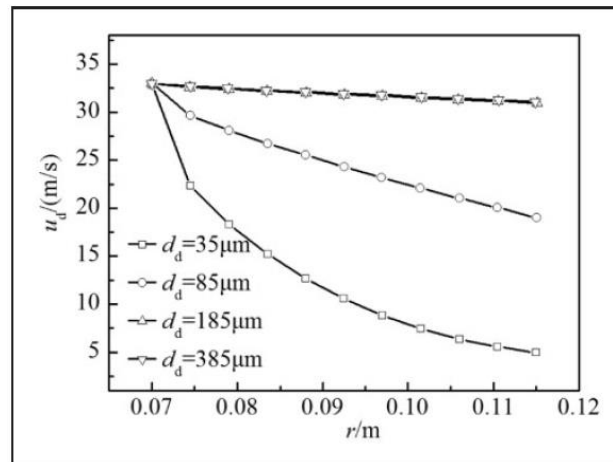


Figure 8.12. Effect on the droplet diameter on its velocity and trajectory (Sun et al., 2016b).

Table 8.1. Calculation of droplet journey time for initial diameters of 385 $\mu\text{m}$ , 185 $\mu\text{m}$ , 85 $\mu\text{m}$  and 35 $\mu\text{m}$  according to Figure 8.12.

diam=385mm and 185mm			diam=85mm		
r(m)	ud (m/s)	t [s]	r(m)	ud (m/s)	t [s]
0.069896	32.98387	<b>0.002119</b>	0.069896	32.98387	<b>0.002119</b>
0.074194	32.74194	<b>0.002266</b>	0.074395	29.67742	<b>0.002507</b>
0.078766	32.41935	<b>0.00243</b>	0.078792	28.22581	<b>0.002791</b>
0.083247	32.17742	<b>0.002587</b>	0.083371	26.77419	<b>0.003114</b>
0.087726	32.09677	<b>0.002733</b>	0.087766	25.56452	<b>0.003433</b>
0.092298	31.85484	<b>0.002897</b>	0.092344	24.35484	<b>0.003792</b>
0.096595	31.69355	<b>0.003048</b>	0.096647	23.22581	<b>0.004161</b>
0.101258	31.53226	<b>0.003211</b>	0.101224	22.17742	<b>0.004564</b>
0.105647	31.37097	<b>0.003368</b>	0.1058	21.12903	<b>0.005007</b>
0.1104	31.29032	<b>0.003528</b>	0.110285	20.16129	<b>0.00547</b>
0.114698	31.04839	<b>0.003694</b>	0.114862	19.03226	<b>0.006035</b>

diam=35mm		
r(m)	ud (m/s)	t [s]
0.069897	32.90323	<b>0.002124</b>
0.074348	22.41935	<b>0.003316</b>
0.078761	18.30645	<b>0.004302</b>
0.083441	15.32258	<b>0.005446</b>
0.087845	12.66129	<b>0.006938</b>
0.092245	10.64516	<b>0.008665</b>
0.096826	8.870968	<b>0.010915</b>
0.101405	7.419355	<b>0.013668</b>
0.10589	6.370968	<b>0.016621</b>
0.110191	5.645161	<b>0.01952</b>
0.114857	5	<b>0.022971</b>

According to the droplet trajectories presented by (Chen et al., 2014).

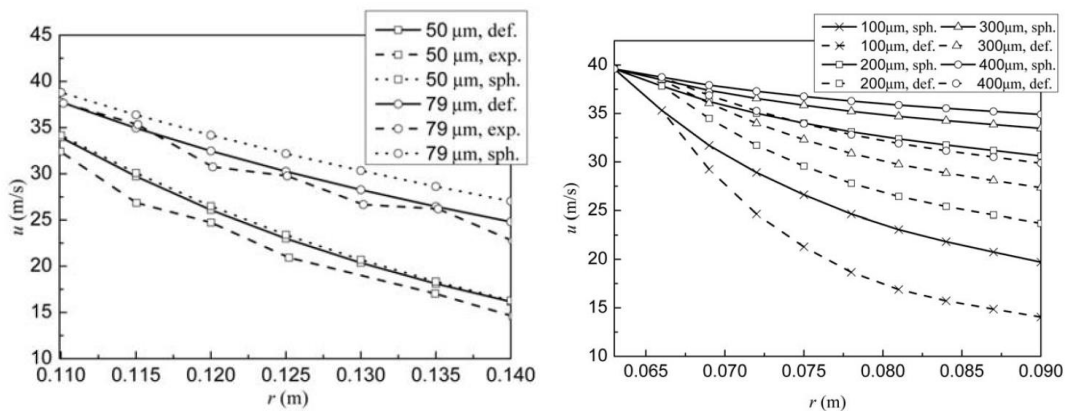


Figure 8.13. Effect on the droplet diameter on its velocity and trajectory (Chen et al., 2014).

Table 8.2. Calculation of droplet journey time for initial diameters of 79 $\mu$ m for a shaft speed of 5000rpm.

diam=79 $\mu$ m	sph simu		diam=79 $\mu$ m	Glahn exp			
	r (m)	ud (m/s)		t [s]	r (m)	ud (m/s)	t [s]
	0.110067634	38.71013	<b>0.002843</b>		0.110220096	37.5815	<b>0.002933</b>
	0.114999618	36.38468	<b>0.003161</b>		0.11515208	35.25605	<b>0.003266</b>
	0.119980894	34.22065	<b>0.003506</b>		0.120189986	30.67282	<b>0.003918</b>
	0.125011693	32.1374	<b>0.00389</b>		0.125118072	29.71833	<b>0.00421</b>
	0.129942301	30.29581	<b>0.004289</b>		0.130201373	26.66748	<b>0.004882</b>
	0.135021704	28.61592	<b>0.004718</b>		0.135227585	26.19712	<b>0.005162</b>
	0.140001376	27.0164	<b>0.005182</b>		0.139963776	22.74211	<b>0.006154</b>

diam=79 $\mu$ m	deformed droplets	
r (m)	ud (m/s)	t [s]
0.110108401	37.6484	<b>0.002925</b>
0.114973096	34.93151	<b>0.003291</b>
0.120033854	32.45434	<b>0.003699</b>
0.124946865	30.2968	<b>0.004124</b>
0.12995785	28.29909	<b>0.004592</b>
0.134870412	26.46119	<b>0.005097</b>
0.13993005	24.78311	<b>0.005646</b>

**Table 8.3. Calculation of droplet journey time for initial diameters of 50 $\mu$ m for a shaft speed of 5000rpm.**

diam=50 $\mu$ m	sph simu	
r (m)	ud (m/s)	t [s]
0.110064345	34.05251	<b>0.003232</b>
0.115029034	30.05708	<b>0.003827</b>
0.119944062	26.46119	<b>0.004533</b>
0.124956729	23.26484	<b>0.005371</b>
0.129968612	20.62785	<b>0.006301</b>
0.13498027	18.15068	<b>0.007437</b>
0.139893057	16.15297	<b>0.008661</b>

diam=50 $\mu$ m	Glahn exp	
r (m)	ud (m/s)	t [s]
0.110115687	32.45434	<b>0.003393</b>
0.11503363	26.78082	<b>0.004295</b>
0.120093828	24.7032	<b>0.004861</b>
0.125254691	20.86758	<b>0.006002</b>
0.134932964	16.87215	<b>0.007997</b>
0.13999361	14.47489	<b>0.009671</b>

diam=50 $\mu$ m	deformed droplets	
r (m)	ud (m/s)	t [s]
0.110015134	34.13242	<b>0.003223</b>
0.114931171	29.81735	<b>0.003855</b>
0.120042934	25.98174	<b>0.00462</b>
0.125055377	22.94521	<b>0.00545</b>
0.13001816	20.30822	<b>0.006402</b>
0.134882071	18.15068	<b>0.007431</b>
0.139893169	16.07306	<b>0.008704</b>

**Table 8.4. Calculation of droplet journey time for initial diameters of 100 $\mu$ m for a shaft speed of 12000rpm.**

diam=100 $\mu$ m	sph simu		diam=100 $\mu$ m	deformed droplets	
r (m)	ud (m/s)	t [s]	r (m)	ud (m/s)	t [s]
0.065042017	39.41581	<b>0.0017</b>	0.064957983	39.48905	<b>0.0016</b>
0.067731092	35.32037	<b>0.0019</b>	0.067773109	35.32025	<b>0.0019</b>
0.070546218	31.8085	<b>0.0022</b>	0.070504202	29.32687	<b>0.0024</b>
0.073319328	28.8807	<b>0.0025</b>	0.073319328	24.50113	<b>0.0030</b>
0.07605042	26.68294	<b>0.0029</b>	0.076134454	21.35423	<b>0.0036</b>
0.078823529	24.63105	<b>0.0032</b>	0.078823529	18.71864	<b>0.0042</b>
0.081722689	23.01675	<b>0.0036</b>	0.081596639	16.88573	<b>0.0048</b>
0.084411765	21.84101	<b>0.0039</b>	0.084495798	15.70938	<b>0.0054</b>
0.087268908	20.73778	<b>0.0042</b>	0.087184874	14.9716	<b>0.0058</b>
0.089915966	19.70815	<b>0.0046</b>	0.09	14.08747	<b>0.0064</b>

**Table 8.5. Calculation of droplet journey time for initial diameters of 200 $\mu$ m for a shaft speed of 12000rpm.**

diam=200 $\mu$ m	sph simu		diam=200 $\mu$ m	deformed droplets	
r (m)	ud (m/s)	t [s]	r (m)	ud (m/s)	t [s]
0.065042017	39.5618	<b>0.0016</b>	0.065042017	39.63479	<b>0.0016</b>
0.067815126	37.80188	<b>0.0018</b>	0.067731092	37.80212	<b>0.0018</b>
0.070504202	36.11519	<b>0.0020</b>	0.070462185	34.43648	<b>0.0020</b>
0.073235294	35.01233	<b>0.0021</b>	0.073361345	31.6543	<b>0.0023</b>
0.076134454	33.83598	<b>0.0023</b>	0.076092437	29.52953	<b>0.0026</b>
0.078907563	33.02496	<b>0.0024</b>	0.078865546	27.84261	<b>0.0028</b>
0.081680672	32.35993	<b>0.0025</b>	0.081680672	26.37453	<b>0.0031</b>
0.084537815	31.62166	<b>0.0027</b>	0.084537815	25.41729	<b>0.0033</b>
0.087310924	31.17561	<b>0.0028</b>	0.087226891	24.46053	<b>0.0036</b>
0.09	30.58382	<b>0.0029</b>	0.089915966	23.72275	<b>0.0038</b>

**Table 8.6. Calculation of droplet journey time for initial diameters of 300 $\mu$ m for a shaft speed of 12000rpm.**

diam=300mm	sph simu		diam=300mm	deformed droplets	
r (m)	ud (m/s)	t [s]	r (m)	ud (m/s)	t [s]
0.065042017	39.41581	<b>0.0017</b>	0.065042017	39.5618	<b>0.0016</b>
0.067815126	38.31283	<b>0.0018</b>	0.067731092	37.72913	<b>0.0018</b>
0.070546218	37.20996	<b>0.0019</b>	0.070588235	36.11495	<b>0.0020</b>
0.073319328	36.61792	<b>0.0020</b>	0.073277311	33.99031	<b>0.0022</b>
0.076134454	35.80678	<b>0.0021</b>	0.076134454	32.30313	<b>0.0024</b>
0.078823529	35.21499	<b>0.0022</b>	0.07894958	30.90805	<b>0.0026</b>
0.081638655	34.62283	<b>0.0024</b>	0.081764706	29.65896	<b>0.0028</b>
0.084453782	34.17665	<b>0.0025</b>	0.084411765	28.70232	<b>0.0029</b>
0.087226891	33.80359	<b>0.0026</b>	0.087184874	27.9643	<b>0.0031</b>
0.09	33.35754	<b>0.0027</b>	0.09	27.22615	<b>0.0033</b>

**Table 8.7. Calculation of droplet journey time for initial diameters of 400 $\mu$ m for a shaft speed of 12000rpm.**

diam=400mm	sph simu		diam=400mm	deformed droplets	
r (m)	ud (m/s)	t [s]	r (m)	ud (m/s)	t [s]
0.065042017	39.5618	<b>0.0016</b>	0.065084034	39.56168	<b>0.0016</b>
0.067731092	38.82402	<b>0.0017</b>	0.067815126	38.75078	<b>0.0018</b>
0.070588235	37.86677	<b>0.0019</b>	0.070546218	36.91799	<b>0.0019</b>
0.073277311	37.34797	<b>0.0020</b>	0.073277311	35.23118	<b>0.0021</b>
0.076134454	36.6827	<b>0.0021</b>	0.076176471	33.98184	<b>0.0022</b>
0.078907563	36.16365	<b>0.0022</b>	0.078865546	32.73312	<b>0.0024</b>
0.081722689	35.86346	<b>0.0023</b>	0.081680672	31.92198	<b>0.0026</b>
0.084495798	35.4904	<b>0.0024</b>	0.084537815	31.11072	<b>0.0027</b>
0.087226891	35.11746	<b>0.0025</b>	0.087226891	30.44593	<b>0.0029</b>
0.09	34.8174	<b>0.0026</b>	0.089957983	29.85401	<b>0.0030</b>

## 8.7 User defined function to calculate the evaporation model in droplets and implement it in ANSYS Fluent

### 8.7.1 Validation of fuel droplets

```

/*****
This is the code to add the source terms to model the evaporation of fuel droplets in order to
validate the Stroto's case and Banerjee's case.

Date: 26-07-2017
Author:
Dafne Gaviria Arcila
Gas Turbine and Transmissions Research Centre (G2TRC)
The University of Nottingham
eaxdgl@nottingham.ac.uk
*****/

#include "udf.h"
#include "mem.h"
#include "sg_mem.h"
#include "sg.h"
#include "sg_mphase.h"

#define T_SAT 300.00 /*Temperature of saturation*/
#define Mair 28.966 /*molecular weight of air*/
#define Mhepv 100.204 /*molecular weight of n-heptane*/

real molefrac(real mass_frac, real M1, real M2)
{
    real x; /* x is mole fraction */
    if (mass_frac <= 0.0)
        x = 0.0;
    else
        x = M2 / (M2 + M1*((1. / mass_frac) - 1.));
    return x;
}

DEFINE_ADJUST(grad_allocation, domain)
{
    Thread *t;
    Thread **pt;
    cell_t c;

    Domain *pDomain = DOMAIN_SUB_DOMAIN(domain, P_PHASE);
    Material *mix_mat = mixture_material(pDomain);
    /*Allocating VOF gradients*/
    {
        Alloc_Storage_Vars(pDomain, SV_VOF_RG, SV_VOF_G, SV_NULL);
        Scalar_Reconstruction(pDomain, SV_VOF, -1, SV_VOF_RG, NULL);/*to calculate the gradients page 16
        tutorial of how to calculate the gradients*/
        Scalar_Derivatives(pDomain, SV_VOF, -1, SV_VOF_G, SV_VOF_RG, Vof_Deriv_Accumulate);
    }

    /*Allocating species gradients*/
    {
        Alloc_Storage_Vars(pDomain, SV_Y_0_RG, SV_Y_0_G, SV_NULL);
        Scalar_Reconstruction(pDomain, SV_Y_0, -1, SV_Y_0_RG, NULL);/*to calculate the gradients page 16
        tutorial of how to calculate the gradients*/
        Scalar_Derivatives(pDomain, SV_Y_0, -1, SV_Y_0_G, SV_Y_0_RG, NULL);
        yi_derivatives(pDomain, 0);
    }
}

```

```

}

/*Looping over Phase Cell threads in a mixture*/
mp_thread_loop_c(t, domain, pt)
{
  Thread *tp = pt[P_PHASE];

  begin_c_loop(c, t)
  {

    /*Storing memory to compute the VOF gradients*/
    #if RP_3D
    C_UDMI(c, t, 0) = sqrt(C_VOF_G(c, tp)[0] * C_VOF_G(c, tp)[0] +C_VOF_G(c, tp)[1] * C_VOF_G(c, tp)[1]
    +C_VOF_G(c, tp)[2] * C_VOF_G(c, tp)[2] );
    C_UDMI(c, t, 1) = sqrt(C_YI_G(c, tp, 0)[0]* C_YI_G(c, tp, 0)[0] + C_YI_G(c, tp, 0)[1]* C_YI_G(c,
    tp, 0)[1] + C_YI_G(c, tp, 0)[2]* C_YI_G(c, tp, 0)[2]);
    #endif

    #if RP_2D
    C_UDMI(c, t, 0) = sqrt(C_VOF_G(c, tp)[0] * C_VOF_G(c, tp)[0] + C_VOF_G(c, tp)[1] * C_VOF_G(c,
    tp)[1]);
    C_UDMI(c, t, 1) = sqrt(C_YI_G(c, tp, 0)[0]* C_YI_G(c, tp, 0)[0] + C_YI_G(c, tp, 0)[1]* C_YI_G(c,
    tp, 0)[1]);
    #endif

    /* Calculating the source term when there is evaporation*/
    C_UDMI(c, t, 2) = 0.0;
    if(C_T(c, pt[1]) > T_SAT)
    {
      C_UDMI(c, t, 2) = C_R(c, pt[0])*C_UDMI(c, t, 0)*C_UDMI(c, t, 1)*C_DIFF_EFF(c, tp, 0);
    }

  }
  end_c_loop(c, t)
}

DEFINE_MASS_TRANSFER(liq_gas_source1, c, t, from_index, from_species_index, to_index,
to_species_index)
{
  real m_lg;
  m_lg = C_UDMI(c, t, 2);
  return (m_lg);
}

```

## 8.7.2 Modelling of oil droplets inside bearing chamber conditions

```

/*****
This is code to add the source terms to model the evaporation of lubricant droplets
under bearing chamber conditions.

```

Date: 10-03-2018

Author:

Dafne Gaviria Arcila

Gas Turbine and Transmissions Research Centre (G2TRC)

The University of Nottingham

eaxdgl@nottingham.ac.uk

\*\*\*\*\*/

```

#include "udf.h"
#include "mem.h"
#include "sg_mem.h"
#include "sg.h"
#include "sg_mphase.h"

```

```

#define T_SAT 334.02 /*Temperature of saturation*/
#define rhoair 1.225 /*density of air kg/m3*/
#define rhooil 1010.8 /*density of oil PEC5*/
#define muair 1.79e-5 /*dynamic viscosity of air kg/ms*/
#define rad 1e-4 /*droplet radius m*/
#define diam 2e-4/*droplet diameter m*/
#define vair 5 /*initial velocity of air m/s*/
#define vd 6.9125431e-08 /*initial velocity of droplet m/s*/
#define pi 3.14159265358979323846 /* pi */

DEFINE_ADJUST(grad_allocation, domain)
{
  Thread *t;
  Thread **pt;
  cell_t c;

  Domain *pDomain = DOMAIN_SUB_DOMAIN(domain, P_PHASE);
  Material *mix_mat = mixture_material(pDomain);
  /*Allocating VOF gradients*/
  {
    Alloc_Storage_Vars(pDomain, SV_VOF_RG, SV_VOF_G, SV_NULL);
    Scalar_Reconstruction(pDomain, SV_VOF, -1, SV_VOF_RG, NULL);/*to calculate the gradients page 16
    tutorial of how to calculate the gradients*/
    Scalar_Derivatives(pDomain, SV_VOF, -1, SV_VOF_G, SV_VOF_RG, Vof_Deriv_Accumulate);
  }

  /*Allocating species gradients*/
  {
    Alloc_Storage_Vars(pDomain, SV_Y_0_RG, SV_Y_0_G, SV_NULL);
    Scalar_Reconstruction(pDomain, SV_Y_0, -1, SV_Y_0_RG, NULL);/*to calculate the gradients page 16
    tutorial of how to calculate the gradients*/
    Scalar_Derivatives(pDomain, SV_Y_0, -1, SV_Y_0_G, SV_Y_0_RG, NULL);
    yi_derivatives(pDomain, 0);
  }

  /*Looping over Phase Cell threads in a mixture*/
  mp_thread_loop_c(t, domain, pt)
  {
    Thread *tp = pt[P_PHASE];

    begin_c_loop(c, t)
    {

      /*Storing memory to compute the VOF gradients*/
      #if RP_3D
      C_UDMI(c, t, 0) = sqrt(C_VOF_G(c, tp)[0] * C_VOF_G(c, tp)[0] +C_VOF_G(c, tp)[1] * C_VOF_G(c, tp)[1]
      +C_VOF_G(c, tp)[2] * C_VOF_G(c, tp)[2] );
      C_UDMI(c, t, 1) = sqrt(C_YI_G(c, tp, 0)[0]* C_YI_G(c, tp, 0)[0] + C_YI_G(c, tp, 0)[1]* C_YI_G(c,
      tp, 0)[1] + C_YI_G(c, tp, 0)[2]* C_YI_G(c, tp, 0)[2]);
      #endif

      #if RP_2D
      C_UDMI(c, t, 0) = sqrt(C_VOF_G(c, tp)[0] * C_VOF_G(c, tp)[0] + C_VOF_G(c, tp)[1] * C_VOF_G(c,
      tp)[1]);
      C_UDMI(c, t, 1) = sqrt(C_YI_G(c, tp, 0)[0]* C_YI_G(c, tp, 0)[0] + C_YI_G(c, tp, 0)[1]* C_YI_G(c,
      tp, 0)[1]);
      #endif

      /* Calculating the source term when there is evaporation*/
      C_UDMI(c, t, 2) = 0.0;
      if(C_T(c, pt[1]) > T_SAT)
      {
        C_UDMI(c, t, 2) = C_R(c, pt[0])*C_UDMI(c, t, 0)*C_UDMI(c, t, 1)*C_DIFF_EFF(c, tp, 0);
      }
    }
  }
}

```

```

/*Calculating radius of droplet in a certain time*/
C_UDMI(c, t, 3) = 0.0;

C_UDMI(c, t, 3) = pow((C_UDMI(c, t, 0) / (4 * pi)), (1 / 2));

/*C_UDMI(c, t, 3) = pow(C_UDMI(c, t, 2) / (C_R(c, pt[0])*C_DIFF_EFF(c, tp, 0)*C_UDMI(c, t, 1) * 4
* pi), (1 / 2));*/

}
end_c_loop(c, t)
}

/*To free the memory allocated for the VOF gradients and species gradients*/

Free_Storage_Vars(pDomain, SV_VOF_RG, SV_VOF_G, SV_NULL);
Free_Storage_Vars(pDomain, SV_Y_0_RG, SV_Y_0_G, SV_NULL);
}

DEFINE_MASS_TRANSFER(liq_gas_source1, c, t, from_index, from_species_index, to_index,
to_species_index)
{
real m_lg;
m_lg = C_UDMI(c, t, 2);
return (m_lg);
}

DEFINE_ZONE_MOTION(fmotion, omega, axis, origin, vel, time, dtime)
{
real r;
real Re;
real Cd;
real C; /*Initial conditions constant*/

r = (sqrt(4e-8 - (1e-7*time))) / 2;
Re = (2 * rhoair*(vair)*r) / muair;
Cd = (24 / Re)*(1 + ((pow(Re, (2 / 3))) / 6));
C = (2 * r*rhooil) / (3 * Cd*rhoair*vair);

vel[2] = ((3*C*Cd*rhoair*vair) + (3 * time*Cd*rhoair*vair)-(2*r*rhooil)) / (3 *Cd*rhoair*(C +
time));

return;
}

```